



**A University of Sussex PhD thesis**

Available online via Sussex Research Online:

<http://sro.sussex.ac.uk/>

This thesis is protected by copyright which belongs to the author.

This thesis cannot be reproduced or quoted extensively from without first obtaining permission in writing from the Author

The content must not be changed in any way or sold commercially in any format or medium without the formal permission of the Author

When referring to this work, full bibliographic details including the author, title, awarding institution and date of the thesis must be given

Please visit Sussex Research Online for more information and further details



**Development of a planar magnetic field  
source for the Geonium Chip Penning  
Trap**

**John Henry Lacy**

Submitted for the degree of Doctor of Philosophy

University of Sussex

June 2018

# Declaration Of Authorship

I, John Henry Lacy, declare that this thesis titled, Development of a planar magnetic field source for the Geonium Chip Penning Trap, and the work presented in it are my own. I conrm that:

- This work was done wholly or mainly while in candidature for a research degree at this University.
- Where any part of this thesis has previously been submitted for a degree or any other qualification at this University or any other institution, this has been clearly stated.
- Where I have consulted the published work of others, this is always clearly attributed.
- Where I have quoted from the work of others, the source is always given. With the exception of such quotations, this thesis is entirely my own work.
- I have acknowledged all main sources of help.
- Where the thesis is based on work done by myself jointly with others, I have made clear exactly what was done by others and what I have contributed myself.

Date:

Signature:

John Henry Lacy

UNIVERSITY OF SUSSEX

JOHN HENRY LACY, DOCTOR OF PHILOSOPHY

Development of a planar magnetic field source for the Geonium Chip Penning TrapSUMMARY

This thesis presents the theoretical foundation and design of a planar magnetic field source for the Geonium Chip Penning trap. Conventional Penning traps are limited in their scalability by the size of their magnetic field sources, which often take the shape of large and expensive superconducting solenoids. For many practical applications, such as portable mass spectrometry and quantum radar, these conventional Penning trap systems would be unsuitable, due to their large size and need for very high currents (of the order of a few hundred amperes). The Geonium Chip Penning trap aims to overcome this problem by proposing a novel planar magnetic field source comprising several superconducting coils confined to a plane. The electrode surfaces of the trap sit less than a millimetre above the magnetic field source such that the trapping magnetic field is oriented parallel to the electrode surfaces.

In this thesis, I explore many of the fundamental design issues concerned with developing such a planar magnetic field source. In particular, I devise an entirely new scheme of remotely magnetising a plurality of closed superconducting loops to carry currents in persistent mode, and show how persistent supercurrents of hundreds of amperes can be remotely induced with input currents of the order of a few (one to two) amperes. I introduce, and experimentally verify, a theoretical framework that allows for a high degree of control over the magnetic field distribution. From this framework, I present an optimised design of a planar persistent current-mode magnetic field source theoretically capable of achieving a 0.1 T field homogeneous up to fourth order in the Taylor expansion about the trapping position. This magnetic field source is due to be constructed and tested in the coming months.

# Acknowledgements

Firstly, I would like to say thank you to my supervisor, José Verdú, for his support throughout my PhD. I would also like to thank my Geonium colleagues, both past, present, and honorary: Jonathan, April, Frances, Alberto, Ryan (Rocky), and Tomas, for your collaborative efforts and social events. Thanks also goes to the technicians, especially Antony and Maria, for keeping a ready supply of liquid nitrogen.

The biggest acknowledgements, of course, go out to those who are closest to me. Tel, without your constant care and nurture, getting to where I am today would simply not have been possible. Jim, Joe, and Bill, you have all done your bit in keeping me motivated and grounded, the way only brothers can. Felicity, you have been a friend I can truly count on, and Becky, growing to know you in the final phase of my PhD has meant ever so much to me. I would also like to say thank you to Rooney's Boxing Gym, especially to Franklin Sarfo, whose mentorship and guidance was always appreciated, and to Double Jab Amateur Boxing Club, who, for the past year, have given me an outlet to de-stress. The University of Sussex Counselling Service has helped me to cope with the more challenging times of the PhD journey, and for that, I am very grateful. A final thanks goes to the various pie and mash shops in London, whose nutritional content has no doubt kept me going on those long commutes from London to Brighton (which, over the years, add up to over  $5\frac{1}{2}$  times the circumference of the earth!)

# Contents

<b>List of Tables</b>	<b>x</b>
<b>List of Figures</b>	<b>xiv</b>
<b>1 Introduction</b>	<b>1</b>
1.1 The need for planarising the magnetic field source . . . . .	3
1.2 Thesis content . . . . .	4
<b>2 The trapping and detection of charged particles</b>	<b>8</b>
2.1 Theory of trapping charged particles . . . . .	8
2.1.1 Trapping charged particles with static fields . . . . .	8
2.1.2 Eigenmodes of trapped charged particles . . . . .	12
2.1.3 Penning trap ellipticity . . . . .	14
2.2 The principle of detecting trapped charged particles in a Penning trap . . .	16
<b>3 The Geonium Chip Penning trap</b>	<b>21</b>
3.1 The Geonium Chip concept . . . . .	21
3.2 Experimental setup of the Geonium Chip Penning trap . . . . .	26
3.3 Trapping fields of the Geonium Chip . . . . .	32
3.3.1 Electric trapping field of the Geonium Chip . . . . .	32
3.3.2 Magnetic trapping field of the Geonium Chip . . . . .	36
3.3.3 Properties of the prototype planar magnetic field source for the Geonium Chip Penning trap . . . . .	40
3.3.4 Summary of the trapping fields of the Geonium Chip Penning trap .	47
3.4 Applications of the Geonium Chip . . . . .	47
3.4.1 The Geonium Chip as a portable mass spectrometer . . . . .	47
3.4.2 The Geonium Chip as a single microwave photon detector . . . . .	48

<b>4</b>	<b>Fundamental elements of superconductivity for the Geonium Chip Penning trap</b>	<b>52</b>
4.1	Superconductor properties relevant to the Geonium Chip . . . . .	52
4.1.1	Zero resistivity . . . . .	52
4.1.2	Meissner-Oschenfeld effect . . . . .	54
4.2	Types of superconductors . . . . .	57
4.2.1	Type I and Type II superconductors . . . . .	57
4.2.2	High-temperature superconductors . . . . .	60
4.3	Superconducting materials . . . . .	62
4.3.1	High-temperature superconductor tapes . . . . .	62
4.3.2	Soldering to high-temperature superconducting tape . . . . .	63
4.3.3	Superconducting heat switches . . . . .	66
4.4	Flux conservation in closed superconducting paths . . . . .	68
4.4.1	Theoretical derivation of flux conservation . . . . .	69
4.4.2	Geometric approximation of self-flux in a closed loop . . . . .	71
4.5	Current distribution in thin superconducting materials of rectangular loop geometry . . . . .	73
4.5.1	Current distribution within a strip of high-temperature superconducting YBCO tape . . . . .	73
4.5.2	Current distribution within a closed rectangular loop of YBCO tape . . . . .	75
<b>5</b>	<b>Remote induction of persistent supercurrents in the Geonium Chip magnetic field source</b>	<b>78</b>
5.1	Introduction . . . . .	78
5.1.1	The need for flux pumping in the Geonium Chip . . . . .	79
5.2	Flux pumping mechanism for the Geonium Chip . . . . .	80
5.2.1	Reverse flux pumping mechanism . . . . .	90
5.2.2	Validity of the mathematical model for flux pumping . . . . .	94
5.2.3	Flux pumping method for several closed superconducting loops . . . . .	97
5.2.4	Hall probe array measurement of $\underline{\Gamma}'$ . . . . .	109
<b>6</b>	<b>Persistent current-mode planar superconducting magnetic field source</b>	<b>114</b>
6.1	Field requirements of the persistent current-mode planar magnetic field source	114
6.1.1	Design considerations . . . . .	116
6.1.2	Determination of dimensions of planar magnetic field source . . . . .	120

6.1.3	Planar magnetic field source design . . . . .	127
6.2	Improvements to the driven-current planar magnetic field source . . . . .	130
6.2.1	Stabilisation coils . . . . .	130
<b>7</b>	<b>Summary and outlook</b>	<b>136</b>
7.1	Summary . . . . .	136
7.2	Outlook . . . . .	138
	<b>Bibliography</b>	<b>140</b>
<b>A</b>	<b>Summary of flux pumping mechanisms</b>	<b>149</b>
<b>B</b>	<b>Magnetic field source data</b>	<b>154</b>

# List of Tables

3.1	Table comparing expected and measured magnetic field distributions for different sets of required currents in the prototype magnetic field source. . .	44
4.1	Table showing simulated distortions to the magnetic field distributions due to the Meissner-Oschenfeld effect. $B_z^{\text{Cu}}$ describes the magnetic field due to current in the simulated copper wire, whilst $B_z^{\text{SC}}$ refers to the magnetic field from the simulated superconducting wire. The data shows that there is significant distortion to the magnetic field distribution, and this is particularly severe for the $\partial_y B_z$ term. . . . .	57
4.2	Table comparing the properties of three commercially available YBCO-based HTS tapes. Two samples of <i>Bruker</i> YBCO tape were obtained, and, despite having the same nominal widths and compositions, they differed in critical current. . . . .	64
5.1	Table showing obtained fitting parameters for different methods of flux pumping. . . . .	91
5.2	Table comparing the expected and measured magnetic field distributions. .	109
5.3	Simulated data for a measurement of the magnetic field distribution using a <i>MULTI-7U Arepoc</i> Hall probe array. . . . .	111
6.1	Table summarising the various dimensions of magnetic field source that were considered. An initial thickness of $t = 1$ mm was considered. . . . .	121
6.2	Table showing, for each proposed magnetic field source geometry, the current densities required to produce target field of 0.5 T at 1.6 mm above the source. The thickness of the loops used in this calculation is $t = 1$ mm. . . .	121

- 6.3 Table showing simulated data for different dimensions of magnetic field source. A target field of 0.5 T at 1.6 mm above the source was used. The table shows the required current densities to achieve this for each geometry. A thickness of 1 mm was considered.  $B_i$  denotes the magnetic field strength on loop  $i$ , and  $F_i$  denotes the force on loop  $i$ . . . . . 122
- 6.4 Table showing the magnetic field strengths and forces on each loop for configuration 9 with different desired fields. In each case, a loop thickness of 1 mm was considered.  $B_i$  denotes the magnetic field on the  $i$ th coil, whilst  $F_i$  denotes the force on the  $i$ th coil. . . . . 125
- 6.5 Table showing the current densities required for various homogeneous magnetic fields at 1.6 mm above the planar magnetic field source for different target fields. The magnetic field source dimensions considered are those corresponding to configuration 9 with a loop thickness of 1 mm. . . . . 126
- A.1 Table summarising the standard flux pumping scheme for a double-loop superconducting structure. When consulting this table, refer to Figure 5.5. 150
- A.2 Table summarising the flux subtraction scheme for a double-loop superconducting structure. When consulting this table, refer to Figure 5.9. . . . . 151
- A.3 Table summarising the flux pumping scheme for double-loop structures with overlapping Target Loops. When consulting this table, refer to Figure 5.12. “U” and “ $u$ ” refer to the upper double-loop superconducting structure, and “L” and “ $l$ ” refer to the lower double-loop superconducting structure. . . . . 152
- A.4 Table summarising the flux pumping scheme for double-loop structures with adjacently placed Target Loops. When consulting this table, refer to Figure 5.12. “L” and “ $l$ ” refer to the left-hand double-loop superconducting structure, and “R” and “ $r$ ” refer to the double-loop superconducting structure on the right-hand side. . . . . 153
- B.1 Table showing the current densities required to achieve a 0.5 T homogeneous field at a height of 1.6 mm above the planar magnetic field source for configuration 9 with various thicknesses. . . . . 155

B.2 Table showing the magnetic fields and forces on each loop of configuration 9 for different thicknesses. For each case, a desired homogeneous magnetic field of 0.5 T at a height of 1.6 mm is considered. Calculations for 0.50 mm and 0.75 mm are not considered because the corresponding current densities exceed $J_c$ of niobium-titanium. . . . .	156
---	-----

# List of Figures

1.1	The FT-ICR mass spectrometer at Warwick University . . . . .	2
1.2	A graph comparing mass spectrometers on their price and mass resolution . . . . .	4
1.3	The prototype planar magnetic field source . . . . .	5
1.4	CAD design of the persistent current-mode planar magnetic field source . . . . .	6
2.1	A sketch of the electric field lines illustrating Earnshaw's theorem . . . . .	9
2.2	Motion of a charge in a uniform magnetic field . . . . .	10
2.3	Depiction of the trapping fields of the Geonium Chip Penning trap . . . . .	11
2.4	Motion of a trapped electron in a Penning trap . . . . .	13
2.5	Electric field lines due to an electron above a conducting surface . . . . .	16
2.6	Schematic diagram of the detection circuit in a Penning trap . . . . .	18
2.7	Detection signal of electrons in a Penning trap . . . . .	20
3.1	The projection of a cylindrical Penning trap onto a plane . . . . .	22
3.2	Coordinate axes of the Geonium Chip . . . . .	22
3.3	Sketch of the electric and magnetic field source arrangements in the Geonium Chip Penning trap . . . . .	23
3.4	A sketch showing the natural symmetry of the Geonium Chip . . . . .	24
3.5	The double Penning trap at Heidelberg . . . . .	26
3.6	Dimensions of the first generation Geonium Chip from <i>MIR Enterprises Ltd.</i> . . . .	27
3.7	Photograph of a Geonium Chip from <i>PW Circuits Ltd.</i> . . . . .	28
3.8	Photograph of the cryogenic vacuum chamber attached to a <i>MIR</i> chip . . . . .	29
3.9	Prototype magnetic field source . . . . .	29
3.10	CAD drawing of magnetic field source and cryogenic vacuum chamber . . . . .	30
3.11	Photograph of the experimental setup inside the cryostat . . . . .	31
3.12	The outer vacuum chamber of the Geonium Chip Penning trap experimental setup . . . . .	32

3.13	A graph showing the frequency shifts as a function of the tuning ratio, $T_c$	35
3.14	A graph showing how the detection signal of a single electron depends on the magnetic field gradient, $B_{010}$	38
3.15	Experimental apparatus for $\Gamma$ matrix measurement	41
3.16	Photograph of a magnetic field mapping calibration measurement of the prototype magnetic field source	41
3.17	A graph showing the axial component of the measured magnetic field for the main wire of the prototype magnetic field source	43
3.18	Data showing the valid range of the first order approximation of the $\Gamma$ matrix	45
3.19	Schematic diagram of single microwave photon detection in the Geonium Chip	49
3.20	CAD drawing of the <i>Sumitomo</i> pulse tube cryostat with Adiabatic Demagnetisation Refrigerator	50
3.21	The transmissivity of the <i>MIR</i> chip to microwave fields at 18 GHz	51
4.1	Critical parameters of YBCO superconductor	53
4.2	A 3 mm neodymium magnet levitating above a strip of <i>Superpower</i> YBCO tape	55
4.3	<i>FEMM</i> simulations of magnetic field distortion due to the Meissner-Oschenfeld effect	56
4.4	A schematic diagram showing the origin of flux creep	58
4.5	A graph showing the magnetic field decay due to flux creep	59
4.6	A schematic diagram of field cooling	60
4.7	A graph of the $E - J$ power law for different $n$ values	61
4.8	Cross-section of the <i>Superpower</i> High Temperature Superconductor (YBCO) tape	62
4.9	Remanent magnetisation in <i>American Superconductor</i> YBCO tape	63
4.10	Soldering to High Temperature Superconducting tape	65
4.11	Photographs of superconducting heat switches for YBCO tape	66
4.12	Standard 4-wire resistance measurement of a superconducting heat switch	67
4.13	Experimental setup for determining heat switch operation in a ‘Y’ shaped superconducting structure by observing a shift in current in the superconducting paths	68
4.14	Magnetic field mapping measurement to determine heat switch operation	69

4.15	Equivalent circuit of a rectangular conductor subjected to a time-varying magnetic field . . . . .	70
4.16	Dimensions of a closed rectangular conducting loop . . . . .	71
4.17	Graphs of self-inductance as a function of perimeter length for closed rectangular and square conducting loops . . . . .	72
4.18	Graphs showing the measured vertical component of the magnetic field distribution above a length of 12 mm wide <i>Superpower</i> YBCO tape carrying 2 A of current . . . . .	74
4.19	Cross-section of a thin-film current-carrying wire. . . . .	74
4.20	Data showing the measured vertical component of the magnetic field distribution, and corresponding inferred current distribution, from a square closed superconducting loop carrying current . . . . .	77
5.1	A sketch showing the excitation of a conventional superconducting magnet .	79
5.2	CAD drawing of a double-loop superconducting structure from the planar magnetic field source . . . . .	81
5.3	Photographic and schematic depictions of a double-loop superconducting structure . . . . .	82
5.4	Sketch of the general geometry of a double loop superconducting structure .	82
5.5	Schematic representation of flux pumping in a double loop superconducting structure . . . . .	84
5.6	A superconducting circuit subjected to flux pumping . . . . .	89
5.7	A characteristic curve of flux pumping showing measured magnetic field against pumping cycle number for various input currents . . . . .	89
5.8	Graphs showing the obtained magnetic field as a function of input current after one cycle, and after the magnetic field plateaus . . . . .	90
5.9	Schematic representation of flux pumping in a double loop superconducting structure . . . . .	95
5.10	A graph of the measured magnetic field for various different flux pumping schemes . . . . .	96
5.11	A depiction of cross-talk between neighbouring superconducting loops . . .	97
5.12	Flux pumping scheme of two double-loop superconducting structures with overlapping Target Loops . . . . .	99
5.13	Flux pumping scheme for two double-loop superconducting structures with adjacently placed Target Loops. . . . .	105

5.14	Experimental setup for $\Gamma'$ matrix measurements . . . . .	106
5.15	Plot of the measured magnetic field as a function of input currents for two adjacently placed double loop structures . . . . .	108
5.16	Plot of the measured magnetic field as a function of input currents for two adjacently placed double loop structures . . . . .	108
5.17	Sketch of the magnetic field source cryogenic calibration setup with Hall probe array . . . . .	109
5.18	Graph showing the effect of overlap parameter, $m$ , on flux pumping . . . .	113
6.1	General dimensions of the magnetic field source for optimisation . . . . .	118
6.2	Top and side views of the planar magnetic field source showing trapping height and superconductor thickness . . . . .	119
6.3	Sketch of two parallel rectangular current-carrying wires . . . . .	123
6.4	Top view scale drawing of the persistent current-mode planar magnetic field source. The direction of the trapping magnetic field is depicted by the green arrows. . . . .	127
6.5	Overall design of the persistent current-mode planar magnetic field source .	128
6.6	CAD drawing showing the superconducting bridges between the Pumping Loops and the Target Loops . . . . .	129
6.7	A schematic diagram illustrating magnetic field stabilisation . . . . .	130
6.8	A schematic drawing of the experimental setup used to test magnetic field source stabilisation . . . . .	131
6.9	Graph showing magnetic field stabilisation for a zero-field cooled set of stabilisation coils . . . . .	132
6.10	Graph showing magnetic field stabilisation for a field-cooled set of stabilisation coils with source configuration $(I_{\text{Left}}, I_{\text{Right}}) = (0, 10)$ A. . . . .	133
6.11	A graph showing magnetic field source stabilisation as a function of height above the stabilisation coils in the setup of Figure 6.8 . . . . .	135

# Chapter 1

## Introduction

A Penning trap uses a combination of static electric and magnetic fields to confine charged particles in space. The first operational Penning trap – built in 1959 by Hans Dehmelt – was inspired by the Penning ion pressure gauge [1], and successfully trapped electrons for around 10 seconds [2]. Since then, Penning trap technology has grown enormously, and has become a vital experimental tool for testing fundamental theories in physics [3]. For instance, the most stringent tests on quantum electrodynamics have been made with Penning traps [4]. Other Penning trap uses include the measurement of fundamental constants, such as the mass of the electron [5], the testing of CPT invariance [6, 7, 8, 9, 10, 11, 12], and the investigation of exotic atomic nuclei [13, 14].

Penning traps also have applications in the industrial world, most notably, in mass spectrometry, where Penning trap-based mass spectrometers are of the highest precision available [15]. Mass spectrometry has applications in the medical, petrochemical, and defence sectors, and has an estimated market of \$ 3Bn [16].

Proposals have also been made for Penning traps to play a vital role in quantum information [17, 18, 19]. Despite Paul traps – ion traps based on radio frequency (RF) trapping fields, rather than static trapping fields [20] – being the leading platform in the quest for the realisation of quantum computers [21, 22, 23, 24, 25],<sup>1</sup> a single electron in a Penning trap can, in principle, also be used for these purposes [17, 18, 26].<sup>2</sup> In such proposals, qubits are encoded in the spin of a trapped electron. A quantum processor is achieved by having an array of such trapped electrons, where two-qubit gates are achieved

---

<sup>1</sup>Among other advantages, Paul traps provide for long trapping lifetimes of ions, strong ion-ion interactions in trapped ion chains, and long-internal state coherence, which are all necessary for the effective operation of gates required for a universal quantum computer. A more detailed discussion is given in [27].

<sup>2</sup>Moreover, decoherence can be more readily addressed in a Penning trap, due their use of static fields and cryogenic temperatures [28].



Figure 1.1: The FT-ICR mass spectrometer in Warwick university [41] showing a typical size magnetic field source (the cylindrical structure on the left). On the right is the electrospray ionisation source.

by inducing effective spin-spin interactions. It was this such proposal which provided the motivation for the very first planar Penning trap [29]. Whilst there have been a number of planar traps since [29, 30, 31, 32], none have conclusively reached single electron resolution. This is attributed to a lack of mirror symmetry in the trapping field [32, 33]. At present, the detection of a single electron in a planar Penning trap therefore remains an open experimental challenge.

The Geonium Chip<sup>3</sup> Penning trap aims to overcome this challenge. Unlike other planar Penning traps, the Geonium Chip trapping magnetic field is oriented parallel to the electrode surfaces [35]. This allows for mirror symmetry in the trapping fields to be imposed explicitly. Its planar magnetic field source [36, 37] means that the Geonium Chip would be the very first *truly* planar Penning trap,<sup>4</sup> and has been shown theoretically to permit for the detection of a single electron [38]. Details on its experimental development are documented in [39, 40]. Single electron detection is expected in the near future.

---

<sup>3</sup>Named after The Geonium Atom – a term coined by Dehmelt to describe a single electron bound to an apparatus fixed on earth [34].

<sup>4</sup>In the sense that *both* the electric and the magnetic field sources are planar.

## 1.1 The need for planarising the magnetic field source

The practical limit of Penning traps is in the size of the magnetic field source [38]. Typical Penning trap magnetic field sources come in the form of superconducting magnets, such as the one shown in Figure 1.1. Whilst excellent in their magnetic field performance (some have temporal magnetic field fluctuations that permit for the motional frequencies of charged particles to be determined with a fractional uncertainty of  $10^{-11}$  [3]), conventional “room-size” Penning trap magnets are grossly unscalable [38]. Their high input currents ( $> 100$  A) and associated thick-rod vacuum feedthroughs add practical complications to the cryostat, such as heat dissipation and unwanted use of space [42]. A miniaturised planar magnetic field source, operating with low input currents, would offer considerable improvements in terms of spatial and energetic efficiency.

A planar magnetic field source could allow for Penning traps to drive innovation in other fields. One example is single microwave photon detection, whose theoretical viability in the Geonium Chip Penning trap was recently demonstrated [19]. An efficient single microwave photon detector is still missing from quantum technology [43], and has a range of potential applications, including observation of the interstellar medium [19], quantum microscopy [44], and quantum radar [45]. Whilst single microwave photons have been detected with an electron in a Penning trap in the past [46], the Geonium Chip<sup>5</sup> setup is significantly more practical, owing to its compact, planar magnetic field source [19].

The planar magnetic field source also provides the Geonium Chip with a potentially favourable position in the mass spectrometry market [16]. Current portable mass spectrometers [47] are limited in their mass resolution, and serve only for fast or preliminary analysis of samples. On the other hand, high precision Fourier Transform Ion Cyclotron Resonance (FT-ICR) mass spectrometers tend to be large and expensive [16]. The Geonium Chip Penning trap offers a compromise, providing a potential five-fold improvement over portable systems in terms mass resolution, whilst being less than a quarter of the price of FT-ICR mass spectrometers (see Figure 1.2). This is particularly appealing for on-site analysis, such as the inspection of foods at ports, or the analysis of petrochemicals near mines. Current portable mass spectrometers do not have the required resolution, while the use of high precision mass spectrometers off-site would be unwantingly slow, and potentially financially penalising.

It is hoped that the above has provided a flavour of the impact a truly planar Penning

---

<sup>5</sup>In this thesis, the term ‘Geonium Chip’ may either refer to the Penning trap as a whole, or the chip-based electrode structure. It is hoped that the context they are used in will eliminate any ambiguity.



Figure 1.2: A graph showing estimated mass resolution against price for various types of mass spectrometers. The Geonium Chip Penning trap offers a considerably higher resolution than those provided by similarly priced alternatives.

trap could have. Planarisation of the magnetic field source is key to achieving impact in the abovementioned fields and markets, and, because Penning traps are so versatile, has the potential to accelerate innovation in areas far removed from fundamental physics.

## 1.2 Thesis content

This thesis details the experimental and theoretical development of a planar magnetic field source for the Geonium Chip Penning trap. Whilst a prototype already exists (see Figure 1.3), it is limited because it runs on driven currents. This means that a power supply must be kept on for as long as the trap is running, which, in addition to poor energy efficiency, inevitably introduces systematic drifts and unwanted fluctuations in the trapping field. In order to compete with conventional Penning traps, a stable magnetic field (with time-dependent fractional fluctuations of around  $10^{-8} - 10^{-9}$  per hour [48, 49]) is a necessity. Hence, a new planar magnetic field source that runs on *persistent currents* is conceived, and this forms the content of the thesis. Its design is pictured in Figure 1.4, and its main features are summarised as follows:

- The magnetic field source consists of five pairs of double-loop superconducting structures (pictured in grey). These loops comprise a smaller *Pumping Loop*, and a larger *Target Loop*. Flux is injected into each superconducting structure via pumping solenoids (depicted as yellow cylinders in Figure 1.4) placed in the Pumping Loop. The

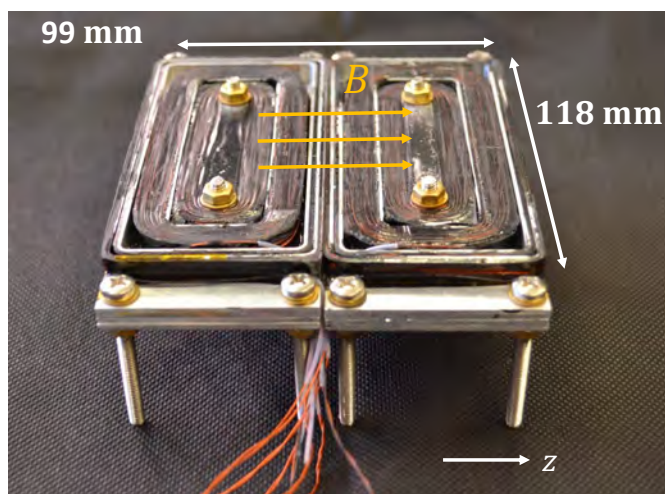


Figure 1.3: The prototype planar magnetic field source (designed by J Verdú and manufactured by J Pinder [39, 40]). It consists of four symmetrically arranged pairs of planar coils made from niobium-titanium wire (0.4 mm in diameter). The coils are set in Stycast epoxy and fixed to aluminium formers. The wires at the bottom of the image are connected to a *Rohde & Schwarz HMP4040* precision power supply. The trapping magnetic field,  $B$ , points parallel to the  $z$  direction, as shown by the orange arrows.

induced persistent currents in the Target Loops provide the trapping magnetic field.

- Excluding the rest of the experimental apparatus, the magnetic field source has an estimated volume of  $6 \text{ cm}^3$ , and weight of 0.1 kg.
- There are 12 input currents (not pictured), all carrying less than one ampere. 10 of these input currents are supplied to the pumping solenoids. The other 2 currents are supplied to the heat switches.
- The currents that provide the trapping field are induced remotely via a novel scheme of magnetic flux pumping (see §5). This scheme uses small input currents ( $\sim 1 \text{ A}$ ) and does not require physical contact with the superconducting circuitry.
- The magnetic field source can be easily calibrated at any chosen location (as discussed in §5.2.4).
- The magnetic field source has full control over the magnetic field distribution up to fourth order in the Taylor expansion about the trapping position. Arbitrary magnetic field distributions, in terms of both the magnetic field strength and the shape of the magnetic field distribution, can be produced and altered at high speed

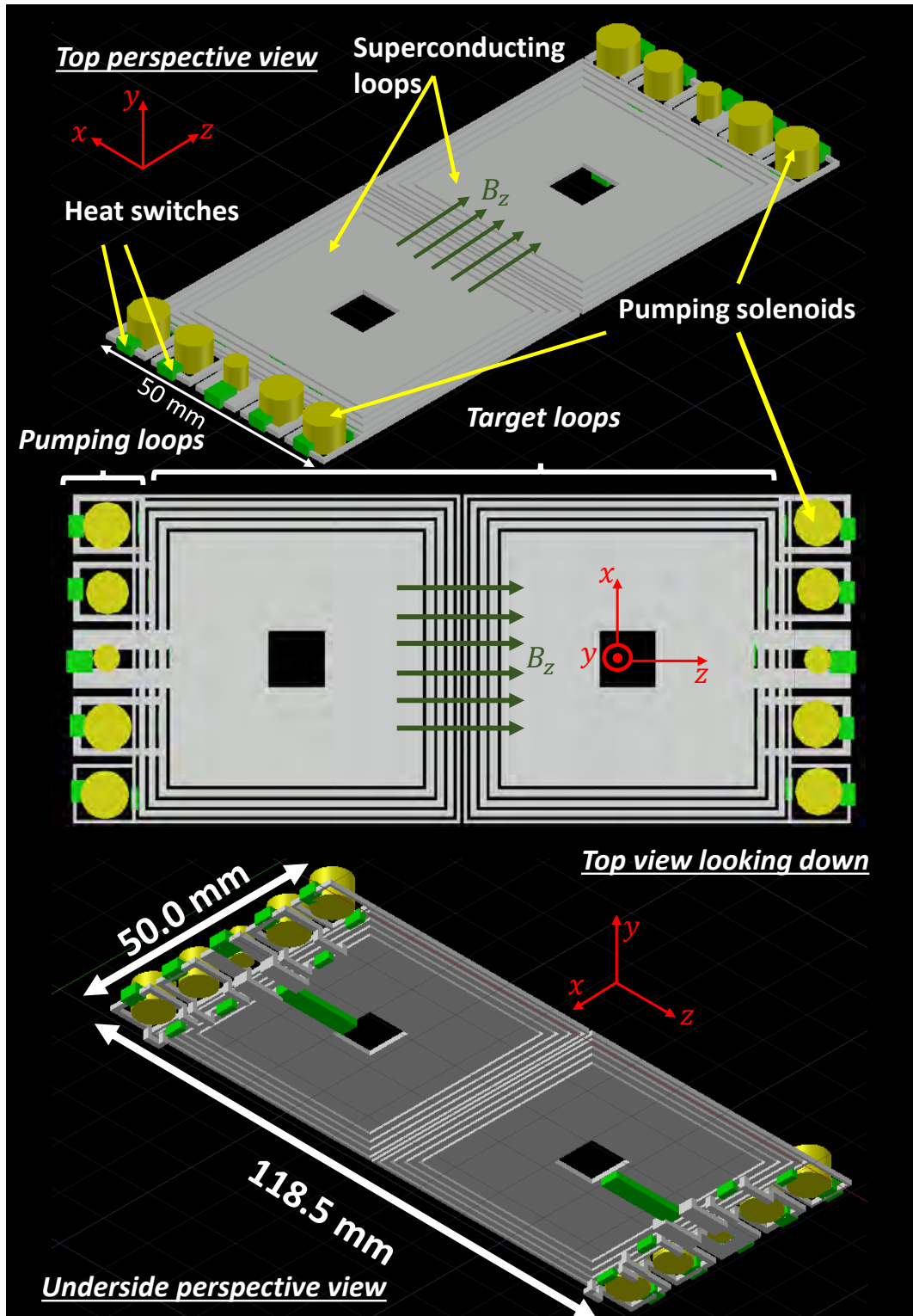


Figure 1.4: CAD model of the persistent current-mode planar magnetic field source. It comprises five pairs of planar superconducting double-loop structures. Magnetic flux is injected into the device by applying currents (not shown) to the pumping solenoids (picture in yellow) and the heat switches (pictured in green) in a carefully controlled sequence of magnetic flux pumping (see §5). The direction of trapping magnetic field,  $B$ , is represented by the green arrows.

(less than a minute) *in situ*, provided the required currents do not exceed the critical parameters of the superconducting materials. The extent of this flexibility in terms of the magnetic field distributions that can be produced will ultimately have to be investigated empirically.

- The use of persistent currents provides excellent magnetic field stability.
- For the design presented, magnetic fields of at least 0.1 T are theoretically achievable. In the future, fields exceeding 0.5 T are expected.
- The magnetic field source is cheap, costing £1000-£2000 to manufacture.<sup>6</sup>
- Whilst the current design operates at  $< 9.3$  K (the critical temperature of niobium-titanium [40, 50]), in future, the use of high-temperature superconductors may permit for operating temperatures of up to 90 K.
- The magnetic field source is energetically efficient, since it does not require continuous running of currents.

The thesis is structured as follows. The fundamental concepts of trapping and detecting charged particles in Penning traps are introduced in §2. §3 discusses the main features of the Geonium Chip Penning trap, including some of its applications. §4 introduces the properties of superconductors that are *essential* for the operation of the planar magnetic field source. §5 gives a comprehensive treatment of a particular scheme of magnetic flux pumping – the method upon which the planar magnetic field source is to be magnetised. A mathematical model for the above-mentioned flux pumping scheme is derived and experimentally verified. In §6, the final design of the planar magnetic field source is presented, along with optimisation schemes for the prototype magnetic field source, sometimes referred to as the *driven-current magnetic field source*, to emphasise that it does not run in persistent current-mode. The thesis is concluded with a summary given in §7.

---

<sup>6</sup>Excluding the cost of research and development investment, and the price of the rest of the experimental setup.

## Chapter 2

# The trapping and detection of charged particles

Before the Geonium Chip Penning trap is discussed in detail in §3, the basic principles of trapping and detecting charged particles in a Penning trap are outlined here. §2.1 is concerned with the field requirements for trapping, along with a description of the distinct motional modes of a trapped particle. §2.2 deals with the fundamental principles of charged particle detection. Although the concepts of this chapter apply to all variations of Penning trap, the reader is encouraged to keep in mind the planar configuration of the Geonium Chip.

## 2.1 Theory of trapping charged particles

### 2.1.1 Trapping charged particles with static fields

#### Earnshaw's Theorem

Charged particles cannot rest in a stable equilibrium under the influence of electrostatic forces alone. This idea dates back to 1842, when Samuel Earnshaw published his seminal work “*On the Nature of the Molecular Forces which regulate the Constitution of the Luminiferous Ether*” [51].<sup>1</sup> The basic concept is that, for an arrangement of objects interacting via inverse-square law forces<sup>2</sup> (such as the electrostatic force), the total force,  $\mathbf{F}$ ,

<sup>1</sup>Although published in 1842, the work was first presented to the Cambridge Philosophical Society in March 1839.

<sup>2</sup>For  $N$  particles each interacting via forces that have a power law dependence on separation, the total force on one particle at position,  $\mathbf{r}$ , is  $\mathbf{F} = \sum_i^N k_i (\mathbf{r} - \mathbf{r}_i) |\mathbf{r} - \mathbf{r}_i|^{n-1}$ , where  $\mathbf{r}_i$  denotes the position of the  $i$ th particle. Thus, in 3-dimensional space, the divergence is  $\nabla \cdot \mathbf{F} = \sum_i^N k_i (n+2) |\mathbf{r} - \mathbf{r}_i|^{n-1}$ , meaning that for inverse-square law forces ( $n = -2$ ) the divergence of the force is always  $\nabla \cdot \mathbf{F} = 0$ .

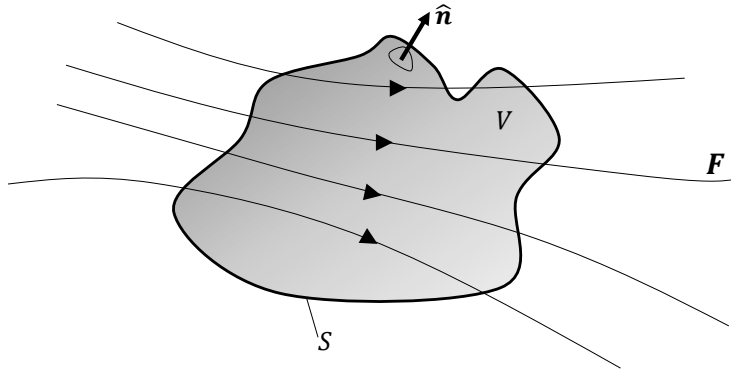


Figure 2.1: A sketch showing the zero divergence property of static force lines. All force lines that enter the volume,  $V$ , also leave. This is true for any arbitrarily shaped volume.

on any object has a vanishing divergence,

$$\nabla \cdot \mathbf{F} = 0. \quad (2.1)$$

Integrating Equation (2.1), and appealing to Gauss' law, this can be recast in a more intuitive form:

$$\int_V \nabla \cdot \mathbf{F} = \int_S \mathbf{F} \cdot d\mathbf{S} = 0. \quad (2.2)$$

Put in words, Equation (2.2) states that for any volume,  $V$ , in space, bounded by a surface,  $S$ , all lines of force that enter into the volume must also leave (see Figure 2.1). Thus, any object residing inside the volume will necessarily be forced out. Given the arbitrariness of the choice of  $V$  (and hence  $S$ ) we see that this is true for any point in space.<sup>3</sup>

In addition to electrostatic forces, it is also the case that charged particles cannot be stably confined with a purely magnetostatic field.<sup>4</sup> A particle of charge,  $q$ , moving in a magnetic field,  $\mathbf{B}$ , with a velocity,  $\mathbf{v}$ , experiences a force given by

$$\mathbf{F} = q(\mathbf{v} \times \mathbf{B}). \quad (2.3)$$

<sup>3</sup>Other discussions of Earnshaw's theorem (found throughout the literature) consider the potential energy landscape instead, but the ideas are equivalent.

<sup>4</sup>There are exceptions to this rule. For example, diamagnetic materials have been confined with static magnetic fields [52]. Storage rings also provide stable confinement of charges, but this is beyond the scope of this work. Here we are concerned with the confinement of a charge *around single equilibrium point in space*. Magnetic mirrors can confine charges, but they are inherently lossy [53].

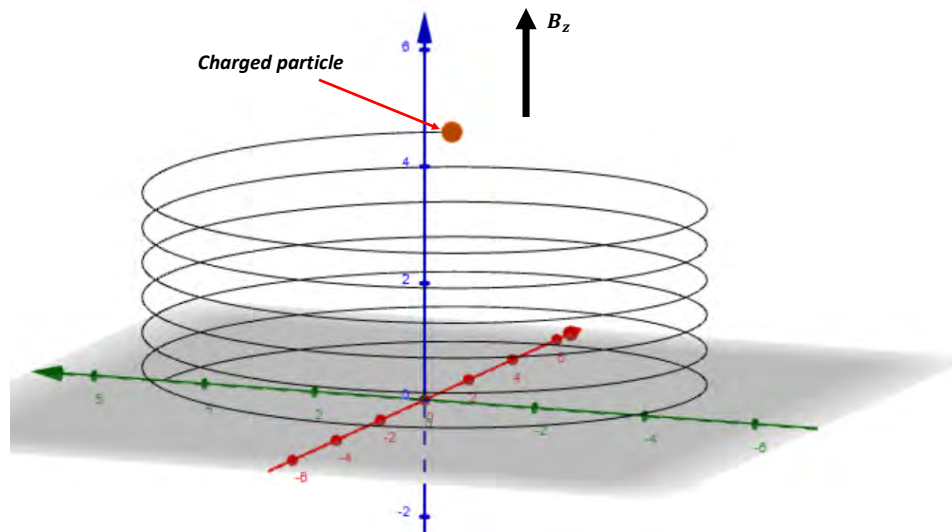


Figure 2.2: A simulation of the trajectory of a charge in a uniform magnetic field. The charge spirals along the direction parallel to the magnetic field. The image was rendered by [54], an open-source simulation program.

The consequence of the cross-product is that the component of velocity parallel to  $\mathbf{B}$  remains unchanged, meaning that the particle traverses a helical path spiralling around the magnetic field lines (see Figure 2.2). Whilst stable trapping may appear possible under the condition that  $\mathbf{v}$  and  $\mathbf{B}$  are perfectly orthogonal, this does not form a *stable* equilibrium. Any perturbation in  $\mathbf{v}$  parallel to  $\mathbf{B}$  will result in the particle veering off indefinitely.

### Combination of electrostatic and magnetostatic fields

Whilst Earnshaw's theorem precludes charged particle confinement with either purely electrostatic or purely magnetostatic fields, when used in combination a certain configuration of static electric and magnetic fields can be chosen which allows for stable trapping of charged particles.<sup>5</sup> Particle confinement can be achieved with a homogeneous magnetic field and a quadrupolar electric field (see Figure 2.2). Intuitively, one can think that the magnetic field confines charged particles *radially*, whilst the electric field prevents the charges from flying off along the *axial* direction (the direction parallel to the magnetic field, conventionally labelled the  $z$  axis). In conventional notation, these trapping fields

<sup>5</sup>It is also possible to trap charged particles with the use of time-varying fields. This is the basis behind the operation of a Paul Trap [20]. Further discussion falls beyond the scope of this thesis.

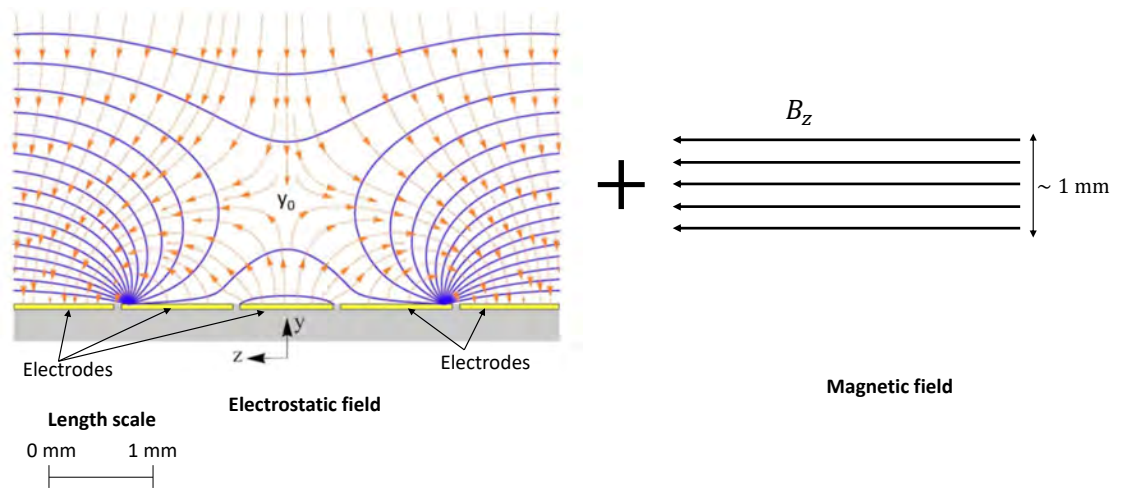


Figure 2.3: **Left:** A sketch of the required quadrupolar trapping field of the Geonium Chip [40]. The blue lines are lines of equipotential, whilst the orange arrows depict the trapping electric field. The trapping position is labelled  $y_0$ , and it can be seen that this field alone would not permit the trapping of charged particles. **Right:** A sketch of a homogeneous magnetic field. Superimposing the electric and magnetic fields gives the trapping fields of the Penning trap. The Geonium Chip magnetic field source is homogeneous in a volume of around  $1 \text{ mm}^3$  around the trapping position. This is sufficient for the trapping of an electron, whose motion is confined to a volume of less than  $500 \text{ } \mu\text{m}^3$ .

are written as  $\mathbf{B} = (0, 0, B_0)$  and  $\mathbf{E} = -\nabla\phi$ , where  $\phi = U_0 C_{002} (z^2 - \frac{1}{2}(x^2 + y^2))$  is the electric potential,  $C_{002}$  is the curvature of the potential along  $z$ , and  $U_0$  is related to the potential energy minimum provided by the electrostatic field. Thus, a particle of charge,  $q$ , and mass,  $m$ , moving in the trapping region will experience a total force given by

$$\mathbf{F} = m\ddot{\mathbf{r}} = -q\nabla\phi + q\dot{\mathbf{r}} \times \mathbf{B}, \quad (2.4)$$

which, in Cartesian coordinates, is rendered as

$$m \begin{pmatrix} \ddot{x} \\ \ddot{y} \\ \ddot{z} \end{pmatrix} = qU_0C_2 \begin{pmatrix} x \\ y \\ -2z \end{pmatrix} + qB_0 \begin{pmatrix} \dot{y} \\ -\dot{x} \\ 0 \end{pmatrix}. \quad (2.5)$$

Solving for  $\mathbf{r}(t) = (x(t), y(t), z(t))$  shows that the particle is confined in space.<sup>6</sup>

### 2.1.2 Eigenmodes of trapped charged particles

The algebraic solution of Equation (2.5) is [55]

$$x(t) = A_+ \cos(-\omega_+ t - \alpha_+) + A_- \cos(-\omega_- t - \alpha_-) \quad (2.6)$$

$$y(t) = y_0 - A_+ \sin(-\omega_+ t - \alpha_+) - A_- \sin(-\omega_- t - \alpha_-) \quad (2.7)$$

$$z(t) = A_z \cos(\omega_z t - \alpha_z). \quad (2.8)$$

Expressed another way, a charged particle in a Penning trap comprises three distinct oscillatory modes: a *cyclotron* mode, with an amplitude,  $A_+$ , angular frequency,  $\omega_+$ , and phase,  $\alpha_+$ ; a *magnetron* mode, with properties denominated similarly to the cyclotron mode, only with “-” replacing “+”; and an *axial* mode, characteristically labelled with a “z” subscript. The general motion of a trapped particle is a superposition of these three modes, and is depicted in Figure (2.4). The spatial centre of the trapped particle’s motion is termed the trapping position, which, in the coordinate system of the Geonium Chip Penning trap, is defined as  $\mathbf{r}_0 = (0, y_0, 0)$ .

The axial mode can be viewed as a simple harmonic oscillation along the  $z$  axis. The cyclotron and magnetron modes are both circular motions in the  $xy$  plane, with the spatially larger (but temporally slower) circular oscillation being the magnetron mode, and the cyclotron mode being the faster but spatially smaller mode. The frequencies of oscillation are given below, and obey the general hierarchy  $\omega_+ \gg \omega_z \gg \omega_-$

<sup>6</sup>Alternatively, the equations of motion can be derived using a Lagrangian method as discussed in [55]. A quantum treatment of a trapped charge in a Penning trap can be found in [56].

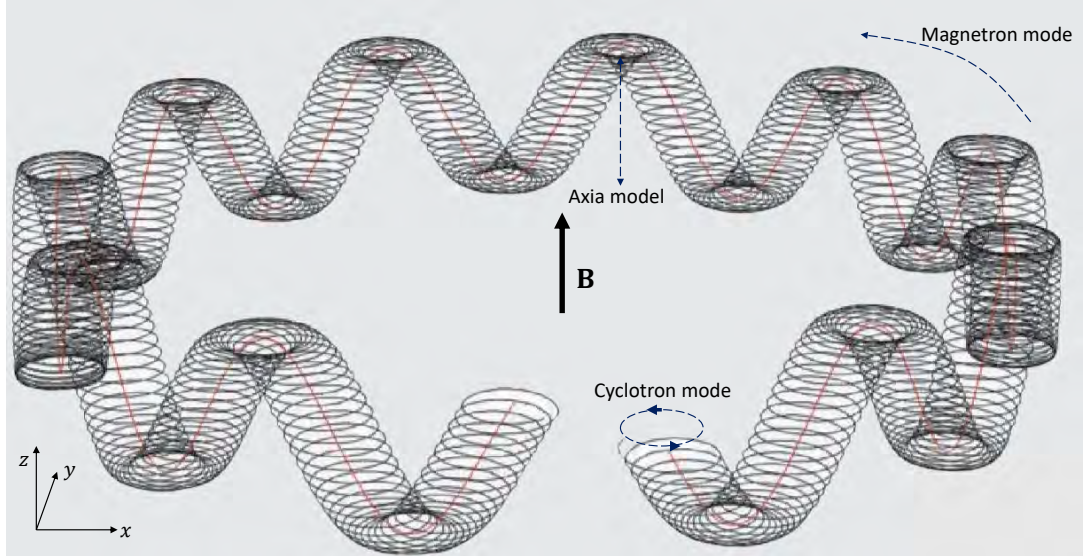


Figure 2.4: General motion of a charge in a Penning trap (not to scale) [25]. The motion is the superposition of three distinct oscillations. The vertical oscillation is the *axial* mode, the slow circular oscillation is the *magnetron*, and the fast circular oscillation is the *cyclotron* mode. The magnetic field,  $\mathbf{B}$ , points along the vertical direction.

$$\omega_z = \sqrt{\frac{2qU_0C_{002}}{m}} \quad (2.9)$$

$$\omega_+ = \frac{\omega_c}{2} + \sqrt{\left(\frac{\omega_c}{2}\right)^2 - \frac{\omega_z^2}{2}} \quad (2.10)$$

$$\omega_- = \frac{\omega_c}{2} - \sqrt{\left(\frac{\omega_c}{2}\right)^2 - \frac{\omega_z^2}{2}}, \quad (2.11)$$

where  $\omega_c = \frac{qB}{m}$  is known as the free cyclotron frequency. These equations reveal an additional condition for trapping; since the frequencies  $\omega_{\pm}$  must be real, it follows that the discriminant in Equations (2.10) and (2.11) must be positive, meaning that

$$\omega_c^2 > 2\omega_z^2 \quad (2.12)$$

must be satisfied. This ultimately gives a lower bound for the strength of the magnetic trapping field.<sup>7</sup> Additionally, it turns out that the sum of squares of each eigenfrequency is equal to the square of the free cyclotron frequency, which is given algebraically by  $\omega_+^2 + \omega_z^2 + \omega_-^2 = \omega_c^2$ . This is known as the Brown-Gabrielse Invariance theorem [57], and holds true even if the electric and magnetic fields are misaligned.

<sup>7</sup>Equation (2.12) can be rearranged to  $B^2 > \frac{4mU_0C_{002}}{q}$ , which determines the minimum magnetic field required for trapping.

The amplitude of each mode depends on its corresponding temperature ( $T_z$ ,  $T_+$ , and  $T_-$  for the axial, cyclotron, and magnetron modes, respectively), and each can be written as [38]

$$A_z = \sqrt{\frac{2k_B T_z}{m\omega_z^2}} \quad (2.13)$$

$$A_+ = \sqrt{\frac{2k_B T_+}{m(\omega_+^2 - \omega_z^2/2)}} \quad (2.14)$$

$$A_- = \sqrt{\frac{2k_B T_-}{m(\omega_-^2 - \omega_z^2/2)}}. \quad (2.15)$$

Note that the magnetron energy,  $k_B T_-$ , is negative, meaning that it is an *unstable* motional mode [58]. The physical consequence of this is that the magnetron radius increases as it loses energy, eventually escaping from the system. However, since the magnetron radiative decay rate is slow (owing to its relatively low frequency), the magnetron degree of freedom is effectively stable and uncoupled from the environment [58]. Moreover, the magnetron radius can be reduced by the method of magnetron cooling, which, because of the unstable nature of the mode, requires increasing the magnetron energy [59]. For a single electron in the Geonium Chip with a 0.5 T magnetic field, the expected amplitudes (after cooling) are  $A_z = 68 \mu\text{m}$ ,  $A_+ = 128 \text{ nm}$ , and  $A_- = 3 \mu\text{m}$  [40].

### 2.1.3 Penning trap ellipticity

So far, it has been assumed that the electrical potential of the trapping field is perfectly hyperbolic. In physical terms, this means that the curvature in the  $x$  and  $y$  directions are symmetric. The curvature of the electrical potential in the  $x$  axis is defined as  $\frac{1}{2} \frac{\partial^2 \phi}{\partial x^2} |_{\mathbf{r}_0}$ , and is often written in shorthand as  $C_{200}$ . The same notational syntax is used to define the  $y$  and  $z$  axis curvatures. For the Geonium Chip Penning trap, however, the electric potential is not symmetric in  $x$  and  $y$  and is therefore categorised as an *elliptical* Penning trap. The degree of dissimilarity between the  $x$  and  $y$  curvatures is quantified by the ellipticity parameter,  $\epsilon$ , and is defined as  $\epsilon = \frac{(1-\xi)}{(1+\xi)}$ , where  $\xi = \frac{C_{200}}{C_{020}}$  is introduced for the purpose of algebraic brevity. The electric potential of the Geonium Chip is then written as [60, 38]

$$\phi = U_0 C_{002} \left\{ \left( z^2 - \frac{x^2 + y^2}{2} \right) + \frac{\epsilon}{2} \left( x^2 - (y - y_0)^2 \right) \right\}. \quad (2.16)$$

The modified motion of a charged particle is then given by

$$x(t) = \xi_+ A'_+ \cos(-\omega'_+ t - \alpha_+) + \xi_- A'_- \cos(-\omega'_- t - \alpha_-) \quad (2.17)$$

$$y(t) = y_0 - \eta_+ A'_+ \sin(-\omega'_+ t - \alpha_+) - \eta_- A'_- \sin(-\omega'_- t - \alpha_-) \quad (2.18)$$

$$z(t) = A'_z \cos(\omega'_z t - \alpha_z), \quad (2.19)$$

where the modified angular frequencies are

$$\omega'_z = \sqrt{\frac{2C_{002}q}{m}} \quad (2.20)$$

$$\omega'_+ = \sqrt{\frac{1}{2}(\omega_c^2 - \omega_z'^2) + \frac{1}{2}\sqrt{\omega_c^2 \omega_1^2 + \epsilon^2 \omega_z'^4}} \quad (2.21)$$

$$\omega'_- = \sqrt{\frac{1}{2}(\omega_c^2 - \omega_z'^2) - \frac{1}{2}\sqrt{\omega_c^2 \omega_1^2 + \epsilon^2 \omega_z'^4}}, \quad (2.22)$$

with  $\omega_1 = \sqrt{\omega_c^2 - 2\omega_z'^2}$ .<sup>8</sup> The corresponding motional amplitudes in the elliptical Penning trap are given as

$$A'_+ = \frac{1}{\omega'_+} \sqrt{\frac{2k_B T_+}{\gamma_+ m}} \quad (2.23)$$

$$A'_- = \sqrt{\frac{2k_B T_-}{(\omega_-'^2 - \omega_z'^2/2)}} \quad (2.24)$$

$$A'_z = \frac{1}{\omega'_z} \sqrt{\frac{2k_B T_z}{m}}, \quad (2.25)$$

where  $\gamma_+ = 1 - \frac{\omega_z'^2}{2\omega_+'^2} \simeq 1$ . The dimensionless coefficients  $\xi_{\pm}$  and  $\eta_{\pm}$  are

$$\xi_{\pm} = \sqrt{\frac{\omega_c^2 + \epsilon \omega_z'^2 \pm \sqrt{\omega_c^2 \omega_1^2 + \epsilon^2 \omega_z'^4}}{2\omega_{\pm}/\omega_1 \sqrt{\omega_c^2 \omega_1^2 + \epsilon^2 \omega_z'^4}}} \quad (2.26)$$

$$\eta_{\pm} = \sqrt{\frac{\omega_c^2 - \epsilon \omega_z'^2 \pm \sqrt{\omega_c^2 \omega_1^2 + \epsilon^2 \omega_z'^4}}{2\omega_{\pm}/\omega_1 \sqrt{\omega_c^2 \omega_1^2 + \epsilon^2 \omega_z'^4}}}. \quad (2.27)$$

The Geonium Chip Penning trap permits for the  $y$ -amplitude of the magnetron motion to be effectively eliminated. This is known as the ultra-elliptical regime, and is discussed in [38]. A practical importance of the ultra-elliptical regime is that it heavily reduces the influence of magnetic field inhomogeneities along the  $y$  axis.

---

<sup>8</sup>Note that  $\omega_+'^2 + \omega_-'^2 + \omega_z'^2 = \omega_c^2$  holds for elliptical traps.

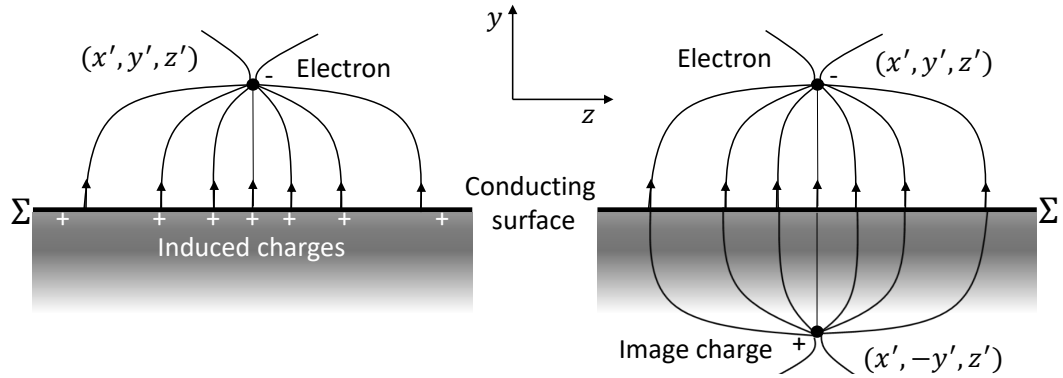


Figure 2.5: Electric field lines due to an electron above a conducting surface. **Left:** A sketch of the electric field lines resulting from an electron placed above a conducting surface. **Right:** The electric field lines due to an electron and an image charge placed symmetrically about the conducting surface. Note that in the region  $y > 0$ , the electric field lines in both cases are identical.

## 2.2 The principle of detecting trapped charged particles in a Penning trap

Generally speaking, charged particle detection is either destructive or non-destructive [3]. Destructive detection techniques (such as time-of-flight measurement methods) measure properties of particles as they are lost from the trap. This has the obvious disadvantage that, if additional measurements are required, then the trap needs to be reloaded. With non-destructive detection, however, particles remain inside the trap as they are being detected. The presence of a trapped particle is determined by the observation of small image currents on the electrode surfaces [61]. It is on this principle that the Geonium Chip Penning trap operates, and is the focus of the remainder of this chapter.

### Method of detection

This section describes the theoretical foundation for the detection of electrons in a Penning trap. The detection method follows closely the content of [62], which was developed with electron detection in a planar Penning trap in mind.

Consider a single electron positioned a perpendicular distance,  $y'$ , above a conducting surface (see Figure 2.5). The charge distribution on the conducting surface will be distorted by the presence of the electron, as, locally, a region of net positive charge develops on the edge of the conductor nearest the electron. The resulting electric field from this distribution of charges (both from the electron itself as well as from the induced charges)

is mathematically equivalent to that of an electron and an image charge symmetrically positioned either side of the upper layer of the conducting surface.<sup>9</sup> The induced charge on the upper side of the conductor is computed by

$$q_{\text{ind}}(x, y, z) = -\frac{q}{4\pi} \int_{\Sigma} \frac{\partial G(\mathbf{r}, \mathbf{r}')}{\partial n'} \Big|_{\mathbf{r}'=\mathbf{r}_0} dS', \quad (2.28)$$

where  $n'$  is the outward-pointing normal to the surface of the conductor  $S'$ ,  $\Sigma$  is the particular electrode on which the surface integral is taken, and  $G(\mathbf{r}, \mathbf{r}')$  is the Green's function that satisfies Dirichlet's boundary condition ( $G(\mathbf{r}, \mathbf{r}') = 0$ ,  $\forall \mathbf{r} \in S'$ ), where the primed coordinates are the positions of charges, the unprimed coordinates are the spatial coordinates with respect to the trap, and  $\mathbf{r}_0$  is the trapping position of the electron. For the situation depicted in Figure 2.5, the Green's function is

$$G(\mathbf{r}, \mathbf{r}') = \frac{1}{\sqrt{(x-x')^2 + (y-y')^2 + (z-z')^2}} - \frac{1}{\sqrt{(x-x')^2 + (y+y')^2 + (z-z')^2}}. \quad (2.29)$$

Equation (2.28) gives the induced charge distribution due to a stationary electron positioned above a conducting surface. As described in §2.1, a trapped particle is constantly in motion, and, consequently, the induced charges become induced currents, given by

$$I_{\text{ind}} = \frac{dq_{\text{ind}}}{dt} = \nabla q_{\text{ind}} \cdot \dot{\mathbf{r}} = \nabla \left( -\frac{q}{4\pi} \int_{\Sigma} \frac{\partial G(\mathbf{r}, \mathbf{r}')}{\partial n'} \Big|_{\mathbf{r}'=\mathbf{r}_0} dS' \right) \cdot \dot{\mathbf{r}} = -q \nabla \Lambda_{\Sigma} \cdot \dot{\mathbf{r}}, \quad (2.30)$$

where the substitution of  $\Lambda_{\Sigma} = \frac{1}{4\pi} \int_{\Sigma} \frac{\partial G(\mathbf{r}, \mathbf{r}')}{\partial n'} \Big|_{\mathbf{r}'=\mathbf{r}_0} dS'$  has been used for the maintenance of clarity. Since the induced currents are driven by the motion of the trapped electron, they too will oscillate at the electron's eigenfrequencies. Detecting an electron requires measuring a signal associated with these induced currents. This is typically achieved by using  $I_{\text{ind}}$  to drive a parallel tank circuit (see Figure 2.6) that is tuned to be in resonance with one of the electron eigenfrequencies.<sup>10</sup> Doing so induces a voltage change on the electrodes given by  $V_{\text{ind}} = I_{\text{ind}} Z(\omega)$ , where  $Z(\omega)$  is the impedance of the tank circuit. The resulting electric field that emanates from this induced voltage change is experienced by the electron, and provides a drag force equal to

$$\mathbf{F}_{\text{ind}} = -q^2 Z(\omega) \nabla (\Lambda_{\Sigma} \nabla \Lambda_{\Sigma} \cdot \dot{\mathbf{r}}), \quad (2.31)$$

<sup>9</sup>Strictly speaking, this is only true for the region of space on the electron-side of the boundary

<sup>10</sup>Whilst the axial frequency is the frequency of choice for the Geonium Chip Penning trap, a future aim is to detect directly through the cyclotron mode as well

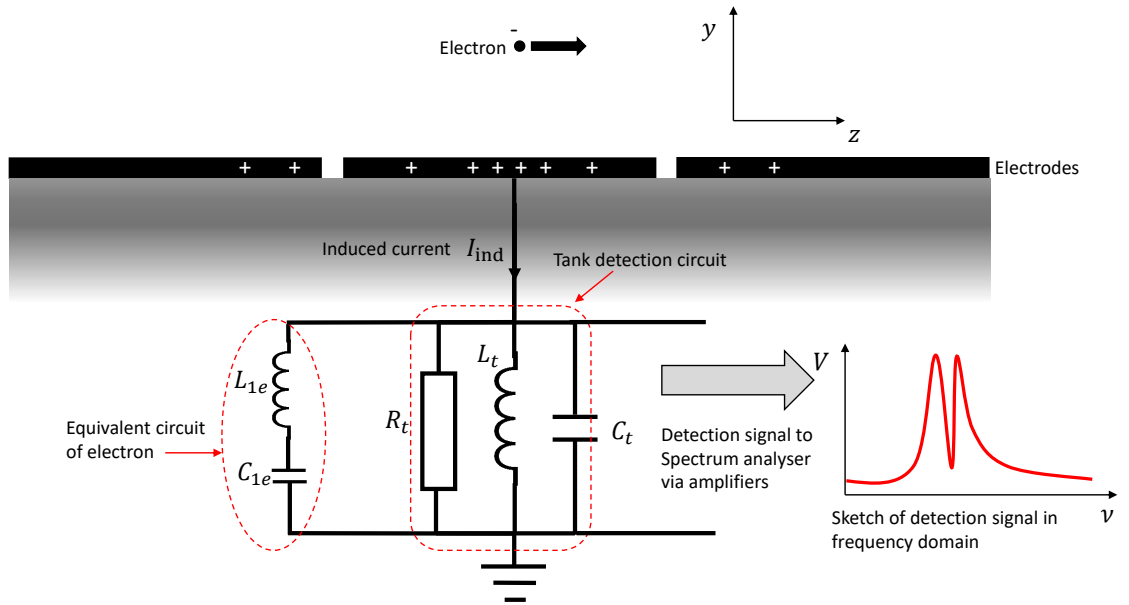


Figure 2.6: A lumped-element equivalent of the tank circuit driven by a trapped electron. The frequency response of the electron appears as an equivalent LC circuit in parallel with the tank circuit.

which damps the electron's motion [59]. It turns out that since the amplitude of the electron's motion is small compared with the electrode surfaces  $\Sigma$ , then this force is approximately [62]

$$\mathbf{F}_{\text{ind}} \approx -q^2 Z(\omega) \mathbf{D}_{\text{eff}}^{-1} (\mathbf{D}_{\text{eff}}^{-1} \cdot \dot{\mathbf{r}}) = q \mathbf{D}_{\text{eff}}^{-1} V_{\text{ind}}. \quad (2.32)$$

The term  $\mathbf{D}_{\text{eff}}$  is called the *effective coupling distance*, and comes from the approximation  $\mathbf{D}_{\text{eff}}^{-1}(\mathbf{r}_0) = \lim_{\mathbf{r} \rightarrow \mathbf{r}_0} \nabla \Lambda_{\Sigma}$ . In physical terms,  $\mathbf{D}_{\text{eff}}^{-1}$  describes the electric field at  $\mathbf{r}_0$  when the electrode  $\Sigma$  is held at 1 volt.

The total force on the electron,  $\mathbf{F}_{\text{tot}}$ , is the sum of the trapping forces and the dissipative force,<sup>11</sup> meaning that the modified equations of motion for an electron in a Penning trap obey

$$\mathbf{F}_{\text{tot}} = m \ddot{\mathbf{r}} = -q \nabla \phi + q \dot{\mathbf{r}} \times \mathbf{B} + q \mathbf{D}_{\text{eff}}^{-1} V_{\text{ind}}. \quad (2.33)$$

Although by no means obvious, Equation (2.33) tells us how an electron can be measured in a Penning trap. Assuming ideal trapping fields, as well as a tank circuit tuned

<sup>11</sup>Here, the Coulomb force between the electron and the induced charges is neglected. More detail is discussed in [63].

to have a resonance frequency equal to the axial frequency, the axial motion of a trapped electron is given by

$$m\ddot{z} = -m\omega_z^2 z + \frac{qV_{\text{ind}}}{D_{\text{eff}}^z}. \quad (2.34)$$

Rewriting in terms of  $I_{\text{ind}}^z = -\frac{q}{D_{\text{eff}}^z}\dot{z}$ , we see that the induced voltage across the tank circuit,  $V_{\text{ind}}$ , is given by

$$V_{\text{ind}}(\omega) = -\frac{mD_{\text{eff}}^{z^2}}{q^2} \frac{dI_{\text{ind}}^z}{dt} - \frac{mD_{\text{eff}}^{z^2}\omega_z^2}{q^2} \int I_{\text{ind}}^z dt. \quad (2.35)$$

Equation (2.35) states that the electron is electrically equivalent to a series LC circuit [62, 64, 63], with effective inductance  $L_{1e} = \frac{mD_{\text{eff}}^{z^2}}{q^2}$ , an effective capacitance  $C_{1e} = \frac{q^2}{mD_{\text{eff}}^{z^2}\omega_z^2}$ , and a resonance frequency equal to the axial frequency,  $\omega = \frac{1}{\sqrt{L_{1e}C_{1e}}} = \omega_z$ . A feature of series  $LC$  circuits is that the total voltage drops to zero at resonance, whilst with parallel tank circuits at resonance, the voltage is maximal [65]. Thus, the total detection signal in the frequency domain consists of a broad maximum (with linewidth  $\Delta\nu_T = \frac{1}{2\pi C_t R_t}$ ) centred on  $\omega_z$  (due to the frequency response of the tank circuit) with a sharp dip (single electron linewidth  $\Delta\nu_{1e} = \frac{R_t}{2\pi L_{1e}}$ ) at  $\omega_z$  from the electron's frequency response (see Figure 2.6). Experimentally, taking the voltage signal across a tank circuit and inputting it into a Fast Fourier Transform spectrometer, the electron signal can be observed (see Figure 2.6).

### Single electron determination

The section above describes how the electrical signal from a single electron can be measured. An obvious question might be: how can one be sure that there is only a *single electron* in the Penning trap? Wineland and Dehmelt [63] solved this problem by considering how the induced signal depends on the number of electrons,  $n$ . They found that, for  $n$  electrons, the effective inductance and effective capacitance are  $L_{ne} = nL_{1e}$  and  $C_{ne} = \frac{C_{1e}}{n}$  respectively, meaning that the linewidth of the dip depends directly on the number of electrons in the trap:  $\Delta\nu_{ne} = n\Delta\nu_{1e}$ . Inspection of the linewidth can therefore determine the number of electrons, where  $\Delta\nu_{ne}$  is the linewidth for  $n$  electrons. Typically, a cloud of electrons are trapped and detected. The number is slowly reduced by the method of evaporative cooling,<sup>12</sup> where the trap voltages are adjusted to allow the more energetic electrons to escape from the trap [3].

---

<sup>12</sup>Or alternatively by applying a drive voltage to knock electrons out of the trap [66].

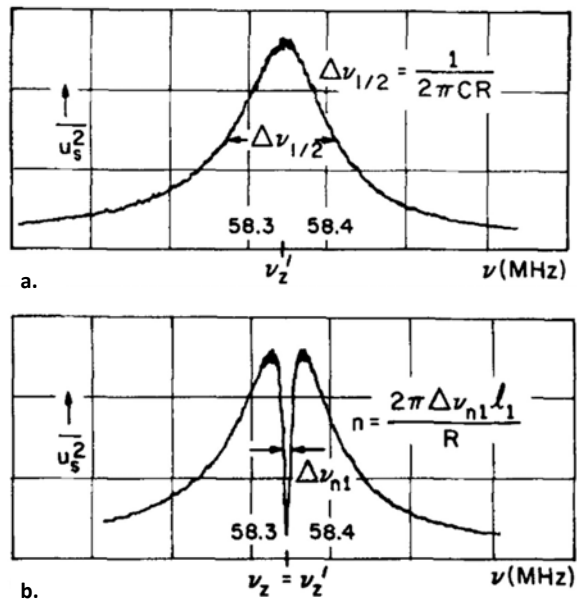


Figure 2.7: Experimental data taken from [63]. Figure 2.4a shows the resonance of the detection circuit alone. Figure 2.4b shows the detection circuit including the electron dip, along with an expression for the number of electrons. In the notation given in this figure, the number of electrons,  $n$ , can be inferred from the width of the signal dip,  $\Delta\nu_{n1}$ , the equivalent resistance of a single electron,  $l_1$ , and the detection circuit resistance at resonance,  $R$ .

## Chapter 3

# The Geonium Chip Penning trap

In §2, the fundamental principles of trapping and detecting charged particles in a Penning trap were outlined. The discussion was kept deliberately general, with a view to discussing the Geonium Chip Penning trap in detail in this chapter. §3.1 introduces the Geonium Chip concept, and focuses on how its geometry offers an advantage over other Penning traps. §3.2 briefly lists some of the main features of the Geonium Chip experimental setup. §3.3 describes how the required trapping fields are formed and optimised. The field characteristics of the prototype magnetic field source are described in detail, in particular its calibration procedure. §3.4 discusses some of the proposed technological applications of the Geonium Chip.

### 3.1 The Geonium Chip concept

The Geonium Chip is based on the projection of a five pole cylindrical Penning trap onto a plane [35] (see Figure 3.1). The central electrode is known as the *ring*, the two end electrodes are called the *end caps*, and the other two electrodes (immediately either side of the ring) are termed the *compensation electrodes*. The surrounding conducting surface provides a ground reference for the other electrodes, and is thus termed *the ground plane*.

The coordinate axes of the trap form an orthogonal Cartesian set, and are defined such that the electrode surfaces lie in the  $xz$  plane (see Figure 3.2). The magnetic field points along the  $z$  axis, and the  $y$  direction is defined as pointing upwards from the electrode surface. The origin of this coordinate frame is the surface of the centre of the ring electrode, and the trapping position is defined as  $(0, y_0, 0)$ . This terminology will be used throughout.

The electrical trapping field of the Geonium Chip is formed by holding each electrode

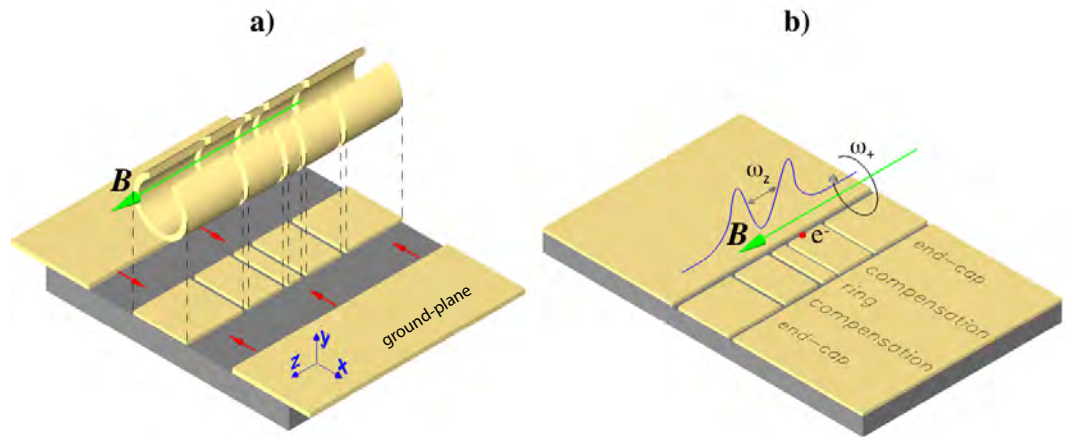


Figure 3.1: The Geonium Chip electrode arrangement **a**. The projection of the cylindrical Penning trap onto a plane. **b**. The names of the electrodes of the Geonium Chip. The magnetic field (green arrow) is directed parallel to the chip surface. [35]

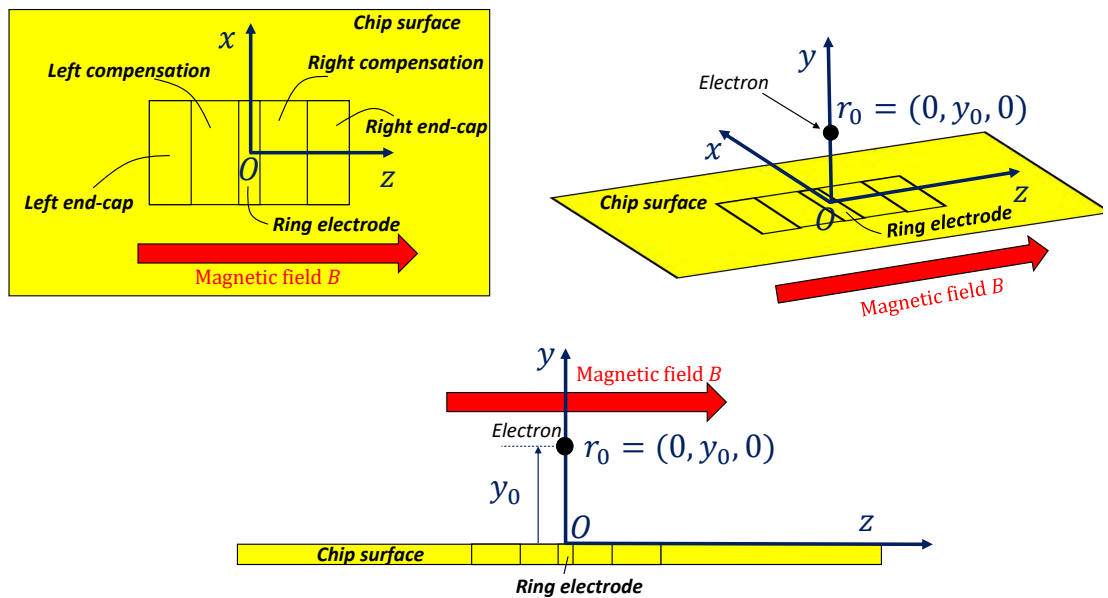


Figure 3.2: A sketch showing the coordinate axes of the Geonium Chip.

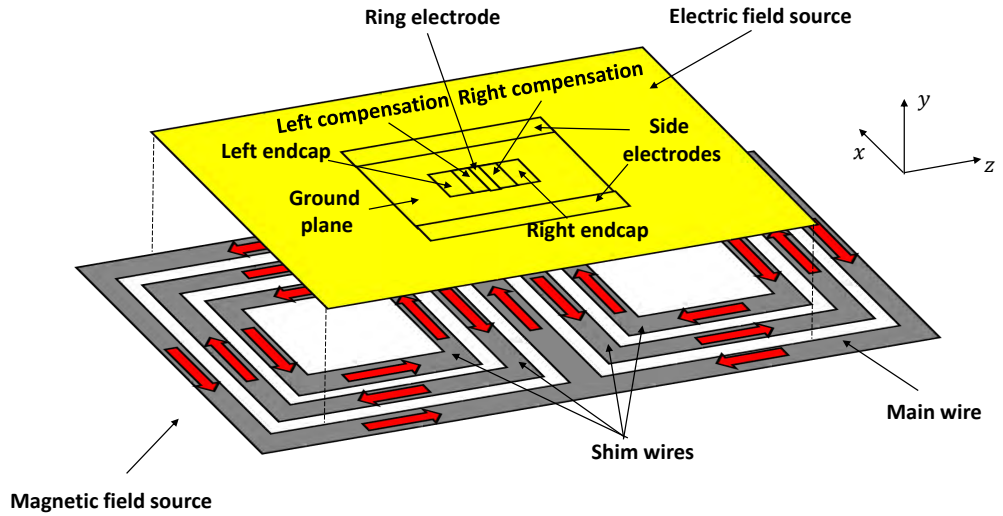


Figure 3.3: A sketch of the trapping field sources in the Geonium Chip. The magnetic field source comprises a number of superconducting coils placed directly underneath the electrode surface. The magnetic fields from each coil add up to provide the trapping field pointing along the  $z$  axis. The coils on the outside perimeter are called the main wires. All other coils are called shim wires.

at a specifically chosen voltage. If the correct voltages are applied, a harmonic potential can be formed to confine charges along the  $z$  axis. Many of the considerations needed to form this harmonic potential are given in §3.3.

Charged particle trapping is then completed with a homogeneous magnetic field oriented along the  $z$  axis. Whilst conventionally provided by large superconducting solenoids, the magnetic field source of the Geonium Chip comprises several coils confined to a plane [36, 37, 38, 39, 40]. The homogeneous trapping field is achieved by applying carefully chosen currents to each coil. The planar magnetic field source is placed directly underneath the trapping electrodes, as is sketched in Figure 3.3. The magnetic field contributions from each current add up to form a homogeneous magnetic field along the  $z$  axis.

### Conceptual advantages of the Geonium Chip compared with other Penning traps

The Geonium Chip is fundamentally different from other proposed planar Penning traps in that the magnetic field is *parallel* to the surface of the chip. Existing planar Penning trap designs [31, 32, 29, 67, 68] have the magnetic field oriented perpendicular to the chip surface. As illustrated in Figure 3.4, this arrangement is limited by natural asymmetry in

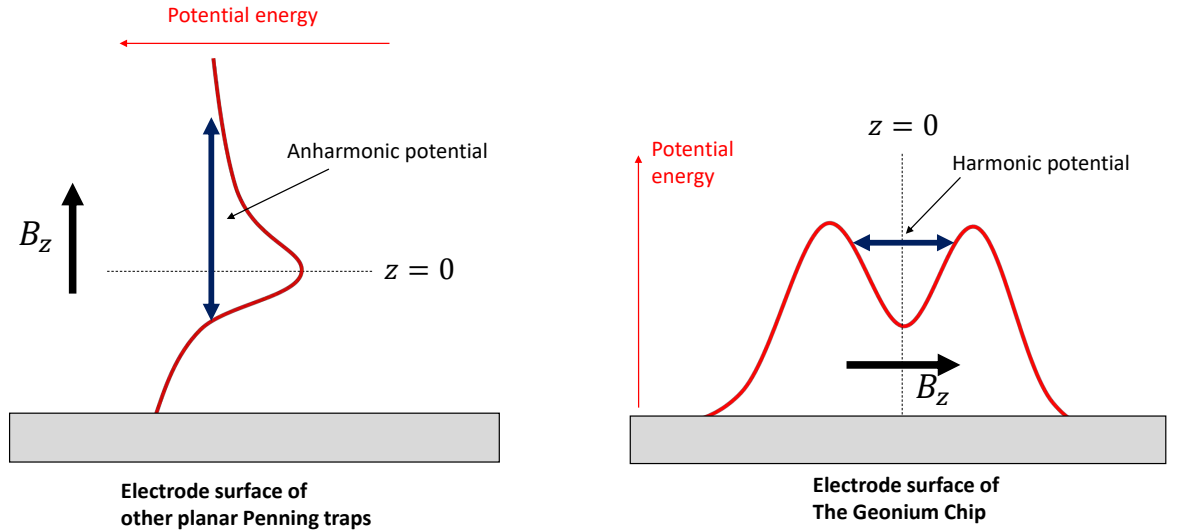


Figure 3.4: A sketch showing the natural symmetry of the Geonium Chip. **Left:** Traps with the magnetic field perpendicular to the electrode surfaces [31, 32, 29, 67, 68] are asymmetric under reflections in the  $z = 0$  plane – no planar arrangement of electrodes can compensate for this. **Right:** With the magnetic field parallel to the electrodes, the Geonium Chip is symmetric about the plane for which  $z = 0$ , allowing for a harmonic potential to be achieved.

the axial trapping potential, and makes single electron resolution virtually impossible [33, 32].<sup>1</sup> An additional issue arises if charged particles are to be transported between multiple traps on the same planar surface (such as with the double Penning trap technique [5, 69, 70]). Shuttling a charge from one trap to another requires for it to move perpendicular to the magnetic field lines. The resulting Lorentz force would be sufficient to push the electron off-course [71]. This is not an issue with the Geonium Chip Penning trap, however, since particles can be shuttled between traps along the direction of the magnetic field, effectively eliminating the Lorentz force.

The novelty of the Geonium Chip lies not only in the orientation of the magnetic field, but in the entire magnetic field source concept [36, 37]. Whilst the practical and financial advantages are obvious (and were introduced in §1), the planar magnetic field source offers significant operational advantages over conventional Penning trap magnets.

One example is in the speed with which the magnetic field distribution can be changed. This is particularly important for the continuous Stern-Gerlach effect [72], which usually

<sup>1</sup>Some designs have been made to compensate for this natural asymmetry, but they involve placing another structure out of the plane of the electrodes [32], greatly limiting the scalability.

requires both a homogeneous and an inhomogeneous magnetic field distribution. The continuous Stern-Gerlach effect is a technique used in many Penning trap experiments whereby the axial and cyclotron modes of a trapped particle are coupled together by a magnetic bottle field,  $\mathbf{B} = (B_{000} + B_{002}z^2)\hat{\mathbf{z}}$ , resulting in the axial frequency becoming dependent on the cyclotron energy. The presence of a magnetic bottle field also results in the axial frequency becoming dependent on the particle spin, and this is true for both electrons and ions [73]. This is because the coupling of the magnetic moment,  $\boldsymbol{\mu}$  (which is the sum of the spin magnetic moment,  $\boldsymbol{\mu}_s$ , and the cyclotron magnetic moment,  $\boldsymbol{\mu}_+$ ) with the position-dependent magnetic bottle field,  $\mathbf{B}$ , results in a force on the trapped charge,  $\mathbf{F} = -\nabla(\boldsymbol{\mu} \cdot \mathbf{B})$ . For a single electron, this force,  $F_z^{\text{sg}}$ , affects the axial motion according to

$$F_z^{\text{sg}} = -2B_{002}\mu_B(2n_+ + 1 + gm_s)z, \quad (3.1)$$

where  $\mu_B$  is the Bohr magneton,  $n_+$  is the cyclotron quantum number,  $g$  is the electron g-factor, and  $m_s = \pm 1/2$  is the spin state of the electron.<sup>2</sup> The force,  $F_z^{\text{sg}}$ , alters the motion of the trapped electron such that its equation of motion becomes

$$\begin{aligned} m\ddot{z} &= -m\omega_z^2 z - 2B_{002}\mu_B(2n_+ + 1 + gm_s)z \\ m\ddot{z} &= -m\omega_z'^2 z, \end{aligned} \quad (3.2)$$

where

$$\omega_z'(n_+, m_s) = \omega_z \sqrt{1 + \frac{2B_{002}\mu_B(2n_+ + 1 + gm_s)}{m\omega_z^2}} \quad (3.3)$$

is the modified axial frequency due to the coupling of the magnetic moment with the magnetic bottle field. Note the explicit dependence of the modified axial frequency on the cyclotron and spin quantum states. Typically,  $2B_{002}\mu_B(2n_+ + 1 + gm_s) \ll m\omega_z^2$ , and so Equation (3.3) is often approximated to

$$\omega_z' \approx \omega_z + \frac{B_{002}\mu_B(2n_+ + 1 + gm_s)}{m\omega_z}. \quad (3.4)$$

For many experiments, such as measurements of the electron g-factor, it is necessary to both make a precise measurement of the motional frequencies of the electron, and to take an accurate reading of the quantum state of the trapped charge ( $n_+, m_s$ ). However, precise measurement of the axial frequency requires a homogeneous magnetic field distribution, whereas the quantum state determination of a trapped particle relies on having a magnetic bottle field. In conventional Penning trap systems, this problem is overcome by having

---

<sup>2</sup>There is also a contribution due to the magnetron motion, but this is negligible [74].

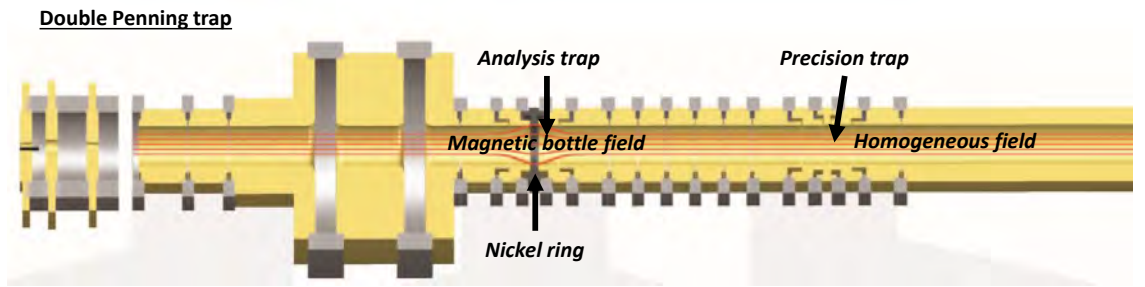


Figure 3.5: The double Penning trap at Heidelberg [5]. The Analysis trap has an inhomogeneous trapping field that is used to detect spin flips. The Precision trap has a homogeneous magnetic field.

two Penning traps in the same setup [5, 69, 70] (see Figure 3.5) – a precision trap with a homogeneous magnetic field, and an analysis trap with a magnetic bottle field, which is produced by magnetic field distortion from a nickel ring [5, 72]. Precision measurements, such as measurements of the g-factor [69], are achieved by continuously shuttling trapped particles between the two. In the Geonium Chip Penning trap, however, changes to the magnetic field distribution can be made *in situ*, meaning that two Penning traps are not required. The magnetic field distribution can be changed from a homogeneous field to a magnetic bottle field in the same trap, meaning that the Geonium Chip behaves as *both* the analysis and the precision trap. Such changes in the magnetic field distribution are estimated to take no longer than a minute, and this does away with the need for having two traps. This is ultimately a consequence of the planar geometry. Since the magnetic field source is placed only millimetres away from the trapping region, significant changes to the trapping field can be achieved with relatively small changes to the input currents.

### 3.2 Experimental setup of the Geonium Chip Penning trap

Before the trapping fields of the Geonium Chip Penning trap are discussed in detail, this section outlines some of the main features of the overall experimental setup. Whilst only a brief outline is given here, a more detailed discussion of the Geonium Chip experimental setup can be found in [39, 40].

The electric trapping field of the Geonium Chip Penning trap is provided by a chip-based electrode structure. The initial design was a microfabricated metal-on-silicon chip provided by *MIR Enterprises*. The batch of chips provided by *MIR Enterprises* varied in substrate thickness, metallisation thickness, and metal purity. The metallisation layer

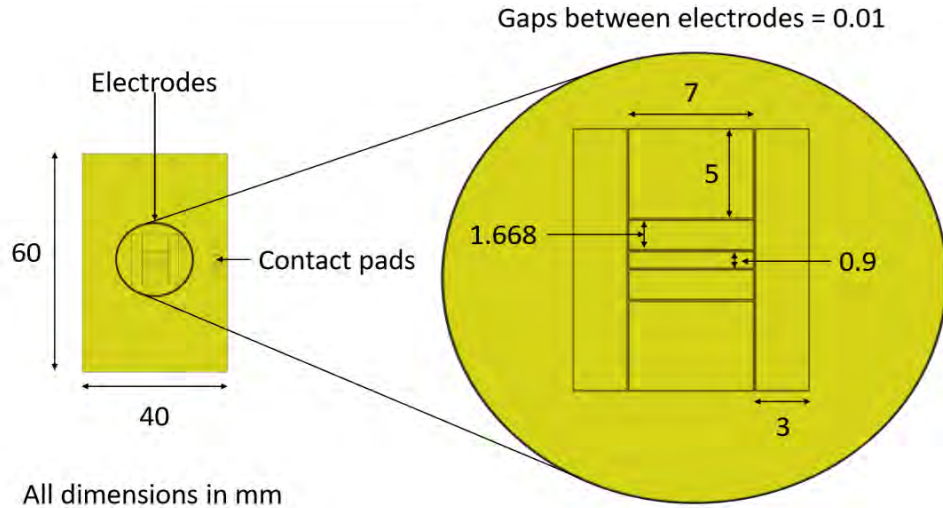


Figure 3.6: Dimensions of the electrode chip from *MIR enterprise*.

came in the following variations: 300 nm of pure gold, 300 nm of gold silver alloy (80:20), and 100 nm gold silver alloy (80:20). Two thickness variations of boron doped silicon substrate were used: 675  $\mu\text{m}$ , and 1000  $\mu\text{m}$ ; and, in each chip, a 900 nm silicon dioxide buffer layer separated the substrate from the metallisation layer. The mechanical and electrical properties of the *MIR* chips have been studied extensively in [39, 40], and so will not be discussed in much detail here.

The electrode dimensions of the *MIR* chips are given in Figure 3.6. These trapping electrodes are positioned in the centre of the chip, with contact pads located near the right-hand edge of the chip. Electrical contact between the two is provided by buried wires, such that the electric trapping field of the Geonium Chip is created by touching these pads with wires held at the correct voltages. Particle detection is achieved by measuring the induced voltage on one of the electrodes with respect to ground through a superconducting resonator. It has been recently discovered, however, that the resistance of the buried wires, along with the inter-electrode capacitances, are far too high for the electron detection signal to be measurable. This has rendered the *MIR* chips unusable.

More recent chip iterations have come in the form of in-house chips manufactured (by J. Pinder) from a *Rogers* circuit board. Unfortunately, these in-house chips exhibited poor mechanical properties, becoming deformed when holding vacuum in the inner vacuum chamber (see Figure 3.8). Currently, alumina-backed chips fabricated by *PW Circuits Ltd.* (see Figure 3.7) are installed in the experiment. Electrical contact between the electrodes and the voltage screw connectors is provided by gold conducting paths on the underside

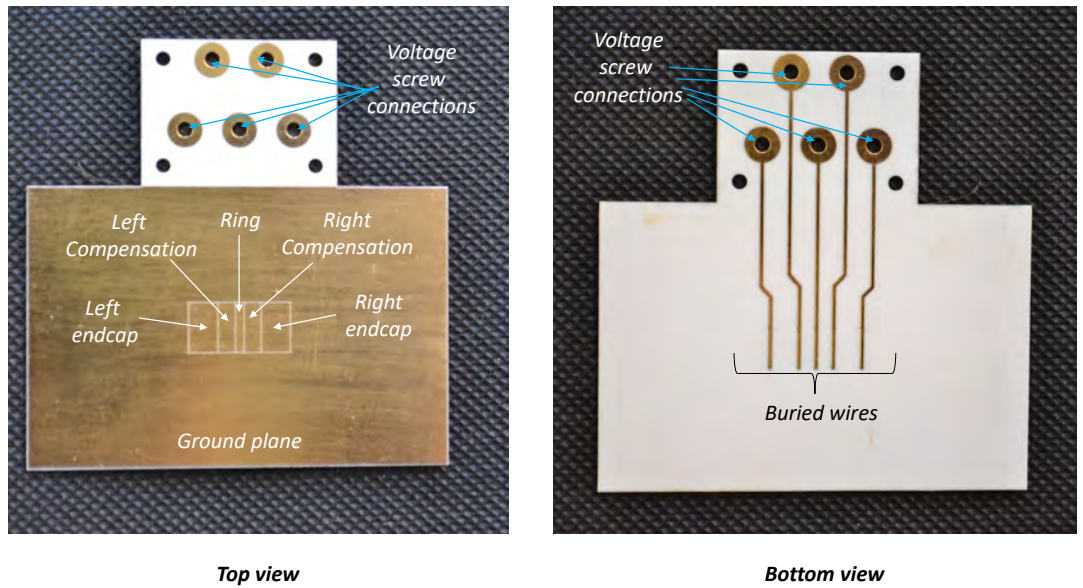


Figure 3.7: The electrode chips from *PW Circuits Ltd.* **Left:** Top view of the chip showing the gold electrode surfaces. All electrodes are 7 mm in height, with the widths of the endcap, compensation, and ring electrodes 4.0 mm, 2.3 mm and 1.1 mm respectively. **Right:** Underside view of the chip showing the buried wires. These connect to the electrodes through 0.2 mm diameter vias. There are two vias per electrode.

of the alumina board.

The trapping region of the Geonium Chip is enclosed in an inner vacuum chamber (see Figure 3.8). The electrode chip forms the floor of this vacuum chamber, and is held in place with an indium seal. On one side of the chamber is a quartz window, which is transparent to ultraviolet light, and adjacent to that is the ‘pinch-off’ tube, which is needed to evacuate the chamber. A UV *Hamamatsu* light source focuses light into the chamber to liberate electrons via the photoelectric effect. The chamber is expected (from observed lifetimes of trapped charges in other cryogenic Penning trap experiments, such as in [75]) to provide pressures of around  $10^{-16}$  mbar. Inside the window is a gold plated copper mesh, such that the inner vacuum chamber forms a microwave cavity. The cavity modes of the chamber are calculated to be off-resonant with the electron cyclotron frequency at 0.5 T, thereby increasing the lifetime of an excited cyclotron mode of the electron by inhibiting spontaneous emission via the Purcell effect [38].

In the current setup, the trapping magnetic field is provided by a prototype magnetic field source (pictured in Figure 3.9), which comprises a symmetric arrangement of four independently driven coils. These coils are made from 0.4 mm copper coated niobium-titanium wire from *Supercon Inc.* encased in black *Stycast* epoxy. The number of turns on the main, shim 1, shim 2, and shim 3 coils are 38, 42, 400, and 376 respectively.

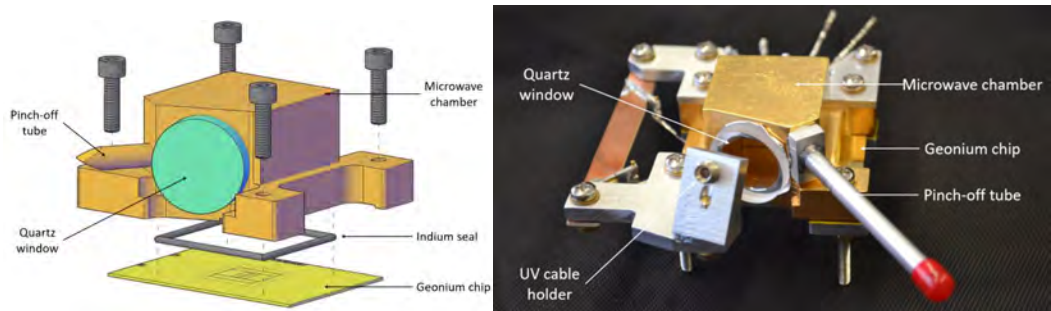


Figure 3.8: The inner (cryogenic) vacuum chamber of the Geonium Chip. **Top:** Exploded CAD drawing of the chip and inner vacuum chamber. The Geonium Chip forms the floor of the chamber, and is held in place by an indium seal. **Bottom:** Photograph of the chip and inner vacuum chamber setup.

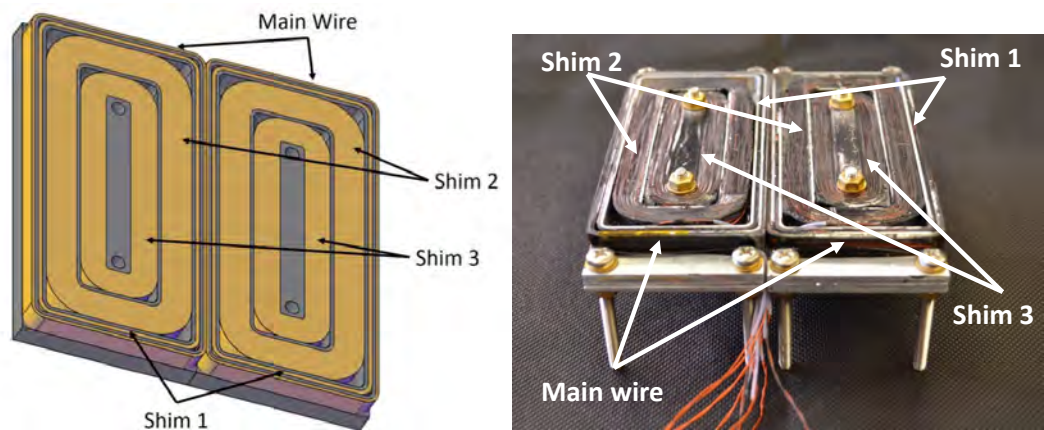


Figure 3.9: **Top:** CAD drawing of the prototype planar magnetic field source. The four independently driven currents – the main wire, and shims 1-3 – are shown. **Bottom:** The prototype magnetic field source, made from 0.4 mm diameter niobium-titanium wire. The number of turns on the main, shim 1, shim 2, and shim 3 coils are 38, 42, 400 and 376 respectively.

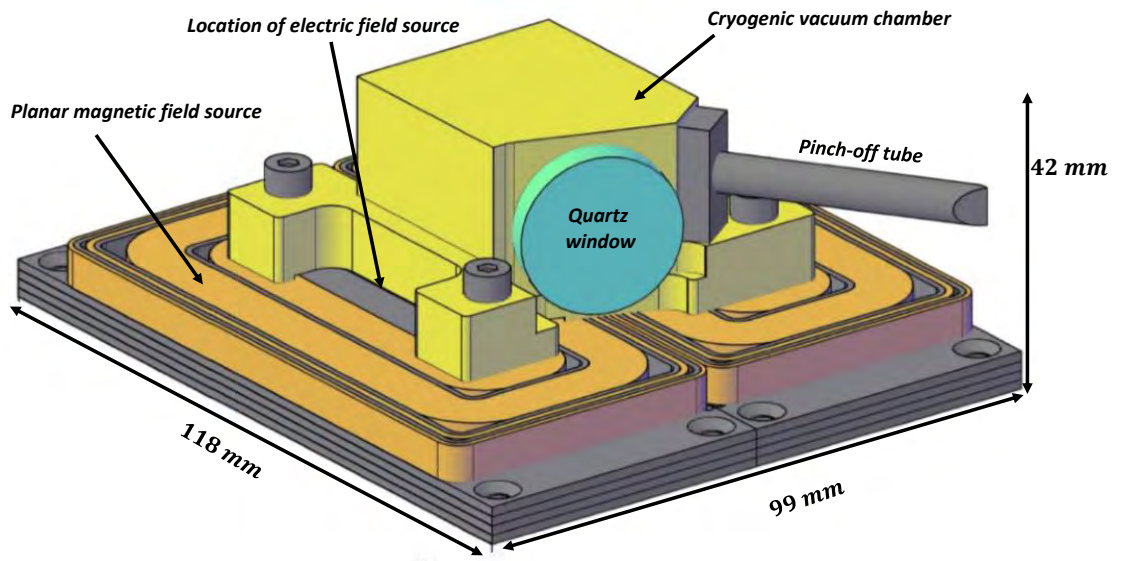


Figure 3.10: A CAD drawing showing how the chip, inner cryogenic vacuum chamber, and planar magnetic field source fit together.

These numbers were chosen because they provide a homogeneous 0.1 T trapping field at relatively low currents.<sup>3</sup> Each coil is driven with currents from a *Rohde & Schwarz HMP4040* precision current supply. The magnetic field source is calibrated (see §3.3.3) such that, for each coil, the magnetic field distribution at the trapping position is known as a function of the current it is carrying. Thus, with careful choice of applied currents, a homogeneous trapping field can be provided at the trapping position. As shown in Figure 3.10, the magnetic field source is placed directly underneath the electric field source. The two field sources are screwed together, which not only aligns the two trapping fields, but also to limits the effect of vibrations, as both field sources vibrate in common mode.

The detection signal of a trapped electron is to be observed by measuring the voltage drop across a tank circuit in the form of a superconducting (niobium) helical resonator. This helical detection resonator is well optimised, with a resonance frequency of 26 MHz, and a reported unloaded Q factor of 34,000. More detail can be found in [39, 40].

Figure 3.11 shows a photograph of some of the main components of the experimental setup. Clearly visible are the gold plated inner vacuum chamber, the planar magnetic field source, and the niobium detection resonator. These components are screwed onto struts that are in thermal contact with the second cooling stage of a two-stage pulse tube cryostat (*Sumitomo SRP-062B*). This second cooling stage has a cooling power of 0.5 W,

<sup>3</sup>No more than 20 A in each coil.

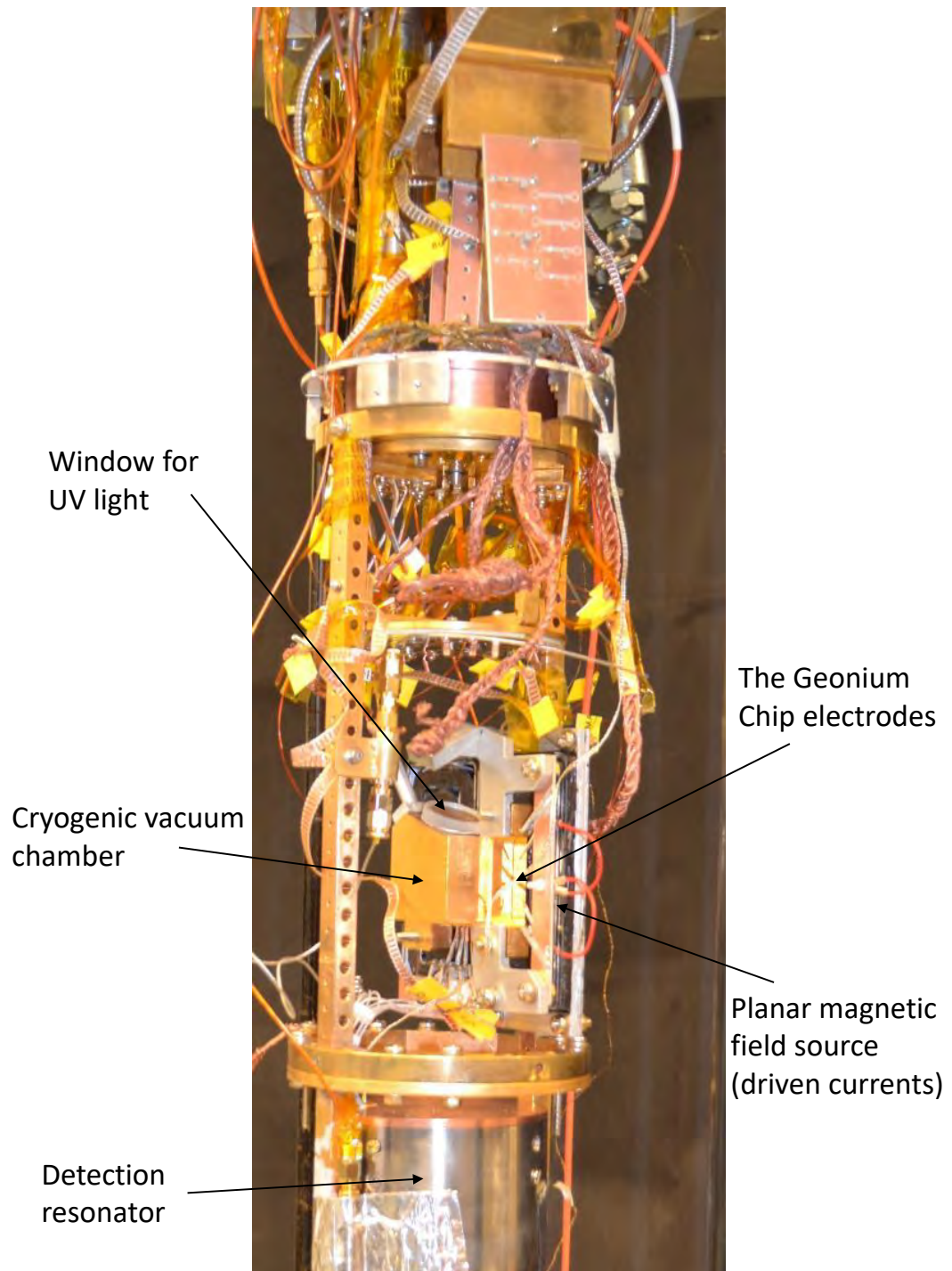


Figure 3.11: A photograph of the experimental setup inside the cryostat showing the Geonium Chip, cryogenic vacuum chamber, detection resonator and prototype magnetic field source.

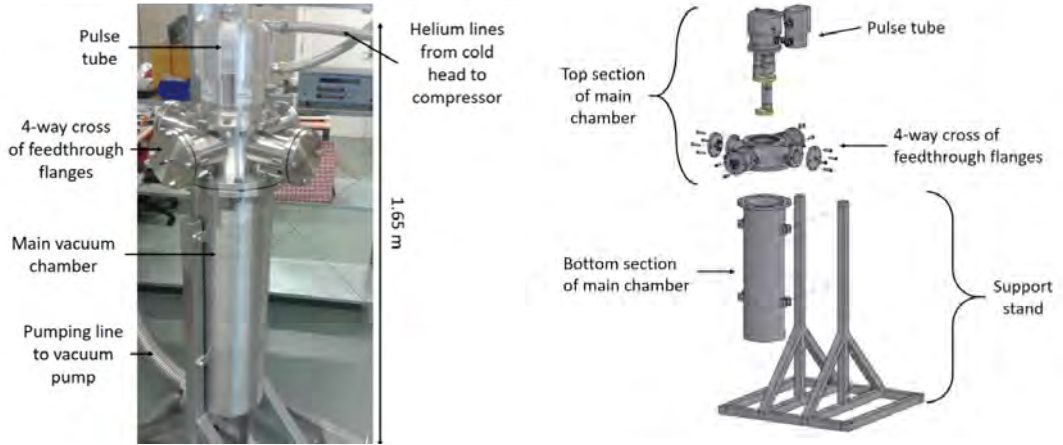


Figure 3.12: **Left:** The outer vacuum casing of the experiment when closed. **Right:** Exploded CAD drawing of the vacuum chamber and pulse tube cryostat.

and can reach temperatures below 4 K. Much of the thermal load is removed by the first cooling stage (not shown), which has a nominal cooling power of 30 W, and is capable of reaching 60 K. Each cooling stage is protected with thermal radiation shields (not shown), and the overall experiment is housed in an outer vacuum chamber, shown in Figure 3.12. This provides a pressure of around  $10^{-7}$  mbar.

### 3.3 Trapping fields of the Geonium Chip

In the last section, the key components of the experimental setup were described. This section discusses, in detail, how the electric and magnetic trapping fields arise in the Geonium Chip Penning trap. The effect of non-ideal trapping fields is also introduced, as well as ways in which the Geonium Chip can be optimised to mitigate their effect.

#### 3.3.1 Electric trapping field of the Geonium Chip

The trapping potential of the Geonium Chip is provided by holding the ring electrode, compensation electrodes, and end-cap electrodes at voltages  $V_r$ ,  $V_c$ , and  $V_e$  respectively, and is given by [35]

$$\phi(x, y, z) = V_r f_r(x, y, z) + V_c f_c(x, y, z) + V_e f_e(x, y, z) + f_{\text{gaps}}(x, y, z | V_r, V_c, V_e); \quad (3.5)$$

$f_r$ ,  $f_c$  and  $f_e$  depend entirely on the trap dimensions, whilst  $f_{\text{gaps}}$  – the contribution to the trapping potential from the gaps between the electrodes – depends on both the sizes

of the gaps between the electrodes, as well as the electrode voltages. For small gap sizes,<sup>4</sup> this can be approximated as a linear interpolation of the voltages between neighbouring electrodes. An analytical expression for the total electric potential of the Geonium Chip enclosed in a metallic rectangular box (corresponding to the cryogenic vacuum chamber) can be found in [38]. The equilibrium trapping position in the Geonium Chip corresponds to the position in space that satisfies  $\left.\frac{\partial\phi(x,y,z)}{\partial y}\right|_{(0,y_0,0)} = 0$  and  $y_0 > 0$ , and for small gaps ( $f_{\text{gaps}} \rightarrow 0$ ) is approximately given by

$$\left.\frac{\partial f_r}{\partial y}\right|_{(0,y_0,0)} + T_c \left.\frac{\partial f_c}{\partial y}\right|_{(0,y_0,0)} + T_e \left.\frac{\partial f_e}{\partial y}\right|_{(0,y_0,0)} = 0. \quad (3.6)$$

Solving Equation (3.6) (which has no analytical solution, and therefore has to be solved numerically) shows that  $y_0$  depends on the ratios of the voltage values,  $T_c = \frac{V_c}{V_r}$  and  $T_e = \frac{V_e}{V_r}$ , rather than their absolute values.

Like any real Penning trap, the trapping potential  $\phi(x, y, z)$  of the Geonium Chip is not the ideal hyperbolic potential described in §2. Mathematically, this means there are position-dependent terms above second order in the Taylor expansion of  $\phi(x, y, z)$  about the equilibrium position,  $r_0 = (0, y_0, 0)$ . These additional terms are called anharmonicities in the trapping potential, and, up to fourth order, are given as follows:

$$\begin{aligned} \phi(x, y, z) = \phi(0, y_0, 0) + \dots + \underbrace{C_{002}z^2 + C_{200}x^2 + C_{020}(y - y_0)^2}_{\phi_{\text{quad}}} + \\ \underbrace{C_{012}z^2(y - y_0) + C_{210}x^2(y - y_0) + C_{030}(y - y_0)^3}_{\text{odd anharmonicities}} + \\ \underbrace{C_{202}z^2x^2 + C_{022}z^2(y - y_0)^2 + C_{220}x^2(y - y_0)^2 + C_{004}z^4 + C_{400}x^4 + C_{040}(y - y_0)^4}_{\text{even anharmonicities}}, \end{aligned} \quad (3.7)$$

where the coefficients  $C_{ijk}$  are defined as

$$C_{ijk} = \frac{1}{i!j!k!} \left.\frac{\partial^{i+j+k}\phi(x, y, z)}{\partial x^i \partial y^j \partial z^k}\right|_{(0,y_0,0)}. \quad (3.8)$$

Note that, because of the symmetry in the  $x$  and  $z$  dimensions (along with the fact that  $\nabla\phi = \mathbf{0}$  has been imposed at the trapping position), terms with odd  $i$  and/or odd  $k$  vanish [35]. The consequence of the anharmonic potential is that it alters the motion of a trapped electron, such that its motional frequencies become dependent on position. Ultimately, this means there are shifts in the motional frequencies of the electron that are directly

---

<sup>4</sup>What determines whether a gap is ‘small’ is how high the trapping height of the electron is compared with the gaps between the electrodes. For the Geonium Chip, the effect of the gap sizes can be neglected.

related to changes in the energy associated with each motional mode. Anharmonicities up to fourth order in position produce linear shifts in frequency, and this is mathematically expressed in matrix form as

$$\begin{pmatrix} \Delta\nu_+ \\ \Delta\nu_z \\ \Delta\nu_- \end{pmatrix} = \begin{pmatrix} M_{11} & M_{12} & M_{13} \\ M_{21} & M_{22} & M_{23} \\ M_{31} & M_{32} & M_{33} \end{pmatrix} \begin{pmatrix} \Delta E_+ \\ \Delta E_z \\ \Delta E_- \end{pmatrix}, \quad (3.9)$$

where  $M_{ij}$  are the elements of this *frequency shifts matrix*. As an example, the frequency shifts matrix for a single electron in the trap described in [35] is

$$M = \begin{pmatrix} 5 \times 10^{-6} & 0.5 & -0.9 \\ 1 \times 10^{-3} & -203 & -411 \\ -2 \times 10^{-6} & -0.4 & 2 \end{pmatrix} \text{Hz K}^{-1}, \quad (3.10)$$

where, for simplicity, the electron energy is given in terms of temperature (i.e., in K rather than J).<sup>5</sup> The Geonium Chip is configured to measure the axial frequency directly, so the matrix elements in the second row are the ones most relevant for precise measurement.<sup>6</sup> The most potentially damaging frequency shift is given by the  $M_{22}$  matrix element, which describes how the axial frequency fluctuates with axial energy. This is because a measurement of  $\omega_z$  results in the axial motion being in thermal equilibrium with the detection system, which has a temperature of  $T_z \approx 4.2$  K. Thus, the axial energy, and therefore  $\omega_z$ , are susceptible to thermal fluctuations, and can make the detection signal unresolvable. These frequency shifts can, however, be eliminated with a careful choice of an optimal tuning ratio,  $T_c^{\text{opt}}$ , such that fluctuations in the axial energy do not produce changes in the axial frequency (see Figure 3.13). Whilst, in principle, the frequency shift  $M_{21}$  is relevant, it turns out that, for the Geonium Chip, it only produces a frequency shift of no more than a few mHz per K. Frequency shifts as a function of changes in magnetron energy are negligible since the magnetron energy is effectively stable with time [58].

### Stray electric fields in the Geonium Chip

The section above discussed how anharmonic imperfections to the trapping electric field affect the motion of a trapped electron, and, importantly, how these imperfections can be dealt with such that their effect is minimised. In this section, the sources and effects of stray electric fields are discussed.

<sup>5</sup>Thus,  $1.38 \times 10^{-23}$  J of energy corresponds to a temperature of 1 K.

<sup>6</sup>Measurement of other frequencies are dependent on a precise measurement of the axial frequency, for instance in [5, 69].

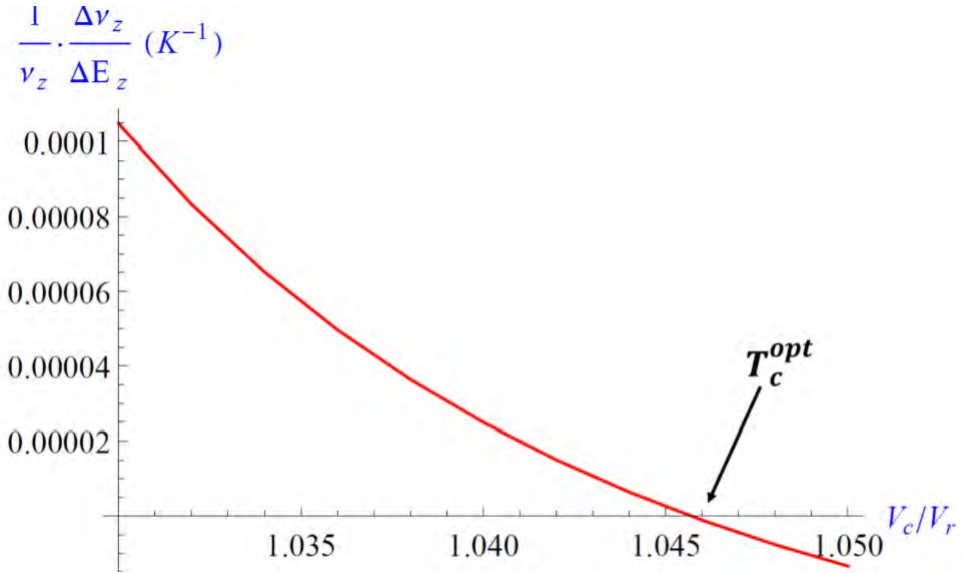


Figure 3.13: A graph showing the axial frequency shifts at  $T = 4.2$  K as a function of  $T_c$ . A tuning ratio exists such that any fluctuations in axial energy produce no shift in the axial frequency.

The trapping electric field of the Geonium Chip Penning trap is provided by high-precision *5018 Multifunction Voltage Calibrators* manufactured by *Time Electronics*. According to data from the manufacturers, these particular devices are highly stable, with voltage fluctuations of the order of  $1 \mu\text{V}$ . Such fluctuations will cause the axial frequency of the electron to shift by less than 1 Hz, which is less than the maximum resolution of the *Rohde & Schwarz* signal analyzer. Thus, for the purposes of single electron detection, such electric field fluctuations from the voltage supply can be neglected.

Stray electric fields can also come from imperfections in the metallic surfaces of the trap. Such imperfections can lead to both static and time-varying distortions in the electric field [76]. The static “patch” potentials are known to have two main origins: variations in the work function of the metallic surface due to different neighbouring crystal orientations, and the presence of surface adsorbates. These surface adsorbates may be chemical in origin (such as surface oxidation), or physical, whereby atoms and molecules in the background gas can stick to the chip surface via Van der Waals forces [77]. Whilst the effect of chemical adsorbates can be reduced with the use of gold electrodes, the effect of the latter could present an issue for the Geonium Chip, since it operates in a cryogenic environment. At 4 K, much of the residual gas molecules stick to the chip surface, and this could distort the trapping electric field. Whilst the effect of time-varying patch potential noise on the

motion of trapped ions in surface traps is well documented, its origin is not completely understood, and for this reason it is often dubbed *anomalous heating*. Improvements in methods of probing surface noise has allowed for its origin to be distinguished from effects that are thermal in nature (i.e., Johnson noise), and has been demonstrated to scale with the ion-electrode distance,  $d$ , according to  $d^{-4}$  [76, 78]. For the Geonium Chip, this effect is expected to be small compared with other surface traps. The trapping height of the Geonium Chip is optimised to be about 0.8 mm above the electrode surface, which is large compared with typical heights in planar RF traps. Its effect, however, is not yet known, and will have to be investigated thoroughly when the trap is running.

Another potential source of stray electric fields is the effect of charge buildup in the electrode gaps. This effect is of particular relevance for the Geonium Chip Penning trap, since its loading procedure relies on illuminating the wall of the inner vacuum chamber with UV light. As discussed in [79, 80, 81], the effects of such charge buildup can be severe, and, in some instances, can even prevent trapping. Furthermore, such effects can linger, with reports ranging from days [79] to several months [80]. In the cases reported, the charge buildup resulted from light being incident near the trapping region. The effect may be less severe in the Geonium Chip Penning trap, where the UV light is directed onto the inner vacuum chamber wall, but this, too, will have to be investigated empirically.

### 3.3.2 Magnetic trapping field of the Geonium Chip

It is not just the non-ideal character of the electric trapping field that causes unwanted frequency shifts. Inhomogeneities in the trapping magnetic field also cause fluctuations in the motional frequencies of a trapped electron. The design of a planar magnetic field source requires for these to be understood so that they can be eliminated. As stated above, the magnetic field source is a planar arrangement of current-carrying loops, and is located directly underneath the electrode surfaces of the trap. Since the magnetic field strength decays inversely with distance, magnetic field inhomogeneities along the vertical direction (i.e.,  $B_z(y)$ ) are the most significant [38]. The  $B_{010}$  and  $B_{020}$  terms are defined as

$$B_{010} = \left. \frac{\partial B_z}{\partial y} \right|_{(0, y_0, 0)} \quad (3.11)$$

$$B_{020} = \left. \frac{1}{2} \frac{\partial^2 B_z}{\partial y^2} \right|_{(0, y_0, 0)}. \quad (3.12)$$

Inhomogeneities of  $B_z$  along  $z$  are largely accounted for by the symmetry of the magnetic field source:  $B_{001}$  is negligible, since the magnetic field is symmetric about the  $xy$  plane

for which  $z = 0$ , and  $B_{020} \approx -B_{002}$  if the current-carrying wires extend long enough along the  $x$  axis.<sup>7</sup>

It is the aim of the planar magnetic field source to eliminate the  $B_{010}$  and  $B_{020}$  inhomogeneities, and how this is achieved will be discussed shortly. Firstly, a brief mention of how these inhomogeneities affect the electron detection signal is given. Like the frequency shifts due to electric field anharmonicities, the magnetic frequency shifts can be represented in matrix form. Each inhomogeneity has an associated matrix. The frequency shifts matrices due to  $B_{010}$  and  $B_{020}$  are given below:

$$M_{B_{010}} = B_{010}^2 \begin{pmatrix} M_{11}^{010} & M_{12}^{010} & M_{13}^{010} \\ M_{21}^{010} & M_{22}^{010} & M_{23}^{010} \\ M_{31}^{010} & M_{32}^{010} & M_{33}^{010} \end{pmatrix} \quad (3.13)$$

$$M_{B_{020}} = B_{020} \begin{pmatrix} M_{11}^{020} & M_{12}^{020} & M_{13}^{020} \\ M_{21}^{020} & 0 & M_{23}^{020} \\ M_{31}^{020} & M_{32}^{020} & M_{33}^{020} \end{pmatrix}, \quad (3.14)$$

where the analytical expressions for the matrix elements  $M_{ij}^{010}$  and  $M_{ij}^{020}$  can be found in [38], and depend on the trap geometry. For the trap discussed in [38], with a 0.5 T trapping field, and gradient and curvature terms of  $B_{010} = -12.5 \text{ mT mm}^{-1}$  and  $B_{020} = 4.8 \text{ mT mm}^{-2}$  respectively, these magnetic frequency shifts matrices (expressed as relative frequency fluctuations) are

$$M_{B_{010}} = \begin{pmatrix} 5.6 \times 10^{-9} & 2.3 \times 10^{-7} & 6.9 \times 10^{-9} \\ 2.3 \times 10^{-7} & -6.5 \times 10^{-2} & 5.6 \times 10^{-10} \\ 6.9 \times 10^{-9} & 5.6 \times 10^{-10} & -9.5 \times 10^{-6} \end{pmatrix} \text{K}^{-1} \quad (3.15)$$

$$M_{B_{020}} = \begin{pmatrix} -1.9 \times 10^{-11} & 7.1 \times 10^{-6} & 8.6 \times 10^{-8} \\ 7.1 \times 10^{-6} & 0 & -7.7 \times 10^{-8} \\ 8.6 \times 10^{-8} & -7.7 \times 10^{-8} & -9.3 \times 10^{-10} \end{pmatrix} \text{K}^{-1}. \quad (3.16)$$

Equation (3.15) shows that with the magnetic gradient of  $B_{010} = -12.5 \text{ mT mm}^{-1}$ , an energy fluctuation corresponding to 1 K in the axial mode of the electron leads to a fractional shift of the axial frequency of  $-6.5 \times 10^{-2}$ . The frequency curvature term, however, has no effect on the axial frequency, regardless of the change in the axial energy of the electron.

---

<sup>7</sup>For static fields, Maxwell's equations give  $\nabla \times \mathbf{B} = \mathbf{0}$  and  $\nabla \cdot \mathbf{B} = 0$ . Taking the curl of the former, and substituting in the latter, gives  $\nabla \times (\nabla \times \mathbf{B}) = -\nabla^2 \mathbf{B} = \mathbf{0}$ . For  $B_z$ , this means  $\partial_{x^2}^2 B_z + \partial_{y^2}^2 B_z + \partial_{z^2}^2 B_z = 0$ . Slow variation along  $x$  gives  $\partial_{y^2}^2 B_z \approx -\partial_{z^2}^2 B_z$ .

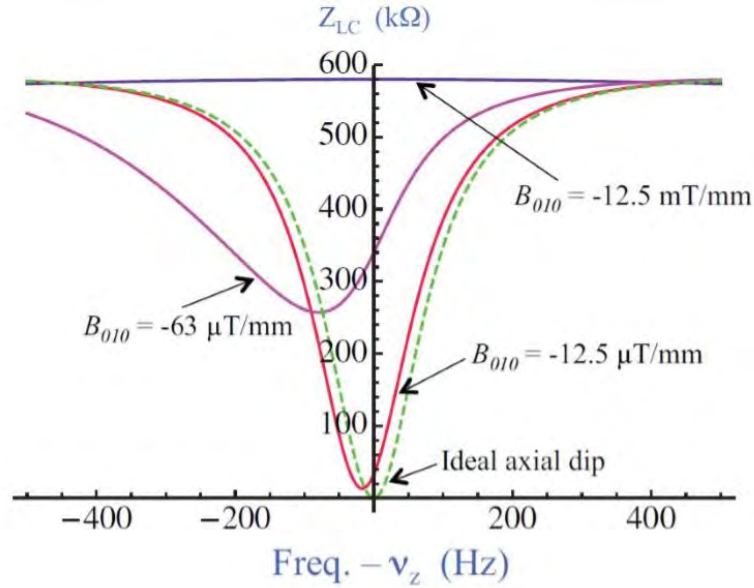


Figure 3.14: A graph showing the simulated detection signal of a single electron for various values of  $B_{010}$ . A magnetic gradient of  $|B_{010}| = 12.5 \text{ mT mm}^{-1}$  is enough to eliminate the electron detection signal entirely. Inhomogeneities of a few tens of  $\mu\text{T mm}^{-1}$  allow for the detection signal of the electron to be seen.

These frequency shifts matrices highlight a few important points. Firstly, the axial frequency shifts due to fluctuations in the axial energy scale with the square of the magnetic field gradient  $B_{010}$ . Calculations in [38] show that for magnetic field gradients in excess of  $12 \text{ mT mm}^{-1}$ , the detection signal of the electron becomes unresolvable (see Figure 3.14). Reducing the magnetic field gradient allows for the detection dip to be seen, with a distorted detection dip for  $B_{010} = 63 \mu\text{T mm}^{-1}$ , and a virtually ideal detection dip below around  $12 \mu\text{T mm}^{-1}$ . Thus, it is imperative that the planar magnetic field source is capable of eliminating the  $B_{010}$  terms of the magnetic field distribution.

It is interesting to note that the magnetic field curvature,  $B_{020}$ , does not cause any fluctuation in axial frequency as a function of axial energy. In fact, given that the magnetron energy is virtually stable (and can be magnetron cooled), we see that, with a non-negligible  $B_{020}$  term (commonly referred to as a *magnetic bottle*), any shifts in the axial frequency are caused by changes in the cyclotron energy. If the cyclotron motion is in the ground state, and the electron absorbs a photon with energy  $E = h\nu_+$ , there will be a visible shift in the axial frequency due to the absorption of a single photon. For a magnetic field of  $B \approx 0.5 \text{ T}$ , the photon frequency is approximately  $14 \text{ GHz}$ , and so falls within the microwave region of the electromagnetic spectrum. It is precisely on this

principle that single microwave photon detection in a Penning trap works. Further details on this are discussed in §3.4.

### Accounting for the magnetic field inhomogeneities with the Geonium Chip magnetic field source – the $\Gamma$ matrix

As seen above, uncompensated magnetic field inhomogeneities can completely destroy the detection signal of the electron. It is therefore essential that the Geonium Chip magnetic field source is capable of eliminating at least the  $B_{010}$  and the  $B_{020}$  terms of the magnetic field distribution. However, the aim of the Geonium Chip is more than just eliminating inhomogeneous fields. For an operational single microwave photon detector, it is necessary to change the magnetic field distribution on demand whilst the trap is running. How this can be achieved is given in this section.

The planar magnetic field source of the Geonium Chip comprises a plurality of current-carrying loops confined to a plane. Each current-carrying loop,  $i$ , carrying current,  $I_i$ , produces a magnetic field distribution (for which we are mainly concerned about the axial component,  $B_z^i(\mathbf{r})$ ), which, about the trapping position, is given by

$$B_z^i(\mathbf{r}) = b_z^i(\mathbf{r}_0)I_i + \sum_{l,m,n} \frac{1}{(l+m+n)!} \frac{\partial^{l+m+n} b_z^i(\mathbf{r})}{\partial x^l \partial y^m \partial z^n} \Big|_{\mathbf{r}_0} I_i x^l (y - y_0)^m z^n, \quad (3.17)$$

where  $b_z^i(\mathbf{r})$  depends on the geometry and location of the  $i$ th current-carrying loop. For  $N$  of these loops, the axial component of the total magnetic field distribution is a superposition of the field distribution from each current, such that

$$B_z^{\text{tot}}(\mathbf{r}) = \sum_i^N b_z^i(\mathbf{r}_0)I_i + \sum_i^N \sum_{l,m,n} b_{l,m,n}^i(\mathbf{r}_0)I_i x^l (y - y_0)^m z^n, \quad (3.18)$$

where  $b_{l,m,n}^i = \frac{1}{(l+m+n)!} \frac{\partial^{l+m+n} b_z^i(\mathbf{r})}{\partial x^l \partial y^m \partial z^n} \Big|_{\mathbf{r}_0}$ . This can be written more conveniently in matrix form as

$$\begin{pmatrix} B_z^{\text{tot}} \\ \frac{\partial B_z^{\text{tot}}}{\partial y} \\ \frac{\partial^2 B_z^{\text{tot}}}{\partial y^2} \\ \vdots \\ \frac{\partial^{l+m+n} B_z^{\text{tot}}}{\partial x^l \partial y^m \partial z^n} \end{pmatrix} = \begin{pmatrix} b_{000}^1 & b_{000}^2 & b_{000}^3 & \cdots & b_{000}^N \\ b_{010}^1 & b_{010}^2 & b_{010}^3 & \cdots & b_{010}^N \\ b_{020}^1 & b_{020}^2 & b_{020}^3 & \cdots & b_{020}^N \\ \vdots & \vdots & \vdots & \ddots & \vdots \\ b_{lmn}^1 & b_{lmn}^2 & b_{lmn}^3 & \cdots & b_{lmn}^N \end{pmatrix} \cdot \begin{pmatrix} I_1 \\ I_2 \\ I_3 \\ \vdots \\ I_N \end{pmatrix}, \quad (3.19)$$

or, better still, as

$$\underline{B}(r_0) = \underline{\Gamma}(r_0) \cdot \underline{I}, \quad (3.20)$$

where the dependence on the trapping position,  $r_0$ , has been made explicit.<sup>8</sup> Equations (3.19) and (3.20) show that, for a given position,  $r_0$ , if  $\underline{\Gamma}(r_0)$  is known,  $\underline{\Gamma}(r_0) = \underline{\Gamma}_{\text{known}}$ , then any chosen magnetic field distribution,  $\underline{B}_{\text{chosen}}$ , can be constructed by applying the following currents

$$\underline{I}_{\text{required}} = \underline{\Gamma}_{\text{known}}^{-1} \cdot \underline{B}_{\text{chosen}}. \quad (3.21)$$

It is therefore a requirement that  $\underline{\Gamma}$  is invertible, and so it must be a square matrix. This means that the number of terms that can be controlled in the magnetic field distribution is equal to the number of independent currents. The operation of the Geonium Chip magnetic field source crucially relies on it being possible to determine  $\underline{\Gamma}(r_0)$ . This can be measured experimentally, and details are discussed below.

### 3.3.3 Properties of the prototype planar magnetic field source for the Geonium Chip Penning trap

Whilst the ultimate aim is to develop a planar superconducting magnetic field source operating in persistent current-mode, the Geonium Chip is currently operating with a prototype magnetic field source (shown in Figure 3.9). A discussion of its calibration is given below.

#### $\Gamma$ measurement

Calibration of the prototype planar magnetic field source is achieved using a field mapping technique. A schematic depiction of the experimental setup is given in Figure 3.15. The magnetic field source is placed on the bed of a Computer Numerical Control (CNC) machine, with each coil connected to a high-precision *Rohde & Schwarz HMP4040* current source. An *Areproc* Hall probe is attached to the moving head of the CNC machine (see Figure 3.16), so that the Hall Probe position can be precisely controlled (with a step resolution of 0.01 mm). A personal computer is set up such that the position data of the Hall probe along with the magnetic field data are taken simultaneously and collated via a LabVIEW program. The  $z = 0$  point is determined by measuring the magnetic field

---

<sup>8</sup>A notational convention is adopted whereby  $\underline{B}$  refers to an array describing the magnetic field distribution, and has, in principle, any chosen number of dimensions, whereas  $\mathbf{B}$  refers to the magnetic field vector at a given position, and has three dimensions.

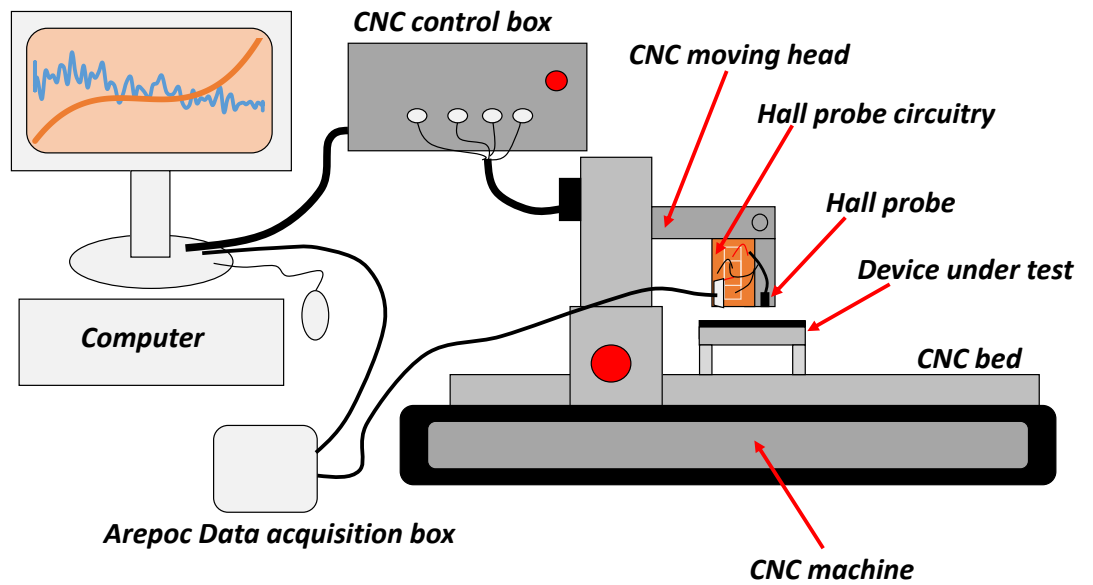


Figure 3.15: A sketch of the experimental apparatus for measuring  $\underline{\Gamma}$ . The position of the Hall probe is controlled by the CNC machine. Magnetic field data is simultaneously taken. The two sets of data are collated and analysed in a LabVIEW program, which calculates the expansion coefficients of the magnetic field distribution.

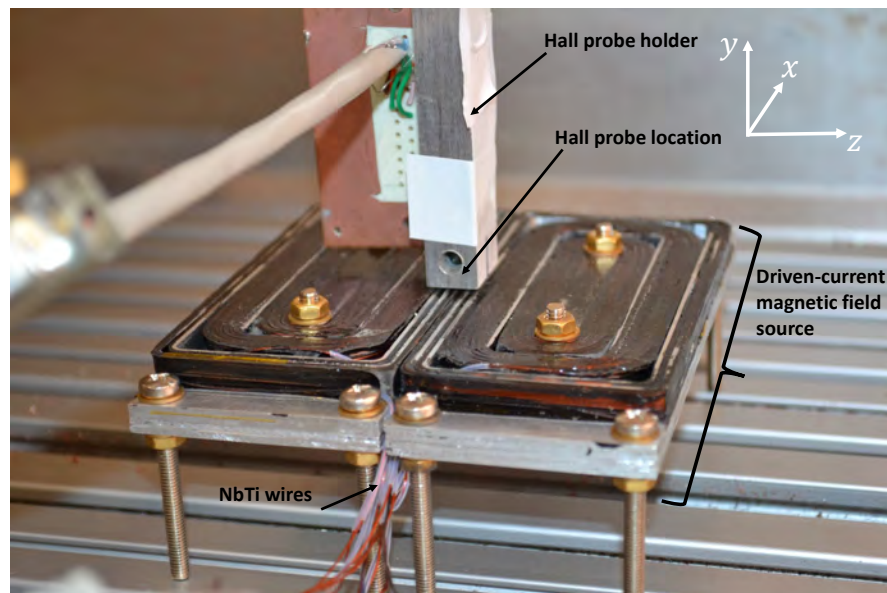


Figure 3.16: A photograph of a magnetic field mapping measurement of the prototype magnetic field source. An *Arepoc AXIS-3* three axis Hall probe is placed inside the bottom of the holder. Magnetic field data along the  $z$  direction is collated with the position data from the CNC machine.

from the main current and finding the turning point in the field distribution by fitting the data to a fourth order polynomial in  $z$  (see Figure 3.17). The vertical error bars in Figure 3.17 are the statistical errors in the magnetic field values at each point due to noise fluctuations, and the errors in the  $z$  position correspond to the step resolution of the CNC machine (0.01 mm). The magnetic field gradient at  $z = 0$  mm is determined by a fourth order polynomial fit to be  $\partial_z B_z = 0.4$  nT mm<sup>-1</sup>. Calibration of the  $x$  and  $y$  coordinates is achieved by aligning the edges of the magnetic field source and the Hall probe holder. Calibration of the Hall probe was performed by the manufacturers.

Once the setup was calibrated, 0.1 A of current was sent into the main wire, and the Hall probe was scanned along the  $y$  axis a distance of 1.5 mm either side of  $(x, y, z) = (0, 1.6, 0)$  mm in the coordinate axis of the magnetic field source. The obtained set of position and magnetic field data  $\{y, B_z\}$  were then fitted to a Taylor expansion (up to fifth order) of  $B_z$  about  $y_0$ ,

$$B_z^{\text{main}}(y) = \sum_{j=0}^5 a_{0j0}^{\text{main}} (y - y_0)^j, \quad (3.22)$$

and the fitting parameters,  $a_{0j0}^{\text{main}}$ , were obtained. This process was repeated five times (i.e., six times in total), and the average value of each coefficient, along with its statistical error, were determined ( $a_{00j}^{\text{main}} \pm \Delta a_{00j}^{\text{main}}$ ). The relevant elements in  $\underline{\underline{\Gamma}}$  ( $b_{0j0}^{\text{main}}$  for  $j = 0, 1, 2, 3$ ) were computed by dividing  $a_{0j0}^{\text{main}}$  and  $\Delta a_{0j0}^{\text{main}}$  by  $I^{\text{main}}$ , to obtain  $b_{0j0}^{\text{main}} = \frac{a_{0j0}}{I^{\text{main}}}$  and  $\Delta b_{0j0}^{\text{main}} = \frac{\Delta a_{0j0}}{I^{\text{main}}}$ . This process was repeated for each of the shim currents, and  $\underline{\underline{\Gamma}}$  was determined to be

$$\underline{\underline{\Gamma}} = \begin{pmatrix} b_{000}^{\text{main}} & b_{000}^{\text{shim1}} & b_{000}^{\text{shim2}} & b_{000}^{\text{shim3}} \\ b_{010}^{\text{main}} & b_{010}^{\text{shim1}} & b_{010}^{\text{shim2}} & b_{010}^{\text{shim3}} \\ b_{020}^{\text{main}} & b_{020}^{\text{shim1}} & b_{020}^{\text{shim2}} & b_{020}^{\text{shim3}} \\ b_{030}^{\text{main}} & b_{030}^{\text{shim1}} & b_{030}^{\text{shim2}} & b_{030}^{\text{shim3}} \end{pmatrix} \quad (3.23)$$

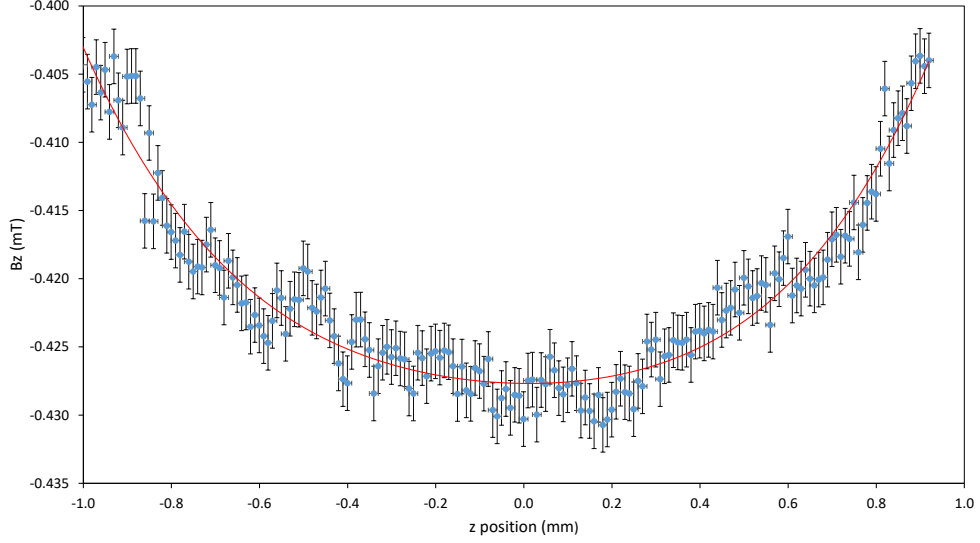


Figure 3.17: A graph showing  $B_z$  variation  $z$ . The gradient at  $z = 0$  mm is  $B_{001} = 0.4 \text{ nT mm}^{-1}$ .

$$\underline{\underline{\Gamma}}(y_0 = 1.6 \text{ mm} ; I^{\text{main}}, I^{\text{shim1}}, I^{\text{shim2}}, I^{\text{shim3}} = 1 \text{ A}) =$$

$$\begin{pmatrix} -2008 \mu\text{T} & 1464 \mu\text{T} & -4560 \mu\text{T} & 930 \mu\text{T} \\ 490 \mu\text{T mm}^{-1} & -120 \mu\text{T mm}^{-1} & -340 \mu\text{T mm}^{-1} & 160 \mu\text{T mm}^{-1} \\ -130 \mu\text{T mm}^{-2} & -190 \mu\text{T mm}^{-2} & 100 \mu\text{T mm}^{-2} & -10 \mu\text{T mm}^{-2} \\ 70 \mu\text{T mm}^{-3} & -20 \mu\text{T mm}^{-3} & -20 \mu\text{T mm}^{-3} & 50 \mu\text{T mm}^{-3} \end{pmatrix} \pm \begin{pmatrix} 8 \mu\text{T} & 8 \mu\text{T} & 10 \mu\text{T} & 10 \mu\text{T} \\ 10 \mu\text{T mm}^{-1} & 10 \mu\text{T mm}^{-1} & 20 \mu\text{T mm}^{-1} & 10 \mu\text{T mm}^{-1} \\ 20 \mu\text{T mm}^{-2} & 9 \mu\text{T mm}^{-2} & 10 \mu\text{T mm}^{-2} & 10 \mu\text{T mm}^{-2} \\ 10 \mu\text{T mm}^{-3} & 20 \mu\text{T mm}^{-3} & 30 \mu\text{T mm}^{-3} & 20 \mu\text{T mm}^{-3} \end{pmatrix}.$$

### Alternative forms of $\underline{\underline{\Gamma}}$

The matrix given above is the most practically useful version of  $\underline{\underline{\Gamma}}$ . However, alternative versions of  $\underline{\underline{\Gamma}}$  were measured and tested. In one alternative matrix, the elements in the bottom row,  $b_{030}$ , are replaced with  $b_{002}$  terms, such that the bottom row becomes  $(b_{002}^{\text{main}}, b_{002}^{\text{shim1}}, b_{002}^{\text{shim2}}, b_{002}^{\text{shim3}}) = ((123 \pm 6), (24 \pm 5), (-83 \pm 8), (8 \pm 4)) \mu\text{T mm}^{-2}$ . Note that, in this form of  $\underline{\underline{\Gamma}}$ , the third and fourth rows are close to being anti-parallel.<sup>9</sup> The consequence of this is that there are a huge number of current configurations that give close

<sup>9</sup>This comes from Maxwell's equations, which assert that  $b_{020} \approx -b_{002}$ .

Desired magnetic field	Measured magnetic field	Required currents
$(B_{z0}, \partial_y B_z, \partial_{y^2}^2 B_z, \partial_{z^2}^2 B_z)$	$(B_{z0}, \partial_y B_z, \partial_{y^2}^2 B_z, \partial_{z^2}^2 B_z)$	$(I^{\text{main}}, I^{\text{shim1}}, I^{\text{shim2}}, I^{\text{shim3}})$
$\begin{pmatrix} -100 \mu\text{T} \\ 0 \mu\text{T mm}^{-1} \\ 0 \mu\text{T mm}^{-2} \\ 0 \mu\text{T mm}^{-2} \end{pmatrix}$	$\begin{pmatrix} (-98 \pm 2) \mu\text{T} \\ (4 \pm 1) \mu\text{T mm}^{-1} \\ (2 \pm 1) \mu\text{T mm}^{-2} \\ (-4 \pm 2) \mu\text{T mm}^{-2} \end{pmatrix}$	$\begin{pmatrix} 18.6 \text{ mA} \\ 73.0 \text{ mA} \\ 63.5 \text{ mA} \\ 128.7 \text{ mA} \end{pmatrix}$
$\begin{pmatrix} -100 \mu\text{T} \\ -50 \mu\text{T mm}^{-1} \\ 10 \mu\text{T mm}^{-2} \\ -10 \mu\text{T mm}^{-2} \end{pmatrix}$	$\begin{pmatrix} (-99 \pm 2) \mu\text{T} \\ (-44 \pm 2) \mu\text{T mm}^{-1} \\ (14 \pm 4) \mu\text{T mm}^{-2} \\ (-13 \pm 2) \mu\text{T mm}^{-2} \end{pmatrix}$	$\begin{pmatrix} -51.5 \text{ mA} \\ 38.5 \text{ mA} \\ 55.0 \text{ mA} \\ -10.3 \text{ mA} \end{pmatrix}$
$\begin{pmatrix} 100 \mu\text{T} \\ 50 \mu\text{T mm}^{-1} \\ -10 \mu\text{T mm}^{-2} \\ 10 \mu\text{T mm}^{-2} \end{pmatrix}$	$\begin{pmatrix} (97 \pm 1) \mu\text{T} \\ (52 \pm 2) \mu\text{T mm}^{-1} \\ (-15 \pm 2) \mu\text{T mm}^{-2} \\ (11 \pm 1) \mu\text{T mm}^{-2} \end{pmatrix}$	$\begin{pmatrix} 51.5 \text{ mA} \\ -38.5 \text{ mA} \\ -55.0 \text{ mA} \\ 10.3 \text{ mA} \end{pmatrix}$

Table 3.1: Table comparing expected and measured magnetic field distributions for different sets of required currents in the prototype magnetic field source.

to the same magnetic field distribution. This is one of the main reasons why using the the definition of  $\underline{\underline{\Gamma}}$  given in Equation (3.23) is advantageous. Nevertheless, this alternative measurement of  $\underline{\underline{\Gamma}}$  was tested by trying to produce and measure a number of *desired* magnetic field distributions. Using the alternative form of  $\underline{\underline{\Gamma}}$ , the currents required to produce a series of desired magnetic field distributions were calculated. These required currents are listed on the right-hand column of Table 3.1, with the corresponding desired magnetic field distributions listed on the left-hand column. The measured magnetic field distributions for each case are given in the central column. The errors in the measured magnetic field distribution are the errors in the fourth-order polynomial fit of the magnetic field data against position. The results are summarised in Table 3.1, and show that the produced fields are in good agreement with the desired magnetic field distributions.

As stated above,  $\underline{\underline{\Gamma}}$  is position-dependent, meaning that, if the magnetic field distribution is to be controlled at another position, then  $\underline{\underline{\Gamma}}$  has to be remeasured. For regions close to  $r_0$ , however,  $\underline{\underline{\Gamma}}$  can be approximated by the first order term of the Taylor expansion about  $y_0$  as follows

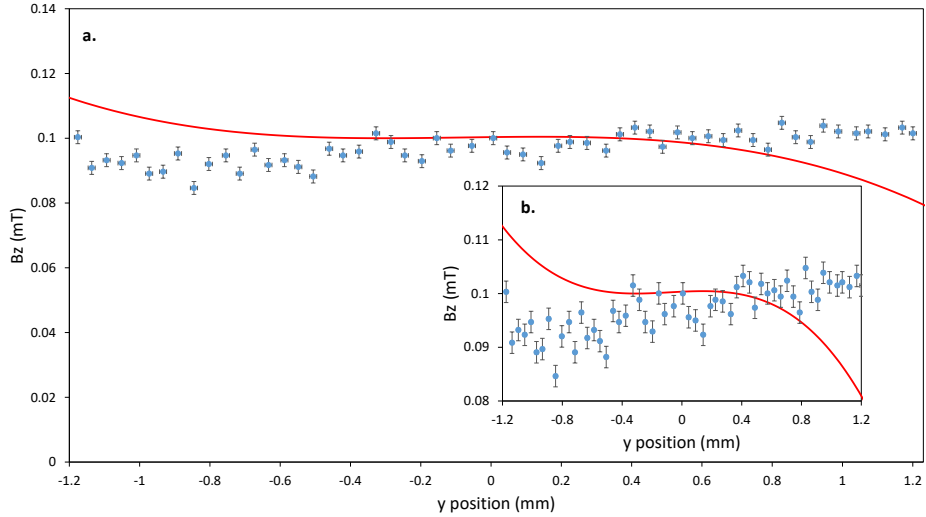


Figure 3.18: A graph showing the measured magnetic field distribution (blue data points) compared with the predicted magnetic field distribution from the first order expansion of  $\underline{\underline{\Gamma}}$  (red curve). The range of validity, as determined by there being a 5 % or less deviation between the measured data points and the expected magnetic field value from Equation (3.24), is approximately  $-0.3 \text{ mm} < y < 0.6 \text{ mm}$ . The graphs **a.** and **b.** display the same data, but have different scales in the vertical axes.

$$\underline{\underline{\Gamma}}(y) \approx \underline{\underline{\Gamma}}(y_0) + \left. \frac{\partial \underline{\underline{\Gamma}}}{\partial y} \right|_{y_0} (y - y_0). \quad (3.24)$$

An important question is over what range,  $\delta y = y - y_0$ , the approximation in Equation (3.24) is valid. This was determined by comparing the measured magnetic field distribution,  $\underline{B}_{\text{meas}}(y)$  with that of the predicted magnetic field distribution from Equation (3.24) for the same input currents,  $\underline{I}_{\text{in}}$ :  $\underline{B}_{\text{pred}}(y) = \left[ \underline{\underline{\Gamma}}(y_0) + \left. \frac{\partial \underline{\underline{\Gamma}}}{\partial y} \right|_{y_0} (y - y_0) \right] \cdot \underline{I}_{\text{in}}$ . The results (see Figure 3.18) show that the valid range, as determined by there being a 5 % or less deviation between the measured magnetic field values and the expected magnetic field values as determined by the expansion, is approximately  $-0.3 \text{ mm} < y < 0.6 \text{ mm}$ .

### Limit of $\underline{\underline{\Gamma}}$

Like any measured quantity,  $\underline{\underline{\Gamma}}$  has an associated uncertainty which can itself be represented as a matrix,  $\Delta \underline{\underline{\Gamma}}$ . The input currents from the precision current supply also have an uncertainty,  $\Delta \underline{I}_{\text{in}}$ , given by the precision of the device. For the *Rohde & Schwarz HMP4040* precision current supply, the uncertainty is  $\pm 0.01 \text{ mA}$ . Thus, there will inevitably be some discrepancy between the desired magnetic field distribution,  $\underline{B}_{\text{desired}} = \underline{\underline{\Gamma}} \cdot \underline{I}_{\text{in}}$ , and the

actual magnetic field distribution,  $\underline{B}_{\text{actual}} = (\underline{\Gamma} \pm \Delta\underline{\Gamma}) \cdot (\underline{I}_{\text{in}} \pm \Delta\underline{I}_{\text{in}})$ . The maximum discrepancy is given by

$$\max\{\underline{B}_{\text{actual}} - \underline{B}_{\text{desired}}\} = \underline{\Gamma} \cdot \Delta\underline{I}_{\text{in}} + \Delta\underline{\Gamma} \cdot \underline{I}_{\text{in}} + \Delta\underline{\Gamma} \cdot \Delta\underline{I}_{\text{in}}. \quad (3.25)$$

For the data displayed in Table 3.1,  $\underline{\Gamma}$ ,  $\underline{I}_{\text{in}}$  and  $\Delta\underline{I}_{\text{in}}$  are known, and so  $\max\{\underline{B}_{\text{actual}} - \underline{B}_{\text{desired}}\}$  can be estimated, and can be compared with  $\max\{\underline{B}_{\text{measured}} - \underline{B}_{\text{desired}}\}$ . The results below show that they are in good agreement for the homogeneous measurement:

$$|\underline{B}_{\text{actual}} - \underline{B}_{\text{desired}}| = \begin{pmatrix} 2.2 \mu\text{T} \\ 3.5 \mu\text{T mm}^{-1} \\ 3.0 \mu\text{T mm}^{-2} \\ 1.5 \mu\text{T mm}^{-2} \end{pmatrix}; |\underline{B}_{\text{measured}} - \underline{B}_{\text{desired}}| = \begin{pmatrix} (2 \pm 2) \mu\text{T} \\ (4 \pm 1) \mu\text{T mm}^{-1} \\ (2 \pm 1) \mu\text{T mm}^{-2} \\ (4 \pm 2) \mu\text{T mm}^{-2} \end{pmatrix}. \quad (3.26)$$

### Cryogenic corrections to $\underline{\Gamma}$

The measurements of  $\underline{\Gamma}$  described above were performed at room temperature ( $T_{\text{room}} \approx 300$  K). At this temperature, the input currents are confined mostly to the copper sheath of the wires. At cryogenic temperatures, the current distribution shifts from being confined primarily in the copper sheath of the wire to travelling in the niobium-titanium portion of the wire. This shift affects the overall magnetic field, and has to be accounted for in a corrected  $\underline{\Gamma}$ . Since each coil is significantly larger than the cross-section of the wire, we can approximate that the resulting corrections to  $\underline{\Gamma}$  are of the form of multiplicative constants to each column of the matrix. These measurements were performed by A Cridland, and the corrected  $\underline{\Gamma}$  is given as follows

$$\underline{\Gamma}_{4K} = \begin{pmatrix} -1869 \mu\text{T} & 1548 \mu\text{T} & -4342 \mu\text{T} & 899 \mu\text{T} \\ 456 \mu\text{T mm}^{-1} & -127 \mu\text{T mm}^{-1} & -324 \mu\text{T mm}^{-1} & 155 \mu\text{T mm}^{-1} \\ -121 \mu\text{T mm}^{-2} & -7 \mu\text{T mm}^{-2} & 95 \mu\text{T mm}^{-2} & -10 \mu\text{T mm}^{-2} \\ 115 \mu\text{T mm}^{-2} & 25 \mu\text{T mm}^{-2} & -79 \mu\text{T mm}^{-2} & 8 \mu\text{T mm}^{-2} \end{pmatrix} \pm \begin{pmatrix} 8 \mu\text{T} & 8 \mu\text{T} & 10 \mu\text{T} & 10 \mu\text{T} \\ 10 \mu\text{T mm}^{-1} & 10 \mu\text{T mm}^{-1} & 20 \mu\text{T mm}^{-1} & 10 \mu\text{T mm}^{-1} \\ 20 \mu\text{T mm}^{-2} & 9 \mu\text{T mm}^{-2} & 10 \mu\text{T mm}^{-2} & 10 \mu\text{T mm}^{-2} \\ 6 \mu\text{T mm}^{-2} & 5 \mu\text{T mm}^{-2} & 8 \mu\text{T mm}^{-2} & 4 \mu\text{T mm}^{-2} \end{pmatrix}. \quad (3.27)$$

More details of the measurement can be found in [39].

### 3.3.4 Summary of the trapping fields of the Geonium Chip Penning trap

This section is concluded with a summary of how the trapping fields can be provided in the Geonium Chip Penning trap. The electric trapping fields are provided by holding the electrodes at carefully chosen voltages. These voltages are computed mathematically using a Green's function technique [82]. Whilst electric inhomogeneities inevitably exist in the trapping electric field, a carefully chosen set of voltage ratios can be obtained such that the axial frequency does not fluctuate with axial energy (for small perturbations). This can be measured experimentally.

The planar magnetic field source comprises a set of planar coils, each carrying an independently driven current. By calibrating the magnetic field source (by measuring  $\Gamma(r_0)$ ), one can find the set of currents required to eliminate unwanted inhomogeneities (most importantly, eliminating  $B_{010}$ ), such to reduce fluctuations in the axial frequency caused by fluctuations in the axial energy. A particularly important non-homogeneous distribution is the magnetic bottle field,  $B_{000} + B_{002}z^2$ . As discussed in §3.1, this causes the axial frequency to shift as a function of cyclotron energy, and is a key feature behind the Geonium Chip as a single microwave photon detector [19].

## 3.4 Applications of the Geonium Chip

This section briefly describes some applications of the Geonium Chip. These are portable mass spectrometry and single microwave photon detection [19].

### 3.4.1 The Geonium Chip as a portable mass spectrometer

Several applications of mass spectrometry are discussed in §1, and so will not be repeated here. This section is concerned with the detail of how the Geonium Chip can act as a portable mass spectrometer.

The Geonium Chip is able to accurately determine the mass-to-charge ratio of a molecule by measuring the three motional frequencies of a trapped charge. Whilst the setup is configured only to measure the axial frequency directly, it is possible to ascertain the cyclotron and magnetron frequencies indirectly. This can be achieved by applying quadrupole RF fields close to the expected values of  $\omega = \omega_+ - \omega_z$  and  $\omega = \omega_- + \omega_z$ . The RF fields modulate the amplitude of the trapped charges, which results in the detection dip splitting. The degree of splitting can be used to determine the cyclotron and magnetron frequencies. These three frequencies can then be combined (using the Brown-Gabrielse

invariance theorem) to obtain the free cyclotron frequency  $\omega_c = \frac{qB}{m}$ . Comparison with the free cyclotron frequency of a known ion allows for the mass of the molecule to be determined.

### 3.4.2 The Geonium Chip as a single microwave photon detector

As mentioned in §1, a device capable of detecting single microwave photons would have applications in a wide range of fields. However, an efficient and scalable microwave photon detector has still not been realised [43]. Whilst single microwave photon detection (at 51 GHz) has been demonstrated with Rydberg atoms strongly coupling to photons in high finesse microwave cavities (see [83]), the required setup, which requires liquid cryogenics and lasers, is not particularly scalable. Moreover, the detection frequency cannot be easily tuned. Other designs of single microwave photon detectors tend to rely on either semiconductor or superconductor technology (see [84, 85, 86]), and have a number of practical limitations, including the need for large and expensive cryogenic systems, as well as the limitation of a maximum photon count of one [19].

With reference to Figure 3.19, single microwave photon detection in the Geonium Chip is now given. An electron is initially trapped (and cooled to its cyclotron ground state) within a harmonic potential and homogeneous field, provided by the set of currents  $\{I\}$ . This is labelled as ‘stage 1’ in Figure 3.20. Since  $\underline{\Gamma}$  for the magnetic field source is known, the required set of currents,  $\{I'\}$  for a magnetic bottle field  $B'_z = B_{000} + B_{002}z^2$  can be determined. Changing the currents  $\{I\} \rightarrow \{I'\}$  (see ‘stage 2’ in Figure 3.20) produces the magnetic bottle field, and the axial frequency (which is being measured continuously) becomes susceptible to frequency shifts as a function of the cyclotron ( $n_+$ ) and spin ( $m_s$ ) quantum states (see Equation 3.3). If the electron absorbs a photon resonant with its cyclotron frequency (‘stage 3’),  $\omega_+$ , (which is 14 GHz for a 0.5 T field) the quantum state of the cyclotron mode raises by one (‘stage 4’).<sup>10</sup> As shown in ‘stage 5’ of Figure 3.20, this results in a shift in the axial frequency, thereby indicating the absorption of a single microwave photon.

An advantage of this detection scheme is that more than one photon can be measured at a time. Using Equation (3.4), it can be shown that a change in cyclotron quantum number,  $\Delta n_+$ , results in an axial frequency change,  $\Delta\omega_z$ , according to

---

<sup>10</sup>Note that the spin state,  $m_s$ , is left unchanged in this process for two reasons: firstly, the Larmor frequency is off-resonant with the cyclotron frequency by a small (but non-negligible) factor of  $(g - 2)/2$ , and, secondly, the spin-microwave interaction is a magnetic dipole transition, and is heavily suppressed compared with the cyclotron transition, which is an electric dipole moment interaction [19].

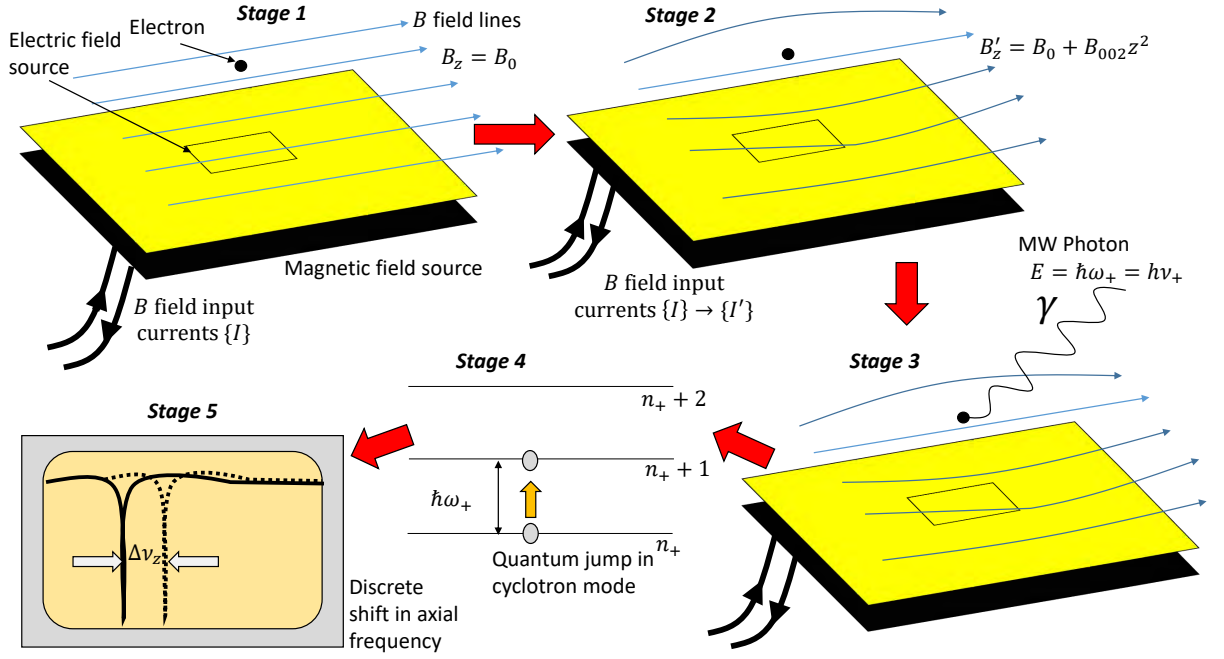


Figure 3.19: A schematic flow chart of single microwave photon detection in the Geonium Chip.

$$\Delta\omega_z(\Delta n_+) = \frac{e\hbar B_{002}}{m_e^2 \omega_{z0}} \Delta n_+, \quad (3.28)$$

where  $e$  is the electron charge,  $m_e$  is the mass of the electron,  $\hbar$  is the reduced Planck constant, and  $\omega_{z0}$  is the axial frequency when the electron is in the cyclotron ground state. In order for the ground state of the cyclotron mode to be reached, temperatures of around 100 mK are required. This is achieved with a miniaturised apparatus, in the form of an adiabatic demagnetisation refrigerator (ADR) currently under development at the Mullard Space Science Laboratory (see Figure 3.20). Typically, temperatures of this order of magnitude are only achieved with large liquid helium-based dilution refrigerators, which are grossly unscalable.

It should be mentioned that single photon detection with an electron in a Penning trap has been achieved before [46], whereby discrete shifts in the axial frequency were observed due to the absorption of thermal photons. An operational single microwave photon detector, however, should be designed to detect external photons from an object under examination. Thus, a method of guiding microwave photons from outside of the device and into the trapping region is required. An obvious candidate would be to use a coplanar waveguide placed immediately underneath (i.e., less than a millimetre) the trapping electrodes, which carries the microwave photon in a quasi-TEM mode. This is a possibility,

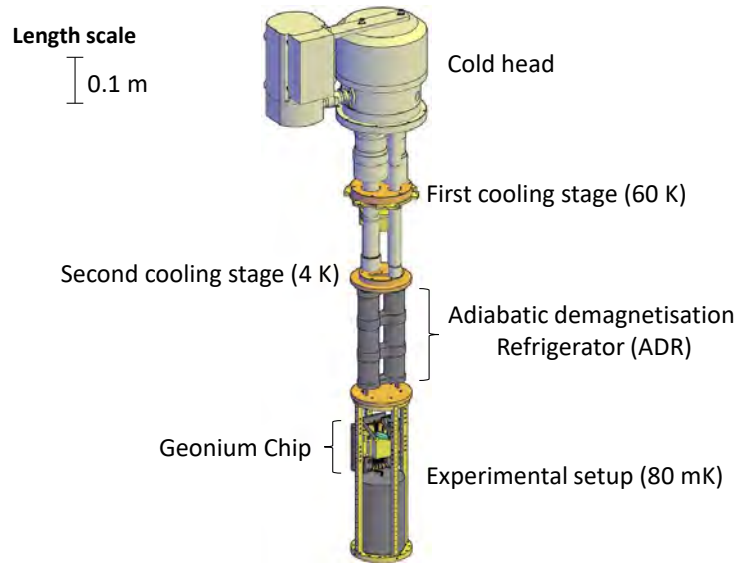


Figure 3.20: CAD drawing of the *Sumitomo* pulse tube cryostat with Adiabatic Demagnetisation Refrigerator. It is estimated that temperatures of around 80mK can be reached. This is sufficient to reach the cyclotron ground state.

since the Geonium Chip has been measured to show some degree of transparency to microwave radiation. This measurement was achieved by placing a short-terminated coplanar waveguide made from FR4 copper circuit board underneath a *MIR* Geonium Chip with 300 nm thick gold metallisation layer. To the input end of the coplanar waveguide, an 18 GHz microwave signal was supplied through an SMA connector from a *Rohde & Schwarz* microwave generator. An SMA pickup antenna was scanned, using a *Hei-Z* CNC machine at height of 1 mm above the surface of the Geonium Chip. Figure 3.21 shows the measured standing wave profile of the microwave signal from the coplanar waveguide both with (red data points) and without (blue data points) the Geonium Chip. Despite the amplitude of the microwave signal as measured with the chip being attenuated to around 30 % of the signal as measured with no chip, the standing wave pattern is clearly observed, thus indicating the transmissivity of the Geonium Chip to microwave radiation at 18 GHz.

Whilst the principle of single microwave photon detection in the Geonium Chip is very promising, a key design issue is in enhancing the quantum efficiency. Estimates in [19] suggest that, with the current setup, a quantum efficiency of 1-2% can be expected (i.e., for every one hundred photons that are captured, only one or two are detected). Whilst this quantum efficiency is relatively modest, it can be improved significantly by greatly increasing the electric field at the trapping position. How this is to be achieved will be the focus of future research.

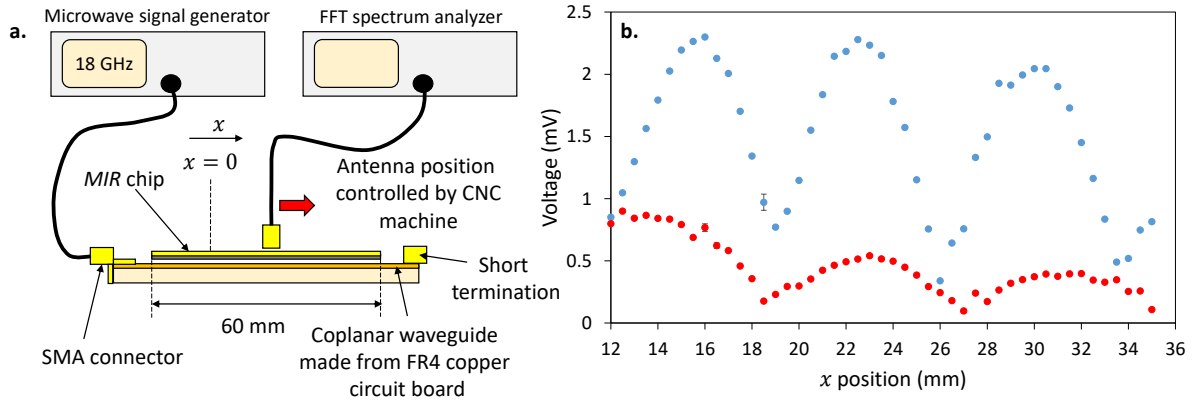


Figure 3.21: A graph showing the transmission of a standing wave at 18 GHz through the *MIR* chip

The main features of the Geonium Chip as a single microwave photon detector can be summarised as follows:

- The measurement of the axial frequency is non-destructive, meaning that the presence of microwave photons can be monitored continuously.
- Measuring the axial frequency does not change the quantum state of the cyclotron mode. This greatly relaxes the temperature requirements of the detection system, meaning that the detection apparatus can be at 4 K, whilst the cyclotron mode is at 80 mK.
- The ground state of the cyclotron mode is obtained with the aid of a novel miniature adiabatic demagnetisation refrigerator capable of reaching 80 mK. Such a miniature setup could provide for a highly portable experimental setup compared with systems based on dilution refrigerators.
- The novel planar magnetic field source of the Geonium Chip allows for the strength of the magnetic field to be varied *in situ*. Since the cyclotron energy is heavily dependent on the magnetic field strength, this means that the Geonium Chip can be tuned to be sensitive to microwave photons in a broad frequency range: (2.8 – 56) GHz for magnetic fields in the range (0.1 – 2.0) T.
- In principle, it is also possible to use the Geonium Chip as a single microwave photon source. As the cyclotron mode of the electron drops down by one quantum from an excited state, the photon can be coupled into the coplanar waveguide placed underneath the electrodes.

## Chapter 4

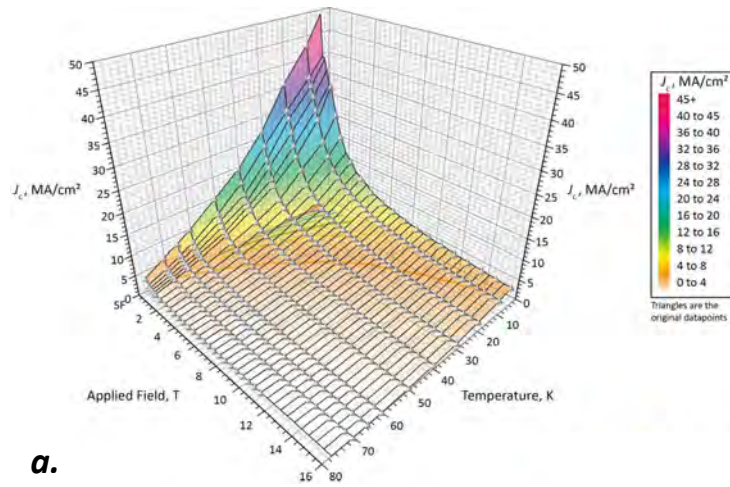
# Fundamental elements of superconductivity for the Geonium Chip Penning trap

This chapter sees a shift in focus from a discussion of the Geonium Chip Penning trap to that of fundamental aspects of superconductivity. As stated earlier, the aim of the Geonium Chip is to simplify the practicality of Penning trap technology. One of the most radical improvements is in the planarisation of the magnetic field source. A crucial aspect of the Geonium Chip magnetic field source is that it operates via the manipulation of magnetic fields provided by persistent currents running in superconducting materials. Thus, for a full appreciation of the operating principles of the Geonium Chip magnetic field source, it is essential that the relevant aspects of superconductivity are discussed.

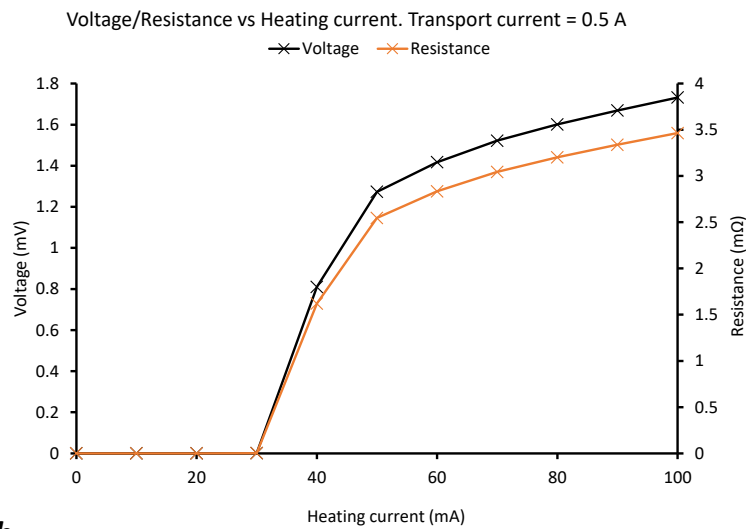
### 4.1 Superconductor properties relevant to the Geonium Chip

#### 4.1.1 Zero resistivity

Perhaps the most well-known property of superconductors is their ability to transport direct current with zero resistance under a certain set of conditions. The conditions below which a material is superconducting are called the *critical parameters*, and include a critical temperature,  $T_c$ , a critical magnetic field,  $H_c$ , and a critical current density,  $J_c$  [87]. These critical parameters are material dependent. If a superconducting material exceeds any of these critical parameters, then the material will cease to be superconducting. Any existing transport current will be dissipated as ohmic loss. The critical values are interdependent, and it is common to see the superconducting properties of a material represented as a



a.



b.

Figure 4.1: **a** Data from [88] showing the critical surface of *Superpower* high-temperature superconducting (HTS) tape illustrating the interdependence of  $H_c$ ,  $T_c$  and  $J_c$ . **b** Experimental data from the Geonium Chip lab showing the superconducting transition in *Superpower* HTS tape transporting a current of 0.5 A. The voltage (black curve) across a nickel-chromium alloy heat switch was measured as a function of the heating current supplied to the switch. The resistance of the tape as a function of heating current is plotted in red. A clear superconducting transition is observed at a heating current of around 30 mA.

critical surface (see Figure 4.1).

The zero resistivity property of superconductors is of fundamental importance for the Geonium Chip planar magnetic field source. In a closed superconducting loop, an induced current may persist *indefinitely* without any measurable signs of decay [87]. For example, in one experiment persistent currents were kept running in a closed superconducting ring for over a year, with an estimated decay rate of over 100,000 years [89]. For thick superconducting loops, mathematical models predict current lifetimes of longer than the age of the universe [90]! For the Geonium Chip, the practical significance is that the associated magnetic field does not decay with time, thus enabling a tremendous degree of magnetic field time stability. For quantum applications, persistent currents are therefore an *essential* requirement. Whilst the use of persistent currents in superconductors is standard in Penning trap systems, the Geonium Chip magnetic field source is novel in its *planar* arrangement of closed superconducting loops. The associated challenges this brings, and how they are overcome, is discussed throughout the remaining chapters of this thesis.

It is worth mentioning that the microscopic theory of superconductivity (known as *BCS theory* after its founders, Bardeen, Cooper, and Schrieffer [91]) is not discussed in this thesis. This is partly motivated by maintaining the scope of the thesis, but also because, at the time of writing, the theory is incomplete in that it does not fully describe how superconductivity arises in high-temperature superconductors [89]. Since much of what follows relies on the properties high-temperature superconductors, it seems appropriate to refrain from such a discussion. A comprehensive treatment can be found in [89].

#### 4.1.2 Meissner-Oschenfeld effect

For a material in its normal (non-superconducting) state, an externally applied magnetic field will penetrate through the material. In its superconducting state, however, the magnetic field is expelled from the interior of the material, with some magnetic field penetrating to a small distance,  $\lambda$ , from the superconductor edge [92].  $\lambda$  is termed the London penetration depth, and is given by

$$\lambda = \sqrt{\frac{m_e}{\mu_0 n (2e)^2}}, \quad (4.1)$$

where  $m_e$  is the mass of the electron,  $n$  is the charge carrier density,  $\mu_0$  is the permeability of free space, and  $2e$  is the charge of the Cooper pairs (where it is noted to be twice the charge of the electron,  $e$ ). For a Cooper pair carrier density of around  $n \approx 10^{28} \text{ m}^{-3}$  (which is typical for a metallic superconductor), the penetration depth is  $\lambda \approx 10 \text{ nm}$  [87]. The



Figure 4.2: Expulsion of the magnetic field lines from the yttrium barium copper oxide (YBCO)-based superconducting tape allows for the neodymium magnet to levitate. The photograph was taken in the Geonium Chip lab and shows a 3 mm diameter neodymium magnet levitating a 10 cm strip of *Superpower* HTS tape. The tape was stuck down onto an aluminium plate placed inside a liquid nitrogen bath.

expulsion of magnetic fields from inside the superconductor is due to induced screening currents on the edge of the material, and can provide enough force to levitate a magnet (see Figure 4.2). Although not discussed here, it is noted that the Meissner-Oschenfeld effect is a fundamental property of superconductors, and is not merely a consequence of zero resistivity [87].

In conventional Penning traps, the Meissner-Oschenfeld effect is of no real significance, since it is an effect that distorts the magnetic field distribution around the surface of a superconductor. Since the trapping region in conventional Penning traps is so far away from the superconducting solenoid (typically several centimetres away or more, such as in [93]), the field distortion in the trapping region is minimal, particularly since the screening current density is typically much smaller than the transport current density. It does, however, need to be carefully considered when designing a planar magnetic field source, where the trapping region is less than 2 mm away from the superconducting magnetic field source.

### **Simulation of the Meissner-Oschenfeld effect for a planar superconducting magnetic field source**

A computational investigation on how the Meissner-Oschenfeld effect distorts the trapping field distribution is made with the aid of an open-source finite element magnetics software

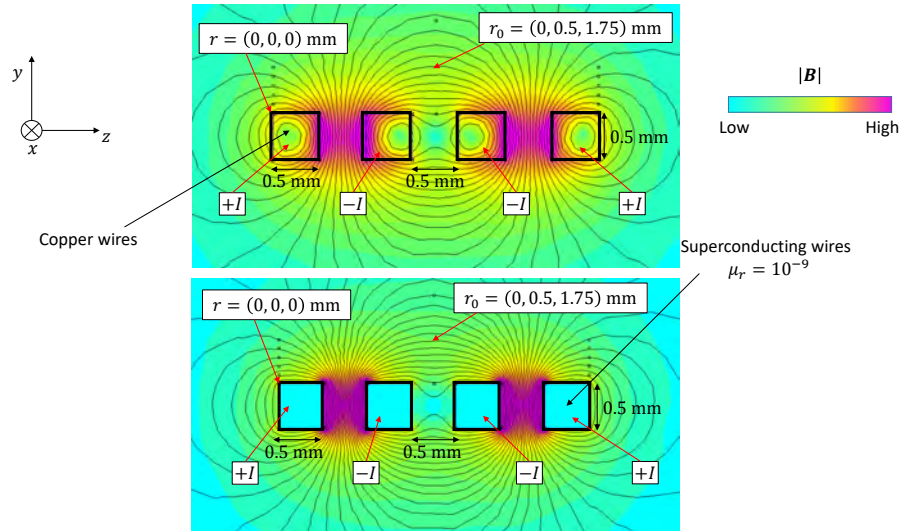


Figure 4.3: *FEMM* simulations showing how expulsion of the magnetic field from superconductors may distort the trapping field if not accounted for. The simulated current in both cases is 50 A. The differences in simulated magnetic field distributions from copper wire (top) and superconducting wire (bottom) are clear.

(*FEMM*). The magnetic field distribution from four current-carrying wires of square cross-section ( $0.5 \text{ mm} \times 0.5 \text{ mm}$ ), each separated from their nearest neighbour by 0.5 mm, and assumed to be infinitely long in the  $x$  dimension (see Figure 4.3) are determined for a number of different currents ranging from 1 A to 50 A. The currents in the wires are uniform along the cross-section, and are directed along the  $x$  axis, with the two outer wires carrying current into the page (denoted by  $+I$ ), and the two inner wires carrying current out of the page (denoted by  $-I$ ). The  $z$  component of the magnetic field distribution about  $r_0 = (0, 0.5, 1.75)$  mm is determined up to third order in both  $y$  and  $z$  for both simulated copper and superconducting wire (where, to avoid computational errors, the relative permeability was chosen to be  $\mu_r = 10^{-9}$ , instead of exactly zero). The simulated field distributions from both are shown in Figure 4.3 for an input current of 50 A. A table of the relative distortions for each current is given in Table 4.1. The field distortion due to the Meissner effect is clearly visible, ultimately meaning that  $\underline{\Gamma}$  depends on temperature, such that  $\underline{\Gamma}(T > T_c) \neq \underline{\Gamma}(T < T_c)$ . It is therefore essential to calibrate the magnetic field source when the material is superconducting.<sup>1</sup> The simulation also shows that the relative field distortion between the copper and superconducting wires does not change with current. Thus, calibration of the magnetic field source can be made with low input

<sup>1</sup>It should be noted that this is in addition to magnetic field distortion due to changes in the current density when a material becomes superconducting. This is discussed in [39], and in §3.

Current (A)	$\frac{B_z^{\text{Cu}}(r_0)}{B_z^{\text{SC}}(r_0)}$	$\frac{\partial_z B_z^{\text{Cu}}(r_0)}{\partial_z B_z^{\text{SC}}(r_0)}$	$\frac{\partial_{z^2} B_z^{\text{Cu}}(r_0)}{\partial_{z^2} B_z^{\text{SC}}(r_0)}$	$\frac{\partial_y B_z^{\text{Cu}}(r_0)}{\partial_y B_z^{\text{SC}}(r_0)}$	$\frac{\partial_{y^2} B_z^{\text{Cu}}(r_0)}{\partial_{y^2} B_z^{\text{SC}}(r_0)}$
1	1.293	1.105	1.203	1.718	0.720
5	1.291	1.107	1.203	1.718	0.720
10	1.291	1.107	1.203	1.718	0.720
20	1.291	1.107	1.203	1.718	0.720
50	1.291	1.107	1.203	1.718	0.720

Table 4.1: Table showing simulated distortions to the magnetic field distributions due to the Meissner-Oschenfeld effect.  $B_z^{\text{Cu}}$  describes the magnetic field due to current in the simulated copper wire, whilst  $B_z^{\text{SC}}$  refers to the magnetic field from the simulated superconducting wire. The data shows that there is significant distortion to the magnetic field distribution, and this is particularly severe for the  $\partial_y B_z$  term.

currents and still be valid when holding strong fields.

## 4.2 Types of superconductors

### 4.2.1 Type I and Type II superconductors

A superconductor is classified as being either Type I or Type II. This classification is based on how the critical properties of the material behave as a function of applied magnetic field,  $H_a$  [87].

Type I superconductors are often termed ‘soft superconductors’, and are characterised as having only one critical field,  $H_c$ . Provided  $T < T_c$ , if a Type I superconductor is placed in an external magnetic field,  $H_a$ , the material will remain superconducting under the condition  $H_a < H_c$ . This is often termed the ‘Meissner state’, since no magnetic field lines penetrate into the material. Upon increasing  $H_a$ , the material remains superconducting until  $H_a > H_c$ , whereby the material immediately becomes normally conducting as a phase transition takes place. Once normal, the external magnetic field penetrates into the material.

Type II superconductors are different in that they are characterised as having two critical magnetic fields: a lower critical field,  $H_{c1}$ , and a higher critical field,  $H_{c2}$ . If a Type II superconductor is held at  $T < T_c$ , and is subjected to an external magnetic field,  $H_a$ , then, provided  $H_a < H_{c1}$ , the material remains superconducting and in the Meissner state, where the applied magnetic field is expelled by the material. If the applied magnetic

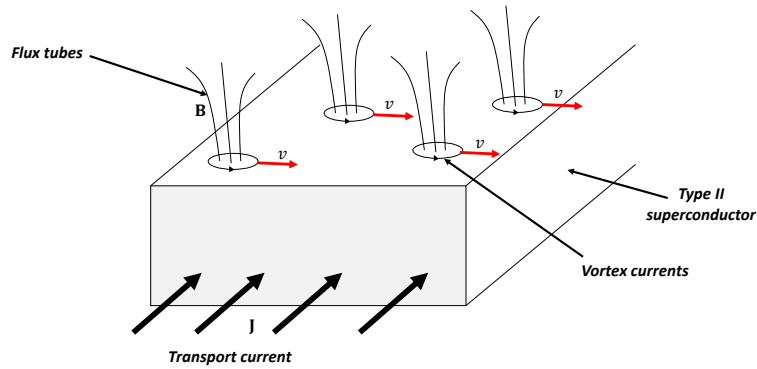


Figure 4.4: A schematic diagram showing the origin of flux creep in a Type II superconductor. Interaction between the flux tubes and the transport current forces the vortices to jump between pinning sites in a thermally activated process, causing the self-flux of a closed superconducting loop to slowly decay. The motion of the vortices is denoted by the red arrows, and  $v$  describes the average velocity of the vortices as they migrate across the superconductor.

field exceeds the upper critical field,  $H_a > H_{c2}$ , then the material is in the normal state, and the applied magnetic field penetrates into the material. However, when the condition  $H_{c1} < H_a < H_{c2}$  is satisfied, the superconductor is said to be in the *Shubnikov phase*, or *mixed state*, whereby the normal and Meissner state of the superconductor coexist. In this state, the external magnetic field is largely expelled, but penetrates into the material through regular triangular arrays of flux tubes, known as fluxons, or Abrikosov vortices [94], with each vortex carrying a single quantum of flux,  $\phi_0 = \frac{h}{2e} \approx 2.07 \times 10^{-17}$  Wb [89]. If the material is transporting some current,  $\mathbf{J}$ , there will be a Lorentz force which pushes the vortices transverse to the direction of current flow (see Figure 4.4). This induces an effective electric field which opposes the transport current, thereby introducing some resistance. This process is known as flux flow. Flux flow can be largely reduced with the presence of defect sites in the material, which aid to ‘pin’ the vortices preventing them from moving.

### Flux creep

At high current densities ( $J \sim J_c$ ), the driving force on the vortices is large enough for them to overcome the pinning force via thermal activation, in a process known as flux creep. Here, available thermal energy enables flux vortices to hop between pinning sites, thereby introducing a small resistance on the transport current. For a persistent current in

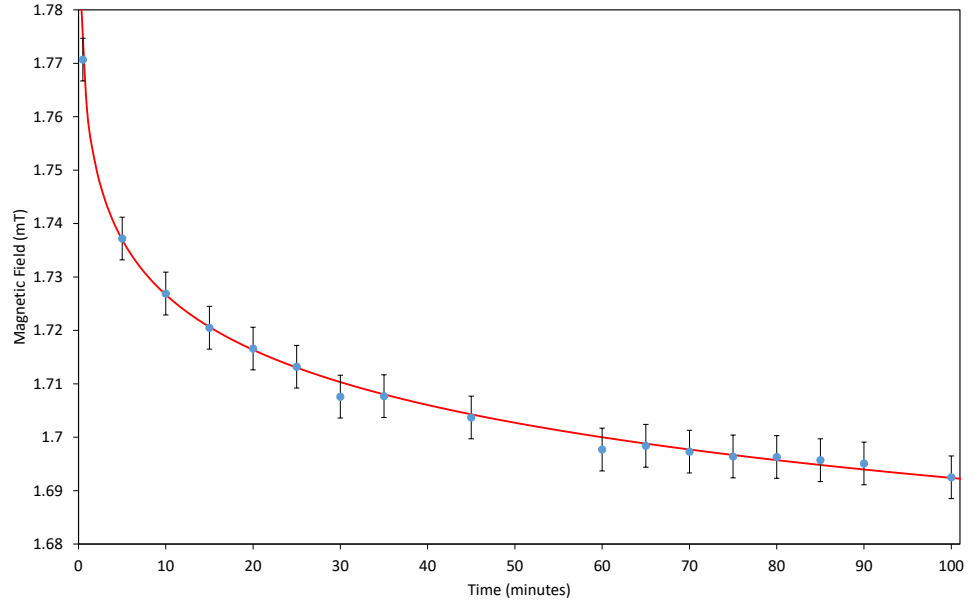


Figure 4.5: Data taken from a closed superconducting loop showing flux creep. The graph shows a good fit (reduced  $\chi^2$  of 1.2) between Equation (4.2) and the data, indicating that flux creep is well-described by the Anderson-Kim model.

a closed superconducting loop, this manifests as a gradual decay of the trapped magnetic field, the time dependence of which is characterised by the Anderson-Kim model [89, 95, 96]

$$B(t) = a - b \ln(t - t_0), \quad (4.2)$$

where  $a$  and  $b$  are constants. An example of such magnetic field decay is given in Figure 4.5, which shows a measurement of the magnetic field over time from a 12 mm  $\times$  12 mm square of *Superpower* HTS tape, with superconducting paths 3 mm wide. The loop is field cooled (see Figure 4.6) by placing a neodymium magnet in the centre of the loop and immersing it in liquid nitrogen. After a number of seconds, the magnet is then removed and the magnetic field in the centre of the loop is measured with a cryogenic Hall probe. The errors in the magnetic field are the statistical errors from the magnetic field measurements in 10 second time intervals. The red curve represents the fit of Equation (4.2) to the data, and has a reduced  $\chi^2$  of approximately 1.2.

Since flux creep is a thermally activated process, its effects are more severe at higher operating temperatures (particularly with high-temperature superconductors), and this could present a practical limit for the operating temperature of the Geonium Chip. However, current decays due to flux creep can be compensated by periodic induction via the method of flux pumping, which is also the method of magnetising the magnetic field source

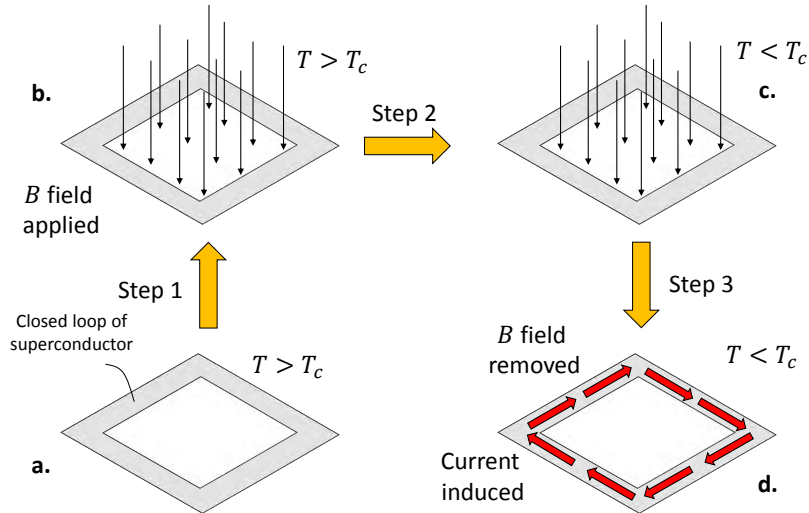


Figure 4.6: A schematic diagram showing field cooling. **a.** A closed loop of superconductor is held at a temperature above its critical temperature ( $T > T_c$ ). **b.** In Step 1, the loop is subjected to an applied field,  $B$ . In this step, the superconductor remains above its critical temperature. **c.** In Step 2, the superconductor is cooled below its critical temperature ( $T < T_c$ ). **d.** In Step 3, the applied field is then removed, and a persistent current is induced in the closed superconducting loop to conserve the flux (see §4.4).

(see §5).

#### 4.2.2 High-temperature superconductors

High-temperature superconductors were first discovered in 1986 by Bednorz and Muller [97],<sup>2</sup> and are materials that display superconducting properties at unusually high temperatures. Whilst there seems to be no universal categorisation, it is generally accepted that a superconductor whose critical temperature,  $T_c$ , is in excess of 30 K is considered a high-temperature superconductor, whilst those with  $T_c < 30$  K are considered low-temperature superconductors. Of particular practical importance for the Geonium Chip Penning trap are high-temperature superconductors with critical temperatures above 77 K (such as rare-earth barium copper oxide (ReBCO)-type superconductors, of which YBCO is an example). These could allow for the Geonium Chip to operate in nitrogen-based cryogenic systems, which would massively simplify and cheapen the experimental setup.

Despite the advantage of a high operating temperature, the use of high-temperature

<sup>2</sup>They were awarded the 1987 Nobel Prize “for their important break-through in the discovery of superconductivity in ceramic materials”.

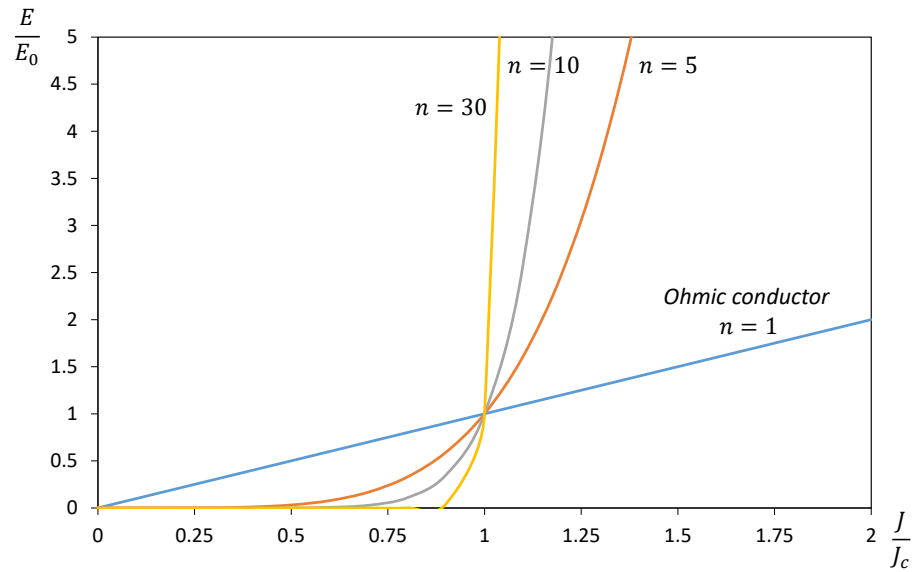


Figure 4.7: A graph depicting the  $E - J$  power law of superconductors.

superconductors comes with its difficulties. As far as is known, all high-temperature superconducting materials are categorised as Type II superconductors, and so display flux creep behaviour when operating near their critical parameters. This non-ideal behaviour is often characterised by an ‘ $n$ ’ number, which describes the voltage per unit length (i.e., the electric field,  $E$ , in the superconductor) that is often written as a function of the current density,  $J$ , transported by the superconductor [87]

$$E = E_c \left( \frac{J}{J_c(B, T)} \right)^{n(B, T)}, \quad (4.3)$$

where the  $n$  dependence on temperature,  $T$ , and magnetic field,  $B$ , is made explicit, and  $E_c = 1 \mu\text{V cm}^{-1}$  is the standard criterion used to define the critical current density,  $J_c$ . The higher the  $n$  value, the more ideal the superconducting behaviour, as shown in Figure 4.7. Whilst low-temperature superconducting materials are approximately ideal (with typical values of  $n > 25$ ), high-temperature superconductors often have non-negligible index values of  $n < 18$  [87]. Another issue with high-temperature superconductors is in their mechanical properties. Most practical high-temperature superconductors (such as YBCO) are ceramic-based materials, and are therefore brittle and difficult to machine. Whilst some 3D printing of high-temperature superconductors has been performed (such as via extrusion free-forming) it is difficult to obtain precisely defined dimensions [98, 99].

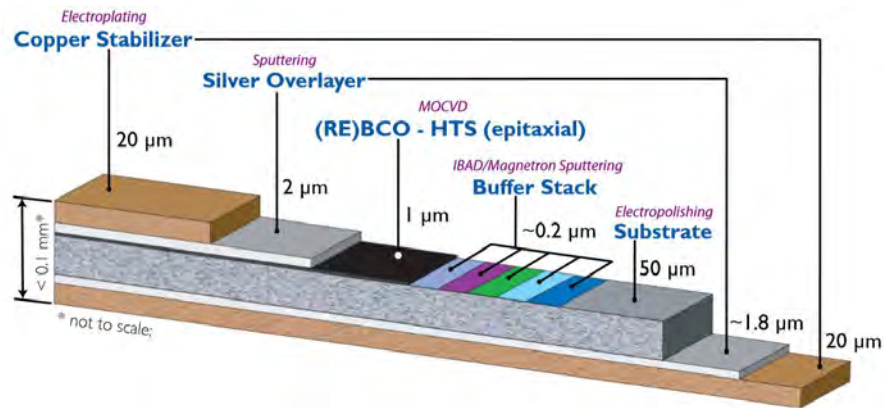


Figure 4.8: Cross-section of the *Superpower* HTS tape [100]. It should be noted that the tape used in the work of this thesis did not have the copper stabilisation layer.

### 4.3 Superconducting materials

This section briefly summarises the main features of the superconducting materials used in this body of work. Whilst the majority of the developmental work in §5 was performed with different types of YBCO-based HTS tape, the proposed magnetic field source (see §6) is designed to be made of bulk niobium titanium (NbTi).

#### 4.3.1 High-temperature superconductor tapes

The majority of the experimental work in §5 was performed using YBCO-based HTS tapes. The tape is chosen for many reasons, including its commercial availability, its planar geometry, and the high critical temperature of YBCO. These properties enable for rapid proof-of-concept experiments to be performed. Additional useful properties of HTS tape are that they are easily machined and easily soldered.

Three types of HTS tape were used in the development of the planar magnetic field source, all of which were YBCO based. The first was a 12 mm wide tape manufactured by *Superpower*. The second was a 46 mm wide tape from *American Superconductor*. The third was 40 mm wide tape from *Bruker*. A comparison of their electrical and physical properties is given in Table 4.2. A schematic depiction of the cross-section of the *Superpower* tape is given in Figure 4.8. All samples of YBCO-based tape came without the copper stabilisation layer.

Aside from their widths, the main difference between the tapes are the electrical properties of the buffer layers. Of particular significance is the nickel based layer in the *American*

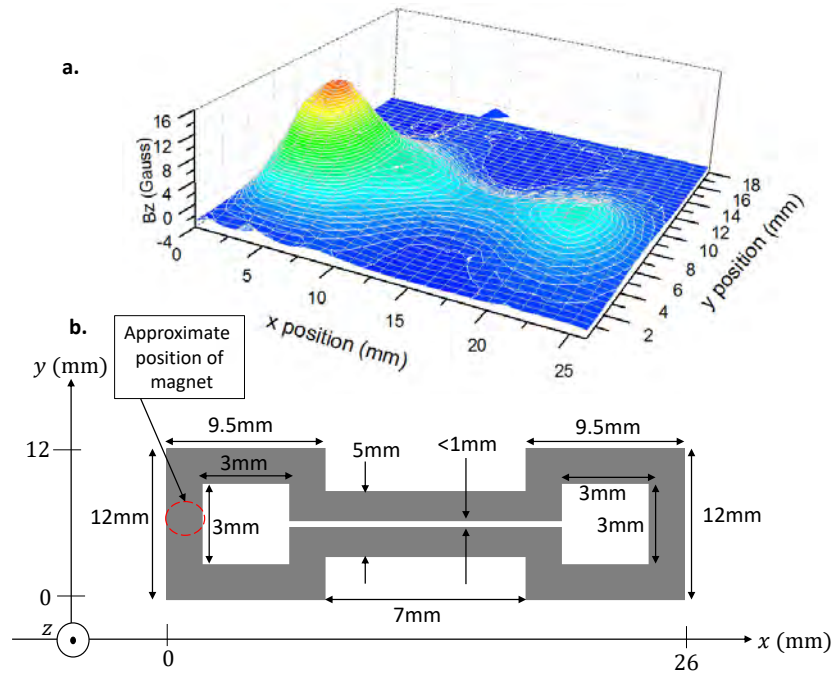


Figure 4.9: The magnetic field distribution from a superconducting structure made from *American Superconductor* tape after being field cooled with a neodymium 3mm magnet. **a.** The measured magnetic field distribution showing remanent magnetisation on the left-hand loop. This was where the neodymium magnet was positioned during field cooling. The magnetic field in the right-hand loop is due to persistent current. **b.** A schematic drawing of the dimensions of the superconducting tape.

*Superconductor* tape, which displayed magnetic remanence when magnetised with a 3 mm neodymium magnet (see Figure 4.9). In this experiment, a 3 mm neodymium magnet was placed about 1 mm above the left-hand loop of the superconducting structure at room temperature. Liquid nitrogen was then added thereby freezing the flux from the magnet into the closed superconducting circuit via the process of field cooling (see Figure 4.6). The magnet was then removed resulting in the induction of a current in the entire loop so as to conserve flux. In addition to this induced current, the presence of the magnet above the tape resulted in some magnetisation of the nickel layer in the *American Superconductor*, with the remanent magnetisation clearly visible on the far left-hand edge. In similar experiments, no visible remanence was observed in either the *Bruker* or *Superpower* tapes.

### 4.3.2 Soldering to high-temperature superconducting tape

In many cases soldering to HTS tapes is necessary. For the purpose of this work, the intention of soldering to HTS tapes is not to achieve exceptionally low resistance values

HTS tape	Width	YBCO thickness	$I_c$ ( $J_c$ )	Composition
<i>American Superconductor</i> (ASC-66)	46 mm	0.8 $\mu\text{m}$	$I_c = 350$ A	Ag (3 $\mu\text{m}$ )/YBCO (0.8 $\mu\text{m}$ )/GeO <sub>2</sub> (75 nm)/
			( $J_c = 9, 511$ A mm <sup>-2</sup> )	YSZ(75 nm)/Y <sub>2</sub> O <sub>3</sub> (75 nm)/Ni(5)W(75 $\mu\text{m}$ )/ Ag(3 $\mu\text{m}$ )
<i>Superrpower</i> (AF12050-AP)	12 mm	1.6 $\mu\text{m}$	$I_c = 330$ A	Ag (1.6 $\mu\text{m}$ )/YBCO (1.6 $\mu\text{m}$ )/
			( $J_c = 17, 188$ A mm <sup>-2</sup> )	Buffer stack ( $\sim 0.2$ $\mu\text{m}$ )/ Hastelloy (50 $\mu\text{m}$ )/Ag (2 $\mu\text{m}$ )
<i>Bruker</i> YBCO tape	40 mm	1.5 $\mu\text{m}$	Piece 1:	Ag (2 $\mu\text{m}$ )/Buffer layer (1.8 $\mu\text{m}$ )-
			$I_c = 530$ A	ABAD-YSZ-PLD-CeO <sub>2</sub> /
			( $J_c = 8, 883$ A mm <sup>-2</sup> )	YBCO(1.5 $\mu\text{m}$ )/Stainless steel (100 $\mu\text{m}$ )/
			Sample 2:	Ag (2 $\mu\text{m}$ )
			$I_c = 590$ A	
			( $J_c = 9, 833$ A mm <sup>-2</sup> )	

Table 4.2: Table comparing the properties of three commercially available YBCO-based HTS tapes. Two samples of *Bruker* YBCO tape were obtained, and, despite having the same nominal widths and compositions, they differed in critical current.

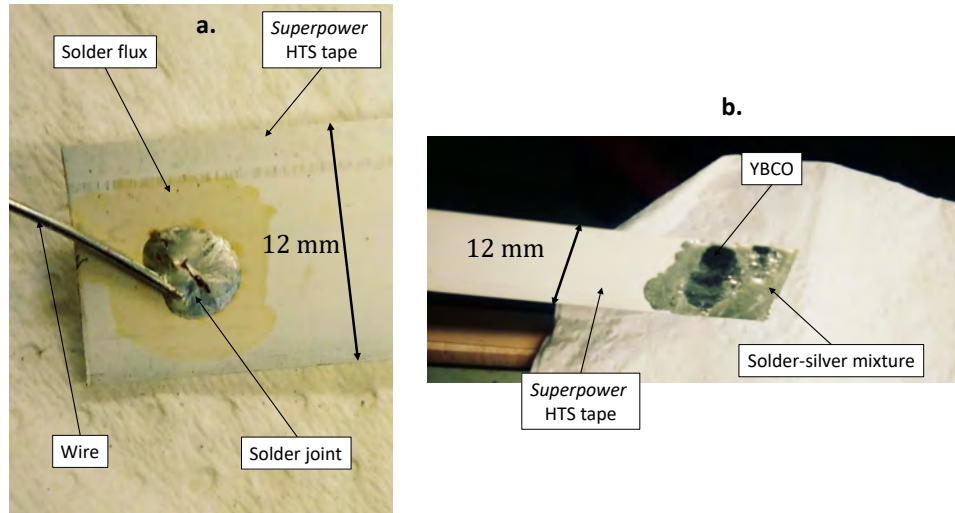


Figure 4.10: **a.** A typical solder joint between wire and *Superpower* high-temperature superconducting tape. The solder flux around the joint is clearly visible. **b.** The *Superpower* tape with silver melted away revealing the black YBCO layer.

like those in [101]. Rather, it is merely to provide an electrical connection between the superconducting tape and a wire.

The method described below applies to all three types of HTS tape listed in Table 4.2. Firstly, the silver layer on the top side of the HTS tape (i.e., the side closest to the YBCO layer) is smeared with either solder paste or solder flux. Then, a conducting wire is pressed into the solder paste/flux, before a “tinned” soldering iron is gently touched onto the smeared paste/flux for less than a second. This causes the solder to melt and dissolve the silver layer, such that the resulting fluid engulfs the end of the wire. Removing the soldering iron quickly enough allows for the silver-solder solution to solidify around the wire such that it is held in place on the tape. An example of such a solder joint is shown in Figure 4.10a. Caution must be taken not to leave the soldering iron touching the tape for too long. The silver layer dissolves into the solder and flows away from the soldering iron, revealing a black YBCO layer underneath (see Figure 4.10b).<sup>3</sup> It should be noted that the solder joint is very fragile, and care must be taken to ensure the silver does not flake away from the tape. In spite of its fragility, solder joints prepared in this way have been able to withstand tens of cryogenic cycles without noticeable degradation.

<sup>3</sup>This is, in fact, a useful method of stripping the tape of its silver layer, although one should be careful when doing this, as the exposure of heat to the YBCO tape can damage its superconducting properties.

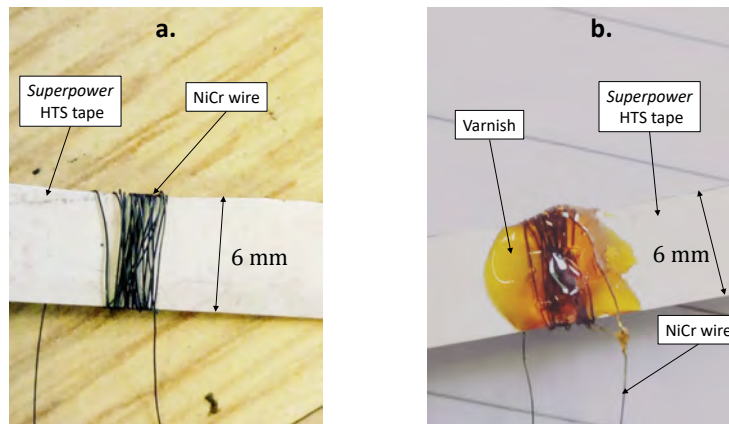


Figure 4.11: Superconducting heat switches. **a.** Nickel-chromium wire wrapped around high-temperature superconducting tape. **b.** The switch is coated in varnish to reduce heat loss via convection when immersed in liquid nitrogen.

### 4.3.3 Superconducting heat switches

A superconducting switch is a device which drives a region of a superconducting material normally conducting. The process is reversible, and the material returns to its superconducting state when the switch is turned off. Superconducting switch operation requires for one of the critical parameters of the material to be exceeded in a localised spot. Magnetic field switches, which exceed  $H_c$  of the material, are difficult to implement with HTS tape made from YBCO due to their high critical field [102]. Thus, heat switches which locally exceed  $T_c$  of the material are most practical. In §5, the need for such switches will become apparent.

Fabrication of heat switches is relatively simple. The HTS tape is wrapped with high resistance ( $62.3 \Omega \text{ m}^{-1}$ ) 0.1 mm diameter nickel-chromium wire. Current supplied to the wire dissipates heat which conducts to the HTS tape raising its temperature. If enough heat is generated, then the temperature of the superconducting material will eventually exceed  $T_c$ . Their efficiency can be improved by insulating the switch (see Figure 4.11) with varnish or epoxy [40]. This is because, when operated in a liquid cryostat where the HTS tape is immersed in liquid nitrogen, the insulating material prevents much of the heat generated in the nickel-chromium wire from being convected away by direct contact with the liquid nitrogen. Such loss of heat via convection is not an issue in a dry cryostat setup, whereby the superconducting switch is operated in vacuum.

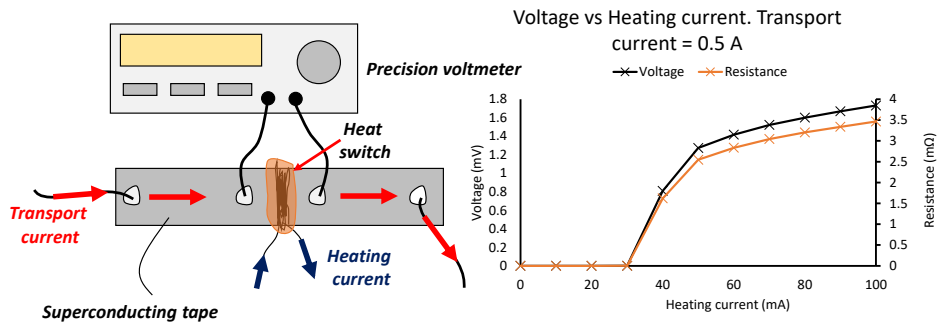


Figure 4.12: Standard 4-wire measurement of resistance. The transition from superconducting to normally conducting is seen with a sudden jump in voltage.

### Heat switch measurements

Three different methods of testing the operation of heat switches are used. The first of which is the standard 4-wire resistance method (see Figure 4.12). A length of superconducting material is cut, and nickel-chromium wire is wrapped around the centre of the tape and smeared with varnish to make a heat switch. The nickel-chromium wire is connected to a power supply through an ammeter. Either side of the heat switch, wires are soldered to the superconducting tape and connected to a voltmeter. Wire is also soldered onto each end of the superconducting tape, and connected to a high precision power supply through another ammeter. The superconducting circuitry is immersed in liquid nitrogen, and 0.5 A current is set to run through the superconducting tape. When superconducting, the voltmeter records 0 V. The heating current is then gradually increased whilst the voltage is monitored. When the material becomes normally conducting (in Figure 4.12, this happens with a heating current of 30 mA), a finite voltage is measured in the voltmeter. The characteristic  $V - I$  curve is shown in Figure 4.12.

A second method comprising a “Y” shaped superconducting circuit is shown in Figure 4.13. Current leads are soldered to each of the three ends of the superconducting Y structure, and on one of the arms is placed a heat switch. An ammeter is placed on the output of the arm without the heat switch. An input current of 0.33 A is set to flow into the superconducting structure, and divide into the two arms of the circuit. This is represented by red arrows in Figure 4.13. The amount of current in each arm depends on the relative resistances. Increasing the heating current raises the temperature of the superconducting material near the heat switch, until eventually  $T_c$  is exceeded. This results in a shift in current to the arm without the heat switch, and is seen as a sudden jump in

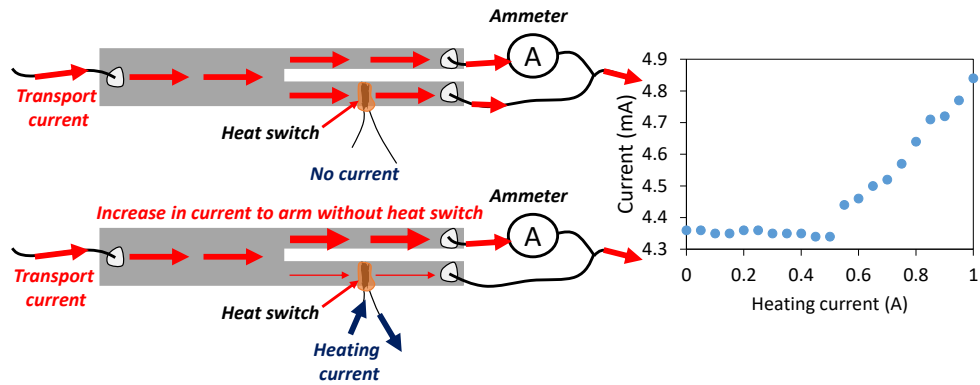


Figure 4.13: A method of testing heat switches using a Y shaped superconducting structure. The top left shows the case when the heat switch is not operating. When the heat switch is operating (depicted on the bottom left) there is a sudden increase in current in the arm that does not have the switch, as shown in the graph.

current measured in the ammeter (see right-hand panel of Figure 4.13). This particular measurement took place in a liquid cryostat, as can be seen by the relatively high heating current of over 0.5 A.

A third method uses a superconducting circuit similar to the Y structure, only with the two arms joined to form a single output lead with a closed loop in the middle. Current flows into the superconducting structure, divides into two arms, before recombining and exiting the superconductor through the output lead (see Figure 4.14). The left-hand side shows two schematic diagrams of the experimental setup. The top left shows the case when both arms are completely superconducting, with the transport current dividing evenly between the two. The measured magnetic field distribution for this case is depicted in the top right, and corresponds to an even distribution of current. The bottom left shows a sketch of the current division when the heat switch is on. In this case, all of the current is now directed along the arm without the heat switch. As a result, there is a drastic change in the measured magnetic field distribution, as is shown in the bottom right-hand graph. Note that the Hall probe is placed several centimetres away from the heat switch such that any magnetic field from the heating current is negligible.

#### 4.4 Flux conservation in closed superconducting paths

The principle of flux conservation in closed superconducting paths is (along with zero resistivity) probably the most important concept in the design and operating principle of

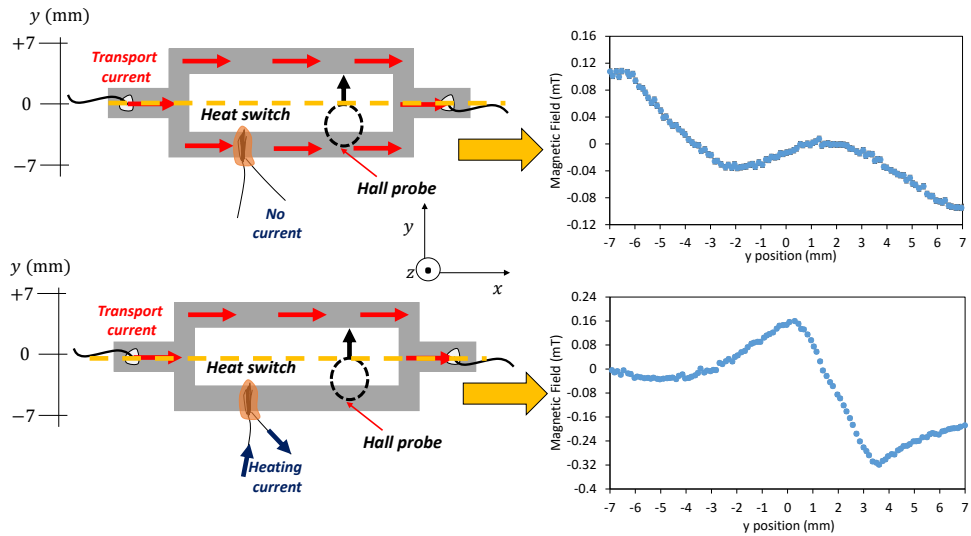


Figure 4.14: A Hall probe scanning method for determining heat switch operation. Heat switch operation is determined by measuring a significant change to the magnetic field distribution.

the Geonium Chip magnetic field source. In fact, its entire design relies on manipulating this effect to precisely control the magnetic field distribution to permit for the trapping and detection of a single electron. Thus, a comprehensive discussion is given here.

#### 4.4.1 Theoretical derivation of flux conservation

Whilst by no means a classical effect, a closed superconducting loop subjected to a time-varying magnetic field,  $B(t)$ , can be approximately described in terms of a lumped-element circuit model. Electrically speaking, a closed normally conducting loop can be approximated as a series  $R-L$  circuit (see Figure 4.15).<sup>4</sup> Magnetic field lines from the time-varying magnetic field flow into the closed conducting loop, creating an electromotive force in accordance with Faraday's law of electromagnetic induction,  $V = -\frac{d\phi_a}{dt}$ , where  $\phi_a$  is the applied flux flowing through the closed loop. A time-varying current,  $I(t)$ , is then induced, obeying Kirchoff's voltage law

$$L \frac{dI}{dt} + IR = -\frac{d\phi_a}{dt}, \quad (4.4)$$

where  $L$  is the inductance of the loop, and  $R$  is the total resistance. This can be rearranged to

<sup>4</sup>Here, it is assumed that the frequency of the applied field is sufficiently low such that the parasitic capacitance of the loops can be ignored.

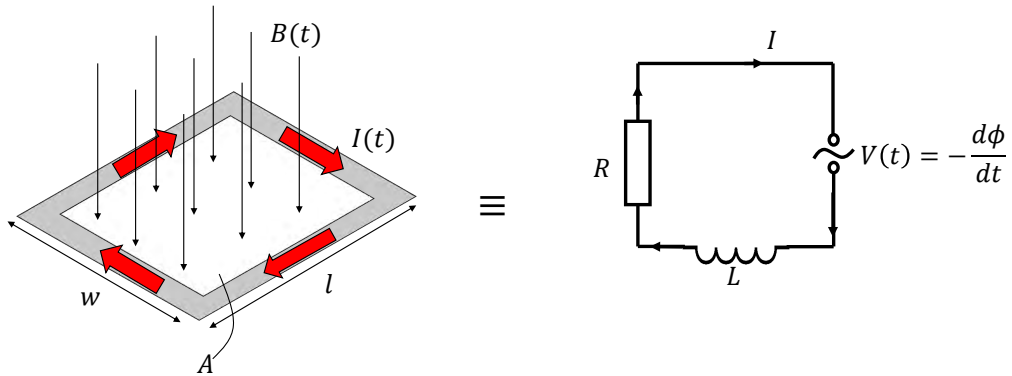


Figure 4.15: A sketch of the equivalent circuit of a square conducting loop subjected to a time varying applied magnetic field.

$$\frac{d}{dt} (LI + \phi_a) = -IR. \quad (4.5)$$

Taking  $R = 0$  (for a superconductor) reveals that the total flux is constant:

$$\underbrace{LI}_{\text{self flux}} + \underbrace{\phi_a}_{\text{applied flux}} = \text{constant}. \quad (4.6)$$

Equation (4.6) shows that any change in applied flux,  $\phi_a$ , is perfectly compensated by a change in the current,  $I$ , so as to keep the total flux in the loop constant. This concept is of key importance to the magnetic field source of the Geonium Chip for a number of reasons. Firstly, it makes remote magnetisation of a closed superconducting loop difficult, since the superconducting loop reacts to changes in applied field. How this is overcome is the content of §5. The second difficulty is *cross-talk* between different superconducting loops. Since the current in any superconducting loop is critically dependent on the external flux that flows through it, one needs to account for the fact that any change in current in one loop will consequently result in changes in the current of a neighbouring loop (see Figure 5.11 in §5 for more details). Failure to control such *cross-talk* would result in failure to control the magnetic field distribution. This is discussed in more detail in §5.

It should be noted that the theoretical discussion above is merely a classical approximation. In the macroscopic quantum theory of Ginzburg and Landau [103, 104], there is an additional non-classical effect which states that not only is a flux-type quantity conserved, but it is also quantised according to

$$\phi' = n\phi_0 = \oint_C \mu_0 \lambda^2 \mathbf{J} \cdot d\mathbf{l} + \int \mathbf{B} \cdot d\mathbf{S}, \quad (4.7)$$

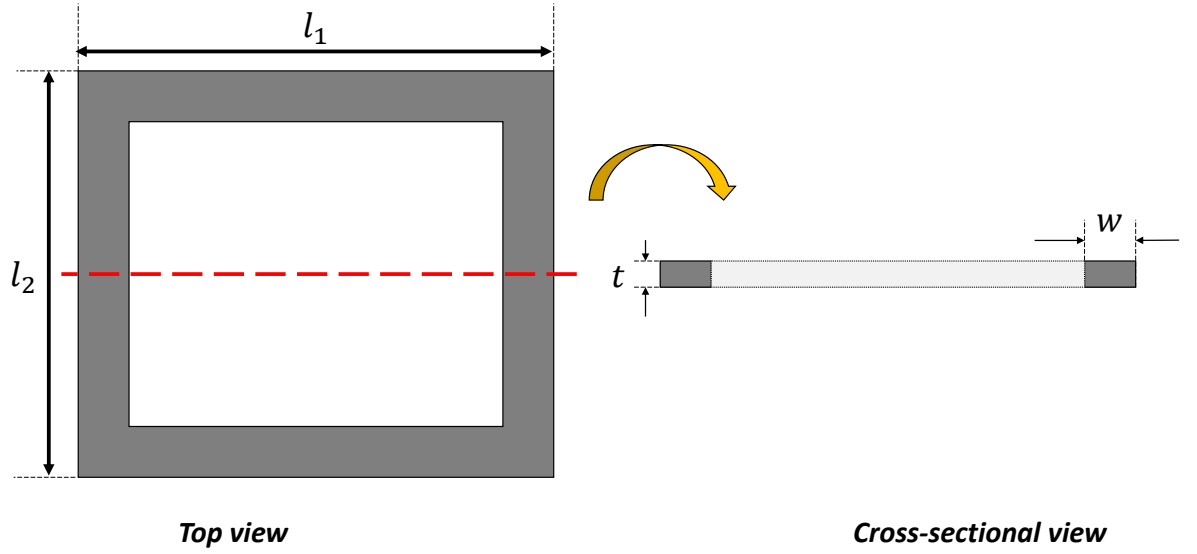


Figure 4.16: A sketch showing the relevant dimensions of a closed rectangular loop. The left-hand side shows the top view, whilst the right-hand side shows an edge on view along the red dashed line.

where  $\phi_0 = \frac{h}{2e}$  is the magnetic flux quantum,  $\mathbf{J}$  is the superconducting current density, and  $n\phi_0$  is the *fluxoid*, which is the parameter that is conserved.  $C$  defines the closed superconducting contour, and  $n$  is an integer. For the types of superconducting geometries relevant to the Geonium Chip magnetic field source, and in particular with structures fabricated from *Superpower* tape, the first term on the right-hand side of Equation (4.7) is negligible [105]. Thus, the classical description of flux conservation suffices.

#### 4.4.2 Geometric approximation of self-flux in a closed loop

The self-flux of a closed loop is equal to the product of the loop inductance,  $L$ , and the circulating current,  $I$ . The loop inductance depends entirely on the geometry of the loop. For our purposes, we are concerned with rectangular loop structures of rectangular cross-section. According to [106], the general formula for the inductance of a rectangular loop of rectangular cross-section is

$$L_{\text{self}} = 4\mu_0 \left\{ l_1 \left[ \ln \left( \frac{2l_1}{w+t} \right) + \frac{1}{2} + \frac{0.2235(w+t)}{l_1} \right] + l_2 \left[ \ln \left( \frac{2l_2}{w+t} \right) + \frac{1}{2} + \frac{0.2235(w+t)}{l_2} \right] \right. \\ \left. - l_1 \ln \left( \frac{l_1 + \sqrt{l_1^2 + d^2}}{d} \right) + l_2 \ln \left( \frac{l_2 + \sqrt{l_2^2 + d^2}}{d} \right) + \sqrt{l_1^2 + d^2} + \sqrt{l_2^2 + d^2} - 2d \right\}, \quad (4.8)$$

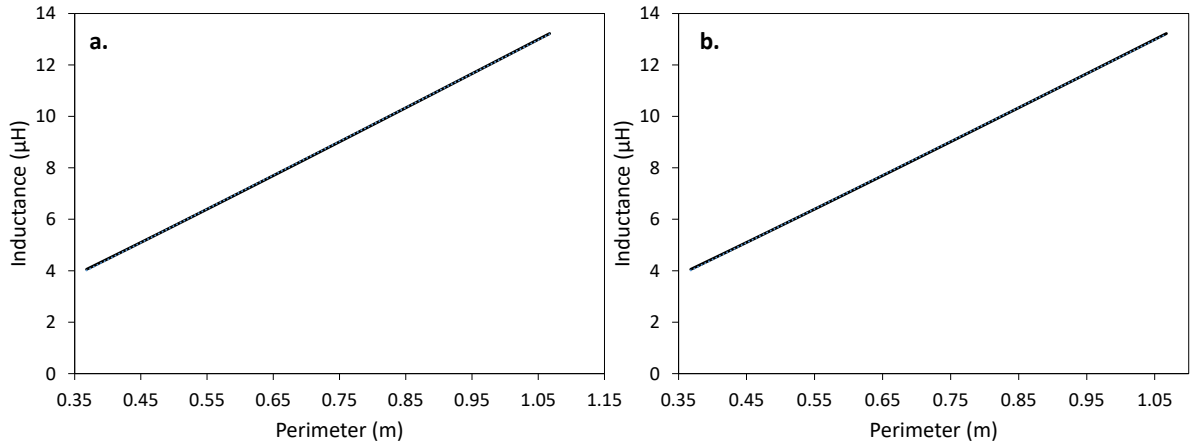


Figure 4.17: Graphs of self-inductance vs perimeter for square and rectangular loops. **a.** Graph of self-inductance against loop perimeter for a square loop of path width  $w = 3$  mm and thickness  $t = 1$   $\mu\text{m}$ . **b.** Graph of self-inductance against perimeter for a rectangular loop of width  $w = 3$  mm, thickness  $t = 1$   $\mu\text{m}$ , and aspect ratio  $l_2 = 3l_1$ . Their relationship can be well approximated as linear.

where  $l_1$  and  $l_2$  are the lengths of the sides of the rectangular loop,  $d = \sqrt{l_1^2 + l_2^2}$  is the diagonal of the rectangular loop,  $w$  is the width of the rectangular cross-section of the wire, and  $t$  is the thickness of the wire (see Figure 4.16). It turns out that Equation (4.8) can be very well approximated as  $L_{\text{self}} = k \times 2(l_1 + l_2)$ , which can be generalised to

$$L_{\text{self}} = k \times \text{“perimeter of loop”}, \quad (4.9)$$

where  $k \sim 10^{-5}$  for loops of  $l_1, l_2 \sim \text{cm}$ . A plot of self-inductance vs perimeter for square and rectangular loops is given in Figure 4.17. The geometries shown correspond to typical dimensions of structures made from the *Superpower* HTS tape.<sup>5</sup> The self-flux,  $\phi_{\text{self}}$ , for a closed loop carrying current,  $I$ , is then

$$\phi_{\text{self}} = k \times \text{“perimeter of loop”} \times I. \quad (4.10)$$

This approximation, which we will call the *linear flux approximation*, is used extensively throughout §5 and §6, and is integral to the design of the planar magnetic field source.

<sup>5</sup>Note that this approximation still holds for rectangular loops scaled up to several metres in length.

## 4.5 Current distribution in thin superconducting materials of rectangular loop geometry

The trapping region of the Geonium Chip Penning trap is only millimetres away from the superconducting magnetic field source. Thus, how the current distributes within the rectangular closed superconducting loops of the magnetic field source has a significant effect on the trapping magnetic field. What is of concern for the Geonium Chip Penning trap is how direct transport currents distribute within the cross-section of the rectangular superconducting loops. Alternating currents, along with vortex currents in Type II superconductors, are not a primary concern. Whilst screening currents do have a distortional effect on the magnetic field distribution (i.e., the Meissner-Oschenfeld effect), the relative distortion was shown not to vary significantly with transport current<sup>6</sup> (see §4.1.2).

### 4.5.1 Current distribution within a strip of high-temperature superconducting YBCO tape

The current distribution in a 60 mm long strip of 12 mm wide YBCO *Superpower* tape (submerged in liquid nitrogen) carrying 2 A of current is inferred from a magnetic field mapping technique. A current of 2 A is run through the superconducting tape from a *Rohde & Schwarz HMP4040* current supply, and the vertical component of the magnetic field is mapped with an *Arepo AXIS-3* cryogenic Hall probe attached to the moving head of a CNC machine. The resulting field distribution appears to be approximately consistent with what is expected from a uniform distribution of current (see Figure 4.18). The theoretical current distribution in a superconducting thin film of width,  $w$ , and thickness,  $d$ , is described by Rhoderick and Wilson [107], and is given by

$$J(x) = \frac{J(0)}{\sqrt{1 - \left(\frac{2x}{w}\right)^2}} \quad (4.11)$$

---

<sup>6</sup>The logic for this statement is as follows: the screening currents are the solution to the London equations which satisfy the boundary condition that the magnetic field is zero deep inside the superconductor (the Meissner-Oschenfeld effect) but non-zero outside. The simulations in §4.1.2 that investigate how the magnetic field distribution is affected by the Meissner-Oschenfeld effect impose these same boundary conditions, and provide a calculation of the magnetic field distribution. The results from these simulations indicate that the relative distortion of the magnetic field distribution between normal conducting and Meissner phases was largely independent on the transport current. Thus, whilst no investigations have been made to determine the field distortion due to screening currents *explicitly*, the simulations, in effect, provide this information.

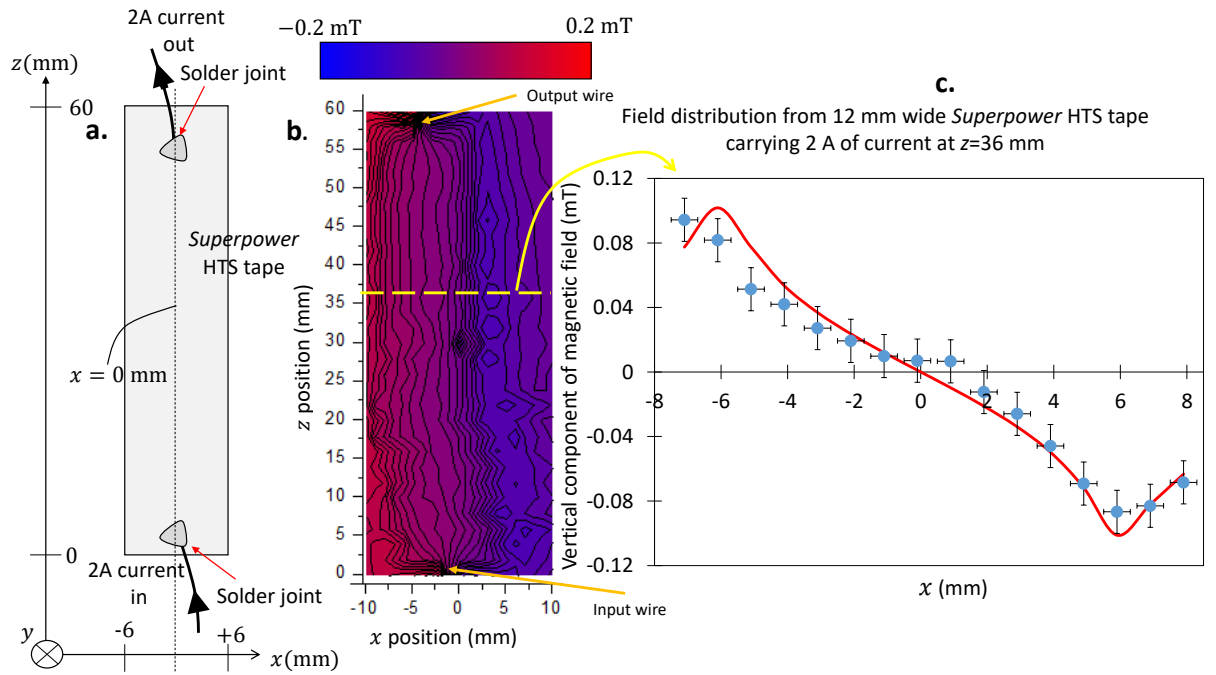


Figure 4.18: **a.** A sketch of a strip of *Superpower* tape. **b.** A field map of the vertical component of the magnetic field from 2A in the superconducting tape. **c.** A graph of the field distribution along a cross-section of the tape. The blue points are experimental data, and the red curve is the theoretical field distribution (assuming a uniform current distribution) at a height of 0.54 mm for a 60 mm  $\times$  40 mm  $\times$  1  $\mu$ m superconducting strip carrying 2 A of current. There is a slight non-uniformity in the current distribution, which can be seen in the data. The experimental data shows a shallower gradient around  $x = 0$  mm than that of the field from an expected uniform distribution of current. This indicates that the current is more heavily distributed near the edges of the superconductor, in agreement with [107]. The vertical errors bars represent the statistical error in the measured vertical component of the magnetic field at each point, and the horizontal error bars are an estimate the uncertainty in the  $x$  position due to misalignment of the Hall probe.

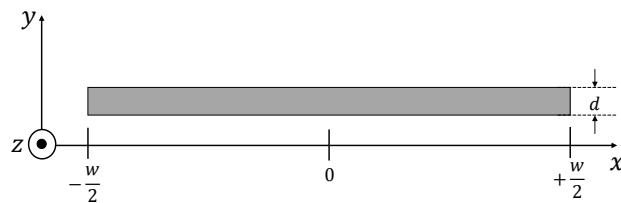


Figure 4.19: Cross-section of thin-film current-carrying wire of width,  $w$ , and thickness,  $d$ . The current density,  $J$ , is directed along the  $z$  axis

for  $x \ll w/2$ , and

$$J(x) = \frac{\exp^{1/2} \sqrt{wd} J(0)}{\lambda \sqrt{2a}} \exp^{-\frac{d(\frac{w}{2}-x)}{a\lambda^2}} \quad (4.12)$$

near the edge of the superconductor, where  $J(0)$  is the current density at  $x = 0$  (see Figure 4.19), and  $a$  is a dimensionless constant of the order of unity. E.F. Talantsev *et al.* [108] demonstrated that for low transport currents in 12 mm *Superpower* YBCO superconducting tape, the current distribution is consistent with the theory of Rhoderick and Wilson. However, as the current density approaches the critical value, the current tends to a uniform distribution within the superconductor. The planar magnetic field source of the Geonium Chip will most likely be operating at currents near to the critical current density, and so the assumption that the current distribution is uniform can be made. The experimentally measured field distribution of Figure 4.18 also shows that the uniform current approximation can be made at low currents. This is particularly useful as it allows for  $\underline{\Gamma}$  to be measured at low currents yet still retain its validity near  $J_c$ .

An interesting artifact of the measurement is the magnetic field distribution about the input and output wires (see Figure 4.18). The measurement clearly shows that current enters the tape from the input wire before distributing evenly in the tape. At the output end, the current funnels into the output wire lead and out of the superconducting material.

#### 4.5.2 Current distribution within a closed rectangular loop of YBCO tape

Whilst Figure 4.18 shows an approximately uniform distribution of current in a thin strip of superconducting material, it should be noted that the Geonium Chip magnetic field source is made up of thin rectangular closed superconducting loops. It is therefore necessary to understand how the current distributes within this geometry.

A 12 mm  $\times$  12 mm square loop with a path width of 3 mm is cut using a CNC machine. A 3 mm-diameter neodymium magnet is placed a few millimetres above the centre of the loop before the loop is field cooled with liquid nitrogen. The neodymium magnet is removed, inducing a current within the superconducting loop so as to conserve the flux in the loop. Scans of the magnetic field  $y$  component are performed along the  $z$  axis for various  $x$  positions using a cryogenic Hall probe attached to the moving head of a CNC machine. The axes are labelled in Figure 4.20a. For each  $x$  position, data for the  $y$  component of the magnetic field are fitted to an analytical expression (calculated by J Verdú [109]) that assumes a uniform current distribution. The results of this fit

provides, for each  $x$  coordinate, a fitted current value of the current. The resulting current values for each  $x$  position are shown to be approximately uniform, and are plotted in Figure 4.20. This suggests that the current distribution within a closed rectangular loop is approximately uniform.

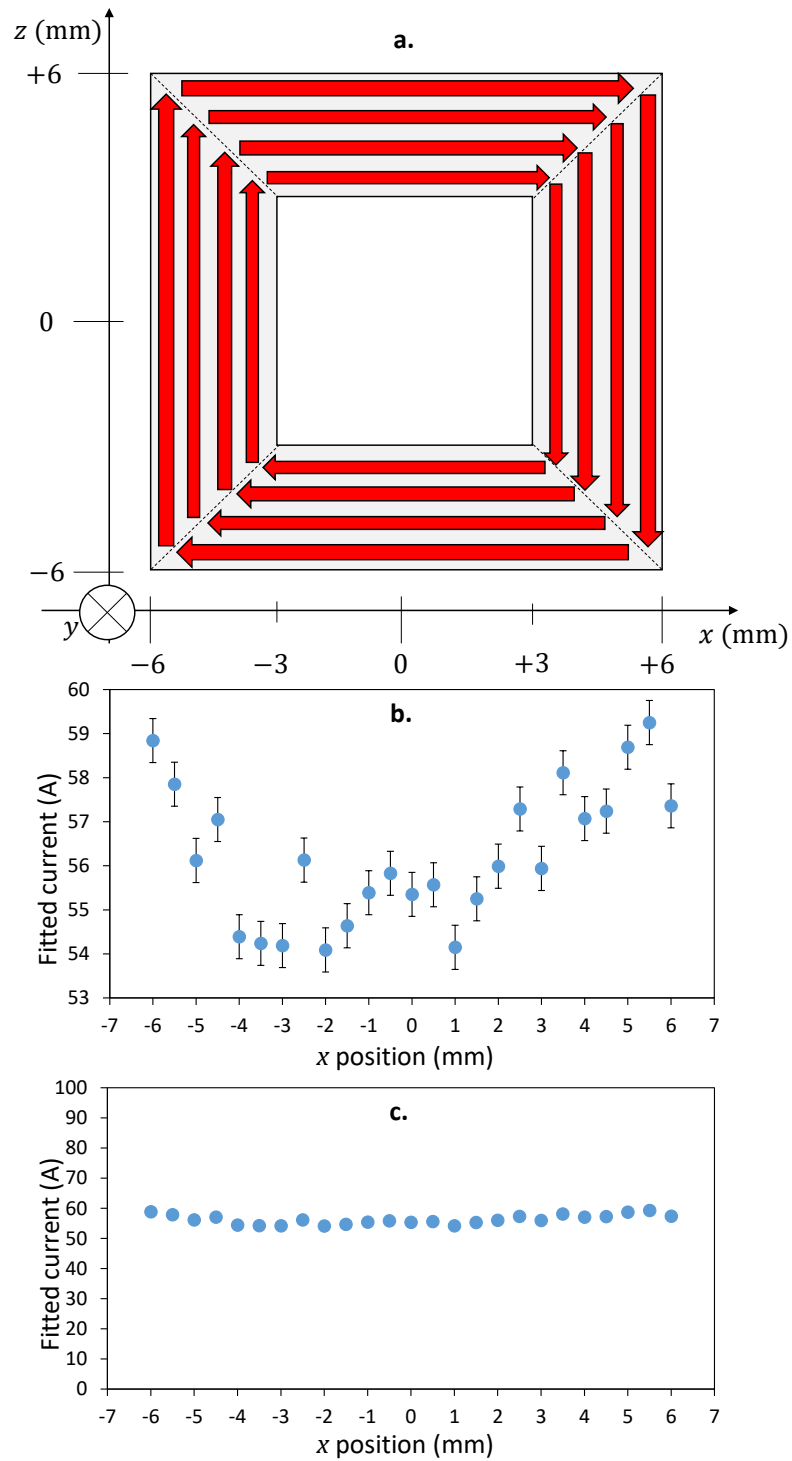


Figure 4.20: Measured current distribution in a square closed superconducting loop. **a.** The dimensions of the superconducting loop. The fitting magnetic field distribution function assumes current is distributed uniformly in four trapezoidal structures. The origin  $(x, z) = (0, 0)$  of the coordinate system is the centre of the loop. **b.** The currents obtained from fitting the experimental data to the analytical expression for current uniformly distributed in trapezoidal structures (see above). **c.** The same data as above, but with a larger scale in the vertical axis.

## Chapter 5

# Remote induction of persistent supercurrents in the Geonium Chip magnetic field source

### 5.1 Introduction

§1–3 dealt with the basic principles of Penning trap technology, and how the Geonium Chip offers a novel architecture with regard to both the electric and magnetic field sources. A very important feature of §3 was the discussion of the operating principle of the planar magnetic field source. Arbitrary field distributions,  $\underline{B}$ , about the trapping position,  $r_0$ , can be produced on the provision that it is characterised (meaning that  $\underline{\Gamma}(r_0)$  is measured). Once  $\underline{\Gamma}(r_0)$  is known, any desired magnetic field distribution,  $\underline{B}_{\text{desired}}$ , can be constructed by simply putting in the required currents,  $\underline{I}_{\text{required}}$ . These required currents are calculated directly from  $\underline{I}_{\text{required}} = \underline{\Gamma}^{-1} \cdot \underline{B}_{\text{desired}}$ . In §3, this principle was demonstrated with a prototype magnetic field source running on *driven* currents from a precision power supply.

The eventual aim is to have a planar magnetic field source that does not run on driven currents, but instead operates in *persistent current mode*. The motivation of §4 was to introduce the necessary aspects of superconductivity required to develop such a magnetic field source. A key element is the principle of flux conservation in closed superconducting loops, and this will feature heavily in this chapter. Now that these fundamental concepts have been introduced, the method of remotely building up persistent currents in the Geonium Chip magnetic field source can be outlined.

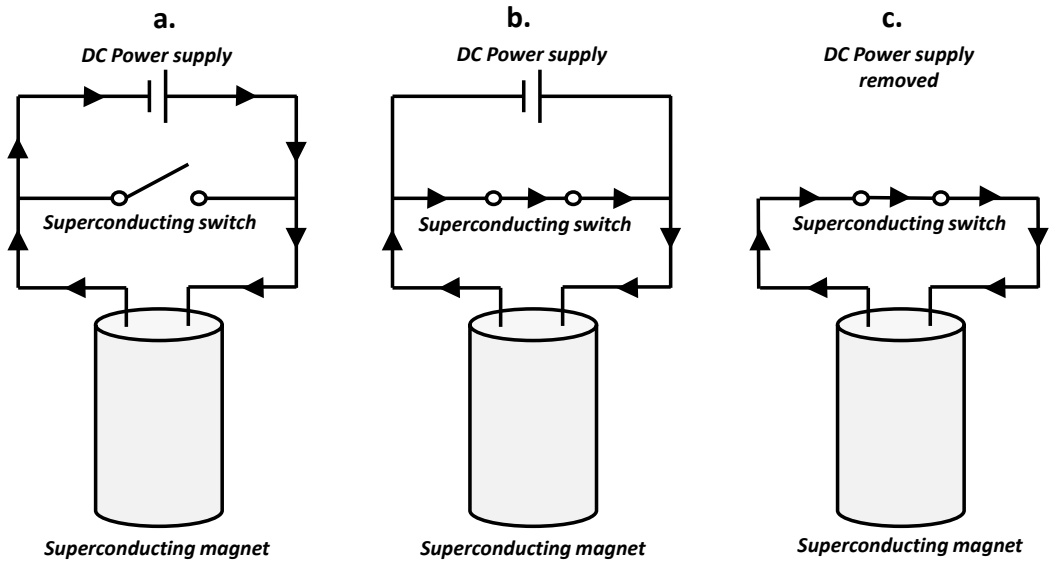


Figure 5.1: A sketch showing the excitation of a conventional superconducting magnet. **a.** With the superconducting switch open, current from a power supply enters the magnet. **b.** The switch is then closed so that the superconductivity is recovered, allowing current to bypass the power supply. **c.** The power supply can then be turned off and removed.

### 5.1.1 The need for flux pumping in the Geonium Chip

Magnetic field instabilities are often the main limitation in terms of the obtainable precision of a Penning trap [10]. For example, a particle of mass,  $m$ , and charge,  $q$ , has a relative mass uncertainty, as determined from measurement of the free cyclotron frequency,  $\omega_c = \frac{qB}{m}$ , given by

$$\frac{\Delta m}{m} = \frac{\Delta B}{B}. \quad (5.1)$$

Thus, fluctuations in the magnetic field,  $\Delta B$ , have a direct effect on the measured value of  $m$ , and so should be kept to a minimum. Ultimately, this means that fluctuations in the trapping currents, which produce the magnetic field, should be minimised, and this is best achieved with the use of persistent currents in superconducting circuits. In conventional superconducting magnets, persistent currents are achieved with the use of a high current power supply along with a superconducting switch (see Figure 5.1). During excitation, the superconducting switch is opened, and current from the power supply enters the magnet. Because the superconductivity in the vicinity of the switch is temporarily ‘broken’ (i.e., the material is in its normal conducting state), direct current flows into the magnet and back out to the power supply. Closing the switch, however, allows for

the superconductivity to reform, and any current already in the magnet then bypasses the power supply and circulates in the magnet instead. The power supply can then be disconnected and removed from the setup, whilst the current in the magnet persists [87]. Although very effective, the method described above has a significant drawback in that it requires high currents ( $> 100$  A) from room temperature power sources [42]. This largely complicates the cryostat system, compromising the scalability of Penning trap technology.

Flux pumping – which is loosely defined as any method of electromagnetically inducing direct current within superconducting circuits without the need for physical contact between the superconducting material and the excitation source [42] – is particularly attractive in overcoming this problem. Flux pumping comes in many different schemes, including travelling wave flux pumps [42, 110, 111, 112], switched transformer-rectifier flux pumps [113, 114], and variable resistance rectifier flux pumps [115]. Although a fascinating topic in its own right, and an active area of research [116], this thesis only details the particular flux pumping schemes used in the Geonium Chip Penning trap.

## 5.2 Flux pumping mechanism for the Geonium Chip

The general architecture of the Geonium Chip magnetic field source is illustrated in Figure 5.2. It shows the planar magnetic field source comprising a number of double rectangular closed superconducting loops. The required flux pumping scheme is therefore one which is compatible with such a geometry, such that persistent currents of hundreds of amperes can be obtained *without the need for high input currents* (i.e., with input currents of only a few amperes). The flux pumping technique that follows operates by making use of flux conservation within multiply-connected superconducting planar structures. Figure 5.3 shows an example of such a double-loop superconducting structure whereby both loops are the same size. Figure 5.4, shows a schematic drawing of a double-loop superconducting structure with general dimension. The Geonium Chip planar magnetic field source requires a scheme of inducing known currents in the Target Loop of a generalised double-loop superconducting structure to be devised. This is discussed below.

Consider the double-loop planar superconducting structure of Figure 5.4. The structure comprises a smaller Pumping Loop, and a larger Target Loop, with the two loops having a shared length of superconducting material. The relevant characteristic lengths of these superconducting structures are labelled  $l_1$ ,  $l_2$ ,  $l_3$ , and  $l_4$ . It is assumed that the thicknesses and widths of the superconducting paths are such that the linear flux approximation (see §4.4.2) can be made. The Pumping Loop is the name which refers to the

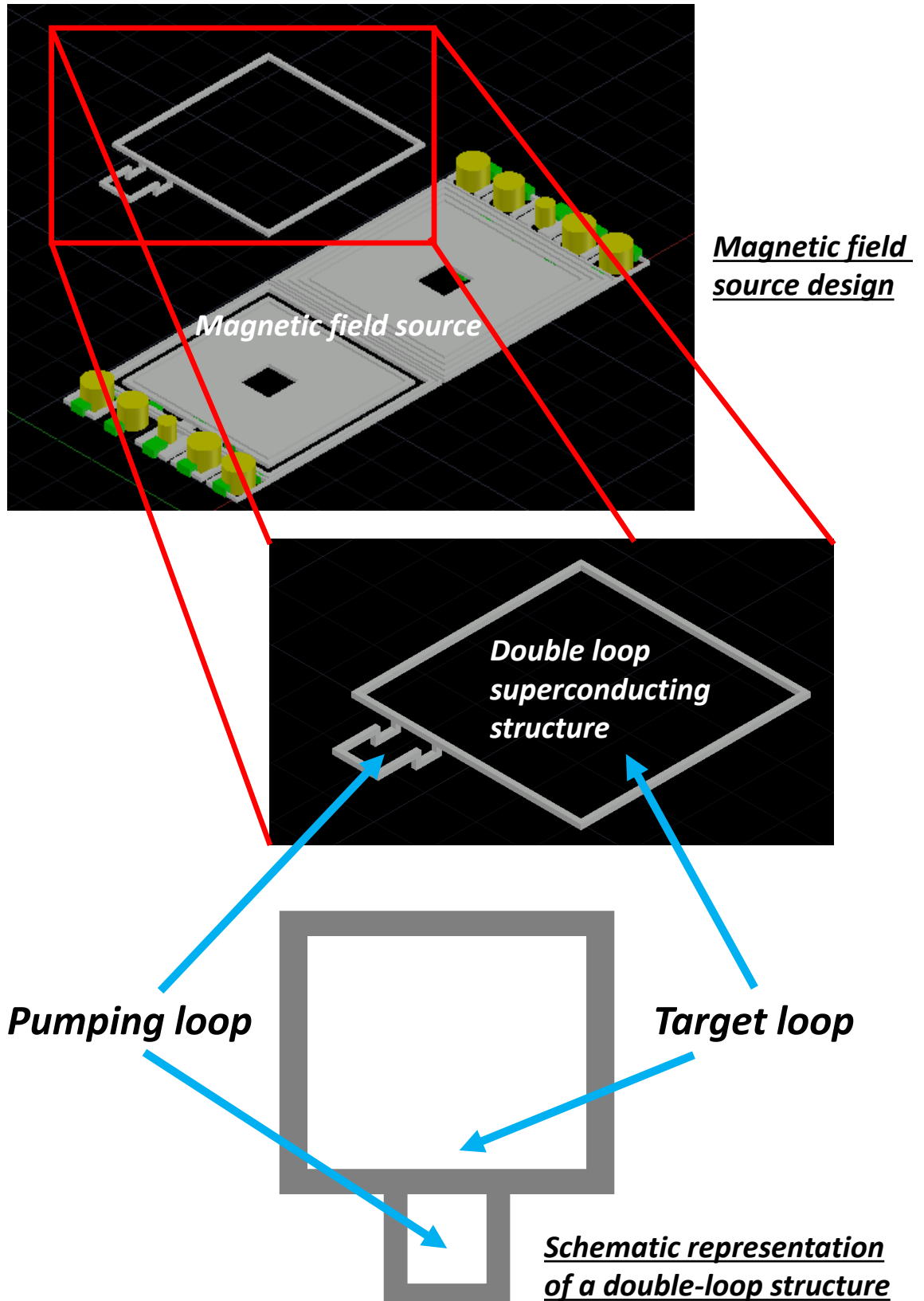


Figure 5.2: A schematic diagram showing an individual double-loop superconducting structure lifted from the planar magnetic field source. It is these double-loop structures that are to be subjected to flux pumping.

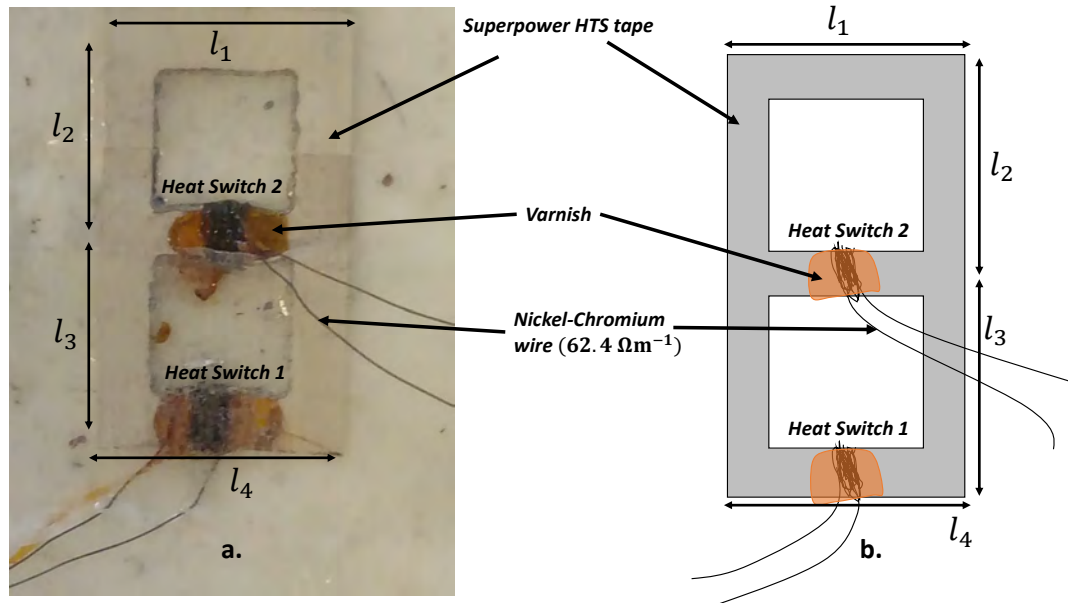


Figure 5.3: An example of a double-loop superconducting structure. **a.** A double-loop superconducting structure made from *Superpower* high-temperature superconducting tape. **b.** Schematic depiction of the double-loop superconducting structure. In both images the characteristic lengths ( $l_1$ ,  $l_2$ ,  $l_3$ , and  $l_4$ ) and locations of the heat switches are clearly labelled.

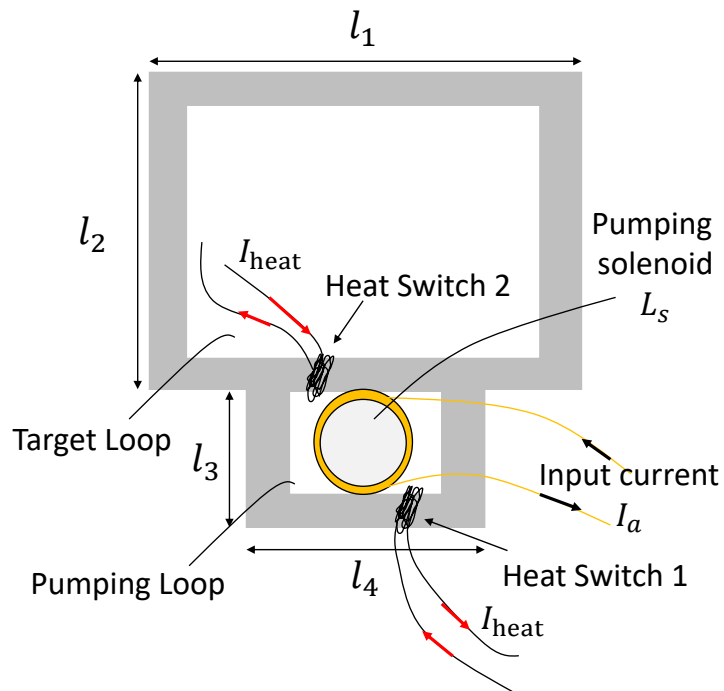


Figure 5.4: A sketch of a double-loop superconducting structure with general loop dimensions.

closed superconducting loop to which flux is injected into the superconducting circuit. Such flux injection comes via the means of a small solenoid of inductance,  $L_s$ . When an input current,  $I_a$ , is applied to the solenoid from a current supply at room temperature, an input flux of  $\phi_a = L_s I_a$  is injected into the circuit. Crucially, the input currents required for this process are *significantly* smaller than what is needed for conventional superconducting magnets.

The Target Loop is the name given to the larger superconducting loop which carries the currents that produce the trapping magnetic field. The aim of flux pumping is to build up a specifically chosen current in the Target Loop. The planar magnetic field source comprises several of these superconducting double-loop structures, with the Target Loop of each set to carry a particularly chosen current. If the currents of each loop are carefully controlled, the magnetic fields from each structure add up to produce the desired magnetic field distribution.

Before dealing with several superconducting structures, consider, first, a single superconducting double-loop structure, with a heat switch attached to the outer arm of the Pumping Loop (Heat Switch 1), whilst another heat switch is placed on the superconducting arm common to both loops (Heat Switch 2) (see Figures 5.3 and 5.4). As stated above, the aim of the flux pumping scheme is to build up a desired current in the Target Loop,  $I_{\text{desired}}$ , by knowing what input current,  $I_a$ , to apply to the solenoid on the Pumping Loop. Crucially,  $I_{\text{desired}} \gg I_a$ . Additional heating currents,  $I_{\text{heat}}$ , are also required, but these do not need to be precisely controlled: they just have to be large enough to raise the local temperature of the superconducting material above  $T_c$ , such that the material temporarily becomes normally conducting. As seen in §4.3.3, these can be of the order of a few tens of milliamperes, and can be insulated so that heat is confined locally. In the mathematical model that follows, the magnetic field from  $I_{\text{heat}}$  is assumed to be negligible.<sup>1</sup>

With close reference to Figure 5.5, suppose there is some initial current,  $I$ , circulating in the Target Loop of the double-loop superconducting structure. The flux pumping procedure (summarised systematically in Table A.1 in the Appendix, and shown schematically in Figure 5.5.) can be described as follows:<sup>2</sup>

---

<sup>1</sup>In reality, the magnetic field from the heating current will have some effect on the flux pumped current. However, in a dry cryostat, this effect is small because of the low currents required to operate the heat switches. Also, their effect can further be minimised by ensuring the wire is bifilarly wound, as described in [87].

<sup>2</sup>The steps in this scheme are the same as those discussed in [113] and referenced in [117]. The main difference, however, is that in the above-mentioned references the steps are used to magnetise low-temperature magnets that are connected to a Type I superconducting film via solder joints. Here, the approach is to

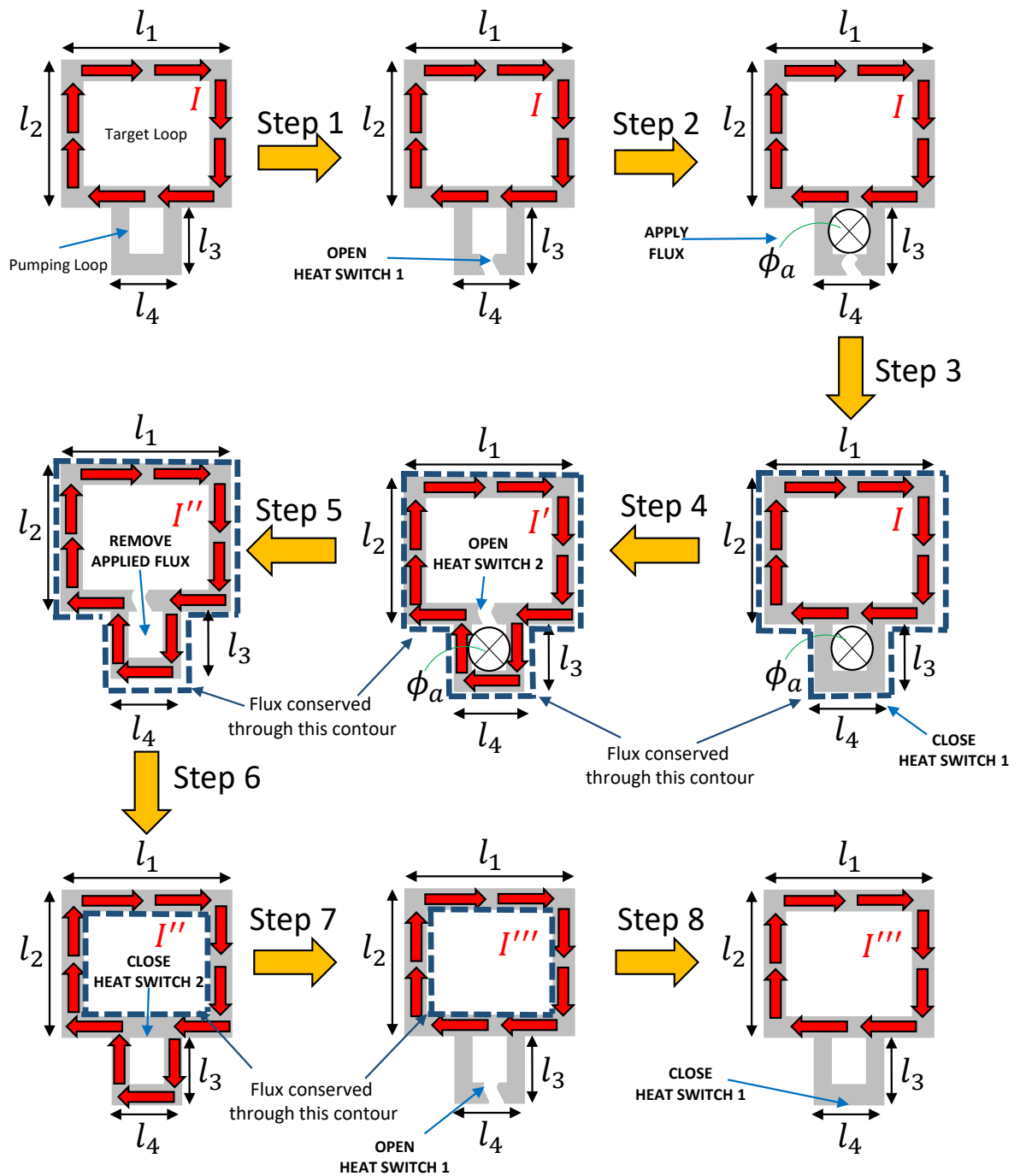


Figure 5.5: A schematic representation of the flux pumping scheme. The grey double-loop structures represent the superconducting circuitry. The red arrows depict persistent current flow. Opening a heat switch is represented as a break in the grey lines defining the superconducting material. Applied flux from the pumping solenoid is represented by the symbol  $\otimes$ . The broken blue line indicates a closed superconducting loop through which flux conservation applies.

- **Step 1:** *Turn ON the current,  $I_{\text{heat}}$ , to Heat Switch 1 so as to locally drive the material normally conducting such that Heat Switch 1 is OPEN.*

Here, the relevant contour of integration (through which flux conservation applies) is the one which defines the Target Loop. Since the magnetic contribution due to the heating current is ignored, it follows that the current,  $I$ , in the Target Loop does not change during this step.

- **Step 2:** *Turn ON the current,  $I_a$ , to the pumping solenoid so as to APPLY flux,  $\phi_a$ , to the Pumping Loop.*

In this model, it is assumed that the applied flux,  $\phi_a = L_s I_a$ , is confined only to the Pumping Loop, and that no flux lines flow into the Target Loop. As such, there is no change in flux flowing through the closed superconducting contour of the Target Loop, and so the current,  $I$ , remains unchanged.

- **Step 3:** *Turn OFF the heating current,  $I_{\text{heat}}$ , to Heat Switch 1 so as to reform the superconductivity and CLOSE the switch.*

At the moment the superconductivity is reformed, the flux that was flowing into the Pumping Loop is ‘frozen’ in. The current in the Target Loop still remains as  $I$ , and there is no current in the lower portion of the Pumping Loop.

- **Step 4:** *Turn ON the heating current,  $I_{\text{heat}}$ , to Heat Switch 2 so as to locally drive the material normally conducting, thereby OPENing the switch.*

The current in the Target Loop is now redistributed to the perimeter of the entire double-loop structure. Applying flux conservation to this outer loop before and after the step is implemented, the current,  $I'$ , after the step is determined as<sup>3</sup>

$$I' = \frac{2l_1 + 2l_2 - l_4}{2(l_1 + l_2 + l_3)} I. \quad (5.2)$$

- **Step 5:** *Turn OFF the current,  $I_a$ , to the pumping solenoid so as to REMOVE the applied flux,  $\phi_a$ , from the superconducting circuit.*

---

use double-loop superconducting structures such that the induced currents run in truly persistent mode, and to be able to understand how these induced persistent currents are mathematically related to the dimensions of these double-loop structures and the input flux.

<sup>3</sup>Here, the current in the central superconducting arm contributes flux to both the Target Loop and the Pumping Loop. These flux contributions are opposite in polarity, and are assumed to be equal in magnitude.

Turning off  $I_a$  takes away the applied flux,  $\phi_a$ . Because of flux conservation, there is a sudden jump in current (from  $I'$  to  $I''$ ) in the outer loop, which is given by

$$I'' = I' + \frac{\phi_a}{2k(l_1 + l_2 + l_3)} = \frac{2l_1 + 2l_2 - l_4}{2(l_1 + l_2 + l_3)} I' + \frac{\phi_a}{2k(l_1 + l_2 + l_3)}. \quad (5.3)$$

- **Step 6:** Turn OFF the heating current,  $I_{\text{heat}}$ , to Heat Switch 2 so as to reform the superconductivity and CLOSE the switch

In this step there is no change in the current  $I''$ .

- **Step 7:** Turn ON the heating current,  $I_{\text{heat}}$ , to Heat Switch 1 so as to locally drive the material normally conducting, thereby OPENing the switch.

Here, the current,  $I''$ , in the outer path is redirected to the Target Loop. Because of flux conservation in the Target Loop,<sup>4</sup> the current,  $I'''$ , becomes

$$I''' = \frac{2l_1 + 2l_2 - l_4}{2(l_1 + l_2)} I''. \quad (5.4)$$

Substituting in for  $I''$  gives

$$I''' = \frac{(2l_1 + 2l_2 - l_4)^2}{4(l_1 + l_2)(l_1 + l_2 + l_3)} I' + \frac{(2l_1 + 2l_2 - l_4)\phi_a}{4k(l_1 + l_2)(l_1 + l_2 + l_3)}. \quad (5.5)$$

- **Step 8:** Turn OFF the current to Heat Switch 1 to reform the superconductivity and CLOSE the switch.

There is no change in current in this step.

The final current in the Target Loop after one cycle is given by Equation (5.5), and depends on the initial current in the Target Loop,  $I$ , the applied flux,  $\phi_a$ , and the geometry of the superconducting structure,  $(l_1, l_2, l_3, l_4)$ . Repeating this cycle several times allows for current to build up in the Target Loop. To quantify this, one can suppose, without loss of generality, that the initially circulating current,  $I$ , was the final current that resulted from  $n - 1$  previous cycles. Adopting this notation, Equation (5.5) then gives the final current after  $n$  cycles as a recursive formula:

$$I_n = \frac{(2l_1 + 2l_2 - l_4)^2}{4(l_1 + l_2)(l_1 + l_2 + l_3)} I_{n-1} + \frac{(2l_1 + 2l_2 - l_4)\phi_a}{4k(l_1 + l_2)(l_1 + l_2 + l_3)}. \quad (5.6)$$

---

<sup>4</sup>Note that, in this step, the flux contribution from the lower portion of the Pumping Loop is assumed to have negligible effect on the flux flowing through the Target Loop.

Supposing the Target Loop initially had no circulating current (i.e.,  $I_0 = 0$ ), the current after the first few cycles then becomes

$$\begin{aligned}
I_0 &= 0, \\
I_1 &= \beta, \\
I_2 &= \beta(\alpha + 1), \\
I_3 &= \beta(\alpha^2 + \alpha + 1), \\
&\dots \\
I_n &= \beta(\alpha^{n-1} + \alpha^{n-2} + \alpha^{n-3} + \dots + \alpha^2 + \alpha + 1),
\end{aligned} \tag{5.7}$$

where

$$\alpha = \frac{(2l_1 + 2l_2 - l_4)^2}{4(l_1 + l_2)(l_1 + l_2 + l_3)} ; \beta = \frac{(2l_1 + 2l_2 - l_4)\phi_a}{4k(l_1 + l_2)(l_1 + l_2 + l_3)}. \tag{5.8}$$

The general solution after  $n = N$  pumping cycles is then

$$I_N = \frac{\beta(1 - \alpha^N)}{(1 - \alpha)} = \frac{(2l_1 + 2l_2 - l_4)\phi_a}{4k(l_1 + l_2)(l_1 + l_2 + l_3)} \left( \frac{1 - \left( \frac{(2l_1 + 2l_2 - l_4)^2}{4(l_1 + l_2)(l_1 + l_2 + l_3)} \right)^N}{1 - \frac{(2l_1 + 2l_2 - l_4)^2}{4(l_1 + l_2)(l_1 + l_2 + l_3)}} \right). \tag{5.9}$$

The maximum obtainable current corresponds to the limit of  $N$  tending to infinity, and is given by

$$I_{\max} = \lim_{N \rightarrow \infty} I_N = \frac{(2l_1 + 2l_2 - l_4)\phi_a}{k[4(l_1 + l_2)(l_3 + l_4) - l_4^2]}. \tag{5.10}$$

Crucially,  $I_{\max}$  is *linear* in  $\phi_a$ , which itself grows linearly with input current ( $\phi_a = L_s I_a$ ). This means there is a one-to-one correspondence between the final obtainable current,  $I_{\max}$ , and the applied current,  $I_a$ . Practically, one can obtain any desired final current,  $I_{\text{desired}}$ , with the correct choice of  $I_a$ . The main drawback of this scheme, however, is that it requires for many pumping cycles to be implemented in order for the obtained current to approach the maximum value. How quickly the final current approaches saturation depends on the value of  $\alpha$ : with a small value of  $\alpha$ , the series converges quickly, whereas, with  $\alpha \approx 1$ , a large number of cycles are required to reach saturation. Another limitation is the time it takes to implement each flux pumping cycle. Since the mechanism relies on heat switches, which typically take around one second to operate, the process of flux pumping from an initial current of zero to a final current of tens or hundreds of amperes

can take one to two minutes. However, this is still shorter than the typical time it takes to energise a conventional superconducting magnet.

To give an order of magnitude of the types of currents obtainable using this flux pumping scheme, consider typical dimensions of superconducting structures machined from *Superpower* HTS tapes, for example  $l_1, l_2, l_3, l_4 \sim 10^{-2}$  m,  $k \sim 10^{-5}$  Hm<sup>-1</sup>. In this case, with a pumping solenoid of  $L_s \sim 1$   $\mu$ H, and an input current of  $I_a = 1$  A, currents of tens of amperes can be obtained. With higher inductance solenoids (which can easily be achieved with the aid of ferromagnetic core materials,<sup>5</sup> or by increasing the number of turns in the pumping coils), the obtainable currents can reach hundreds of amperes, which is enough to exceed the critical current of most practical superconductors for these dimensions.

Figure 5.7 shows the measured magnetic field from a double-loop superconducting structure machined from a section of *Superpower* HTS tape. A schematic representation of the superconducting circuitry is given in Figure 5.6. A small solenoid (with an inductance of  $L = 13.84$  mH) was constructed by wrapping thin magnet wire (0.063 mm in diameter) around a ferromagnetic screw. An *Areproc* cryogenic Hall Probe was placed in the centre of the Target Loop, and was configured to measure the vertical component of the magnetic field (i.e., the magnetic field pointing out of the page).

The double-loop structure was subjected to several cycles of flux pumping with input currents,  $I_a = 0.1$  A, 0.2 A, 0.3 A, and 0.5 A. A plot of the measured magnetic field,  $B$ (mT), as a function of flux pumping cycle number,  $n$ , is given in Figure 5.7 for these input currents. Each set of data is fitted to the equation for a geometric series,  $B_{\text{fit}}(n) = \frac{\beta(1-\alpha^n)}{(1-\alpha)}$  (see Equation (5.9)). The fitting parameters,  $\alpha$  and  $\beta$ , for these input currents are listed in the first four rows of Table 5.1. The obtained data shows good agreement with the model for input currents of 0.1 A and 0.2 A. For input currents greater than 0.2 A, the measured magnetic field saturates at 5.17 mT when the critical current of the HTS tape is reached (shown as a dashed line in Figure 5.7). For  $I_a = 0.3$  A, the critical current is reached after three pumping cycles, and for  $I_a = 0.5$  A, the critical current is reached after only two. Conservative estimates, based on data from the manufacturers, and the assumption of a uniform critical current along the width of the HTS tape, suggest that for this particular geometry the critical current is around 50 A. Thus, with this flux pumping scheme it is possible to obtain currents over 200 times larger than the input currents. This is a significant degree of amplification.

---

<sup>5</sup>Ideally, ferromagnetic materials should be avoided because they can cause distortions to the magnetic field distribution.

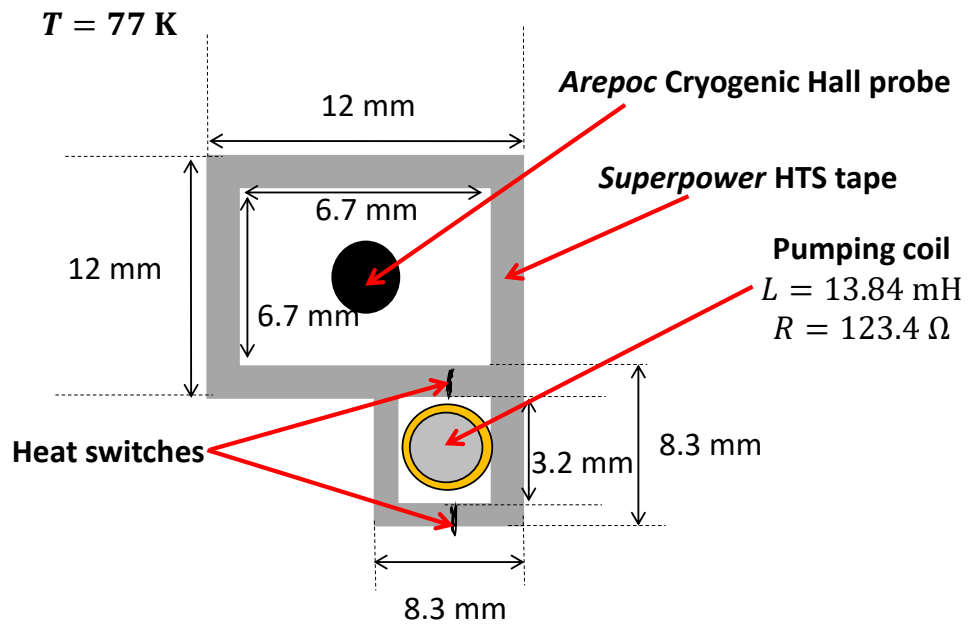


Figure 5.6: Schematic diagram of a superconducting structure subjected to flux pumping.

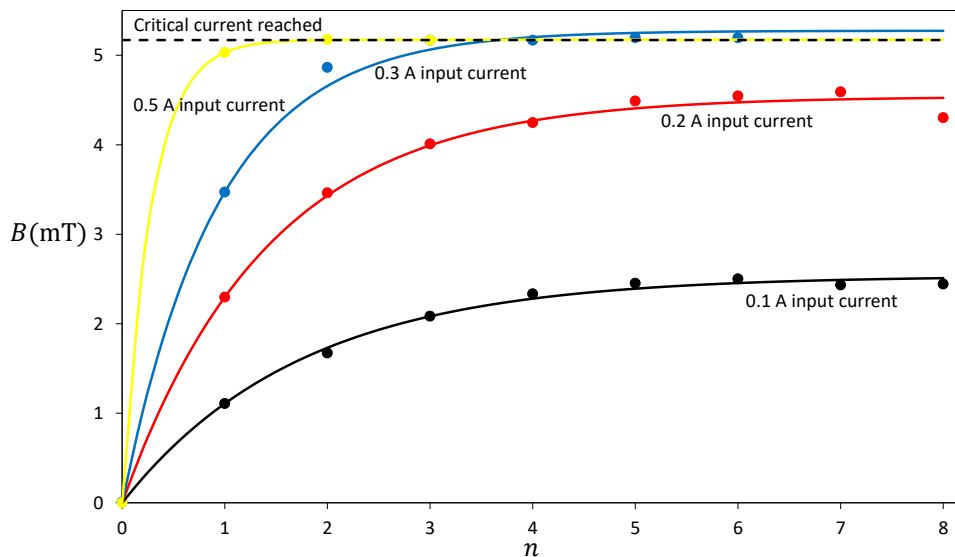


Figure 5.7: A graph showing the measured magnetic field,  $B(\text{mT})$ , as a function of flux pumping cycle number,  $n$ , for various input currents,  $I_a$ , for a superconducting circuit of geometry depicted in Figure 5.6.

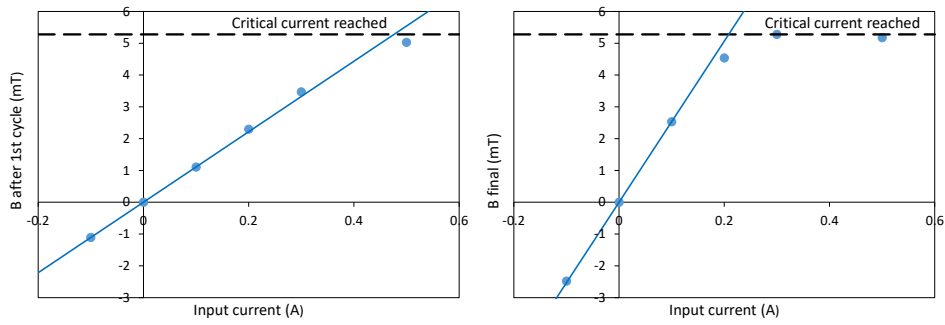


Figure 5.8: Data showing the linearity of flux pumping with input current. **Left:** The measured magnetic field after a single pumping cycle increases linearly with the applied current. **Right:** The measured magnetic field at saturation no longer has a linear relationship with input current because the critical current of the superconductor has been reached. This explains the plateau.

An interesting feature of Figure 5.7 is that the line of best fit for  $I_a = 0.3$  A (the blue curve) overshoots the critical current line. This is thought to be a consequence of there only being data for 6 pumping cycles. As a result, the data point for  $n = 2$  skews the line of best fit to saturate at a magnetic field value above the critical current line. With more data points at higher values of  $n$ , however, it is expected that the line of best fit will plateau to coincide with the critical current line.

The linearity of flux pumping is illustrated by the graphs in Figure 5.8. Note that, in addition to the previous input currents of 0.1 A, 0.2 A, 0.3 A, and 0.5 A, Figure 5.8 also shows flux pumping data for  $I_a = -0.1$  A. The left-hand graph shows the relationship between input current and the measured magnetic field after 1 cycle. A conclusively linear relationship is observed. There is some deviation from linearity with an input current of  $I_a = 0.5$  A, whereby the flux pumped current after one cycle is at a value close to the critical current. The final magnetic field after a number of cycles ( $n = 8$  for  $I_a = 0.1$  A and 0.2 A,  $n = 6$  for  $I_a = 0.3$  A, and  $n = 3$  for  $I_a = 0.5$  A) is given in the right-hand graph of Figure 5.8. Here, there is a linear region for small input currents ( $I_a < 0.2$  A), but this begins to plateau as the input currents increase. This is a clear indication that the critical current is being reached.

### 5.2.1 Reverse flux pumping mechanism

In many instances (such as in situations where a homogeneous magnetic field may need to be switched quickly to a magnetic bottle field) it will be necessary to reduce the current

$I_a$ (A)	$\alpha_{\text{measured}}$	$\alpha_{\text{theory}}$	$\frac{\beta_{\text{measured}}(I)}{\beta_{\text{measured}}(I_a=0.1 \text{ A})}$	$\frac{\beta_{\text{theory}}(I)}{\beta_{\text{theory}}(I_a=0.1 \text{ A})}$	$\frac{B_{\text{measured}}(I_a)}{B_{\text{measured}}(I_a=0.1 \text{ A})}$	$\frac{B_{\text{theory}}(I_a)}{B_{\text{theory}}(I_a=0.1 \text{ A})}$	Flux pumping mechanism
0.1	$0.563 \pm 0.005$	$0.496 \leq \alpha \leq 0.626$	1	1	1	1	Standard
0.2	$0.494 \pm 0.005$	$0.496 \leq \alpha \leq 0.626$	2.07	2	1.79	2	Standard
0.3	$0.324 \pm 0.007$	$0.496 \leq \alpha \leq 0.626$	3.13	3	2.08	3	Standard
0.5	$0.028 \pm 0.001$	$0.496 \leq \alpha \leq 0.626$	4.54	5	2.04	5	Standard
-0.1	$0.546 \pm 0.003$	$0.496 \leq \alpha \leq 0.626$	-1.02	-1	-0.98	-1	Standard <sup>†</sup>
0.1	$0.589 \pm 0.009$	$0.496 \leq \alpha \leq 0.626$	0	0	0	0	Flux subtraction
0.2	$0.66 \pm 0.02$	$0.496 \leq \alpha \leq 0.626$	0	0	0	0	Flux subtraction

<sup>†</sup> Standard flux pumping with negative input flux

Table 5.1: Table showing obtained fitting parameters for different methods of flux pumping.

in the Target Loop, perhaps even reversing its polarity from circulating clockwise to anti-clockwise, or *vice versa*. Thus, a method of reverse flux pumping needs to be devised. Equation (5.10) shows that the final current is directly proportional to the input flux, meaning that its polarity depends on the sign of the input current. Thus, reversing the input current will change the direction of the flux pumped current. However, reversing the input current risks introducing some systematic discrepancy between forward and reverse pumping schemes, since switching mechanisms or two-way power supplies may not be perfectly symmetric (i.e.,  $|I_{\max}(I_a)| \neq |I_{\max}^{\text{reverse}}(-I_a)|$ ). Ultimately, this would introduce unwanted distortions to the magnetic trapping field. Additionally, schemes whereby the currents need to be physically reversed would be impractical.

Fortunately, there are schemes that enable for the flux pumped current to be reversed without having to switch the polarity of the input current. Rather intuitively, reversing the steps of the procedure given in Figure 5.5 allows for current to be built up in the opposite sense. This is the same scheme as described in [118].

Another reverse pumping scheme is summarised systematically in Table A.2 (see Appendix), and differs from the ones stated above in that it serves only to remove existing flux from the loop, and is hence termed “flux subtraction”. Successive cycles with this scheme result in a final current tending to zero. Interestingly, the final current is *independent* on the applied flux, and instead depends only on geometry (as well as the value of the initially circulating current). The steps of this flux subtraction scheme are depicted in Figure 5.9, and are discussed as follows. As before, consider a current,  $I$ , initially circulating in the Target Loop of the double-loop superconducting structure. The method of flux subtraction can be summarised in the following steps:

- **Step 1:** Turn ON the current,  $I_a$ , to the pumping solenoid so as to APPLY flux,  $\phi_a$ , to the Pumping Loop.

Here, there are three relevant contours of integration: one that defines the outer perimeter of the double-loop superconducting structure, one that defines the Target Loop, and one that defines the Pumping Loop. In addition, Kirchoff’s current law states that  $I'_1 = I'_2 + I'_3$ . Applying flux conservation to each and every closed superconducting contour, the currents  $I'_1$ ,  $I'_2$  and  $I'_3$  after this step can be written in terms of the initial current,  $I$ :

$$I'_1 = I - \frac{\phi_a l_4}{k[(2l_1 + 2l_2 - l_4)l_4 + (2l_3 + l_4)(2l_1 + 2l_2)]}$$

$$\begin{aligned}
I'_2 &= \frac{-\phi_a(2l_1 + 2l_2)}{k[(2l_1 + 2l_2 - l_4)l_4 + (2l_3 + l_4)(2l_1 + 2l_2)]} \\
I'_3 &= I + \frac{(2l_1 + 2l_2 - l_4)\phi_a}{k[(2l_1 + 2l_2 - l_4)l_4 + (2l_3 + l_4)(2l_1 + 2l_2)]}.
\end{aligned} \tag{5.11}$$

- **Step 2:** Turn ON the current,  $I_{\text{heat}}$ , to Heat Switch 2 so as to locally break the superconductivity and OPEN the switch.

In this step, all of the current is now redirected to the perimeter of the double-loop superconducting structure. Applying flux conservation to the outer loop of the superconducting structure, the current,  $I''$ , after this step becomes:

$$I'' = \left( \frac{2l_1 + 2l_2 - l_4}{2l_1 + 2l_2 + 2l_3} \right) I - \frac{\phi_a}{k(2l_1 + 2l_2 + 2l_3)}. \tag{5.12}$$

- **Step 3:** Turn OFF the current,  $I_a$ , to the pumping solenoid so as to REMOVE the applied flux,  $\phi_a$ .

In this step there is a sudden jump in current from  $I''$  to  $I'''$ . Applying flux conservation in the outer loop of the double-loop superconducting structure, the current  $I'''$  becomes:

$$I''' = \left( \frac{2l_1 + 2l_2 - l_4}{2l_1 + 2l_2 + 2l_3} \right) I. \tag{5.13}$$

Note that  $I'''$  is now independent on  $\phi_a$ .

- **Step 4:** Turn OFF the heating current,  $I_{\text{heat}}$ , to Heat Switch 2 thereby CLOSING the switch.

There is no current change in this step.

- **Step 5:** Turn ON the heating current,  $I_{\text{heat}}$ , to Heat Switch 1 to locally break the superconductivity and OPEN the switch..

In this step the current is redistributed to the Target Loop of the double-loop superconducting structure. Applying flux conservation to the superconducting contour defining the Target Loop, the current,  $I''''$ , becomes:

$$I'''' = \frac{(2l_1 + 2l_2 - l_4)^2}{(2l_1 + 2l_2)(2l_1 + 2l_2 + 2l_3)} I. \tag{5.14}$$

- **Step 6:** Turn OFF the heating current,  $I_{\text{heat}}$ , to Heat Switch 1 so as to reform the superconductivity and CLOSE the switch

In this step there is no change in the current  $I''''$ .

Equation (5.14) gives the final current after one cycle of flux subtraction. Without loss of generality, it can be written as the final current after  $n$  cycles in terms of the current after  $n - 1$  previous cycles:

$$I_n = \frac{(2l_1 + 2l_2 - l_4)^2}{(2l_1 + 2l_2)(2l_1 + 2l_2 + 2l_3)} I_{n-1}. \quad (5.15)$$

Suppose there is some initially circulating current,  $I_0$ . After  $n = N$  cycles, the current is

$$I_N = \left( \frac{(2l_1 + 2l_2 - l_4)^2}{(2l_1 + 2l_2)(2l_1 + 2l_2 + 2l_3)} \right)^N I_0. \quad (5.16)$$

Since  $\left( \frac{(2l_1 + 2l_2 - l_4)^2}{(2l_1 + 2l_2)(2l_1 + 2l_2 + 2l_3)} \right) < 1$ , it follows that, as  $N \rightarrow \infty$ , the final current in the Target Loop falls to zero.

Figure 5.10 shows the measured magnetic field when the superconducting circuit depicted in Figure 5.6 is subjected to a number of different flux pumping schemes. The first flux pumping scheme is the original scheme outlined in Figure 5.5. With an input current of 0.1 A, a magnetic field of just over 2.5 mT is obtained. After 7 cycles, the superconducting structure is then subjected to a flux subtraction scheme, with an applied flux of 0.1 A. After 7 cycles of flux subtraction, the measured magnetic field is effectively zero,<sup>6</sup> which is consistent with Equation (5.16). The superconducting structure is then subjected to another 5 cycles of flux pumping, until a magnetic field of just 2.5 mT is measured again. Then, the superconducting structure is subjected to a reverse flux pumping scheme wherein the pumping currents are reversed. Crucially, the final magnetic field is not zero, but around -2.5 mT, in agreement with the model.

### 5.2.2 Validity of the mathematical model for flux pumping

The fitting parameters,  $\alpha_{\text{measured}}$  and  $\beta_{\text{measured}}$ , obtained for various flux pumping configurations are listed in Table 5.1. In each row,  $\alpha_{\text{measured}}$  (the second column) is compared with  $\alpha_{\text{theory}}$ , the theoretical value of  $\alpha$  as calculated using the dimensions given in Figure 5.6, along with Equation (5.8). Because of the finite widths of the superconducting paths, maximum and minimum values of  $\alpha$  are calculated, constraining  $\alpha$  to lie in the range  $0.496 \leq \alpha_{\text{theory}} \leq 0.626$ , as listed in the third column. In addition to the  $\alpha$  values, the fourth column in Table 5.1 shows the ratio of the obtained fitting parameter,  $\beta_{\text{measured}}$ , as measured for each flux pumping configuration, with the obtained fitting parameter,  $\beta_{\text{measured}}$ , for the standard flux pumping mechanism with an input current of  $I_a = 0.1$  A.

<sup>6</sup>Note that the measured magnetic field is not exactly 0 mT due to remanent magnetisation in the ferromagnetic pumping solenoid.

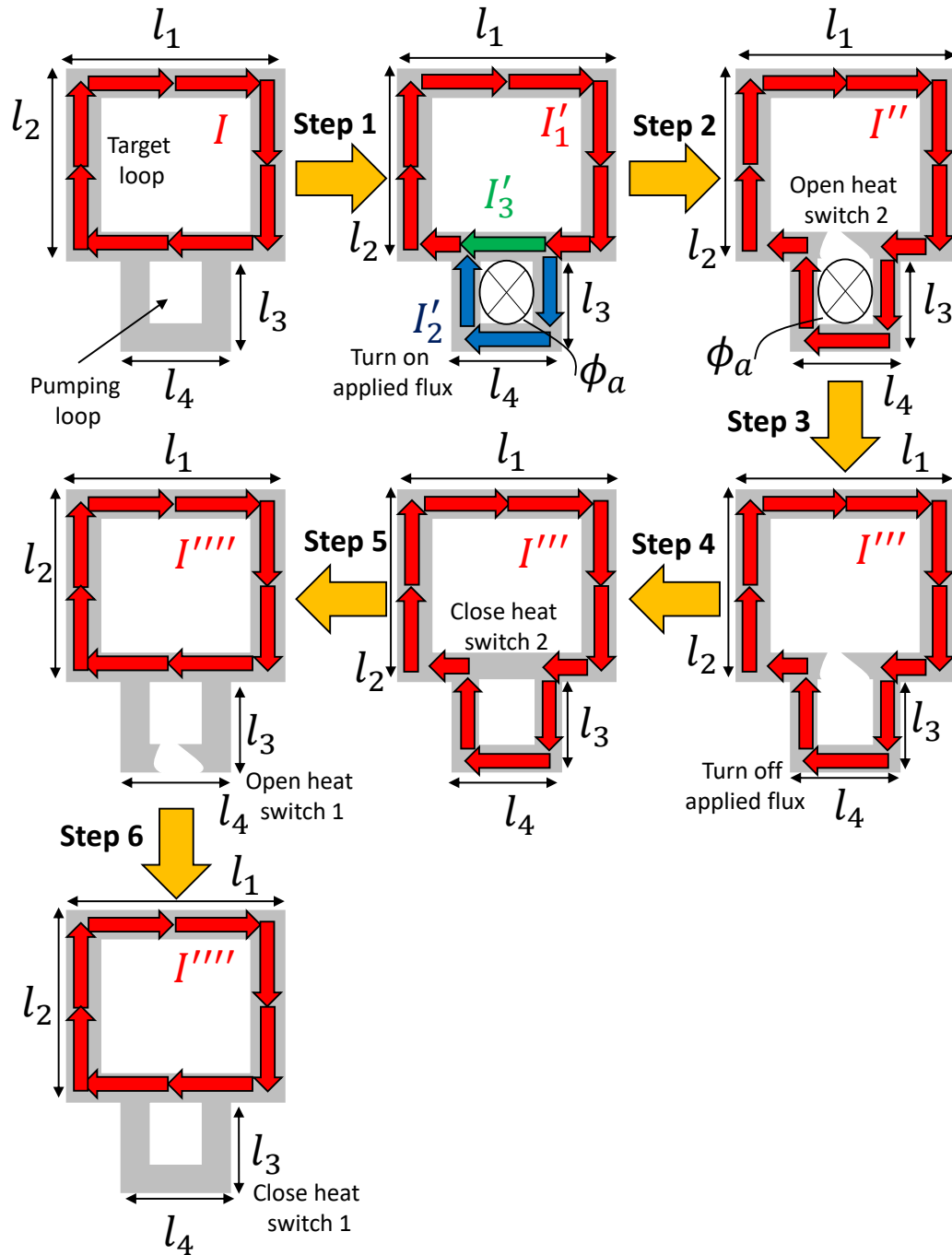


Figure 5.9: A schematic representation of the flux subtraction scheme. The grey double-loop structures represent the superconducting circuitry. The red, blue, and green arrows depict persistent current flow. Opening a heat switch is represented as a break in the grey lines defining the superconducting material. Applied flux from the pumping solenoid is represented by the symbol  $\otimes$ .

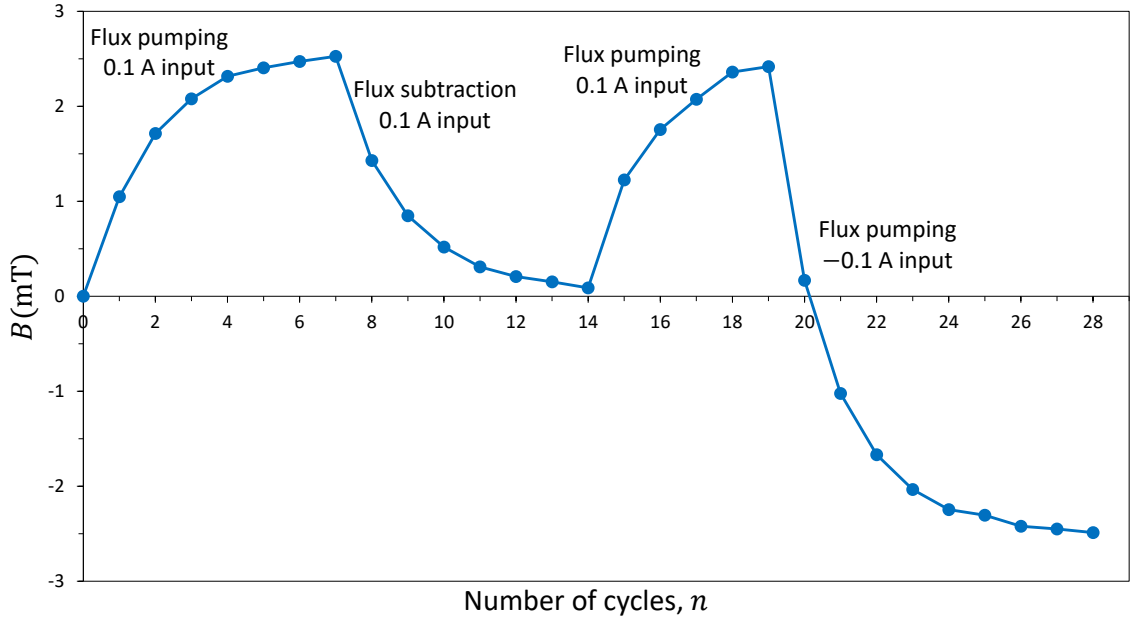


Figure 5.10: A graph showing a comparison between different types of flux pumping schemes

The fifth column lists the theoretical values for this ratio according to the model. Column six gives the ratio of the saturated magnetic field value for each pumping scheme with the saturated magnetic field value obtained for an input current of  $I_a = 0.1$  A with the standard flux pumping scheme. Column seven gives the theoretical value of this ratio according to the model. Column eight lists the type of flux pumping mechanism, and the first column lists the associated input current,  $I_a$ .

The parameters in Table 5.1 show that the obtained data is in good agreement with the model. This is especially true with input currents of  $I_a \leq 0.2$  A, irrespective of the flux pumping mechanism. There is some slight discrepancy between the data and the model with the flux subtraction mechanism with input current  $I_a = 0.2$  A, where the value for  $\alpha_{\text{measured}}$  falls just outside of the range of  $\alpha_{\text{theory}}$ . This, however, is attributed to remanent magnetisation in the ferromagnetic core, which systematically distorts the measured magnetic field. As discussed earlier, data for higher input currents (i.e.,  $I_A = 0.3$  A and 0.5 A) does not fit the model so well because the critical current of the superconducting tape has been reached. As a result, the measured magnetic field can no longer increase with pumping cycle,  $n$ , in accordance with the model because the maximum field value permitted by the material is obtained. Thus, when the data for these cases (i.e., the standard flux pumping mechanism with input currents  $I_a = 0.3$  A and 0.5 A) are fit to

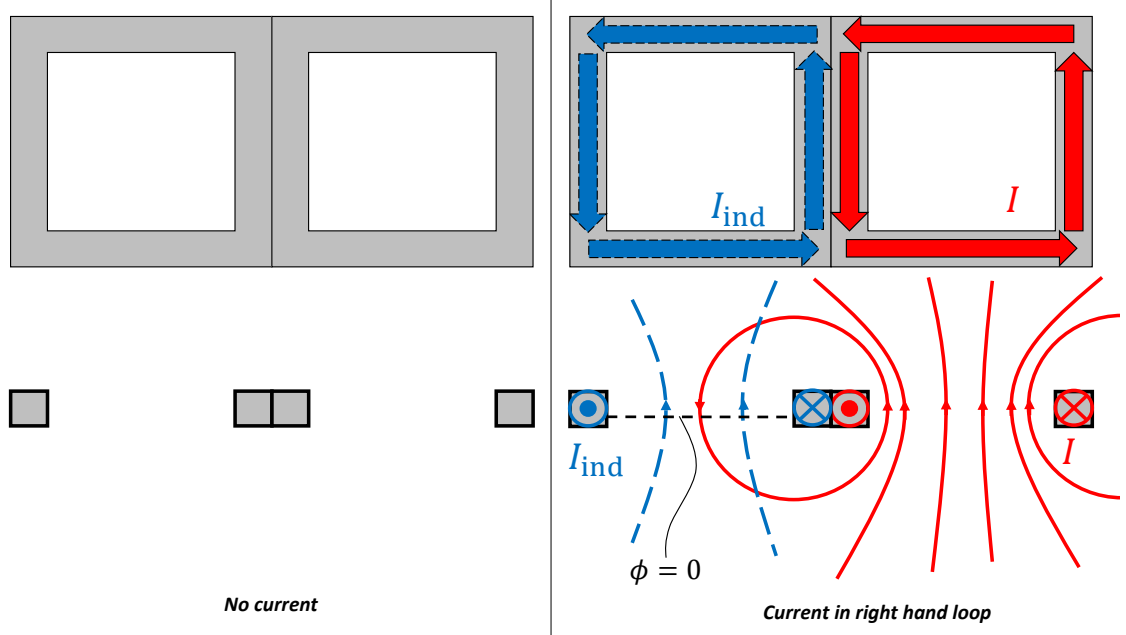


Figure 5.11: A sketch of how cross-talk arises. **Left:** A schematic picture of two adjacently placed superconducting loops carrying current. The top image is the top view of the two loops, whilst the bottom image gives the cross-sectional view. **Right:** The same loop configuration as depicted in the left-hand side, but with current flowing in the right-hand loop. The magnetic field from current in the right-hand loop flows into the left-hand loop. To ensure flux is conserved (in this case, the total flux in the left-hand loop is  $\phi = 0$ ), an induced current,  $I_{ind}$  flows to oppose the flux from the current in the right-hand loop.

Equation (5.9), the obtained parameters,  $\alpha_{measured}$  and  $\beta_{measured}$ , are skewed.

### 5.2.3 Flux pumping method for several closed superconducting loops

The flux pumping schemes described above have all been applied to individual double-loop superconducting structures. The planar magnetic field source, however, relies on magnetising several closed superconducting coils simultaneously. However, because of flux conservation, trying to magnetise two or more sets of coils poses problems, due to cross-talk. Any changes in current in one loop will produce changes in the magnetic field, which will then flow into neighbouring loops. This is shown schematically in Figure 5.11. On the left-hand side, there are two superconducting loops carrying no current. Suppose that the right-hand loop is then magnetised to carry a current,  $I$ . The magnetic field from the current,  $I$ , in the right-hand loop will then flow into the left-hand loop, inducing some current,  $I_{ind}$ . Thus, for a plurality of closed superconducting loops, addressing the current in one loop automatically changes the current in other loops. This ultimately precludes

complete control over the magnetic field distribution.

Fortunately, there is a scheme that allows for cross-talk to be accounted for, and it is described in the following subsection.

### **Simultaneous flux pumping of two coaxial triply connected planar superconducting structures**

In order to determine the effect of cross-talk between superconducting structures, it should be noted that the Geonium Chip planar magnetic field source comprises both adjacent and concentric arrangements of closed superconducting loops (see Figure 5.2). The effect of cross-talk in both arrangements therefore needs to be investigated.

Firstly, consider the concentric case, consisting of two double-loop superconducting structures with overlapping Target Loops, and adjacently placed Pumping Loops (see Figure 5.12). For simplicity, the Target and Pumping Loops of both superconducting double-loop structures are squares of length,  $l$ , and are assumed to be of dimensions such that the linear flux approximation is valid. The Target Loops of the upper and lower double-loop superconducting structures are assumed to carry initial currents of  $I_1$  and  $I_2$  respectively, and that the fraction of flux from the Target Loop of one superconducting structure that couples to the other is given by  $m$ . Note that in Figure 5.12, the Target Loop of the lower superconducting structure (i.e., the superconducting structure located lower on the page) is placed on top of the Target Loop of the upper superconducting structure. The simultaneous flux pumping mechanism can be summarised with the following steps:

- **Step 1:** *Turn ON the heating current to Heat Switch 1 of both double-loop structures simultaneously to locally drive the superconducting material normally conducting so as to OPEN the switches.*

There are two relevant superconducting contours, corresponding to the two overlapping Target Loops. There is no change in current in either loop.

- **Step 2:** *Turn ON the input currents to the pumping solenoids of the upper and lower superconducting structures to provide input fluxes of  $\phi_1$  and  $\phi_2$  respectively.*

Assuming no stray flux lines from the solenoids flow into any of the Target Loops, there is no change in current in either superconducting structure.

- **Step 3:** *Turn OFF the heating current to Heat Switch 1 of both superconducting structures.*

Here, there is no change in current in either superconducting structure.

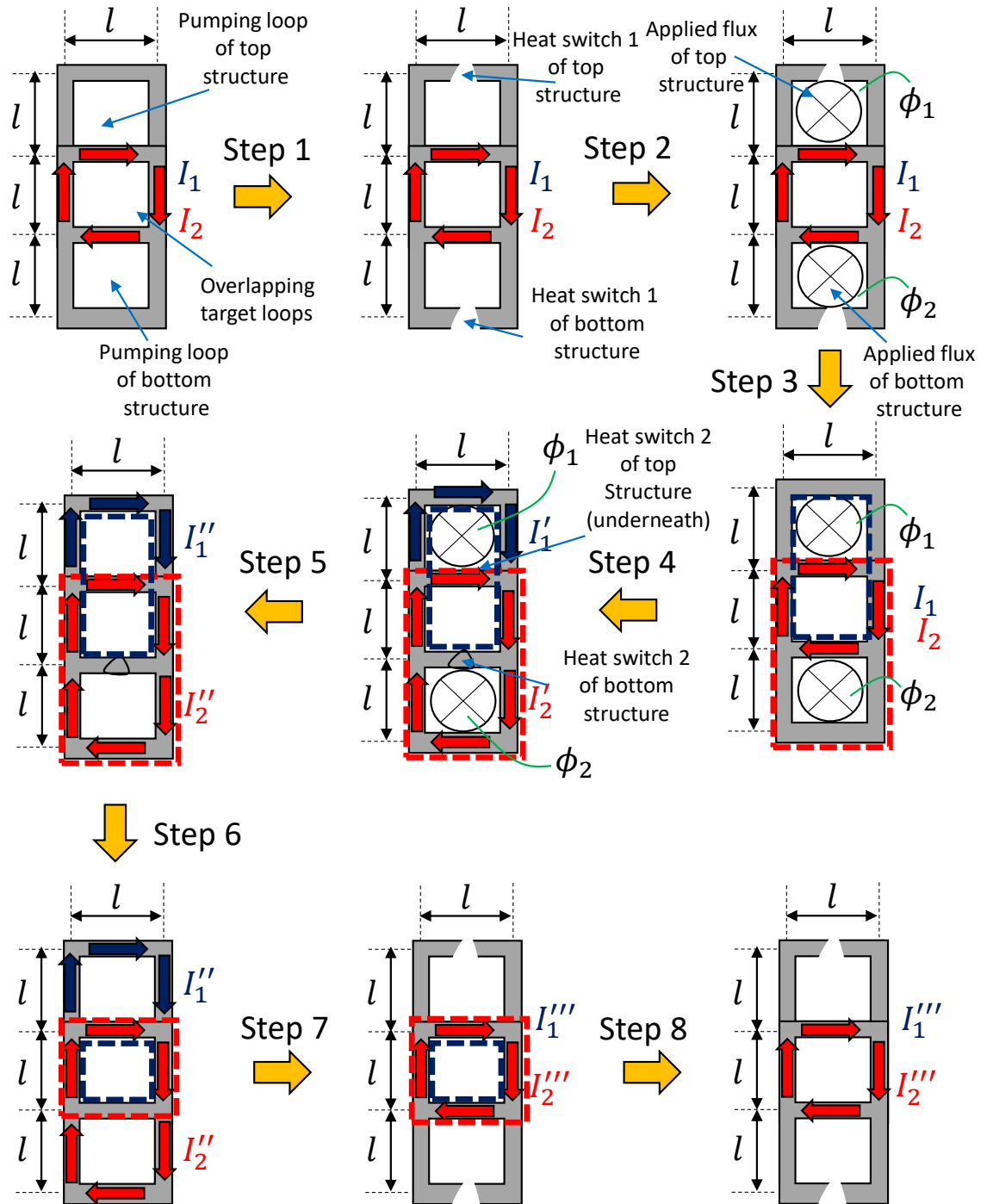


Figure 5.12: Flux pumping scheme of two double-loop superconducting structures with overlapping Target Loops. The Target Loop of the lower double-loop superconducting structure is placed on top of the Target Loop of the upper double-loop structure. Current in the upper double-loop structure is represented by a blue arrow. Current in the lower superconducting double-loop structure is depicted in blue. Applied flux is represented by  $\otimes$ .

- **Step 4:** Turn ON the heating current to Heat Switch 2 of both superconducting structures so as to OPEN the two switches simultaneously.

The currents are now redistributed to the outer loops of each superconducting structure, and their values are transformed according to  $\{I_1, I_2\} \rightarrow \{I'_1, I'_2\}$ . Applying flux conservation to the perimeter of each superconducting structure allows for  $\underline{I}' = (I'_1, I'_2)$  to be determined:

$$\text{Upper double-loop structure} \quad 3klI_1 + 3klI_2m + \phi_1 = 6klI'_1 + 2klI'_2m + \phi_1, \quad (5.17)$$

$$\text{Lower double-loop structure} \quad 3klI_1m + 3klI_2 + \phi_2 = 6klI'_2 + 2klI'_1m + \phi_2, \quad (5.18)$$

where the left-hand side of each equation describes the flux before the step, and the right-hand side describes the flux after the step. Representing equations (5.17) and (5.18) in vector-matrix form, gives

$$\begin{pmatrix} I'_1 \\ I'_2 \end{pmatrix} = \frac{1}{36 - 4m^2} \begin{pmatrix} 18 - 6m^2 & 12m \\ 12m & 18 - 6m^2 \end{pmatrix} \begin{pmatrix} I_1 \\ I_2 \end{pmatrix}. \quad (5.19)$$

- **Step 5:** Turn OFF the input currents to the solenoids so as to remove the applied flux from each superconducting circuit.

Removing  $\phi_1$  and  $\phi_2$  results in a jump in current in both superconducting structures such that  $\{I'_1, I'_2\} \rightarrow \{I''_1, I''_2\}$ . Applying flux conservation to the perimeters of each superconducting structure gives:

$$\text{Upper double-loop structure} \quad 6klI'_1 + 2klI'_2m + \phi_1 = 6klI''_1 + 2klI''_2m. \quad (5.20)$$

$$\text{Lower double-loop structure} \quad 6klI'_2 + 2klI'_1m + \phi_2 = 6klI''_2 + 2klI''_1m. \quad (5.21)$$

In vector-matrix form, these are represented as

$$kl \begin{pmatrix} 6 & 2m \\ 2m & 6 \end{pmatrix} \begin{pmatrix} I'_1 \\ I'_2 \end{pmatrix} + \begin{pmatrix} \phi_1 \\ \phi_2 \end{pmatrix} = kl \begin{pmatrix} I''_1 \\ I''_2 \end{pmatrix}. \quad (5.22)$$

Solving for  $\underline{I}'' = (I''_1, I''_2)$ , we get

$$\begin{pmatrix} I''_1 \\ I''_2 \end{pmatrix} = \begin{pmatrix} I'_1 \\ I'_2 \end{pmatrix} + \frac{1}{kl(36 - 4m^2)} \begin{pmatrix} \phi_1 \\ \phi_2 \end{pmatrix}, \quad (5.23)$$

$$\begin{pmatrix} I''_1 \\ I''_2 \end{pmatrix} = \frac{1}{36 - 4m^2} \begin{pmatrix} 18 - 6m^2 & 12m \\ 12m & 18 - 6m^2 \end{pmatrix} \begin{pmatrix} I_1 \\ I_2 \end{pmatrix} + \frac{1}{kl(36 - 4m^2)} \begin{pmatrix} 6 & -2m \\ -2m & 6 \end{pmatrix} \begin{pmatrix} \phi_1 \\ \phi_2 \end{pmatrix}. \quad (5.24)$$

- **Step 6:** Turn OFF the heating currents to Heat Switch 2 of each double-loop structure so as to CLOSE the switches.

There are no current changes in this step.

- **Step 7:** Turn ON the heating currents to Heat Switch 1 of each superconducting structure so as to OPEN the switches.

Here, the current is redirected to the Target Loop of each superconducting structure.

The currents are transformed according to  $\{I_1'', I_2''\} \rightarrow \{I_1''', I_2'''\}$ . Applying flux conservation, the currents become

$$\text{Upper double-loop structure} \quad 3klI_1'' + 3klI_2''m = 4klI_1''' + 4klI_2'''m. \quad (5.25)$$

$$\text{Lower double-loop structure} \quad 3klI_1''m + 3klI_2'' = 4klI_1'''m + 4klI_2'''. \quad (5.26)$$

The equations above, represented in vector-matrix form, are given as follows:

$$\begin{pmatrix} I_1''' \\ I_2''' \end{pmatrix} = \frac{(12 - 12m)}{(16 - 16m^2)(36 - 4m^2)} \left[ \begin{pmatrix} (18 - 6m^2) & 12m \\ 12m & (18 - 6m^2) \end{pmatrix} \begin{pmatrix} I_1 \\ I_2 \end{pmatrix} + \frac{1}{kl} \begin{pmatrix} 6 & -2m \\ -2m & 6 \end{pmatrix} \begin{pmatrix} \phi_1 \\ \phi_2 \end{pmatrix} \right]. \quad (5.27)$$

- **Step 8:** Turn OFF the heating currents to Heat Switch 1 of each superconducting structure so as to CLOSE the switches. There are no current changes in this step.

The current vector,  $\underline{I}''' = (I_1''', I_2''')$ , describes the final current after one flux pumping cycle in terms of the initial current,  $\underline{I} = (I_1, I_2)$ , and the input fluxes,  $\underline{\Phi} = (\phi_1, \phi_2)$ . In a similar fashion to before, this equation can be written, without loss of generality, as the current vector,  $\underline{I}_n = (I_n^{(1)}, I_n^{(2)})$  after  $n$  cycles, in terms of the current after  $n - 1$  cycles,  $\underline{I}_{n-1} = (I_{n-1}^{(1)}, I_{n-1}^{(2)})$ :

$$\begin{pmatrix} I_n^{(1)} \\ I_n^{(2)} \end{pmatrix} = \frac{(12 - 12m)}{(16 - 16m^2)(36 - 4m^2)} \left[ \begin{pmatrix} (18 - 6m^2) & 12m \\ 12m & (18 - 6m^2) \end{pmatrix} \begin{pmatrix} I_{n-1}^{(1)} \\ I_{n-1}^{(2)} \end{pmatrix} + \frac{1}{kl} \begin{pmatrix} 6 & -2m \\ -2m & 6 \end{pmatrix} \begin{pmatrix} \phi_1 \\ \phi_2 \end{pmatrix} \right], \quad (5.28)$$

In general form, this is rendered as:

$$\underline{I}_n = \underline{M} \cdot \underline{I}_{n-1} + \underline{N} \cdot \underline{\Phi}. \quad (5.29)$$

If  $n = N$ , the vector describing the current in each loop becomes

$$\underline{I}_N = (\underline{1} - \underline{M})^{-1} \cdot (\underline{1} - \underline{M}^N) \cdot \underline{N} \cdot \underline{\Phi}. \quad (5.30)$$

However, the magnetic field distribution,  $\underline{B}$ , is related to the current,  $\underline{I}$ , via  $\underline{\Gamma}$ , and so the magnetic field distribution after  $N$  cycles becomes

$$\underline{B}_N = \underline{\Gamma} \cdot (\underline{1} - \underline{M})^{-1} \cdot (\underline{1} - \underline{M}^N) \cdot \underline{N} \cdot \underline{\Phi}. \quad (5.31)$$

Importantly, Equation (5.31) shows that the magnetic field distribution is *linearly* related to the input fluxes. Thus, despite the occurrence of cross-talk between the loops, there is still a one-to-one relationship between the final magnetic field distribution and the input fluxes. This ultimately means that the magnetic field distribution can still be controlled.

Equation (5.31) shows how the magnetic field distribution after  $N$  cycles depends on the flux applied to each superconducting structure. For an infinite number of repetitions, the final magnetic field distribution becomes

$$\lim_{N \rightarrow \infty} \underline{B}_N = \underline{\Gamma} \cdot (\underline{1} - \underline{M})^{-1} \cdot \underline{N} \cdot \underline{\Phi}, \quad (5.32)$$

where it is noted that  $\det \underline{M} < 1$ . However,  $\underline{\Phi}$  is simply the magnetic input flux vector, and is related to the currents applied to each solenoid by

$$\underline{\Phi} = \underline{K} \cdot \underline{I}_a, \quad (5.33)$$

where  $\underline{K}$  is a diagonal matrix related to the inductances of each pumping solenoids, and  $\underline{I}_a$  is the vector of applied currents to each solenoid. The final magnetic field distribution is therefore related to the applied currents according to

$$\lim_{N \rightarrow \infty} \underline{B}_N = \left[ \underline{\Gamma} \cdot (\underline{1} - \underline{M})^{-1} \cdot \underline{N} \cdot \underline{K} \right] \cdot \underline{I}_a. \quad (5.34)$$

The expression within the square brackets is nothing other than another matrix (which is termed  $\underline{\Gamma}'$ ), and so the final magnetic field distribution is related to the input currents by a single matrix,

$$\boxed{\underline{B}_{\text{final}} = \underline{\Gamma}' \cdot \underline{I}_a}. \quad (5.35)$$

The presence of cross-talk therefore does not change the principle of operation for the planar magnetic field source, since there is a linear relationship between the currents that are put in,  $\underline{I}_a$ , and the magnetic field distribution,  $\underline{B}_{\text{final}}$ , that is achieved. Thus, so long as each loop is flux pumped *simultaneously*, any arbitrary magnetic field distribution can be achieved if the correct input currents are applied to each loop.

It is also worth noting that Equation (5.35) also holds for the case of adjacent superconducting structures, as is discussed here. Consider two double-loop structures placed as shown in Figure 5.13, with the Target Loop of the left-hand structure carrying a clockwise circulating initial current,  $I_1$ , and the Target Loop of the right-hand structure carrying an initial current of  $I_2$ . The flux pumping scheme has exactly the same steps as for the case with overlapping Target Loops, and so will not be repeated here, but are illustrated in Figure 5.13, and are summarised systematically in Table A.4 in the Appendix. Here,  $m$  describes the fraction of flux that couples from the left-hand Target loop into the right-hand Target loop (and *vice versa*) from the current in the edges of the Target Loops that are touching. As can be seen in Figure 5.13., current changes only occur in steps 4, 5, and 7. Applying conservation of flux in step 4 to the outer loops of both the left and right-hand superconducting structures yields a current vector of  $\underline{I}' = (I'_1, I'_2)$ :

$$\text{Left-hand double loop} \quad 3klI_1 + \phi_1 + klI_2m = 6klI'_1 + \phi_1 + klI'_2, \quad (5.36)$$

$$\text{Right-hand double loop} \quad 3klI_2 + \phi_2 + klI_1m = 6klI'_2 + \phi_2 + klI'_1. \quad (5.37)$$

After a few lines of linear algebra, the current after step 4 becomes:

$$\begin{pmatrix} I'_1 \\ I'_2 \end{pmatrix} = \frac{1}{36 - m^2} \begin{pmatrix} 18 - m^2 & 3m \\ 3m & 18 - m^2 \end{pmatrix} \begin{pmatrix} I_1 \\ I_2 \end{pmatrix}. \quad (5.38)$$

The next step where there is a change in current is step 5, where the current transformation  $\{I'_1, I'_2\} \rightarrow \{I''_1, I''_2\}$  occurs. Applying flux conservation to the outer loop of each superconducting structure gives

$$\text{Left-hand double loop} \quad 6klI''_1 + \phi_1 + klI'_2m = 6klI''_1 + klI''_2m, \quad (5.39)$$

$$\text{Right-hand double loop} \quad 6klI''_2 + \phi_2 + klI'_1m = 6klI''_2 + klI''_1m, \quad (5.40)$$

which can be reformed in vector-matrix form as

$$\begin{pmatrix} I''_1 \\ I''_2 \end{pmatrix} = \begin{pmatrix} I'_1 \\ I'_2 \end{pmatrix} + \frac{1}{(36 - m^2)kl} \begin{pmatrix} 6 & -m \\ -m & 6 \end{pmatrix} \begin{pmatrix} \phi_1 \\ \phi_2 \end{pmatrix},$$

$$\Rightarrow \begin{pmatrix} I_1'' \\ I_2'' \end{pmatrix} = \frac{1}{36 - m^2} \left[ \begin{pmatrix} 18 - m^2 & 3m \\ 3m & 18 - m^2 \end{pmatrix} \begin{pmatrix} I_1 \\ I_2 \end{pmatrix} + \frac{1}{kl} \begin{pmatrix} 6 & -m \\ -m & 6 \end{pmatrix} \begin{pmatrix} \phi_1 \\ \phi_2 \end{pmatrix} \right]. \quad (5.41)$$

The final current change comes in step 7. Applying flux conservation in the Target Loops of each double-loop structure, it can be shown that the final current after one flux pumping cycle is given by

$$\begin{pmatrix} I_1''' \\ I_2''' \end{pmatrix} = \frac{1}{(16 - m^2)(36 - m^2)} \begin{pmatrix} 12 - m^2 & m \\ m & 12 - m^2 \end{pmatrix} \left[ \begin{pmatrix} 18 - m^2 & 3m \\ 3m & 18 - m^2 \end{pmatrix} \begin{pmatrix} I_1 \\ I_2 \end{pmatrix} + \frac{1}{kl} \begin{pmatrix} 6 & -m \\ -m & 6 \end{pmatrix} \begin{pmatrix} \phi_1 \\ \phi_2 \end{pmatrix} \right]. \quad (5.42)$$

Once again, we can make the argument that, without loss of generality, that the initial current,  $\underline{I}$ , is the final current after  $n - 1$  cycles,  $\underline{I}_{n-1}$ , such that  $\underline{I}'''$  gives the current after  $n$  cycles. Using the same reasoning as before, Equation (5.42) can be written in general form as

$$\underline{I}_n = \underline{M}' \cdot \underline{I}_{n-1} + \underline{N}' \cdot \underline{\Phi}_a, \quad (5.43)$$

thereby demonstrating the linearity of the flux pumping scheme.

### Measurement of $\underline{\Gamma}'$

In the previous section it was shown that there is a linear relationship between the final magnetic field distribution,  $\underline{B}_{\text{final}}$ , and the input currents,  $\underline{I}_a$ . The two are related by the matrix,  $\underline{\Gamma}'$ , and full control over the magnetic field distribution requires that  $\underline{\Gamma}'$  is to be characterised empirically. The procedure for measuring  $\underline{\Gamma}'$  is different to that needed for measuring  $\underline{\Gamma}$ . This is primarily because  $\underline{\Gamma}'$  relates the *final* magnetic field distribution after a large number of pumping cycles to the input currents applied to each pumping solenoid. Thus, before the matrix elements can be measured, several flux pumping cycles have to be performed in order for the magnetic field distribution to finalise. Also,  $\underline{\Gamma}'$  relies on *all* of the superconducting double-loop structures being flux pumped simultaneously, even in loops where there is no explicitly applied input flux. A summary of the  $\underline{\Gamma}'$  measuring procedure is now given.

Suppose there are  $k$  independent double-loop structures that are to be flux pumped with  $k$  magnetic solenoids independently driven by  $k$  applied currents,  $\underline{I}_a$ . Since  $\underline{\Gamma}'$  must be

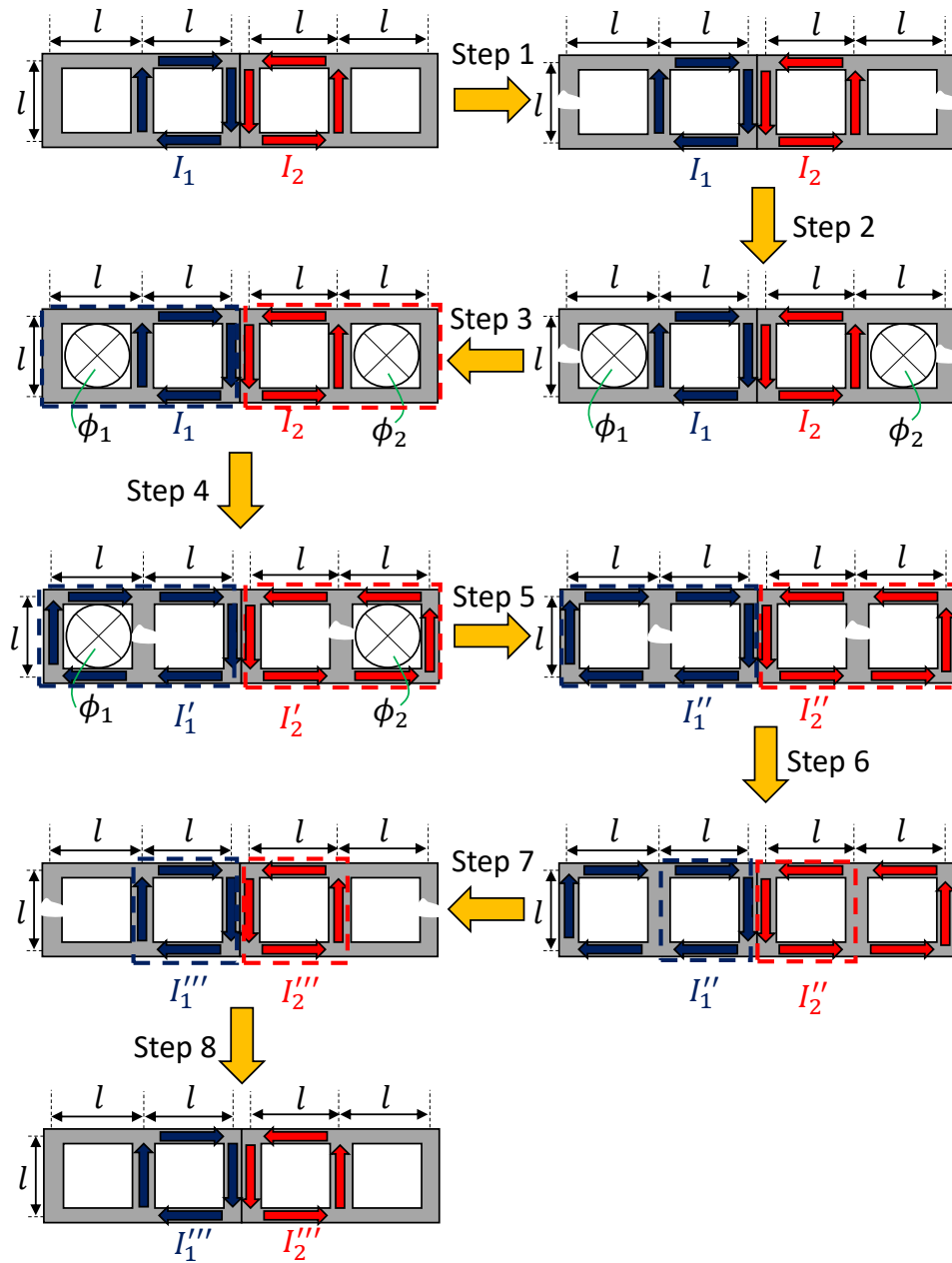


Figure 5.13: Flux pumping scheme for two double-loop superconducting structures with adjacently placed Target Loops. Persistent current flow in the left-hand double-loop superconducting structure is represented by blue arrows, whereas in the right-hand superconducting structures, it is represented by red arrows. The dashed lines represent closed superconducting contours. Applied flux is given by  $\otimes$ , and heat switch operation is denoted by gaps in the superconducting paths.

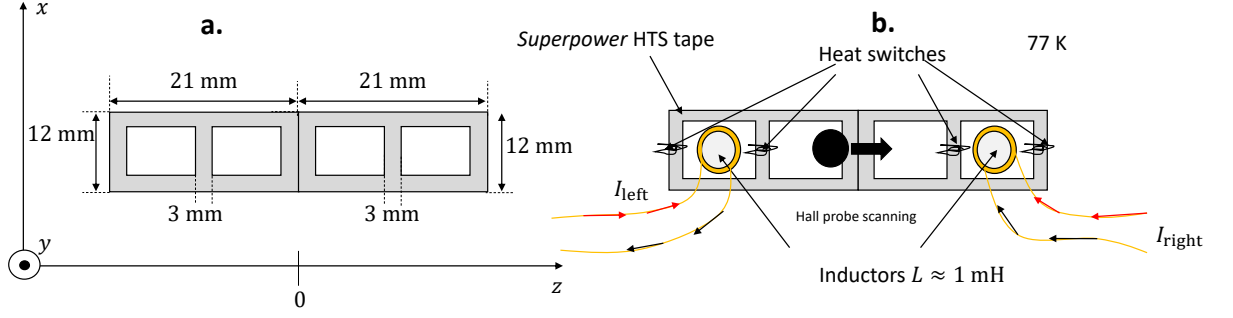


Figure 5.14: Experimental setup of a  $\Gamma'$  matrix measurement. **a.** The dimensions of the superconducting structures. **b.** Experimental setup showing two adjacent superconducting double-loop structures. Both structures are flux pumped simultaneously, before a Hall probe is scanned above the structures to measure the magnetic field distribution.

a square matrix, it follows that  $k$  expansion coefficients in the magnetic field distribution can be controlled. Since we are most concerned with the variation of  $B_z$  along the  $y$  axis, we choose the relevant  $\underline{\underline{\Gamma}}'$  matrix to be

$$\underbrace{\begin{pmatrix} B_{000}^z \\ B_{010}^z \\ B_{020}^z \\ \vdots \\ B_{0(k-1)0}^z \end{pmatrix}}_{\underline{\underline{B}}} = \underbrace{\begin{pmatrix} \Gamma'_{11} & \Gamma'_{12} & \Gamma'_{13} & \cdots & \Gamma'_{1k} \\ \Gamma'_{21} & \Gamma'_{22} & \Gamma'_{23} & \cdots & \Gamma'_{2k} \\ \Gamma'_{31} & \Gamma'_{32} & \Gamma'_{33} & \cdots & \Gamma'_{3k} \\ \vdots & \vdots & \vdots & \ddots & \vdots \\ \Gamma'_{k1} & \Gamma'_{k2} & \Gamma'_{k3} & \cdots & \Gamma'_{kk} \end{pmatrix}}_{\underline{\underline{\Gamma}}'} \cdot \underbrace{\begin{pmatrix} I_1 \\ I_2 \\ I_3 \\ \vdots \\ I_k \end{pmatrix}}_{\underline{\underline{I}}_a}. \quad (5.44)$$

Determining the elements of  $\underline{\underline{\Gamma}}'$  requires for each loop to be simultaneously flux pumped a large number of times until the magnetic field distribution finalises. Once finalised, the magnetic field distribution,  $\underline{\underline{B}}$ , can then be measured via a Hall Probe array magnetic field mapping measurement. The first column of  $\underline{\underline{\Gamma}}'$  is most easily determined by measuring the magnetic field distribution with an applied input current of  $\underline{\underline{I}} = (I, 0, 0, \dots, 0)$ , and dividing each measured coefficient by  $I$ . Any built up current should then be removed by turning on every heat switch, before the second column is determined. This is measured by repeating the same procedure as before, only with an input current of  $\underline{\underline{I}} = (0, I, 0, \dots)$ . Repeating for all the input currents allows for  $\underline{\underline{\Gamma}}'$  to be determined.

A proof-of-concept measurement of  $\underline{\underline{\Gamma}}'$  was performed for a simple superconducting system comprising two adjacently placed double-loop structures made from *Superpower* HTS tape, as shown in Figure 5.14. The left-hand double-loop structure has an input current of  $I_{\text{left}}$ , and the right-hand structure has an input current of  $I_{\text{right}}$ . The superconducting

structures are subjected to several cycles of flux pumping with various combinations of applied currents, all within the range  $0 \text{ A} \leq |I_{\text{left}}, I_{\text{right}}| \leq 0.5 \text{ A}$ . The magnetic field distribution,  $B_z(z)$ , is measured by scanning an *Arepoc* cryogenic Hall probe along the  $z$  axis at a height of  $y \approx 1 \text{ mm}$  above the tape using a CNC machine. The data is fit to a fourth order polynomial in  $z$  about the  $z = 0$  position:

$$B_z(z) = B_{z0} + B_{z1}z + B_{z2}z^2 + B_{z3}z^3 + B_{z4}z^4 \quad (5.45)$$

where  $B_{z0} = B_z(0)$ , and  $B_{zi} = \frac{1}{i!} \frac{\partial^i B_z}{\partial z^i} \Big|_{z=0}$ . The  $B_{z0}$  and  $B_{z1}$  terms depend on the input currents  $I_{\text{left}}, I_{\text{right}}$  via the following set of equations

$$\underbrace{\begin{pmatrix} B_{z0} \\ B_{z1} \end{pmatrix}}_{\underline{B}} = \underbrace{\begin{pmatrix} \Gamma'_{11} & \Gamma'_{12} \\ \Gamma'_{21} & \Gamma'_{22} \end{pmatrix}}_{\underline{\Gamma'}} \cdot \underbrace{\begin{pmatrix} I_{\text{left}} \\ I_{\text{right}} \end{pmatrix}}_{\underline{I_a}}. \quad (5.46)$$

These equations define two planes: one in  $(B_{z0}, I_{\text{left}}, I_{\text{right}})$  space, and the other plane in  $(B_{z1}, I_{\text{left}}, I_{\text{right}})$  space. Thus, if the model described above is correct, then the measured values of  $B_{z0}$  and  $B_{z1}$  should also lie in planes in their respective coordinate space. The obtained results show good agreement with the theory, at least for the  $B_{z0}$  terms, as shown in Figure 5.15. The measured values of  $B_{z0}$  for various combinations of  $(I_{\text{left}}, I_{\text{right}})$  appear to lie in the plane of best fit, depicted in light blue. The measured values of  $B_{z1}$ , do not fit so well, with many of the points lying above and below the plane of best fit (see Figure 5.16). However, the plane of best fit still falls within the error bars of each measured value of  $B_{z1}$ , with each error bar representing the uncertainty in the obtained fitting parameter,  $B_{z1}$ , for each scan.<sup>7</sup> The relatively large value of these errors is attributed to electromagnetic noise in the scanning measurement. Since the values of  $B_{z1}$  being measured are so small, they are largely affected by noise fluctuations, which, in this measurement, are of the order of 0.05 mT.

Further support of this model is given by data taken from an additional measurement with a similar setup. Here, the magnetic field distribution is first measured with input currents of  $(I_{\text{left}}, I_{\text{right}}) = (0.1, 0.0) \text{ A}$  and  $(I_{\text{left}}, I_{\text{right}}) = (0.0, 0.1) \text{ A}$ , and the coefficients  $B_{z0}$  and  $B_{z1}$  are determined. These coefficients define the calibration of the setup. Then, measurements of the magnetic field distribution for applied currents of  $(I_{\text{left}}, I_{\text{right}}) = (0.31, 0.31) \text{ A}$  and  $(I_{\text{left}}, I_{\text{right}}) = (0.31, -0.31) \text{ A}$  are taken, and values of  $B_{z0}^{\text{meas}}$  and  $B_{z1}^{\text{meas}}$  are determined from fitting the scanning data to Equation (5.45). Then using the coefficients obtained in the calibration measurements, the expected values of

<sup>7</sup>Similarly, the error bars for  $B_{z0}$  are the errors in the fitted  $B_{z0}$  term.

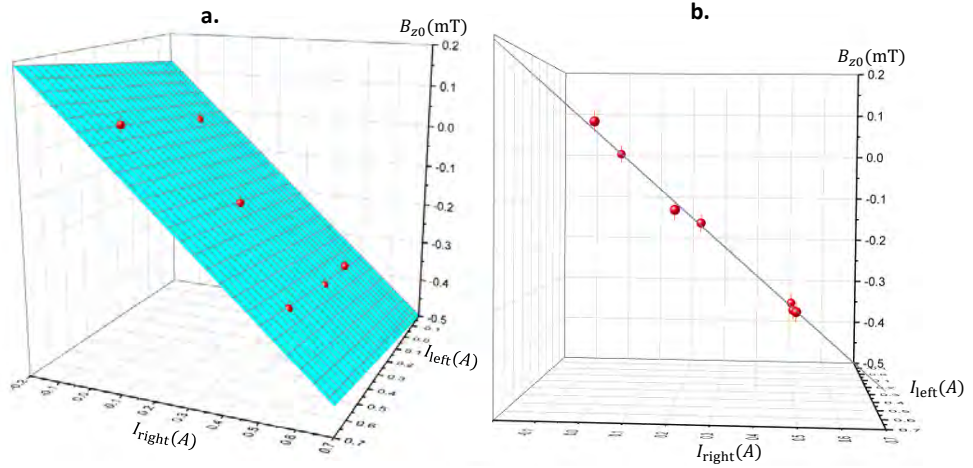


Figure 5.15: **a.** A graph of measured  $B_{z0}$  values for different combinations of  $I_{\text{left}}$  and  $I_{\text{right}}$ . The blue *plane of best fit* is a plot of  $B_{z0} = (0.076 \text{ mT A}^{-1})I_{\text{left}} + (-0.694 \text{ mT A}^{-1})I_{\text{right}}$ . The fitting error for both coefficients is  $\pm 0.015 \text{ mT A}^{-1}$ . **b.** The same graph as in **a.** but looking along the plane of best fit.

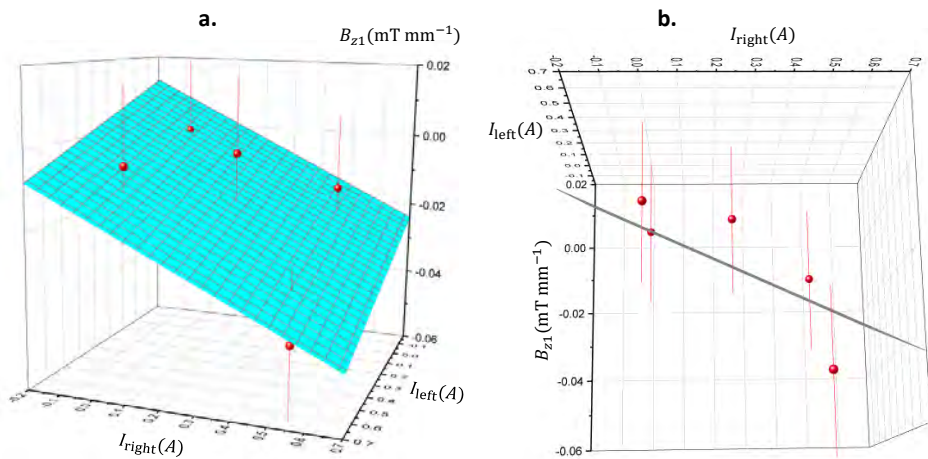


Figure 5.16: **a.** A graph of measured  $B_{z1}$  for different combinations of  $I_{\text{left}}$  and  $I_{\text{right}}$ . The blue *plane of best fit* is a plot of  $B_{z1} = (-0.023 \text{ mT mm}^{-1} \text{ A}^{-1})I_{\text{left}} + (-0.041 \text{ mT mm}^{-1} \text{ A}^{-1})I_{\text{right}}$  with a fitting error for both coefficients of  $\pm 0.020 \text{ mT mm}^{-1} \text{ A}^{-1}$ . **b.** The same graph as in **a.** but looking along the plane of best fit.

$\underline{I}_a = (I_{\text{left}}, I_{\text{right}})(\text{A})$	$B_{z0}^{\text{exp}} (\text{mT})$	$B_{z0}^{\text{meas}} (\text{mT})$	$B_{z1}^{\text{exp}} (\text{mT mm}^{-1})$	$B_{z1}^{\text{meas}} (\text{mT mm}^{-1})$
(0.31, 0.31)	$1.22 \pm 0.01$	$1.20 \pm 0.01$	$-0.39 \pm 0.04$	$-0.40 \pm 0.01$
(0.31, -0.31)	$-0.95 \pm 0.01$	$-0.93 \pm 0.01$	$0.31 \pm 0.04$	$0.29 \pm 0.02$

Table 5.2: Table comparing the expected and measured magnetic field distributions.

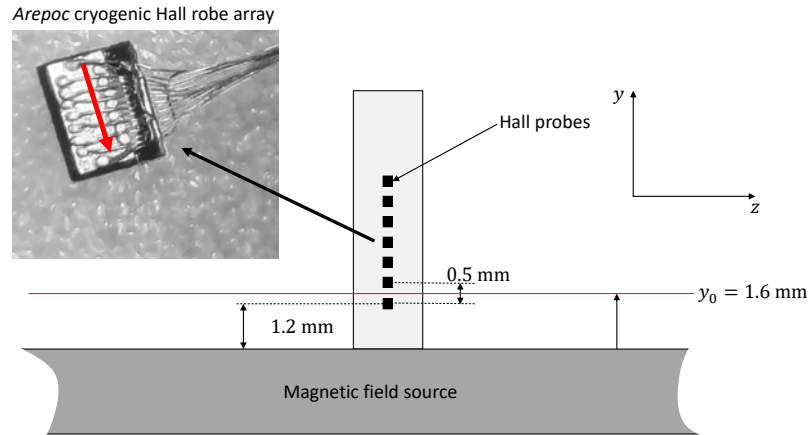


Figure 5.17: A sketch of the Hall probe array set to calibrate the magnetic field source. The red arrow shows the direction of current in the Hall probe.

the coefficients  $B_{z0}^{\text{exp}}$  and  $B_{z1}^{\text{exp}}$  for the applied currents of  $(I_{\text{left}}, I_{\text{right}}) = (0.31, 0.31)$  A and  $(I_{\text{left}}, I_{\text{right}}) = (0.31, -0.31)$  A are determined. A comparison between the expected coefficient values and the measured values is given in Table 5.2. The results show that the expected and measured magnetic field distributions agree within error (which, once again, refer to the fitting errors of the data to Equation (5.45)).

#### 5.2.4 Hall probe array measurement of $\underline{\underline{\Gamma'}}$

The results discussed in the previous section have demonstrated that it is possible to control the magnetic field distribution by simultaneously flux pumping two double-loop superconducting structures. However, the measurement procedure described above is somewhat limited. Firstly, because it relies on scanning a Hall probe a distance of several millimetres in 0.05 mm steps using the moving head of a CNC machine, the process is time-consuming, often taking several hours to obtain a complete measurement of  $\underline{\underline{\Gamma'}}$ . As a consequence, the errors in the obtained  $\underline{\underline{\Gamma'}}$  matrix elements are often relatively large, as it is not always possible to take several averages of the magnetic field distribution to smooth out the effects of electromagnetic noise. This is particularly true when using liquid cryogenics, where there might be a limited amount of time to perform a measurement before all

the cryogen has evaporated. A second issue is that the measurement procedure described above requires that the Geonium Chip planar magnetic field source be calibrated outside of the Geonium Chip experimental setup. This ultimately introduces the possibility of systematic errors in the measurement of  $\underline{\Gamma}'$ , such as misalignment of the Hall probe with the trapping region, or magnetic field distortion due to the presence of ferromagnetic materials in the vicinity of the CNC machine. Thus, a method of measuring  $\underline{\Gamma}'$  inside the Geonium Chip cryostat system is required.

One such method is to use an array of regularly spaced cryogenic Hall probes, such as the *MULTI-7U* Hall probe array from *Arepoc s.r.o.* This array comprises seven Hall probes, each  $100\ \mu\text{m} \times 100\ \mu\text{m}$  in area, and each separated by a distance of  $500\ \mu\text{m}$  (see Figure 5.17). The probes are positioned in series, and the same 10 mA current runs through all of the probes. Because the Hall probes are positioned along the direction of current flow, the same magnetic field from this current is picked up by all Hall probes (see Figure 5.17). There may be some interference between the Hall probe leads, but these can be minimised by arranging the wires from each active area into twisted pairs.

A simulation of how the *MULTI-7U* Hall probe array can be used to measure the magnetic field distribution is given as follows. In the simulation, the Hall probe array, whose first Hall probe sensor is 1.2 mm from the edge, is placed upright on the magnetic field source, such that the probes are sensitive to magnetic fields along the  $z$  axis (see Figure 5.18). In the simulation, two different magnetic field distributions are imposed along with an overlying random noise of  $\pm 0.1\ \text{mT}$ .<sup>8</sup> The first magnetic field distribution (without noise) is

$$B_z(y) = -20.08\ \text{mT} + 4.90(y - y_0)\ \text{mT mm}^{-1} - 1.30(y - y_0)^2\ \text{mT mm}^{-2}, \quad (5.47)$$

where  $y_0 = 1.6\ \text{mm}$  corresponds to the Geonium Chip trapping position above the surface of the magnetic field source. A LabVIEW program is run to simulate measuring the magnetic field (including noise) at each sensor, where the positions of each sensors are chosen to correspond to the nominal positions given in the *Arepoc* data sheet. The ‘measured’ magnetic field values are continuously averaged, and the averaged magnetic field distribution is continuously fitted to a fourth order polynomial function in  $(y - y_0)$ . The same process is then repeated for a homogeneous field distribution of  $B_z(y) = 50\ \text{mT} + 0.1\ \text{mT noise}$ .

The obtained fitting parameters for different numbers of averages are given in Table 5.3. The top panel shows the simulated fitting parameters for the first magnetic field

---

<sup>8</sup>It should be noted that the noise distribution is random within a range of  $\pm 0.1\ \text{mT}$ , rather than a zero-centered Gaussian noise distribution with a standard deviation of  $0.1\ \text{mT}$ .

Input field distribution:			
$B_z(y) = -20.08 \text{ mT} + 4.90 (y - y_0) \text{ mT mm}^{-1} - 1.30 (y - y_0)^2 \text{ mT mm}^{-2} + \text{NOISE} (\pm 0.1 \text{ mT})$			
No. averages	$B_z(\text{mT})$ (% difference)	$\partial_y B_z(\text{mT mm}^{-1})$ (% difference)	$\partial_{y^2}^2 B_z(\text{mT mm}^{-2})$ (% difference)
1	-20.0092 (0.35 %)	5.0738 (3.55 %)	-1.6569 (27.45 %)
5	-20.0971 (0.085 %)	4.8744 (0.52 %)	-1.2911 (0.69 %)
10	-20.0783 (0.008 %)	4.9030 (0.06 %)	-1.3536 (4.12 %)
20	-20.0684 (0.058 %)	4.8882 (0.24 %)	-1.3223 (1.71 %)
337	-20.0809 (0.004 %)	4.8882 (0.24 %)	-1.2866 (1.03 %)
652	-20.0747 (0.001 %)	4.8910 (0.18 %)	-1.2931 (0.53 %)
1065	-20.0818 (0.009 %)	4.8916 (0.08 %)	-1.2885 (0.88 %)
1692	-20.0809 (0.004 %)	4.8942 (0.12 %)	-1.2916 (0.65 %)

Input field distribution: $B_z(y) = 50.0 \text{ mT} + \text{NOISE} (\pm 0.1 \text{ mT})$			
No. averages	$B_z(\text{mT})$ (% difference)	$\partial_y B_z(\text{mT mm}^{-1})$	$\partial_{y^2}^2 B_z(\text{mT mm}^{-2})$
1	50.0014 (0.0028 %)	-0.0792	0.0708
5	49.9934 (0.0132 %)	-0.0148	-0.0155
10	50.0004 (0.0008 %)	-0.0002	-0.0584
20	50.0000 (0 %)	-0.0063	-0.0166
337	50.0000 (0 %)	-0.0136	0.0066
652	50.0009 (0.0018 %)	-0.0058	0.0003
1065	50.0011 (0.0022 %)	-0.0016	0.0011
1692	49.9999 (0.0002 %)	-0.0007	0.0036

Table 5.3: Simulated data for a measurement of the magnetic field distribution using a *MULTI-7U Arepoc* Hall probe array.

distribution, whilst the bottom panel shows the fitting parameters for the second magnetic field distribution. The results in the table show that, in spite of the conservatively chosen  $\pm 0.1$  mT noise, it is possible to measure the coefficients of the magnetic field distribution to an accuracy of a few thousandths of a per cent. This incredible accuracy is due to the parallelisation of the measurement, whereby the entire magnetic field distribution can be averaged many times in a short space of time.<sup>9</sup> As a result, the presence of noise, which dominates the scanning measurements described in the previous section, can now be regarded as negligible.

In spite of its exceptional performance in terms of accounting for electromagnetic noise, there are limitations to this Hall probe array measurement procedure. Firstly, this measurement procedure is still susceptible to systematic uncertainties, in particular the errors that arise from positional misalignment of the probes, and sources of stray magnetic fields (see §6.1). Secondly, the final measurement of the magnetic field distribution is ultimately limited by the fact there are only seven sensors. Thus, whilst the errors in the individual readings in each sensor are very low (because the readings can be averaged many times), when one performs a polynomial fit of the data, this does not mean that the errors in the obtained fitted coefficients will necessarily be low. Thus, whilst the obtained coefficients in Table 5.3 are very close to the true magnetic field distribution, the errors in these fitting coefficients will likely be substantially larger than the percentage values listed in Table 5.3 (these are not listed). It would be very interesting to explore this limitation of the measurement further.

### **The effect of cross-talk on the achievable current**

Equation (5.28) shows the recursive formula for flux pumping two superconducting structures with overlapping Target Loops. The level of overlap between the Target Loops is quantified by  $m$ , which describes how much flux from the Target Loop of one structure couples to the Target Loop of the other. The proposed planar magnetic field source comprises concentrically arranged superconducting loops, and, for this arrangement, the value of  $m$  is expected to be close to unity. It is therefore relevant to ask how the final obtainable magnetic field depends on  $m$ . This can be done by plotting the sum of the two currents,  $I_n^{(1)} + I_n^{(2)}$ , after an infinite number of cycles (i.e.,  $n \rightarrow \infty$ ) as a function of  $m$  for the same input fluxes in each loop ( $\phi_1 = \phi_2$ ). The sum of currents is chosen since the total magnetic field distribution at any position is proportional to this. The graph depicted

---

<sup>9</sup>With the *MULTI-7U* array, all seven sensors can typically provide magnetic field readings in a fraction of a second.

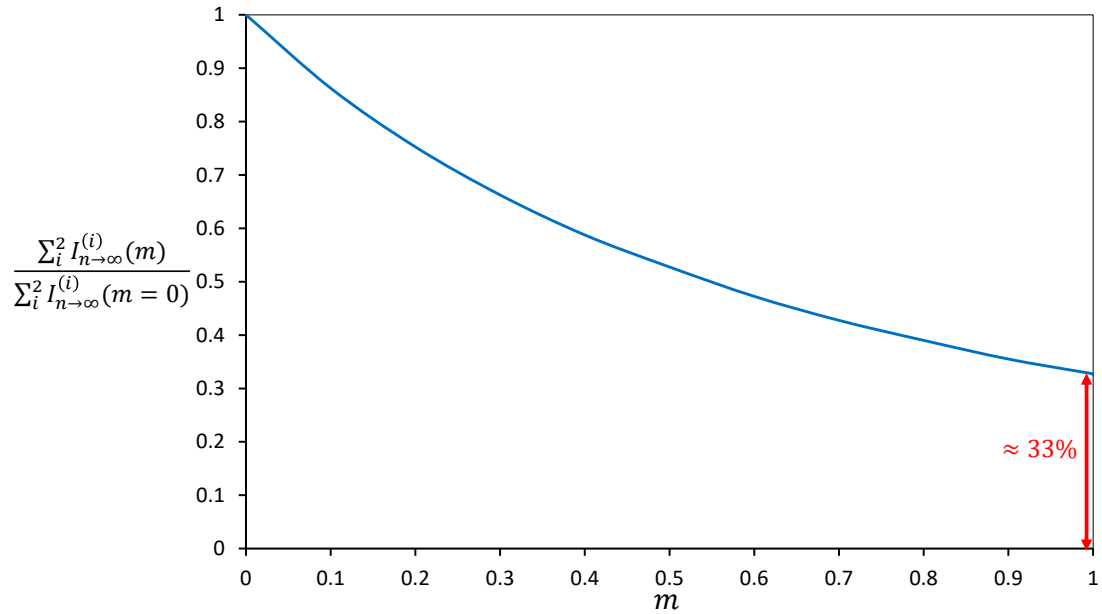


Figure 5.18: A graph showing how the level of overlap between two Target Loops affects the final flux pumped current. As can be seen, increasing the level of overlap reduces the final current for the same set of input parameters.

in Figure 5.18 shows the total currents as a function of  $m$  normalised by the case where there is no cross-talk (i.e., when  $m = 0$ ). The results show that as the level of overlap gets higher, the expected achievable currents goes down. However, with perfect overlap, the achievable current does not reach zero, but saturates at around 33 %. The practical consequence of this is that when flux pumping superconducting structures with overlapping Target Loops, three times as much flux is required to achieve the same currents as is expected with non-interacting loops.

## Chapter 6

# Persistent current-mode planar superconducting magnetic field source

The previous chapter was directed towards understanding the mechanism behind building up persistent currents in superconducting circuits. There, the emphasis was on establishing the physical principles of flux pumping, and was therefore presented from a more theoretical point of view. This chapter, however, focuses on the engineering principles behind manufacturing a working planar magnetic field source. A range of practical considerations are discussed, and a final design of the planar magnetic field source is presented. At the time of writing, this is due to be constructed within the coming months. Also discussed in this chapter is a method of improving the performance of the driven-current planar magnetic field source to help minimise fluctuations and drifts in the trapping magnetic field.

### 6.1 Field requirements of the persistent current-mode planar magnetic field source

The design of the planar magnetic field source ultimately depends on the magnetic field requirements of the trap. These are summarised in this section.

#### **Magnetic field strength**

The Geonium Chip Penning trap has a desired magnetic field strength of at least 50.0 mT (preferably up to 0.5 T) at a height of 1.6 mm above the surface of the magnetic field

source. It must be directed parallel to the chip surface, along the  $z$  axis (see Figure 3.2).

### Magnetic field gradient

The magnetic field gradient along  $y$  must be such that  $|B_{010}| < 12 \mu\text{T mm}^{-1}$ . This is to enable single electron resolution, as is discussed in §3.3.2.

### Control over the magnetic field distribution

The magnetic field distribution must be controllable up to at least the second order in the Taylor expansion about the trapping position in  $z$  (i.e., up to  $B_{002}$ ). This is because a non-zero  $B_{002}$  term (a magnetic bottle) is needed to enable single microwave photon detection via the continuous Stern-Gerlach effect (see §3.4.2). It is desirable for the Geonium Chip Penning trap to achieve magnetic bottle fields of  $|B_{002}| > 0.61 \text{ mT mm}^{-2}$ . For an electron axial frequency of 26 MHz, this  $B_{002}$  value corresponds to frequency shifts of 12 Hz per single jump in the cyclotron quantum state. Frequency shifts of this magnitude are resolvable, and have been used in the past to detect individual microwave photons from background thermal radiation [46].

### Temporal stability of the magnetic field

In order to compete with high precision Penning trap experiments, the Geonium Chip magnetic field must have a high degree of time stability, with fractional magnetic field fluctuations of the order of around  $10^{-8}$  per hour. Temporal instability in the magnetic field has several possible sources. For the driven-current magnetic field source, short-term variations in the magnetic field (on the scale of less than a second) are predominantly caused by fluctuations in the currents from the power supply. It is estimated that these can introduce a fractional magnetic field instability of the order of  $10^{-3}$  per hour.<sup>1</sup> In addition, long-term drifts in the magnetic field are often the result of temperature changes in the system, and this is particularly true for liquid based cryostats, where the magnetic permeability of the dewar material can change with temperature as the cryogen level drops over time [119]. Whilst this particular issue is not a problem for the Geonium Chip experiment, since it relies on a dry *Sumitomo* pulse tube cryostat, for the driven-current planar magnetic field source temperature changes in the power supply can still lead to

---

<sup>1</sup>This is based on observed 1 mA current fluctuations from the *HMP4040* power supply every few seconds. Using the measured  $\underline{\Gamma}$  given in Equation (3.23), this gives a time instability of  $10^{-3}$  per hour. Note that, because the fluctuations occur over a short time-scale (i.e., over no more than a few seconds) the fractional change per unit time is large compared with slow drifts in the magnetic field.

drifts in the magnetic field. To what extent temperature changes in the power supply affects the trapping magnetic field has not yet been measured, but estimations based on data from the manufacturers of the *HMP4040* power supply suggests that the magnetic field changes by 5  $\mu\text{T}$  per 1 K change in the temperature of the power supply.

The most effective way of addressing the magnetic fluctuations discussed above is to replace the driven-current magnetic field source with one that runs in persistent current-mode. However, whilst this may help to limit the effect of fluctuations from a power supply, it does not prevent external sources of noise from affecting the trapping magnetic field. Identifying the sources of such noise is a difficult task, and fluctuations as high as 10  $\mu\text{T}$  per hour can be caused by changes in solar activity, ionospheric conditions, or the presence of nearby subways in urban areas [49]. Although not present in the current setup of the Geonium Chip experiment, we plan to encase the outer vacuum chamber with a high permeability metal (“mu metal”) sheet to shield much of this external noise.

### **Fast changing of the magnetic field distribution**

The ultimate aim of the Geonium Chip experiment is to develop a practical single microwave photon detector, meaning that the process of detecting a single microwave photon from a target or sample of interest must happen in an acceptable timescale. What defines an acceptable timescale depends on the intention of the user, but for the Geonium Chip Penning trap it should be possible to change the magnetic field distribution from a homogeneous trapping field to a magnetic bottle field in less than a minute.

#### **6.1.1 Design considerations**

In the last section, the magnetic field requirements for the Geonium Chip Penning trap were outlined. In this section, the practical considerations necessary for the design of the planar magnetic field source are now given.

#### **Choice of material**

The choice of superconducting material requires careful consideration. The requirement for high trapping fields means that a superconducting material with a high critical field,  $H_c$ , and a high critical current density,  $J_c$ , is essential. In addition to the electromagnetic properties of the material, there are several mechanical specifications that also have to be met. Not only does the material need to be easily machinable, but the large magnetic forces between neighbouring coils requires for the chosen material to be strong and robust.

Thus, ceramic-based superconductors, such as YBCO, are ruled out due to their brittleness. Whilst a superconducting material with a high critical temperature,  $T_c$ , would be important for the commercialisation of the Geonium Chip (in that a Penning trap operable at relatively high temperatures ( $> 77$  K) is cheaper to run than a low temperature Penning trap), for the initial design, it is preferable to have a superconducting material with a critical temperature just above the expected ambient temperature of  $\sim 4$  K. This is to maximise the efficiency of the superconducting heat switches, such that the switches only need to raise the temperature of the superconducting material by a few K. From the abovementioned considerations, niobium-titanium alloy ( $T_c \approx 10$  K,  $H_c \approx 13$  T) [120] is the material of choice for the planar magnetic field source.

### **Number of current-carrying coils**

There are many factors to consider when choosing the number of independently controlled current-carrying coils. The first (and perhaps most obvious) consideration is that the greater the number of current-carrying coils, the greater the achievable magnetic field strength. The second consideration is that, as stated in §3.3.2, the level of control over the magnetic field distribution (in terms of the number of coefficients in the Taylor expansion of the magnetic field distribution that can be controlled) is equal to the number of independently controlled currents. Thus, in terms of magnetic field performance, the greater the number of coils, the better. However, increasing the number of currents introduces practical difficulties, not only in terms of the size of the magnetic field source, but also in terms of the amount of heat dissipation in the cryostat. The second cooling stage of the *Sumitomo* pulse tube cryostat has a cooling power of 0.5 W, and so heat input should be kept as low as possible. Also, having a higher number of magnetic field source coils increases the number of vacuum feedthroughs that are required, which then complicates the wiring inside the cryostat. Taking into account all of the above, it was decided that there should be five independent currents (i.e., five pairs of coils) in the planar magnetic field source.

### **Dimensions of the Target Loops**

The Target Loop currents are what produce the trapping magnetic field, and so it would be desirable to optimise their geometry so that they produce the highest and most homogeneous fields possible for the smallest currents. Whilst it is thought that a mathematical

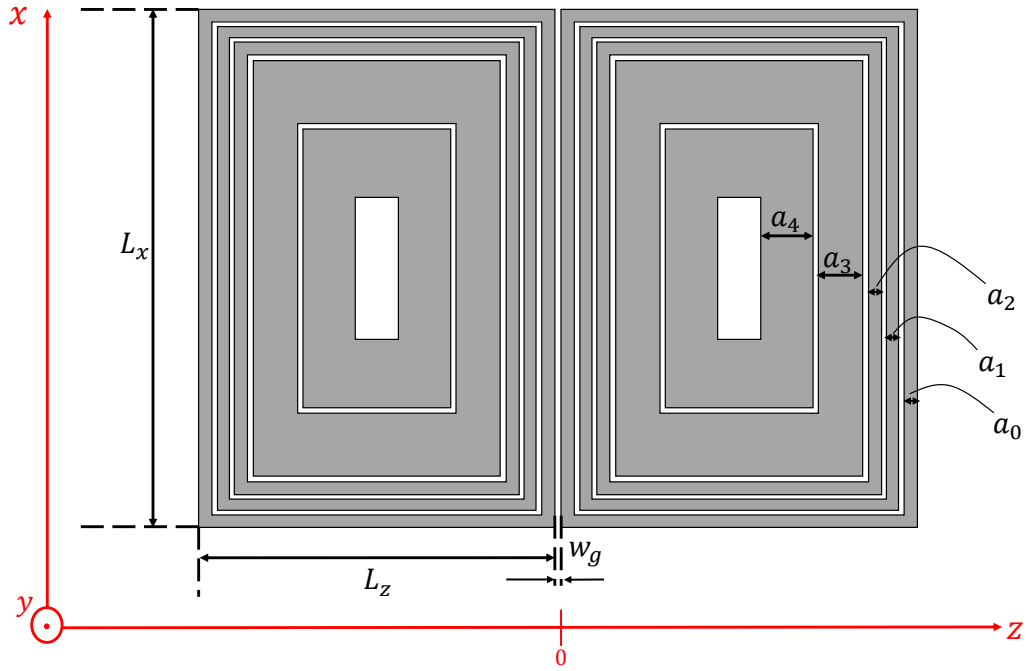


Figure 6.1: Top view of the magnetic field source arrangement with general dimensions to be optimised.

solution to this optimisation problem may exist,<sup>2</sup> this approach has not been taken here. Instead, a somewhat systematic way of settling on the loop dimensions was taken, and this is what is discussed here.

*Magnetic field source symmetry:* The very first requirement is that the magnetic field source must be symmetric in the  $x$  and  $z$  dimensions to naturally impose  $x$  and  $z$  symmetry in the trapping field. Thus, an arrangement of coils symmetrically placed about the  $xy$  plane for which  $z = 0$  was chosen (see Figure 6.1).

*Outer dimensions of the planar magnetic field source:* Secondly, a choice needs to be made on the outer dimensions of the planar magnetic field source. Ultimately, this is limited by the amount of available space in the experimental setup. Under this constraint, the following range of dimensions were considered:  $42 \text{ mm} \leq L_z \leq 70 \text{ mm}$ , and  $46 \text{ mm} \leq L_x \leq 50 \text{ mm}$ .

*Thickness of Target Loops:* Another consideration to be made is the thickness,  $t$ , of the superconducting material (see Figure 6.2). Whilst thicker loops are able to carry more current, they increase the heat required for heat switch operation, since more of the superconducting material needs to be raised above  $T_c$ . As a result, loop thicknesses in the

<sup>2</sup>i.e., for a given volume of material, and a chosen number of loops, it may be possible to find the optimum magnetic field source dimensions such that the currents required to produce a given homogeneous magnetic field at the trapping position is minimised.

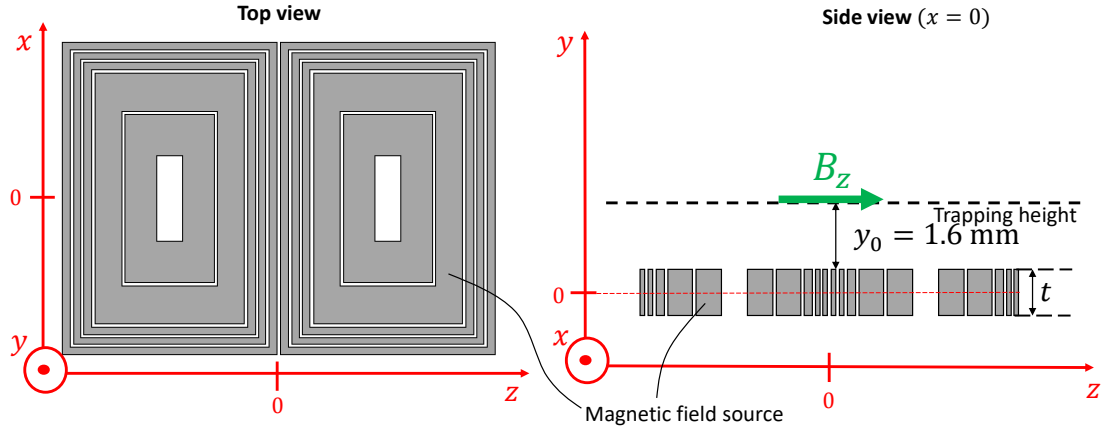


Figure 6.2: Top and side views of the planar magnetic field source showing trapping height and superconductor thickness. The location and orientation of the desired magnetic field,  $B_z$ , is clearly labelled.

range  $0.5 \text{ mm} \leq t \leq 3.0 \text{ mm}$  were considered.

*Optimal position:* Another design consideration is the position at which the magnetic field should be optimised. This is nothing other than the trapping position, and for the present setup corresponds to  $y_0 = 1.6 \text{ mm}$  above the magnetic field source (see Figure 6.2).

*Gap size:* The size of the gaps between neighbouring superconducting coils,  $w_g$ , (see Figure 6.1) is also something that needs to be considered. Smaller gaps are naturally advantageous as they allow for the majority of the structure to be filled with current-carrying wires. This is thought to enable for higher obtainable magnetic fields, particularly along the  $z$  direction, which should make it easier to achieve a high degree of magnetic field homogeneity just above the surface of the magnetic field source. The problem with small gaps, however, is that it results in very high local fields between the coils. Magnetic field expulsion from the superconducting material ultimately pushes the field lines into the small gaps, creating a region of very high magnetic flux density. This can locally exceed the critical field of the material, which can cause current dissipation. In the driven-current magnetic field source, the main and shim wires are separated by about 1 mm, and magnetic fields of over 0.1 T have been achieved without the local magnetic flux density quenching the magnet. Thus, for the persistent-mode planar magnetic field source, similar (but slightly smaller) gap sizes in the range  $0.1 \text{ mm} \leq w_g \leq 0.5 \text{ mm}$  are considered.

*Widths of loops:* The widths of the loops (depicted in Figure 6.1 as  $a_0$  for the width of the main coil,  $a_1$  for the width of shim 1,  $a_2$  for the width of shim 2, and so on) are of

primary importance to the design of the planar magnetic field source. Firstly, the wider the superconducting material of the loops, the more current the loop can take, which ultimately contributes to a higher trapping field. However, it is important to decide on how wide each loop should be relative to the other loops. Some loops are further away from the trapping position than others, and so their contribution to the overall trapping field will be smaller. To compensate for this, as a rough rule of thumb, it is best to have a thin main wire, and thicker shims, of the general hierarchy  $a_0 < a_1 < a_2 < a_3 \dots$

### 6.1.2 Determination of dimensions of planar magnetic field source

The point of the above was to develop a number of general design guidelines to help determine the dimensions of the planar magnetic field source. Now these guidelines have been established, individual designs can be proposed, and their magnetic performance can be analysed numerically.

Based on the guidelines above, 12 different geometries of planar magnetic field source were considered, and the relevant dimensions are summarised in Table 6.1. For each geometry listed, a thickness of  $t = 1$  mm was initially considered. The very first step was to calculate, for each geometry, the current densities in each loop that are required to produce a homogeneous magnetic field of 0.5 T at a height of 1.6 mm above the magnetic field source. These calculations were performed using a *Mathematica* program written by Dr José Verdú. In the program, the Biot-Savart law is used to determine, for each configuration, the current densities required in each loop to produce the desired magnetic field at the trapping position. The program assumes, for each loop, that the current is distributed uniformly along its cross-section. As discussed in §4.5, this is valid assumption. The results of these calculations are given in Table 6.2, which lists the current densities required to produce a 0.5 T homogeneous field at a height of 1.6 mm above the magnetic field source for each proposed magnetic field source geometry. Importantly, all of the calculated current densities are below the critical current density of niobium-titanium ( $J_c = 3000 \text{ A mm}^{-2}$ ).

In addition to the required currents, it is also important to consider the strength of the magnetic field on the surface of the superconducting loops. As discussed in §6.1.1, when the magnetic field source is carrying current, large magnetic fields can exist in the gaps between the loops. If these fields are large enough to exceed  $H_c$  of niobium-titanium, then the superconducting material is driven into its normal state, and the magnet is quenched. Given the dimensions listed in Table 6.1, and the required current densities displayed in

Configuration #	$L_z$ (mm)	$L_x$ (mm)	Gaps (mm)	$a_0$ (mm)	$a_1$ (mm)	$a_2$ (mm)	$a_3$ (mm)	$a_4$ (mm)
1	70.0	46.0	0.1	0.5	1.0	1.0	1.5	6.0
2	70.0	46.0	0.2	0.5	1.0	1.0	1.5	7.0
3	70.0	46.0	0.5	0.5	1.0	1.0	1.2	15.0
4	46.0	46.0	0.5	0.5	1.0	1.0	1.2	15.0
5	60.0	46.0	0.1	0.5	1.0	1.0	1.0	8.0
6	46.0	46.0	0.5	0.5	0.9	1.0	1.2	15.0
7	46.0	46.0	0.5	0.5	0.8	1.0	1.3	15.0
8	46.0	46.0	0.5	0.5	0.8	1.0	1.5	15.0
<b>9</b>	<b>50.0</b>	<b>50.0</b>	<b>0.5</b>	<b>0.5</b>	<b>1.0</b>	<b>1.0</b>	<b>1.2</b>	<b>15.0</b>
10	42.0	50.0	0.5	0.5	1.0	1.0	1.2	15.0
11	50.0	46.0	0.5	0.5	1.0	1.0	1.2	15.0
12	46.0	50.0	0.5	0.5	1.0	1.0	1.2	15.0

Table 6.1: Table summarising the various dimensions of magnetic field source that were considered. An initial thickness of  $t = 1$  mm was considered.

Configuration #	$J_0$ (Amm <sup>-2</sup> )	$J_1$ (Amm <sup>-2</sup> )	$J_2$ (Amm <sup>-2</sup> )	$J_3$ (Amm <sup>-2</sup> )	$J_4$ (Amm <sup>-2</sup> )
1	1047	656	2028	-1776	2904
2	1165	830	1840	-1506	2802
3	1635	1104	2185	-2465	2773
4	1635	1099	2274	-2837	2995
5	1054	635	2204	-2899	2365
6	1635	1114	2297	-2738	2928
7	1634	1137	2271	-2334	2900
8	1633	1142	2208	-1885	2984
<b>9</b>	<b>1634</b>	<b>1105</b>	<b>2164</b>	<b>-2352</b>	<b>2657</b>
10	1635	1100	2246	-2702	2872
11	1635	1100	2243	-2708	2915
12	1635	1103	2196	-2486	2737

Table 6.2: Table showing, for each proposed magnetic field source geometry, the current densities required to produce target field of 0.5 T at 1.6 mm above the source. The thickness of the loops used in this calculation is  $t = 1$  mm.

Configuration #	$B_0$ (T)	$B_1$ (T)	$B_2$ (T)	$B_3$ (T)	$B_4$ (T)	$F_0$ (N)	$F_1$ (N)	$F_2$ (N)	$F_3$ (N)	$F_4$ (N)
1	2.1	6.9	9.2	39.4	6.2	77	206	825	4509	4238
2	1.9	4.2	5.6	21.9	3.1	78	157	455	2112	2318
3	2.5	4.0	5.9	18.0	2.0	146	197	563	2250	2807
4	2.7	4.2	6.4	19.6	2.3	102	209	635	2796	3378
5	2.4	7.7	10.8	43.0	6.7	76	222	1050	5382	4910
6	2.7	4.2	6.2	19.2	2.2	103	188	625	2637	3212
7	2.7	4.0	5.9	18.9	2.1	102	166	580	2413	3000
8	2.6	4.0	5.6	19.3	2.0	100	163	541	2289	2943
<b>9</b>	<b>2.4</b>	<b>3.9</b>	<b>5.7</b>	<b>17.4</b>	<b>2.0</b>	<b>101</b>	<b>208</b>	<b>587</b>	<b>2258</b>	<b>2896</b>
10	2.6	4.1	6.2	18.8	2.2	91	221	660	2802	3481
11	2.7	4.1	6.3	19.1	2.2	109	204	609	2598	3170
12	2.5	3.9	5.9	18.0	2.0	96	213	614	2458	3110

Table 6.3: Table showing simulated data for different dimensions of magnetic field source. A target field of 0.5 T at 1.6 mm above the source was used. The table shows the required current densities to achieve this for each geometry. A thickness of 1 mm was considered.  $B_i$  denotes the magnetic field strength on loop  $i$ , and  $F_i$  denotes the force on loop  $i$ .

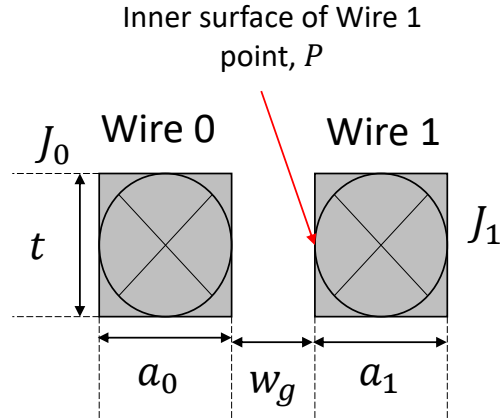


Figure 6.3: Sketch of two parallel rectangular current-carrying wires

Table 6.2, it is possible to get a rough estimate of the sorts of magnetic fields that can be expected on the inner surface of the superconducting material for each loop. To illustrate how this calculation is made, consider two wires (Wire 0 and Wire 1) carrying respective current densities of  $J_0$  and  $J_1$ , separated by a distance  $w_g$  (see Figure 6.3). The wires have the same thickness,  $t$ , but differ in their widths, with  $a_0$  being the width of Wire 0, and  $a_1$  being the width of Wire 1. The purpose of this calculation is to determine the magnetic field on the inner surface of Wire 1, at point  $P$ . The magnetic field at  $P$  is the sum of the magnetic field contributions from Wire 1,  $B_{\text{Wire 1}}$ , and from Wire 0,  $B_{\text{Wire 0}}$ . Using Ampere's law,  $B_{\text{Wire 1}}$  can be approximated as

$$B_{\text{Wire 1}} \sim \frac{\mu_0 J_1 a_1 t}{2\pi(a_1/2)} = \frac{\mu_0 J_1 t}{\pi}, \quad (6.1)$$

where  $\mu_0$  is the permeability of free space. Similarly,  $B_{\text{Wire 0}}$ , can be approximated as

$$B_{\text{Wire 0}} \sim \frac{\mu_0 J_0 a_0 t}{2\pi(a_0/2 + w_g)}. \quad (6.2)$$

For the arrangement in Figure 6.3, the magnitude of the net magnetic field at  $P$  is actually  $|B_{\text{Wire 1}} - B_{\text{Wire 0}}|$ , since, at  $P$ , the magnetic contributions from Wire 0 and Wire 1 point in the opposite direction. However, in this calculation, the sum of the magnitudes of the magnetic fields is considered (i.e.,  $|B_{\text{Wire 1}}| + |B_{\text{Wire 0}}|$ ). This is to ensure that the calculations always overestimate the magnetic field on the superconductor surface, as a safety precaution. Whilst only two wires have been considered here, this principle can be

extended for any number of wires.

Using the calculation principle described above, the magnetic field on each loop, for each configuration listed in Table 6.1, and carrying the corresponding current densities listed in Table 6.2, was determined. The magnetic fields were calculated on the position of each loop in the  $xz$  plane for which  $y = 0$  that is closest to the trapping region, and the results are listed in Table 6.3.

In addition to the magnetic field values, estimates of the forces experienced by each loop were made. As is well known, a wire of length,  $l$ , carrying a current,  $I$ , in a magnetic field,  $B$ , oriented perpendicular to the direction of current flow, will experience a force,  $F$ , of magnitude  $F = BIl$ . Thus, using the calculated magnetic field values, along with the dimensions given in Table 6.1, and the current densities in Table 6.2, the force on each superconducting loop can be estimated. These are listed on the right-hand side of Table 6.3.

The results in Table 6.3 indicate that a trapping field of 0.5 T is unlikely for any of the geometries listed in Table 6.1. In every case, the maximum value of the magnetic field on the superconductor edge exceeds the critical field of niobium-titanium. In addition, for every configuration, the calculated force on shim 4 is extremely large, being approximately equal to the weight of half a ton with configuration 5, and, with these forces, it would be difficult to keep the loops from moving apart. It is therefore necessary to scale down the desired magnetic field.

Whilst the results displayed in Table 6.3 suggest that a target magnetic field of 0.5 T may not be possible, they do give some indication as to which of the 12 considered geometries is best. Inspection of the calculated magnetic field and force values shows that configuration 9 is the best choice of all the 12 proposed geometries. For this reason, the numbers for configuration 9 in Table 6.1 and 6.2 are in bold.

Once configuration 9 was chosen, further calculations were made to see what effect different superconductor thicknesses would have on the magnetic field source performance, in particular on the currents required in each loop, on the magnetic field values on the inner edge of each loop, and on the expected magnetic forces. Using the *Mathematica* program mentioned above, the current densities needed to achieve a 0.5 T homogeneous magnetic field at 1.6 mm above the magnetic field source were calculated for the dimensions of configuration 9 but with thicknesses ranging from 0.50 mm to 3.00 mm. The results are summarised in Table B.1 in the Appendix, and show, as expected, that with thicker loops the required current density goes down. This suggests that it is better to have

Desired Field (T)	$B_0$ (T)	$B_1$ (T)	$B_2$ (T)	$B_3$ (T)	$B_4$ (T)	$F_0$ (N)	$F_1$ (N)	$F_2$ (N)	$F_3$ (N)	$F_4$ (N)
0.50	2.4	3.9	5.7	17.4	2.0	101	208	587	2258	2898
0.40	2.0	3.1	4.6	13.9	1.5	65	133	373	1444	1852
0.30	1.5	2.3	3.4	10.5	1.2	36	75	212	830	1055
0.20	1.0	1.5	2.3	7.0	0.8	16	31	87	360	460
0.10	0.5	0.8	1.1	3.5	0.4	4	8	23	90	115
0.09	0.4	0.7	1.0	3.1	0.4	3	7	19	73	94
0.08	0.4	0.6	0.9	2.8	0.3	3	5	15	58	74
0.07	0.3	0.5	0.8	2.4	0.3	2	4	12	44	57
0.06	0.3	0.5	0.7	2.1	0.2	2	3	9	33	42
0.05	0.2	0.4	0.6	1.7	0.2	1	2	6	23	29

Table 6.4: Table showing the magnetic field strengths and forces on each loop for configuration 9 with different desired fields. In each case, a loop thickness of 1 mm was considered.  $B_i$  denotes the magnetic field on the  $i$ th coil, whilst  $F_i$  denotes the force on the  $i$ th coil.

Desired Field (T)	$J_0(\text{Amm}^{-2})$	$J_1(\text{Amm}^{-2})$	$J_2(\text{Amm}^{-2})$	$J_3(\text{Amm}^{-2})$	$J_4(\text{Amm}^{-2})$
0.50	1634	1105	2164	-2352	2657
0.40	1308	884	1781	-1881	2125
0.30	981	663	1298	-1441	1594
0.20	654	422	806	-941	1063
0.10	327	221	433	-470	531
0.09	294	199	396	-423	478
0.08	262	177	346	-376	425
0.07	229	155	303	-329	372
0.06	196	133	260	-282	319
0.05	163	111	216	-235	266

Table 6.5: Table showing the current densities required for various homogeneous magnetic fields at 1.6 mm above the planar magnetic field source for different target fields. The magnetic field source dimensions considered are those corresponding to configuration 9 with a loop thickness of 1 mm.

thicker superconducting loops. However, when the magnetic fields and magnetic forces are considered (see Table B.2 in the Appendix), it turns out that it is better to have thinner superconducting loops, with the optimal superconductor thickness is 1 mm.

The calculations described above have shown that, for the 12 geometries listed in Table 6.1, configuration 9, with a superconductor thickness of 1 mm, is expected to perform the best. An important question is therefore what is the highest magnetic field that can be achieved with configuration 9? As mentioned above, a target field of 0.5 T was deemed unlikely because the calculated magnetic fields on the inner edges of the superconducting loops exceed the critical field of niobium-titanium. To determine what magnetic field strength is likely, the expected magnetic field strengths on the superconductor edges, along with the corresponding magnetic forces, were calculated for configuration 9 for various desired fields ranging from 0.05 T to 0.50 T. The results are displayed in Table 6.4, and, for completeness, the corresponding current densities are displayed in Table 6.5. From considering the magnetic field strength on the superconductor edge alone, it would seem that a desired field of 0.30 T is achievable, since the magnetic field experienced by each loop is less than the critical field of niobium-titanium. However, the corresponding inter-loop forces for this case are large, with an expected force on shim 4 of over 1000 N. Fortunately, these forces scale with the square of the desired magnetic field, and so with a desired field of 0.10 T, the force is reduced to 115 N. Given that the formers for the driven-current planar magnetic field source have been able to sustain similar forces, it is expected that, with the persistent current-mode planar magnetic field source, 0.10 T

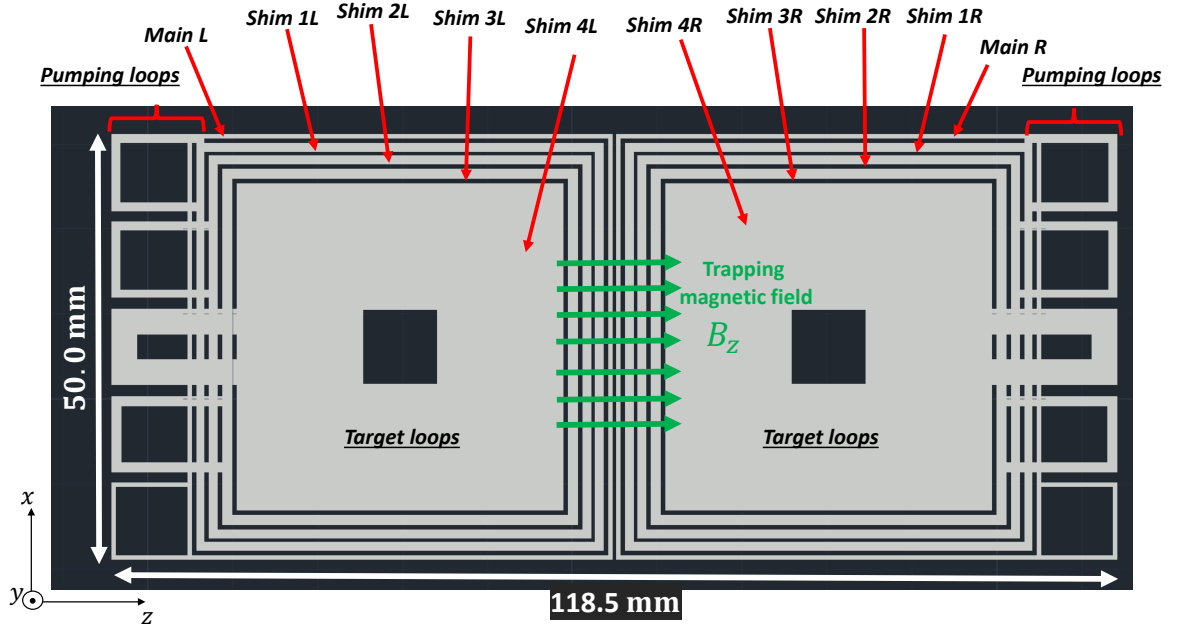


Figure 6.4: Top view of the proposed planar magnetic field source

should be achievable.

### 6.1.3 Planar magnetic field source design

The final geometry of the planar magnetic field source is presented in Figures 6.4 and 6.5. Figure 6.4 shows the top view of the planar magnetic field source. The green arrows show the direction of the desired magnetic field. As is shown, there are five pairs of square Target Loops whose widths correspond to the dimensions of configuration 9. The thicknesses of the superconducting paths is 1 mm. In addition to the Target Loops, five pairs of Pumping Loops are located on the far left and right-hand sides of the magnetic field source. It is into these Pumping Loops that flux is to be injected via the method of flux pumping described in §5. Of crucial importance is that each Pumping Loops and its corresponding Target Loop are electrically connected, such that they form a double-loop superconducting structure as described in §5. To ensure this connection is present, superconducting paths from the Pumping Loops are required to bridge over to connect to the Target Loops (see Figure 6.5). The height of the bridges is chosen to be 2 mm, to ensure they do not pass closer to the Target Loops than the gap width of 0.5 mm.

A major consideration with the planar magnetic field source is the number of input currents that are required for its operation. For each pair of loops, four heat switches and two pumping solenoids are required. If they are driven individually, then for each pair of

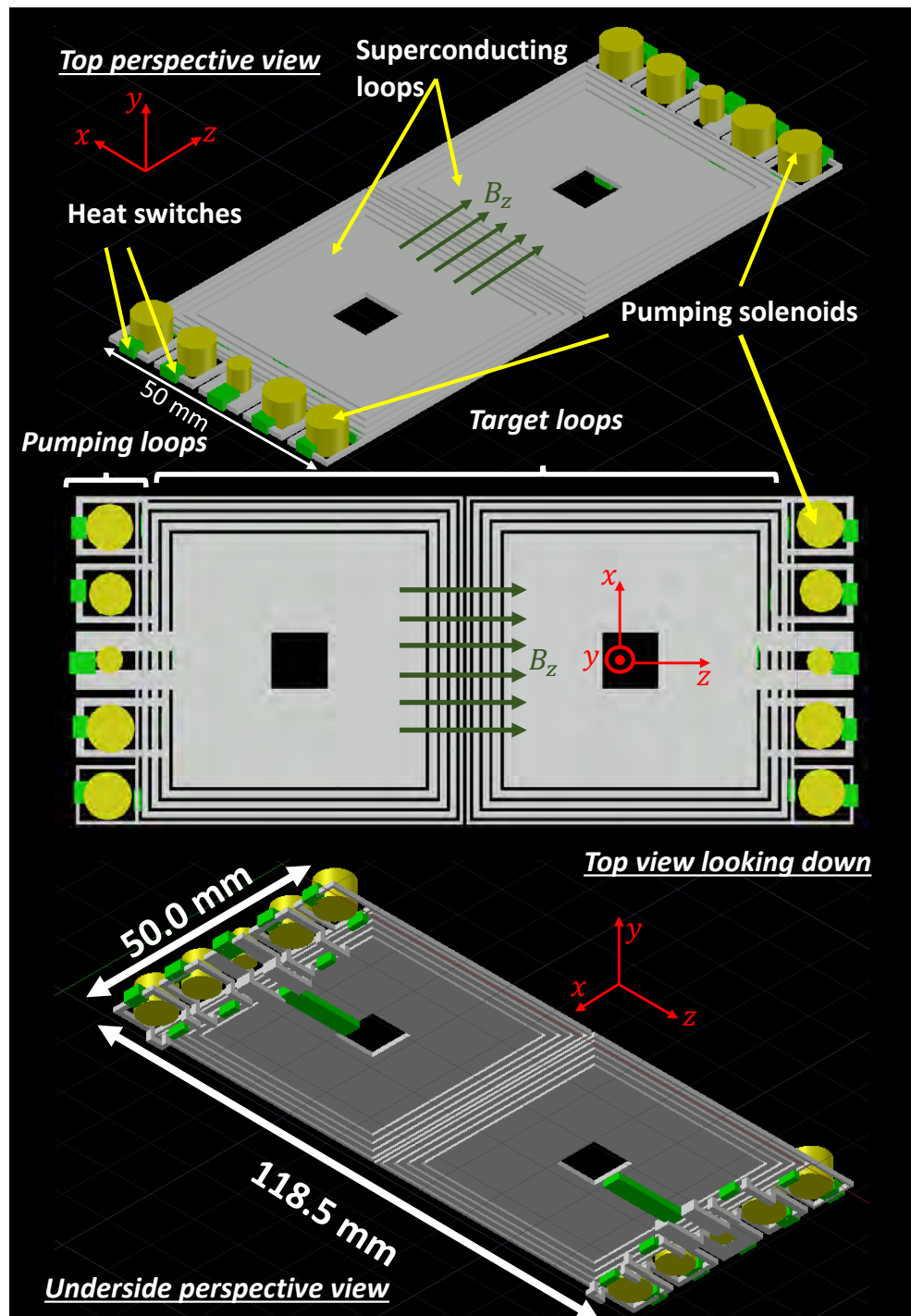


Figure 6.5: Various perspective views of the proposed persistent current-mode planar magnetic field source. The direction of the magnetic field,  $B_z$ , is indicated by the green arrows. The magnetic field source comprises five pairs of double-loop superconducting structures. The yellow cylinders represent the pumping solenoids needed to inject flux into the each double-loop superconducting structure. The light green blocks depict the location of the heat switches. **Top:** Top perspective view of the planar magnetic field source. **Middle:** Top view looking down on the planar magnetic field source. **Bottom:** Underside perspective view looking up at the bottom of the planar magnetic field source.

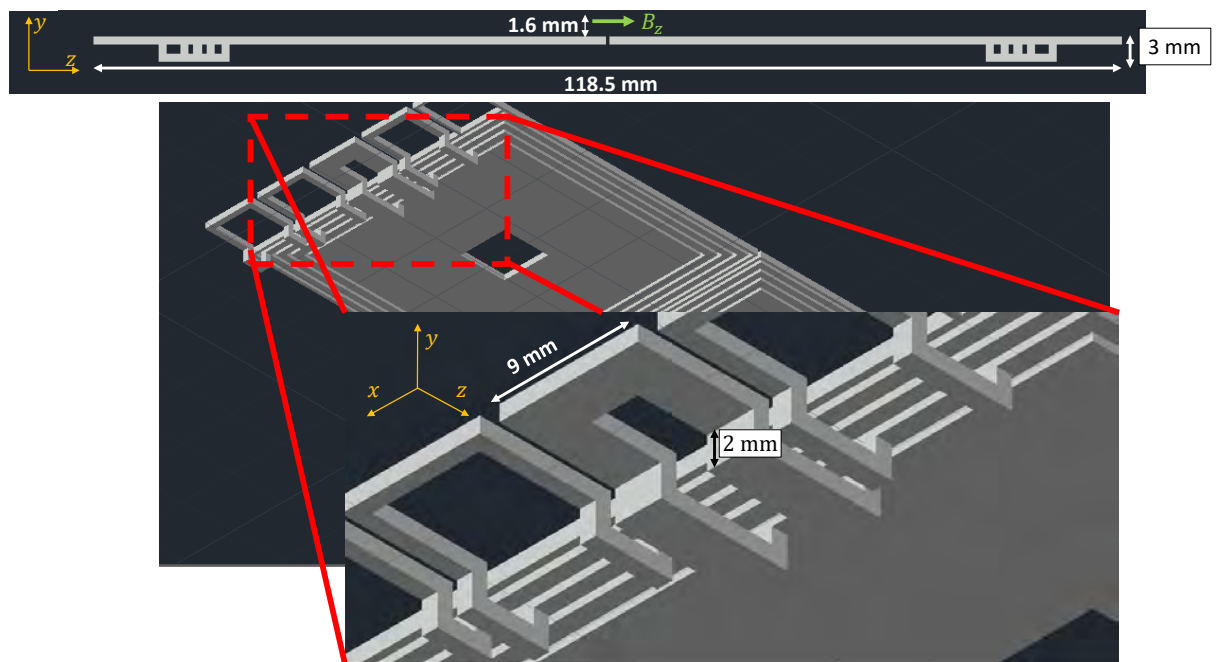


Figure 6.6: CAD drawing showing the superconducting bridges between the Pumping Loops and the Target Loops. **(Top:)** A side on view of the proposed planar magnetic field source. The location of the trapping field,  $B_z$ , is clearly shown at 1.6 mm above the magnetic field surface. **(Middle:)** A perspective view of the superconducting bridges as seen from below. **(Bottom:)** Zoomed-in image of the superconducting bridges as seen from below. A bridge height of 2 mm is clearly labelled.

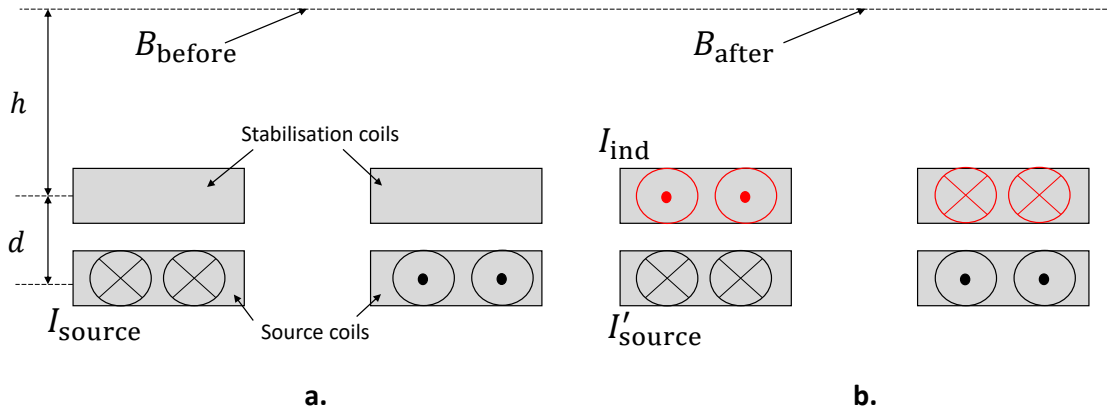


Figure 6.7: A schematic diagram showing how flux conservation can be used to stabilise fluctuations in the source coils. Changes to the source current induce a current in the stabilisation coils (depicted in red) that opposes the current change in the source coils.

coils 12 current feedthroughs (in and out) are required. For a five coil setup illustrated in Figure 6.5, 60 feedthroughs are required. This can, however, be greatly reduced with careful planning. For instance, it should be noted that during the flux pumping procedure, Heat Switch 1 on every loop needs to be operated simultaneously, as does Heat Switch 2. Thus, connecting these switches in series can reduce the required number of heating currents from 40 to 4. Similarly, the pumping currents for each pair of coils can be driven simultaneously with the same current supply.

## 6.2 Improvements to the driven-current planar magnetic field source

The planar magnetic field source, as proposed in the previous section, is, at the time of writing, still under development. The Geonium Chip Penning trap is therefore currently set to operate with the driven-current planar magnetic field described in §3.2. As discussed in §6.1, the issue with a driven-current magnetic field source is that it can likely produce fluctuations and drifts in the trapping field. It would therefore be advantageous to have a method of improving the time-stability of the driven-current magnetic field source.

### 6.2.1 Stabilisation coils

As discussed in §4.4.1, flux through a closed superconducting loop is a conserved quantity. Any changes in external magnetic field that couple into a closed superconducting loop

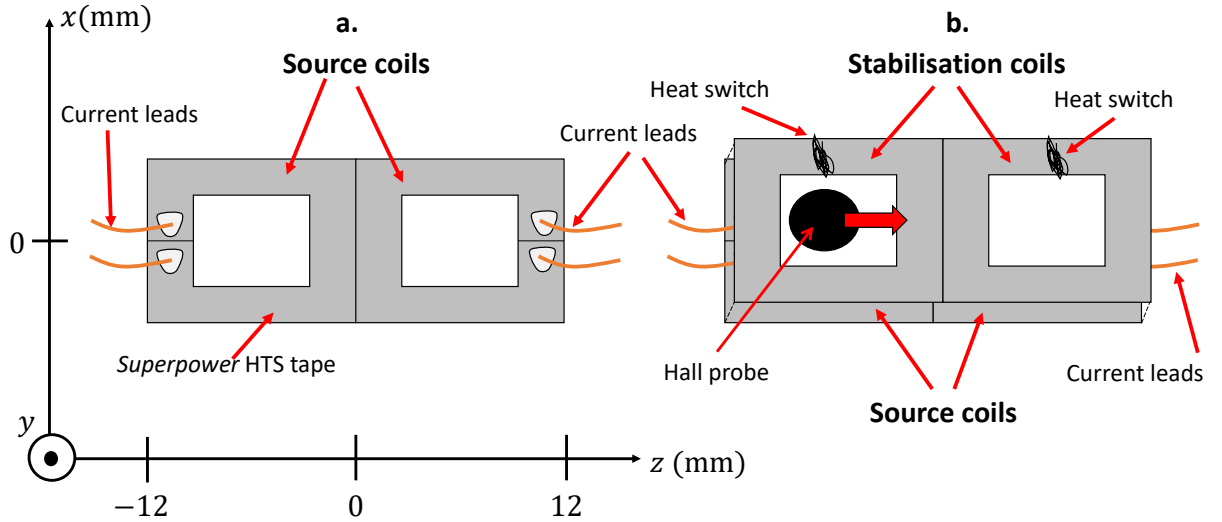


Figure 6.8: A schematic drawing of the experimental setup used to test magnetic field source stabilisation. **a.** Depiction of the source coils running on driven currents. Current flows into the source coils from a *HMP4040* power supply. **b.** Closed loop stabilisation coils are placed directly on top of the source coils. Changes in current from the *HMP4040* power supply are compensated by induced currents in the stabilisation coils.

result in induced currents that serve to oppose such changes. It therefore follows that this property could be used as a way to stabilise fluctuations in the driven-current planar magnetic field source. This could be achieved by placing passive superconducting closed loops directly on top of the coils of the driven-current magnetic field source. If the closed loops mimic the geometry of the coils of the magnetic field source, and are placed as close to them possible (i.e., directly on top of each coil), then any fluctuations in the magnetic field source will be compensated by the induced currents. Of course, the closed superconducting loops need to be field-cooled to ensure that it is the flux from the planar magnetic field source that is conserved.

The concept can be understood as follows. Consider a square superconducting coil carrying a current,  $I_{\text{source}}$ , which will be termed the “source” coil. Suppose, now, there is another superconducting coil of precisely the same dimensions as the source coil, but placed at a perpendicular distance,  $d$ , above it (see Figure 6.7). This will be termed the “stabilisation coil”. The stabilisation coil is set to conserve flux from the source coil when it is carrying current  $I_{\text{source}}$ , as is shown in Figure 6.7a. In this case, the flux flowing through the stabilisation coil is precisely equal to the flux that was field-cooled into it. As a result, no current flows in the stabilisation coil, and the total magnetic field at the position,  $h$ , above the stabilisation coil, is  $B_{\text{before}}$ . Suppose now there is a fluctuation in the current in the source coil, such that  $I_{\text{source}} \rightarrow I'_{\text{source}}$ . The change in current results

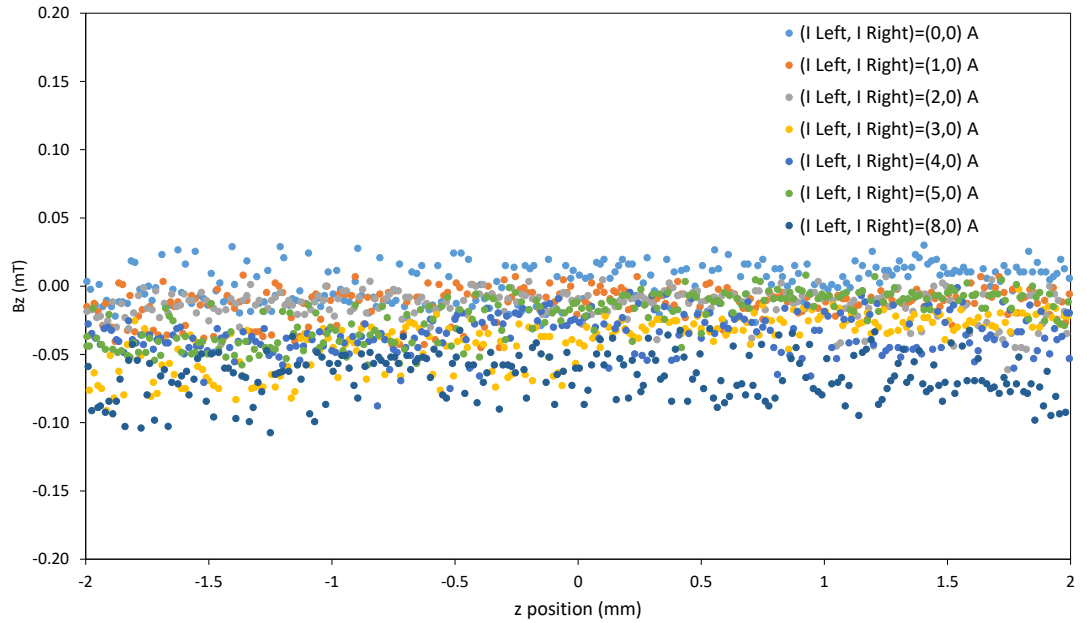


Figure 6.9: Graph showing magnetic field stabilisation for a zero-field cooled set of stabilisation coils. In spite of the different input current configurations, the measured magnetic field distribution remains largely homogeneous.

in a change in flux flowing through the stabilisation coil, which induces a current,  $I_{\text{ind}}$ , that opposes this change (see Figure 6.7b). The magnetic field at a height,  $h$ , above the stabilisation coil is the sum of the magnetic field from the source coil and the magnetic field from the stabilisation coil, and is labelled  $B_{\text{after}}$  in Figure 6.7b. The degree to which the source coil is stabilised is quantified by the stabilisation parameter,  $S$ , which is defined as one minus the relative change in magnetic field,  $\Delta B/B = (B_{\text{after}} - B_{\text{before}})/B_{\text{before}}$  per relative change in current,  $(I'_{\text{source}} - I_{\text{source}})/I_{\text{source}}$ :

$$S = 1 - \frac{\Delta B/B}{\Delta I/I}. \quad (6.3)$$

For no shielding, we expect the relative change in magnetic field to be directly proportional to the relative change in current, and so in this case  $S = 0$ . For perfect shielding, on the other hand, for any change in current there is no change in the magnetic field ( $\Delta B = 0$ ), hence  $S = 1$ . In some circumstances, the contribution from the shielding current may dominate the magnetic field at some point, and so we may get  $S > 1$ . This regime is called *over stabilisation*, and is distinguished from the case where  $S < 1$ , which we call *under stabilisation*.

The concept of magnetic field stabilisation was tested with a rather simple setup using

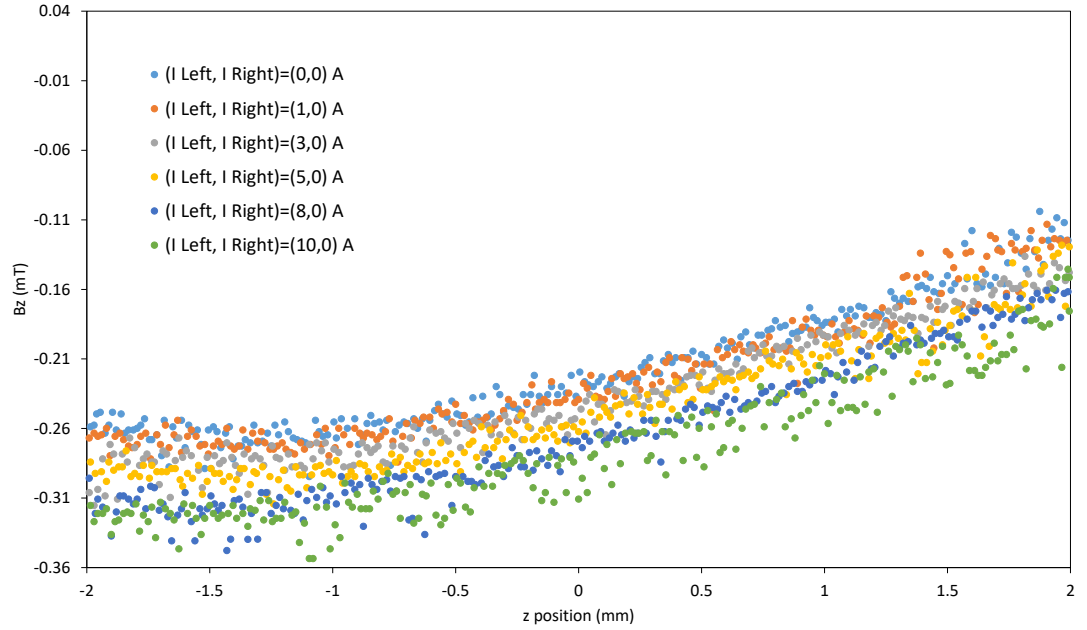


Figure 6.10: Graph showing magnetic field stabilisation for a field-cooled set of stabilisation coils with source configuration  $(I_{\text{Left}}, I_{\text{Right}}) = (0, 10)$  A.

*Superpower* HTS tape, as is illustrated in Figure 6.8. Here, two  $12 \text{ mm} \times 12 \text{ mm}$  squares were milled from HTS tape using a CNC machine. The superconducting paths were 3 mm wide. A slit was cut in each square, such that they were no longer closed superconducting loops, and to each end was soldered copper wire. These wires were connected to a *HMP4040* current supply, such that this setup defines the source coils. Two stabilisation coils, of exactly the same dimensions as the source coils, although with no slit nor soldered wire, and with one heat switch on each loop, were stacked directly on top of the source coils (see Figure 6.8b). Between the stabilisation and source coils was placed a thermal insulating sheet (not shown in Figure 6.8) to prevent the heat from the heat switch from breaking the superconductivity of the source coils. Adhesive tape was used to ensure the coils remained in position. The entire system was then submerged in liquid nitrogen, and the following experimental procedure was carried out.

Firstly, the stabilisation coils were zero-field cooled. This means that when the stabilisation coils became superconducting, they had no input flux from the source coils flowing through them. The stabilisation coils therefore react to changes in the magnetic field so as to conserve zero flux through the coils. Once zero-field cooled, 1 A of current was sent into the right-hand source loop, and the horizontal component of the magnetic field distribution was scanned along the  $z$  axis at  $x = 0$  mm, and a height of  $y = 1.6$  mm, using a

cryogenic Hall probe attached to a CNC machine. This process was repeated several times for right-hand input currents ranging from 1 A to 8 A. A plot of the measured magnetic field distributions for every case is given in Figure 6.9. The results displayed are the raw data as measured by the Hall probe, with one magnetic field reading per position (in steps of  $z = 0.05$  mm). Because there is only one data point per  $z$  position, statistical errors are not shown. Any systematic errors in the  $z$  position are present in each scan, and so are also not plotted. The results show that in spite of a highly asymmetric change in the input currents, the magnetic field distribution is largely uniform, with no obvious trend in the gradient above noise. This is a clear demonstration of the concept of passive-loop stabilisation. Whilst there is a base line change in field of around 0.1 mT, this effect in the Geonium Chip Penning trap will likely be much smaller, since current fluctuations will be at least  $10^4$  times smaller than this.

After these measurements were performed, the heat switches in the stabilisation coils were turned on, so as to break the closed superconducting loop. A current of 10 A was then sent into the right-hand loop, and the heat switches in the stabilisation coils were turned off so as to reform the superconductivity. Now the stabilisation coils are configured to conserve the flux from 10 A in the right-hand coil only. The magnetic field distribution was then mapped along the  $z$  axis at a height of  $y = 1.6$  mm for input currents to the right-hand coil ranging from 10 A to 0 A. A graph of the data is given in Figure 6.10. Rather interestingly, even when there is no input current to the source coils, the stabilisation coils maintain the asymmetric distribution. Once again, there is some change in the base level magnetic field (by a similar factor of around just under 0.1 mT), but, by inspection, the distribution retains roughly the same gradient.

The results above give a qualitative indication of how fluctuations in the magnetic field source can be stabilised. It is also interesting to see how the stabilisation factor,  $S$ , changes with height. Using the same setup as given in Figure 6.8, this was investigated by measuring the stabilisation factor,  $S$ , at  $(x, z) = (0, 0)$  mm for different heights,  $y$ . In this experiment, the stabilisation coils were field cooled with a current configuration of  $(I_{\text{Left}}, I_{\text{Right}}) = (0, 10)$  A. The stabilisation factor at each height was determined by measuring changes in the magnetic field at each height with the following current configurations  $(I_{\text{Left}}, I_{\text{Right}}) = (0, 0)$  A, and  $(0, 10)$  A at heights ranging from 0.8 mm to 2.2 mm. A plot of stabilisation factor,  $S$ , against height is given in Figure 6.11, and qualitatively shows that stabilisation improves at heights closer to the stabilisation coils. It is not understood why this is the case, but it will be interesting to investigate this further.

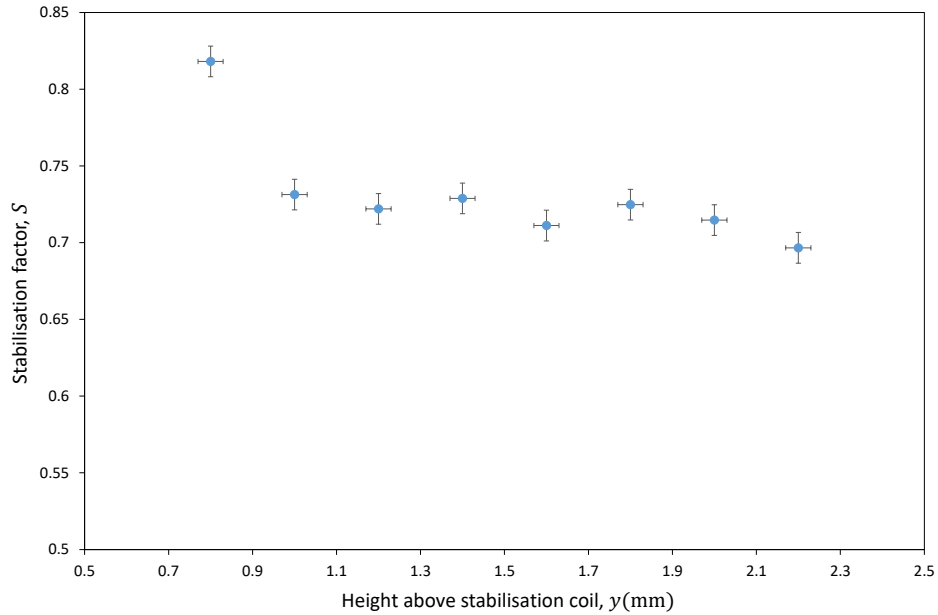


Figure 6.11: A graph showing magnetic field source stabilisation as a function of height above the magnetic field source.

The results above hint at the prospect of stabilising fluctuations in the trapping magnetic field. By placing passive coils directly on top of the magnetic field source coils, conservation of flux can be used to counteract inevitable current changes in the magnetic field source. In future, it would be interesting to investigate the possibility of perfect shielding, whereby the height,  $h$ , distance between the coils,  $d$ , and geometries of the coils are chosen appropriately to achieve  $S = 1$  for any fluctuation in current.

Finally, it is worth pointing out a potential possibility passive loop stabilisation can bring for the Geonium Chip. Whilst the concept was initially devised as a method of stabilising the currents for the driven-current magnetic field source, in future it may be possible to perfectly trap the the flux from the source coils, such that the source currents can be turned off completely and the magnetic field distribution can be retained. As was seen in Figure 6.10, the magnetic field distribution was largely intact even when there were no input currents. Such a method of providing a trapping field would be particularly useful for portable applications.

## Chapter 7

# Summary and outlook

### 7.1 Summary

This thesis has presented the theoretical foundation and design of the Geonium Chip magnetic field source – a novel planar magnetic field source which has the potential to revolutionise Penning trap technology. The proposed design, which comprises a symmetric arrangement of closed superconducting loops, scales down the size of conventional superconducting solenoids, which for many years has limited the scalability of Penning traps in terms of their application to quantum technology, to the size of a smartphone. Conservative estimates indicate that this first design is capable of achieving homogeneous trapping fields of over 0.1 T. The main results of this thesis are summarised as follows:

#### **Calibration of the driven-current planar magnetic field source**

In this thesis, the calibration of the driven-current planar magnetic field source was described. This measurement is crucial to the operation of the Geonium Chip Penning trap, because it provides a detailed understanding of how the trapping magnetic field can be controlled. This is an essential requirement for the trapping of electrons. The effect of temperature on the driven-current magnetic field source calibration was numerically investigated, and it was proposed that magnetic field distortions from the Meissner-Oschenfeld effect, along with changes to the current density in the wires when the magnetic field source becomes superconducting, may mean that the calibration matrix,  $\underline{\Gamma}$ , has to be re-measured at 4 K. A proposed method of cryogenically calibrating the driven-current planar magnetic field source using an array of seven Hall sensors was discussed, and simulations indicate that this method is promising in terms of eliminating electromagnetic noise from the measurement.

### **Method of stabilising the driven-current planar magnetic field source**

A method of stabilising the driven-current planar magnetic field source was proposed in §6. By placing passive closed superconducting coils on top of the coils of the planar magnetic field source, it is possible to use the principle of flux conservation to compensate for fluctuations in the trapping magnetic field from the current supply. Proof-of-concept measurements were performed, which indicate the principle of magnetic field stabilisation, but more research needs to be done before it can be implemented in the Geonium Chip Penning trap.

### **The linear flux approximation**

The linear flux approximation states that, for a given current, the self-flux of a closed rectangular conducting loop is approximately directly proportional to its perimeter. This was demonstrated in §4 by plotting the inductance against perimeter length for various square and rectangular shaped loops. The real importance of this approximation is revealed in §5, whereby it serves as a very simple mathematical tool for calculating the flux inside various structures made from rectangular shaped loops.

### **Development of a mathematical model for flux pumping**

The principle of flux conservation in closed superconducting loops is well-established. In this thesis, this result is used, along with the linear flux approximation, to develop a novel method of analysing methods of flux pumping. By noting that the self-flux of any closed superconducting contour is proportional to the perimeter that the persistent current travels, and that flux is conserved through any closed superconducting loop, the current in any step of flux pumping can be calculated. This model is well supported by experiment (see §5).

### **Devising methods of flux pumping**

In this thesis, several flux pumping methods were devised and experimentally verified. Whilst the method of flux pumping an individual double-loop superconducting structure was known, the method of mathematically characterising it (see above) was not. Armed with this newly devised mathematical model, new methods of flux pumping were then developed. Of particular importance to the Geonium Chip Penning trap is the method of *simultaneously* flux pumping a number of double-loop superconducting structures. The

important feature of this method is that in spite of cross-talk between the different loops, the final current configuration can be controlled.

### **Design of the persistent current-mode planar magnetic field source**

This thesis also presents the first design of the Geonium Chip persistent current-mode planar magnetic field source. It is expected to achieve homogeneous trapping fields of 0.1 T, and is currently under construction.

## **7.2 Outlook**

In addition to summarising the content of this thesis, it is also important to discuss further experiments that can be extended from this work. Whilst the planar magnetic field source designed in this thesis is currently being manufactured in the school workshop, trapping attempts are underway in the Geonium Chip experiment with the driven-current magnetic field source. It is hoped that a cloud of electrons will be trapped in the coming months, with the hope of reducing the number of trapped electrons down to one. This would be a milestone in Penning trap technology, as it would be the first conclusive detection of a single electron in a planar Penning trap. One of the main foreseeable challenges is in the loading process, and in particular if the use of UV light to liberate electrons results in disturbances to the trapping potential via charge buildup in the gaps between the electrodes. This will have to be investigated thoroughly.

In terms of the persistent current-mode planar magnetic field source, once it is fabricated, and the necessary formers needed to hold the coils in place are made, then the very first thing to do will be to see what magnetic field strengths it can achieve. If, as is predicted in §6, it is possible to achieve magnetic fields in excess of 0.1 T, then the aim will be to try to trap electrons with this planar magnetic field source in place. Once trapped, the ultimate aim will be to use a single electron to detect individual microwave photons, making use of the continuous Stern-Gerlach effect.

Of course, over the coming years, it is likely that the planar magnetic field source described in this thesis will be adapted. In particular, if the gap sizes of 0.5 mm between the superconducting loops proves to be too small (in that the magnetic field strength on the surface of the superconductor is so high that it quenches the magnet), then new designs with larger gaps will have to be drawn up. Additionally, if the additive manufacturing of ceramics continues to improve at, then, in the near future, it may be possible to 3D print a planar magnetic field source from YBCO. This would offer a huge advantage for the

Geonium Chip Penning trap, not only in terms of the speed of manufacturing, but also in that it would be able to operate above the boiling temperature of liquid nitrogen.

Whilst the scientific and technological motivations for this work have hopefully been successfully asserted throughout, it seems only appropriate that the final comment of this thesis is given to outlining the *real* inspiration for this undertaking. It is hoped that, in some way or another, whether directly, or indirectly, deliberate, or inadvertent, immediately, or in the distant future, the enclosed content will have a positive impact on society, however humble that might be.

# Bibliography

- [1] F.M. Penning. Die glimmentladung bei niedrigem druck zwischen koaxialen zylindern in einem axialen magnetfeld. *Physica*, 3(9):873-894, 1936.
- [2] Hans G. Dehmelt - Biographical. Nobelprize.org. Nobel Media AB 2014. Web. 25 Jun 2018. [http://www.nobelprize.org/nobel\\_prizes/physics/laureates/1989/dehmelt-bio.html](http://www.nobelprize.org/nobel_prizes/physics/laureates/1989/dehmelt-bio.html)
- [3] K. Blaum, Yu.N. Novikov, and G. Werth. Penning traps as a versatile tool for precise experiments in fundamental physics. *Contemporary Physics*, 51(2):149175, 2010.
- [4] Hanneke, D.; Fogwell, S.; Gabrielse, G. New Measurement of the Electron Magnetic Moment and the Fine Structure Constant. *Phys. Rev. Lett.* 2008, 100, 120801
- [5] Sturm, S.; Kohler, F.; Zatorski, J.; Wagner, A.; Harman, Z.; Werth, G.; Quint, W.; Keitel, C.H.; Blaum, K. High-precision Measurement of the Atomic Mass of the Electron. *Nature* 2014, 506, 467470.
- [6] H. Nagahama *et al.*, *Nature Communications* 8, 14084 (2017)
- [7] Van Dyck, R. Jr, Schwinberg, P. & Dehmelt, H. New high-precision comparison of electron and positron g factors. *Phys. Rev. Lett.* 59, 2629 (1987).
- [8] Gabrielse, G. et al. Precision mass spectroscopy of the antiproton and proton using simultaneously trapped particles. *Phys. Rev. Lett.* 82, 31983201 (1999)
- [9] H. Dehmelt, Experiments with an isolated subatomic particle at rest, *Rev. Mod. Phys.* 62 (1990), pp.525-531
- [10] K. Blaum, H. Kracke, S. Kreim, A. Mooser, C. Mrozik, W. Quint, C.C. Rodegheri, B. Schabinger, S. Sturm, S. Ulmer, A. Wagner, J. Walz, and G. Werth, g-factor experiments on simple systems in Penning traps, *J. Phys. B* 42 (2009), 154021

- [11] G. Gabrielse, Antiproton mass measurements, *Int. J. Mass. Spectr.* 251 (2006), pp. 273-280
- [12] M. Hori, A. Dax, J. Eades, K. Gomikawa, R.S. Hayano, W. Ono, N. Pirkl, E. Widmann, H.A. Torii, B. Juhász, D. Barna and D. Horváth, Determination of the antiproton-to electron mass ratio by precision laser spectroscopy of  $p^-He^+$ , *Phys. Rev. Lett.* 96 (2006), p. 243401.
- [13] K. Blaum, High-accuracy mass spectrometry with stored ions, *Phys. Rep.* 425 (2006), pp. 1-78
- [14] M Block *et al.*, Discovery of a nuclear isomer in  $^{65}Fe$  with penning trap mass spectrometry, *Phys Rev Lett.* 2008 Apr 4;100(13):132501.
- [15] Scigelova, M *et al.*, *Mol Cell Proteomics.* 2011 Jul; 10(7): M111.009431.
- [16] P. Edwards. Initial report on the application of The Geonium Chip for Accurate Mass Spectrometry. Technical report, Polestar Engineering, 2015.
- [17] G. Ciaramicoli, I. Marzoli, and P. Tombesi. Scalable quantum processor with trapped electrons. *Physical Review Letters*, 91(1):017901, 2003.
- [18] G. Ciaramicoli, I. Marzoli, and P. Tombesi. Trapped electrons in a vacuum for a scalable quantum processor. *Physical Review A*, 70(3):032301, 2004.
- [19] Cridland, April, Lacy, John Henry, Pinder, Jonathan and Verdú, José (2016) Single microwave photon detection with a trapped electron. *Photonics*, 3 (4). p. 59.
- [20] Paul, W. and Steinwedel, H., Ein neues Massenspektrometer ohne Magnetfeld *Zeitschrift fur Naturforschung A* 8 (7): 448-550
- [21] Jungsang Kim, Viewpoint: Trapped Ions Make Impeccable Qubits, *Physics* 7, 119 (2014)
- [22] C.J. Ballance, T.P. Harty, N.M. Linke, M.A. Sepiol, and D.M. Lucas, *Phys. Rev. Lett.* 117, 060504 (2016)
- [23] T.P. Harty, M.A. Sepiol, D.T.C. Allcock, C.J. Ballance, J.E. Tarlton, and D.M. Lucas *Phys. Rev. Lett.* 117, 140501 (2016))
- [24] S. Weidt, J. Randall, S. C. Webster, K. Lake, A. E. Webb, I. Cohen, T. Navickas, B. Lekitsch, A. Retzker, and W. K. Hensinger, *Phys. Rev. Lett.* 117, 220501 (2016)

- [25] M.H. Holzscheiter. Ion-Trap Quantum Computation. Los Alamos Science, 27:264283, 2002.
- [26] Lamata, L.; Porras, D.; Cirac, J.I.; Goldman, J.; Gabrielse, G. Towards Electron-electron Entanglement in Penning Traps. *Phys. Rev. A* 2010, 81, 022301.
- [27] Colin D. Bruzewicz, John Chiaverini, Robert McConnell, and Jeremy M. Sage, Trapped-Ion Quantum Computing: Progress and Challenges, arXiv:1904.04178 (2019)
- [28] I. Marzoli, P. Tombesi, G. Ciaramicoli, G. Werth, P. Bushev, S. Stahl, F. Schmidt-Kaler, M. Hellwig, C. Henkel, G. Marx, I. Jex, E. Stachowska, G. Szawiola, and A. Walaszyk. Experimental and theoretical challenges for the trapped electron quantum computer. *Journal of Physics B: Atomic, Molecular, and Optical Physics* 42(15):154010, 2009.
- [29] S. Stahl, F. Galve, J. Alonso, S. Djekic, W. Quint, T. Valenzuela, J. Verdú, M. Vogel, and G. Werth. A planar Penning trap. *The European Physical Journal D*, 32(1):139-146, 2005.
- [30] J.R Castrejón-Pita, R.C. Thompson, Proposal for a planar Penning ion trap, *Phys. Rev. A* 72 (2005)
- [31] M. Hellwig *et al.* 2010, *New J. Phys.* 12, 005019
- [32] J. Goldman and G. Gabrielse, Optimized Planar Penning Traps for Quantum Information Studies, *Phys. Rev. A* 81, 052335, 2010
- [33] P. Bushev, S. Stahl, R. Natali, G. Marx, E. Stachowska, G. Werth, M. Hellwig, and F. Schmidt-Kaler. Electrons in a cryogenic planar Penning trap and experimental challenges for quantum processing. *The European Physical Journal D*, 50(1):97-102, 2008.
- [34] R.S. Van Dyck, P.B. Schwinberg, and H.G. Dehmelt. Precise Measurements of Axial, Magnetron, Cyclotron, and Spin-Cyclotron-Beat Frequencies on an Isolated, 1-meV Electron. *Physical Review Letters*, 38(7):310-314, 1977.
- [35] J. Verdú. Theory of the co-planar waveguide Penning trap. *New Journal of Physics*, 13(11):113029, 2011.
- [36] Jose Verdu Galiana (2013) *Ion Trap* US 8,362,423 B1

- [37] Jose Verdu Galiana (2013) *Ion Trap* WO 2013/041615 A2
- [38] J. Pinder, J. Verdú, A planar Penning trap with tunable dimensionality of the trapping potential, *Int. J. Mass Spectrom.* 356 (2013) 49-59
- [39] A. Cridland, Development of a planar Penning trap for quantum applications with electrons. PhD thesis, University of Sussex, 2018.
- [40] J. Pinder, The Geonium Chip - engineering a scalable planar Penning trap. PhD thesis, University of Sussex, 2016.
- [41] Image retrieved from <https://warwick.ac.uk/fac/sci/chemistry/research/barrow/barrowgroup/>, 25 June 2018.
- [42] Zhenan Jiang *et al.*, Dynamic resistance of a high- $T_c$  superconducting flux pump, *Applied Physics Letters* 105, 112601 (2014)
- [43] Manninen, A.J.; Kemppinen, A.; Lehtinen, J.; Mykknen, E.; Amato, G.; Enrico, E.; Lacquaniti, V.; Kataoka, M.; Lindström, T.; Dolata, R.; et al. Towards measurement and control of single-photon microwave radiation on chip. In Proceedings of the 2015 1st URSI Atlantic Radio Science Conference (URSI AT-RASC), Gran Canaria, Spain, 1624 May 2015; p. 1.
- [44] A. Imtiaz, T. M. Wallis and P. Kabos, “Near-Field Scanning Microwave Microscopy: An Emerging Research Tool for Nanoscale Metrology,” in *IEEE Microwave Magazine*, vol. 15, no. 1, pp. 52-64, Jan.-Feb. 2014.
- [45] F. Crimin, I. Marzoli and J. Verdú, Quantum Illumination in the Geonium Chip, a feasibility study, Confidential report for Leonardo MW Ltd. Funded under private research contract #4500138590 / University of Sussex (2018)
- [46] S. Peil and G. Gabrielse, Observing the Quantum Limit of an Electron Cyclotron: QND Measurements of Quantum Jumps between Fock States, *Phys. Rev. Lett.* 83, 1287 (1999)
- [47] Mo Yang, Tae-Young Kim, Hyun-Chul Hwang, Seok-Kyung Yi, and Do-Hoon Kim, Development of a Palm Portable Mass Spectrometer, *J. Am. Soc. Mass Spectrom.* 2008, 19, 1442-1448
- [48] G.S. Gabrielse and J.N. Tan, *Shielding Superconducting Solenoids* US4,974,113 (1990)

- [49] G. Gabrielse and J. Tan, Self-shielding superconducting solenoid systems, *J. Appl. Phys.*, Vol. 63, No. 10, (1988)
- [50] S W Van Sciver. Helium Cryogenics. International Cryogenics Monograph Series. Springer New York, 2012.
- [51] Earnshaw, Samuel (1842) “On the Nature of the Molecular Forces which Regulate the Constitution of the Luminiferous Ether.” *Trans. Camb. Phil. Soc* **7** 97-112
- [52] M.D. Simon and A.K. Geim, Diamagnetic levitation: Flying frogs and floating magnets (invited), *Journal of Applied Physics* 87, 6200 (2000)
- [53] Masatomo Sato, Notes on the Magnetic Mirror Effect, *Progress of Theoretical Physics*, Vol. 20, No. 5, (1958)
- [54] Image rendered from, <http://ophysics.com/em8.html>, oPhys open-source simulation software on 26 June 2018
- [55] Ghosh, Pradip K., *Ion Traps*, Oxford : Clarendon Press 1995, International series of monographs on physics, 90
- [56] F. Crimin, B. M. Garraway J. Verdú (2017) The quantum theory of the Penning trap, *Journal of Modern Optics*, 65:4, 427-440, DOI: 10.1080/09500340.2017.1393570
- [57] L. S. Brown and G. Gabrielse, Precision spectroscopy of a charged particle in an imperfect Penning trap, *Physical Review A* 25(4) (1982)
- [58] L. S. Brown and G. Gabrielse. Geonium theory: Physics of a single electron or ion in a Penning trap. *Reviews of Modern Physics*, 58(1):233-311, 1986
- [59] Itano, W. M., Bergquist, J. C., Bollinger, J.J., Wineland, D.J., Cooling methods in ion traps, *Phys. Scr. T.* 59 106
- [60] M. Kretzschmar, Theory of the elliptical Penning Trap, *Int. J. Mass Spectrom.* 275 (2008) 21
- [61] Dehmelt, H. G. and Walls, F. L. (1986), “Bolometric” technique for the rf spectroscopy of stored ions, *Physical Review Letters*, Vol 21, Number 3
- [62] Al-Rjoub, A and Verdú, J (2012) Electronic detection of a single particle in a coplanar-waveguide Penning trap. *Applied Physics B*, 107 (4). pp. 955-964.

- [63] D. J. Wineland and H. G. Dehmelt, Principles of the stored ion calorimeter, *Journal of Applied Physics* **46**, 919 (1975)
- [64] Feng, X Charlton, M Holzscheiter, Michael Lewis, RA Yamazaki, Yasunori. (1996). Tank circuit model applied to particles in a Penning trap. *Journal of Applied Physics*. 79. 8 - 13. 10.1063/1.360947.
- [65] D. M. Pozar. Microwave Engineering. John Wiley Sons, 4th edition, 2012.
- [66] D. Wineland, P. Ekstrom, and H. Dehmelt, *Phys. Rev. Lett*, 31, 1279 (1973)
- [67] F. Galve, P. Fernández, and G. Werth. Operation of a planar Penning trap. *The European Physical Journal D*, 40(2):201-204, 2006.
- [68] F. Galve and G. Werth. Motional frequencies in a planar Penning trap. *Hyperfine interactions*, 174(1-3):41-46, 2007
- [69] Haffner, H., Beier, T., Djekić, S. et al. Eur. Phys. J. D (2003) 22: 163. <https://doi.org/10.1140/epjd/e2003-00012-2>
- [70] J Verdú *et al.*, Electronic g-factor of Hydrogenlike Oxygen  $^{16}\text{O}^{7+}$ , *Phys. Rev. Lett.* 92, 093002, 2004
- [71] D. R. Crick, S. Donnellan, S. Ananthamurthy, R. C. Thompson<sup>1</sup>, and D. M. Segal, *Review of Scientific Instruments* 81, 013111 (2010)
- [72] H Dehmelt, Continuous Stern-Gerlach effect: Principle and idealized apparatus, *Proc Natl Acad Sci U S A*, (1986) Apr; 83(8): 22912294.
- [73] Sturm, S., Werth, G., and Blaum, K., Electron g-factor determination in Penning traps, *Annalen der Physik*, Volume 525, Issue 8-9, pp. 620-635, (2013)
- [74] D. Hanneke, Cavity Control in a Single-Electron Quantum Cyclotron: An Improved Measurement of the Electron Magnetic Moment, PhD thesis, Harvard University, 2007.
- [75] M. Wiesel, G. Birkl, M. S. Ebrahimi, A. Martin, W. Quint, N. Stallkamp, and M. Vogel, Optically transparent solid electrodes for precision Penning traps, *Review of Scientific Instruments*, **88**, 123101, (2017)
- [76] G.H. Low, P.F. Herskind, and I.L. Chuang, Finite-geometry models of electric field noise from patch potentials in ion traps, *Physical Review A*, **84**, 053425, (2011)

- [77] J.B. Camp, T.W. Darling, and R.E. Brown, *J. Appl. Phys.*, **69**, 7126, (1991)
- [78] I. Boldin, A. Kraft, and C. Wunderlich, *Phys. Rev. Lett.*, **120**, 023201, (2018)
- [79] M. Harlander *et al.*, *New J. Phys.*, **12**. 093035, (2010)
- [80] S. Narayanan *et al.*, *J. Appl. Phys.*, **110**, 114909, (2011)
- [81] S. Charles Doret *et al.*, *New J. Phys.*, **14**, 073012, (2012)
- [82] J. Verdú, S. Kreim, K. Blaum, H. Kracke, W. Quint, S. Ulmer, and J. Walz. Calculation of electrostatic fields using quasi-Green's functions: application to the hybrid Penning trap. *New Journal of Physics*, 10(10):103009, 2008. 146
- [83] G. Nogues, A. Rauschenbeutel, S. Osnaghi, M. Brune, J. M. Raimond, and S. Haroche, Seeing a single photon without destroying it, *Nature*, **400**, pp. 239242 (1999)
- [84] Romero, G.; Garca-Ripoll, J.J.; Solano, E. Microwave Photon Detector in Circuit QED. *Phys. Rev. Lett.* (2009), 102, 173602.
- [85] Peropadre,B.;Romero,G.;Johansson,G.;Wilson,C.M.;Solano,E.;Garca-Ripoll,J.J. Approaching perfect microwave photodetection in circuit QED. *Phys. Rev. A* (2011), 84, 063834.
- [86] Sathyamoorthy, S.R.; Stace, T.M.; Johansson, G. Detecting itinerant single microwave photons. *Comptes Rendus Physique* (2016), 17, 756765.
- [87] Yishun Wang, Fundamental Elements of Applied Superconductivity in Electrical Engineering, *Wiley Science Press*
- [88] Aixa Xu at NHMFL, March 2011. Retrieved from <http://fs.magnet.fsu.edu/lee/plot/plot.htm>, 26 June 2018
- [89] M. Tinkham, *Introduction to Superconductivity*. (Dover, New York, 2004).
- [90] Bertrand I. Halperin, Gil Refael, and Eugene Demler, *Int. J. Mod. Phys. B* 24, 4039 (2010)
- [91] J. Bardeen, L. N. Cooper, and J. R. Schrieffer, *Phys. Rev.* 108, 1175 (1957)
- [92] F. and H. London, *Proc. Roy. Soc. (London)* A149, 71 (1935)
- [93] Zoran Andelkovic, Setup of a Penning trap for precision laser spectroscopy at HITRAP, PhD thesis, Johannes Gutenberg-Universität Mainz, (2012)

- [94] A.A. Abrikosov, *Zh. Eksperim. i. Teor. Fiz* 32, 1442 (1957)
- [95] P.W. Anderson, Theory of flux creep in hard superconductors, *Physical Review Letters*, Volume 9, Number 7 (1962)
- [96] M.R. Beasley *et al.*, Flux creep in Type-II superconductors, *Physical Review*, Volume 181, Number 2, (1969)
- [97] G. Bednorz and K. A. Muller, *Z. Phys.* B64, 189 (1986)
- [98] X. Wei *et al.*, *Ceramics International* 42 (2016) 15836-15842
- [99] X. Wei *et al.*, *J. Mater. Chem. C.* (2017) 5, 3382
- [100] Retrieved from <http://www.superpower-inc.com/content/2g-hts-wire> 26 June 2018
- [101] J Kato-Yoshioka, N Sakai, S Tajima1,, S Miyata, T Watanabe,, Y Yamada, N Chikamoto, K Nakao, T Izumi and Y Shiohara, Low resistance joint of the YBCO coated conductor, *Journal of Physics: Conference Series*, Volume 43, (2006)
- [102] Geng, J. and Coombs, T.A., Mechanism of a high- $T_c$  superconducting flux pump: Using alternating magnetic field to trigger flux flow, *Applied Physics Letters* 107, 152601 (2015)
- [103] V. L. Ginzburg and L. D. Landau, *Zh. Eksperim. i. Teor. Fiz.* 20, 1064 (1950)
- [104] T.P. Orlando and K. A. Delin, *Foundations of Applied Superconductivity*, Addison Wesley
- [105] George A. Levin *et al.*, Persistent current coils made out of second generation high temperature superconductor wire, *Applied Physics Letters* 93, 062504 (2008)
- [106] Edward B. Rosa and Frederick W. Grover, *Formulas and Tables For the Calculation of Mutual and Self-Inductance*
- [107] E.H. Rhoderick and E. M. Wilson, Current distribution in thin superconducting films, *Nature* 194, 1167-1168 (1962)
- [108] E.F. Talantsev *et al.*, Universal scaling of the self-field critical current in superconductors: from sub-nanometre to millimetre size, *Scientific Reports* 7, 10010 (2017)
- [109] J. Verdú, *Private Communication*, (2016)
- [110] T. Coombs, Superconducting systems, WO2007045929 (2007)

- [111] Christian Hoffmann, Donald Pooke, and A. David Caplin, Flux Pump for HTS Magnets, *IEEE Transactions on Applied Superconductivity*, Vol. 21, No. 3, (2011)
- [112] Lin Fu *et al.*, Linear Flux Pump Device Applied to High Temperature Superconducting (HTS) Magnets, *IEEE Transactions on Applied Superconductivity*, Vol. 25, No. 3, (2015)
- [113] L.J.M. van de Klundert and H.H.J. ten Kate, Fully superconducting rectifiers and fluxpumps Part 1: Realized methods for pumping flux, *Cryogenics*, Vol 21, (1981)
- [114] L. J. M. van de Klundert and H. H. J. ten Kate, On fully superconducting rectifiers and flux pumps. A review. Part 2: Commutation modes, characteristics and switches, *Cryogenics*, vol. 21, no. 5, pp. 267277, May (1981).
- [115] J. Geng *et al.*, *J. Phys D. Appl. Phys.* 49 (2016)
- [116] T.A.Coombs, J. Geng, L. Fu, K. Matsuda, An Overview of Flux Pumps for HTS Coils, *IEEE Transactions on Applied Superconductivity* ( Volume: 27, Issue: 4, June 2017 )
- [117] Wei Wang, An investigation into High Temperature Superconducting flux pump technology with the circular type magnetic flux pump devices and YBaCuO films, PhD thesis, (2014)
- [118] Yong-Soo Yoon, Sang-Jin Lee, Tae-Su Han, Ho-Min Kim, Chang-Yul Lee, Yong Chu, Tae Kuk Ko, Design, Fabrication and Testing of a Heater-Triggered High-Tc Superconducting Power Supply, *IEEE Transactions on Applied Superconductivity* Vol. 10, No. 1, (2000)
- [119] R.S. Van Dyck, D. L. Farnham, S. L. Zafonte, and P.B. Schwinberg, Ultrastable superconducting magnet system for a Penning trap mass spectrometer, *Review of Scientific Instruments*, **70**, 1665 (1999)
- [120] P. J. Lee, Superconductor: wires and cables: materials and processes, The Applied Superconductivity Center, University of Wisconsin-Madison, <https://pdfs.semanticscholar.org/b01a/93621fc95eb050269c9adb464f30e5437a23.pdf>, (May 2016)

## Appendix A

# Summary of flux pumping mechanisms

In §5, the flux pumping mechanisms used for the operation of the planar magnetic field source of the Geonium Chip were discussed. In this Appendix, tabular summaries for flux pumping mechanisms are given: standard flux pumping (Table A.1), reverse flux pumping (Table A.2.), flux pumping of two double-loop superconducting structures with overlapping Target Loops (Table A.3), and flux pumping of two double-loop superconducting structures with adjacently placed Target Loops (Table A.4). When consulting Tables A.1, A.2, A.3, and A.4, the reader is advised to refer to Figures 5.5, 5.9, 5.12, and 5.13 respectively.

Step #	Heat Switch 1	Heat Switch 2	Applied flux $\phi_a$	Current
1	OFF $\rightarrow$ ON	OFF $\rightarrow$ OFF	OFF $\rightarrow$ OFF	$I \rightarrow I$
2	ON $\rightarrow$ ON	OFF $\rightarrow$ OFF	OFF $\rightarrow$ ON	$I \rightarrow I$
3	ON $\rightarrow$ OFF	OFF $\rightarrow$ OFF	ON $\rightarrow$ ON	$I \rightarrow I$
4	OFF $\rightarrow$ OFF	OFF $\rightarrow$ ON	ON $\rightarrow$ ON	$I \rightarrow I'$
5	OFF $\rightarrow$ OFF	ON $\rightarrow$ ON	ON $\rightarrow$ OFF	$I' \rightarrow I''$
6	OFF $\rightarrow$ OFF	ON $\rightarrow$ OFF	OFF $\rightarrow$ OFF	$I'' \rightarrow I''$
7	OFF $\rightarrow$ ON	OFF $\rightarrow$ OFF	OFF $\rightarrow$ OFF	$I'' \rightarrow I'''$
8	ON $\rightarrow$ OFF	OFF $\rightarrow$ OFF	OFF $\rightarrow$ OFF	$I''' \rightarrow I'''$

$$I' = \frac{2l_1+2l_2-l_4}{2(l_1+l_2+l_3)} I ; I'' = \frac{2l_1+2l_2-l_4}{2(l_1+l_2+l_3)} I + \frac{\phi_a}{2k(l_1+l_2+l_3)} ; I''' = \frac{(2l_1+2l_2-l_4)^2}{4(l_1+l_2)(l_1+l_2+l_3)} I + \frac{(2l_1+2l_2-l_4)\phi_a}{4k(l_1+l_2)(l_1+l_2+l_3)}$$

**Recursive formula:**  $I_n = \frac{(2l_1+2l_2-l_4)^2}{4(l_1+l_2)(l_1+l_2+l_3)} I_{n-1} + \frac{(2l_1+2l_2-l_4)\phi_a}{4k(l_1+l_2)(l_1+l_2+l_3)}$

**Current after N cycles:**  $I_N = \frac{(2l_1+2l_2-l_4)\phi_a}{4k(l_1+l_2)(l_1+l_2+l_3)} \left( 1 - \left( \frac{(2l_1+2l_2-l_4)^2}{4(l_1+l_2)(l_1+l_2+l_3)} \right)^N \right)$

**Maximum current:**  $I_\infty = \frac{(2l_1+2l_2-l_4)\phi_a}{k[4(l_1+l_2)(l_3+l_4)-l_4^2]}$

Table A.1: Table summarising the standard flux pumping scheme for a double-loop superconducting structure. When consulting this table, refer to Figure 5.5.

Step #	Heat Switch 1	Heat Switch 2	Applied flux $\phi_a$	Current
1	OFF $\rightarrow$ OFF	OFF $\rightarrow$ OFF	OFF $\rightarrow$ ON	$I \rightarrow \{I'_1, I'_2, I'_3\}$
2	OFF $\rightarrow$ OFF	OFF $\rightarrow$ ON	ON $\rightarrow$ ON	$\{I'_1, I'_2, I'_3\} \rightarrow I''$
3	OFF $\rightarrow$ OFF	ON $\rightarrow$ ON	ON $\rightarrow$ OFF	$I'' \rightarrow I'''$
4	OFF $\rightarrow$ OFF	ON $\rightarrow$ OFF	OFF $\rightarrow$ OFF	$I''' \rightarrow I''''$
5	OFF $\rightarrow$ ON	OFF $\rightarrow$ OFF	OFF $\rightarrow$ OFF	$I'''' \rightarrow I''''$
6	ON $\rightarrow$ OFF	OFF $\rightarrow$ OFF	OFF $\rightarrow$ OFF	$I'''' \rightarrow I''''$

$$I'_1 = I - \frac{\phi_a l_4}{k[(2l_1+2l_2-l_4)l_4+(2l_3+l_4)(2l_1+2l_2)]}; I'_2 = \frac{-\phi_a(2l_1+2l_2)}{k[(2l_1+2l_2-l_4)l_4+(2l_3+l_4)(2l_1+2l_2)]}; I'_3 = I + \frac{(2l_1+2l_2-l_4)\phi_a}{k[(2l_1+2l_2-l_4)l_4+(2l_3+l_4)(2l_1+2l_2)]}$$

$$I'' = \left( \frac{2l_1+2l_2-l_4}{2l_1+2l_2+2l_3} \right) I - \frac{\phi_a}{k(2l_1+2l_2+2l_3)}; I''' = \left( \frac{2l_1+2l_2-l_4}{2l_1+2l_2+2l_3} \right) I; I'''' = \frac{(2l_1+2l_2-l_4)^2}{(2l_1+2l_2)(2l_1+2l_2+2l_3)} I$$

**Recursion formula:**  $I_n = \frac{(2l_1+2l_2-l_4)^2}{(2l_1+2l_2)(2l_1+2l_2+2l_3)} I_{n-1}$

**Current after  $N$  cycles:**  $I_N = \left( \frac{(2l_1+2l_2-l_4)^2}{(2l_1+2l_2)(2l_1+2l_2+2l_3)} \right)^N I_0$

Table A.2: Table summarising the flux subtraction scheme for a double-loop superconducting structure. When consulting this table, refer to Figure 5.9.

Step #	Heat Switch 1U	Heat Switch 2U	Heat Switch 1L	Heat Switch 2L	Applied flux $\phi_a^{(u)}$	Applied flux $\phi_a^{(l)}$	Currents
1	OFF $\rightarrow$ ON	OFF $\rightarrow$ OFF	OFF $\rightarrow$ ON	OFF $\rightarrow$ OFF	OFF $\rightarrow$ OFF	OFF $\rightarrow$ OFF	$\{I^{(u)}, I^{(l)}\} \rightarrow \{I^{(u)}, I^{(l)}\}$
2	ON $\rightarrow$ ON	OFF $\rightarrow$ OFF	ON $\rightarrow$ ON	OFF $\rightarrow$ OFF	OFF $\rightarrow$ ON	OFF $\rightarrow$ ON	$\{I^{(u)}, I^{(l)}\} \rightarrow \{I^{(u)}, I^{(l)}\}$
3	ON $\rightarrow$ OFF	OFF $\rightarrow$ OFF	ON $\rightarrow$ OFF	OFF $\rightarrow$ OFF	ON $\rightarrow$ ON	ON $\rightarrow$ ON	$\{I^{(u)}, I^{(l)}\} \rightarrow \{I^{(u)}, I^{(l)}\}$
4	OFF $\rightarrow$ OFF	OFF $\rightarrow$ ON	OFF $\rightarrow$ OFF	OFF $\rightarrow$ ON	ON $\rightarrow$ ON	ON $\rightarrow$ ON	$\{I^{(u)}, I^{(l)}\} \rightarrow \{I^{(u)'}, I^{(l)'}\}$
5	OFF $\rightarrow$ OFF	ON $\rightarrow$ ON	OFF $\rightarrow$ OFF	ON $\rightarrow$ ON	ON $\rightarrow$ OFF	ON $\rightarrow$ OFF	$\{I^{(u)'}, I^{(l)'}\} \rightarrow \{I^{(u)'}, I^{(l)'}\}$
6	OFF $\rightarrow$ OFF	ON $\rightarrow$ OFF	OFF $\rightarrow$ OFF	ON $\rightarrow$ OFF	OFF $\rightarrow$ OFF	OFF $\rightarrow$ OFF	$\{I^{(u)'}, I^{(l)'}\} \rightarrow \{I^{(u)'}, I^{(l)'}\}$
7	OFF $\rightarrow$ ON	OFF $\rightarrow$ OFF	OFF $\rightarrow$ ON	OFF $\rightarrow$ OFF	OFF $\rightarrow$ OFF	OFF $\rightarrow$ OFF	$\{I^{(u)'}, I^{(l)'}\} \rightarrow \{I^{(u)'}, I^{(l)'}\}$
8	ON $\rightarrow$ OFF	OFF $\rightarrow$ OFF	ON $\rightarrow$ OFF	OFF $\rightarrow$ OFF	OFF $\rightarrow$ OFF	OFF $\rightarrow$ OFF	$\{I^{(u)'}, I^{(l)'}\} \rightarrow \{I^{(u)'}, I^{(l)'}\}$

$$\begin{pmatrix} I_u' \\ I_l' \end{pmatrix} = \frac{1}{36-4m^2} \begin{pmatrix} 18-6m^2 & 12m \\ 12m & 18-6m^2 \end{pmatrix} \begin{pmatrix} I_u \\ I_l \end{pmatrix}$$

$$\begin{pmatrix} I_u'' \\ I_l'' \end{pmatrix} = \frac{1}{36-4m^2} \begin{pmatrix} 18-6m^2 & 12m \\ 12m & 18-6m^2 \end{pmatrix} \begin{pmatrix} I_u \\ I_l \end{pmatrix} + \frac{1}{kl(36-4m^2)} \begin{pmatrix} 6 & -2m \\ -2m & 6 \end{pmatrix} \begin{pmatrix} \phi_u \\ \phi_l \end{pmatrix}$$

$$\begin{pmatrix} I_u''' \\ I_l''' \end{pmatrix} = \frac{(12-12m)}{(16-16m^2)(36-4m^2)} \left[ \begin{pmatrix} 18-6m^2 & 12m \\ 12m & 18-6m^2 \end{pmatrix} \begin{pmatrix} I_u \\ I_l \end{pmatrix} + \frac{1}{kl} \begin{pmatrix} 6 & -2m \\ -2m & 6 \end{pmatrix} \begin{pmatrix} \phi_u \\ \phi_l \end{pmatrix} \right]$$

$$\text{Recursion formula : } \begin{pmatrix} I_n^{(u)} \\ I_n^{(l)} \end{pmatrix} = \frac{(12-12m)}{(16-16m^2)(36-4m^2)} \left[ \begin{pmatrix} 18-6m^2 & 12m \\ 12m & 18-6m^2 \end{pmatrix} \begin{pmatrix} I_n^{(u)} \\ I_n^{(l)} \end{pmatrix} + \frac{1}{kl} \begin{pmatrix} 6 & -2m \\ -2m & 6 \end{pmatrix} \begin{pmatrix} \phi_a^{(u)} \\ \phi_a^{(l)} \end{pmatrix} \right]$$

Table A.3: Table summarising the flux pumping scheme for double-loop structures with overlapping Target Loops. When consulting this table, refer to Figure 5.12. ‘‘U’’ and ‘‘u’’ refer to the upper double-loop superconducting structure, and ‘‘L’’ and ‘‘l’’ refer to the lower double-loop superconducting structure.

Step #	Heat Switch 1L	Heat Switch 2L	Heat Switch 1R	Heat Switch 2R	Applied flux $\phi_a^{(l)}$	Applied flux $\phi_a^{(r)}$	Currents
1	OFF $\rightarrow$ ON	OFF $\rightarrow$ OFF	OFF $\rightarrow$ ON	OFF $\rightarrow$ OFF	OFF $\rightarrow$ OFF	OFF $\rightarrow$ OFF	$\{I^{(l)}, I^{(r)}\} \rightarrow \{I^{(l)}, I^{(r)}\}$
2	ON $\rightarrow$ ON	OFF $\rightarrow$ OFF	ON $\rightarrow$ ON	OFF $\rightarrow$ OFF	OFF $\rightarrow$ ON	OFF $\rightarrow$ ON	$\{I^{(l)}, I^{(r)}\} \rightarrow \{I^{(l)}, I^{(r)}\}$
3	ON $\rightarrow$ OFF	OFF $\rightarrow$ OFF	ON $\rightarrow$ OFF	OFF $\rightarrow$ OFF	ON $\rightarrow$ ON	ON $\rightarrow$ ON	$\{I^{(l)}, I^{(r)}\} \rightarrow \{I^{(l)}, I^{(r)}\}$
4	OFF $\rightarrow$ OFF	OFF $\rightarrow$ ON	OFF $\rightarrow$ OFF	OFF $\rightarrow$ ON	ON $\rightarrow$ ON	ON $\rightarrow$ ON	$\{I^{(l)}, I^{(r)}\} \rightarrow \{I^{(l)'}, I^{(r)'}\}$
5	OFF $\rightarrow$ OFF	ON $\rightarrow$ ON	OFF $\rightarrow$ OFF	ON $\rightarrow$ ON	ON $\rightarrow$ OFF	ON $\rightarrow$ OFF	$\{I^{(u)'}, I^{(r)'}\} \rightarrow \{I^{(l)''}, I^{(r)''}\}$
6	OFF $\rightarrow$ OFF	ON $\rightarrow$ OFF	OFF $\rightarrow$ OFF	ON $\rightarrow$ OFF	OFF $\rightarrow$ OFF	OFF $\rightarrow$ OFF	$\{I^{(l)''}, I^{(r)''}\} \rightarrow \{I^{(l)'''}, I^{(r)'''}\}$
7	OFF $\rightarrow$ ON	OFF $\rightarrow$ OFF	OFF $\rightarrow$ ON	OFF $\rightarrow$ OFF	OFF $\rightarrow$ OFF	OFF $\rightarrow$ OFF	$\{I^{(l)'''}, I^{(r)'''}\} \rightarrow \{I^{(l)''''}, I^{(r)''''}\}$
8	ON $\rightarrow$ OFF	OFF $\rightarrow$ OFF	ON $\rightarrow$ OFF	OFF $\rightarrow$ OFF	OFF $\rightarrow$ OFF	OFF $\rightarrow$ OFF	$\{I^{(l)''''}, I^{(r)''''}\} \rightarrow \{I^{(l)'''''}, I^{(r)'''''}\}$

$$\begin{pmatrix} I_l''' \\ I_r''' \end{pmatrix} = \frac{1}{(16-m^2)(36-m^2)} \begin{pmatrix} 12-m^2 & m \\ m & 12-m^2 \end{pmatrix} \begin{pmatrix} 18-m^2 & 3m \\ 3m & 18-m^2 \end{pmatrix} \begin{pmatrix} I_l'' \\ I_r'' \end{pmatrix} = \frac{1}{36-m^2} \begin{pmatrix} 18-m^2 & 3m \\ 3m & 18-m^2 \end{pmatrix} \begin{pmatrix} I_l' \\ I_r' \end{pmatrix} = \frac{1}{36-m^2} \begin{pmatrix} 18-m^2 & 3m \\ 3m & 18-m^2 \end{pmatrix} \begin{pmatrix} I_l \\ I_r \end{pmatrix}$$
  

$$\begin{pmatrix} I_l'''' \\ I_r'''' \end{pmatrix} = \frac{1}{(16-m^2)(36-m^2)} \begin{pmatrix} 12-m^2 & m \\ m & 12-m^2 \end{pmatrix} \left[ \begin{pmatrix} 18-m^2 & 3m \\ 3m & 18-m^2 \end{pmatrix} \left[ \begin{pmatrix} 18-m^2 & 3m \\ 3m & 18-m^2 \end{pmatrix} \left[ \begin{pmatrix} I_l \\ I_r \end{pmatrix} + \frac{1}{kl} \begin{pmatrix} 6 & -m \\ -2 & 6 \end{pmatrix} \begin{pmatrix} \phi_l \\ \phi_r \end{pmatrix} \right] + \frac{1}{kl} \begin{pmatrix} 6 & -m \\ -m & 6 \end{pmatrix} \begin{pmatrix} \phi_l \\ \phi_r \end{pmatrix} \right] \right]$$
  
**Recursion formula :** 
$$\begin{pmatrix} I_n^{(l)} \\ I_n^{(r)} \end{pmatrix} = \frac{1}{(16-m^2)(36-m^2)} \begin{pmatrix} 12-m^2 & m \\ m & 12-m^2 \end{pmatrix} \left[ \begin{pmatrix} 12-m^2 & m \\ m & 12-m^2 \end{pmatrix} \left[ \begin{pmatrix} 18-m^2 & 3m \\ 3m & 18-m^2 \end{pmatrix} \left[ \begin{pmatrix} I_n^{(l)} \\ I_n^{(r)} \end{pmatrix} + \frac{1}{kl} \begin{pmatrix} 6 & -m \\ -m & 6 \end{pmatrix} \begin{pmatrix} \phi_a^{(l)} \\ \phi_a^{(r)} \end{pmatrix} \right] \right] \right]$$

Table A.4: Table summarising the flux pumping scheme for double-loop structures with adjacently placed Target Loops. When consulting this table, refer to Figure 5.12. “L” and “r” refer to the left-hand double-loop superconducting structure, and “R” and ‘r’ refer to the double-loop superconducting structure on the right-hand side.

## Appendix B

# Magnetic field source data

The design of the planar magnetic field source is discussed in §6. This Appendix presents tables of data showing the required current densities, the magnetic forces between each loops, and the magnetic field strengths on each loop vary with superconductor thickness. The proposed design is that corresponding to the dimensions of configuration 9 (see Table 6.1), and the data in the tables presented in this Appendix correspond to calculations for a desired 0.5 T homogeneous magnetic field a height of 1.6 mm above the planar magnetic field source.

Thickness (mm)	$J_0(\text{Amm}^{-2})$	$J_1(\text{Amm}^{-2})$	$J_2(\text{Amm}^{-2})$	$J_3(\text{Amm}^{-2})$	$J_4(\text{Amm}^{-2})$
0.50	3266	2215	4392	-4986	5396
0.75	2178	1482	2829	-3044	3628
1.00	1634	1105	2164	-2352	2657
1.25	1309	875	1807	-2032	2154
1.50	1092	719	1586	-1860	1827
1.75	937	607	1439	-1759	1597
2.00	821	523	1335	-1696	1427
2.25	730	458	1258	-1655	1296
2.50	657	406	1198	-1628	1192
2.75	598	363	1150	-1610	1108
3.00	548	329	1112	-1598	1039

Table B.1: Table showing the current densities required to achieve a 0.5 T homogeneous field at a height of 1.6 mm above the planar magnetic field source for configuration 9 with various thicknesses.

Thickness (mm)	$B_0$ (T)	$B_1$ (T)	$B_2$ (T)	$B_3$ (T)	$B_4$ (T)	$F_0$ (N)	$F_1$ (N)	$F_2$ (N)	$F_3$ (N)	$F_4$ (N)
0.50										
0.75										
1.00	2.4	3.9	5.7	17.4	2.0	101	208	587	2258	2896
1.25	2.6	4.0	5.9	17.7	2.0	104	211	629	2479	3094
1.50	2.6	4.1	6.1	18.1	2.2	107	214	685	2783	363
1.75	2.7	4.2	6.3	18.5	2.4	111	212	753	3144	3681
2.00	2.8	4.3	6.6	19.0	2.5	115	222	831	3554	4040
2.25	2.9	4.5	6.8	19.5	2.7	119	226	917	4000	4429
2.50	3.0	4.1	7.1	20.0	2.9	123	232	1011	4442	4849
2.75	2.8	4.4	6.7	18.7	2.8	105	194	918	4147	4378
3.00	3.2	5.0	7.7	21.1	2.3	132	240	1219	5582	5777

Table B.2: Table showing the magnetic fields and forces on each loop of configuration 9 for different thicknesses. For each case, a desired homogeneous magnetic field of 0.5 T at a height of 1.6 mm is considered. Calculations for 0.50 mm and 0.75 mm are not considered because the corresponding current densities exceed  $J_c$  of niobium-titanium.